Pion Single Charge Exchange on the Deuteron

by

Hojoon Timothy Park

B.S., Physics
Lehigh University
June 1986

Submitted to the Department of Physics
in partial fulfillment of the requirements for the degree of

Doctor of Philosophy

at the

MASSACHUSETTS INSTITUTE OF TECHNOLOGY

February 1995

Signature of Author .....
Department of Physics
February 24, 1995

Certified by .....
Professor June L. Matthews
Professor of Physics
Thesis Supervisor

Accepted by .....
Professor George F. Koster
Chairman of the Graduate Committee

Science

Pion Single Charge Exchange on the Deuteron

by

Hojoon Timothy Park

Submitted to the Department of Physics
on February 24, 1995, in partial fulfillment of the
requirements for the degree of
Doctor of Philosophy

Abstract

Cross sections for the pion single charge exchange (SCX) reaction on the deuteron ($\pi^- + d \rightarrow \pi^0 + n + n$) for $\theta_{\pi^0}^{\rm Lab} = 0^\circ \sim 150^\circ$ at incident pion energies of 164, 263, and 371 MeV have been measured at the Los Alamos Meson Physics Facility (LAMPF). No previous measurement exists between 164 MeV and 500 MeV.

One crate of the LAMPF Neutral Meson Spectrometer, composed of 60 CsI crystals, was used to detect both photons from the π^0 decay. The absolute value of the detector acceptance was obtained by comparing the yields from SCX on the proton ($\pi^- + p \rightarrow \pi^0 + n$) to the known cross sections, while its energy dependence was provided by a Monte Carlo calculation.

The measurements aimed to examine the effect of the extra nucleon in the deuteron, beyond the one required for the charge exchange, on the SCX process. An impulse approximation calculation including a realistic nucleon momentum distribution describes the energy spectra in the doubly differential cross section well, showing the dominance of the quasifree process. The low energy tail in the spectrum which deviates from the calculation can be attributed to multiple scattering effects. The angular distribution at forward angles shows suppression of the cross sections as compared to the impulse approximation values. A phenomenological model in which the spin-non-flip part of the impulse approximation cross section was suppressed by Pauli-blocking describes the shape of the angular distribution well at all energies. A Faddeev calculation at 164 MeV incorporating Pauli-blocking and multiple scattering agrees well with the measured angular distribution.

Thesis Supervisor: Professor June L. Matthews
Title: Professor of Physics

Acknowledgements

First I'd like to thank my thesis adviser June Matthews for her guidance in my work. She was always very supportive and allowed for lots of freedom in my research.

I'd like to thank every member of the experiment 1272 collaboration. They are June Matthews, Steve Pate, Mark Whitton, Jim Amann, Ed Kinney, Chris Morris, Dick Boudrie, Mohini Rawool-Sullivan, Christoff Mertz, Dave Rowntree, Lynn Nguyen-Tansill, Patrick Hui. Their expertise and hard work made the experiment successful. Gerald Montoya and Scott Schilling at the drafting, Byron McCloud, Laurens Quintana at MP-10 machine shop, Ronald Richardson at the LEEP, Frederick Montoya, Arthur Gonzales at the Scintillator shop and Jeff and Warren from GWU provided essential support at every stage of the experimental preparation.

Peter Gram was a kind and patient teacher during the early stage of my training at LAMPF. Lupe Newdeckeer, Becky Fernandes, Bernedette Pesenti and Charles Woodard were very helpful in getting things done in the Lab and fun to talk to.

Seonhoon Hyung and I shared lots of fun times at Los Alamos and along with Yi-Fen, we enjoyed our lunch discussions.

I'd like to thank Mark Yuly, Mark Wang, Dr. Kim, Wilson Fong, Nik Gregory, Art Mateos, for our discussions on physics, work, and life. Tom, DJ, Shiaobin, Ying and Vladmir made the penthouse a fun place to work. Joanne Gregory was always very helpful and was good to talk to. I'd like to thank Sam, Kevin Wilson, Roz, Subhendu, Vipul, Kevin Lee, BS, Kyungseon and Taeksu for their close friendship to me. Dave and Frank helped me through some of the toughest times.

I'd like to thank my God-parents, Daniel, Heidi for their love and support for me. I'd like to thank TTangga Halmuni, Mom and Dad, Sue, Darrel and the memory of YunPeung Halmuni for their love and support for me.

My wife Mary was always accepting and supportive of me and brought so much joy into my life.

I'd like to thank God through whom all things are made [John 1:3].

Contents

List of Figures

List of Tables

Chapter 1

Introduction

This thesis presents a study of the single charge exchange (SCX) reaction in which an incoming negative pion exchanges one unit of charge with the proton in the deuteron: $\pi^- + d \rightarrow \pi^0 + n + n$. In this work the differential cross sections for this reaction were measured at incident energies $T_{\pi^-} =$ 164, 263 and 371 MeV and outgoing π^0 angles $0° < \theta_{\pi^0}^{\mathrm{LAB}} < 150°$.

1.1 Quark Model of the Baryons and Mesons

In the quark model, the baryons (such as protons and neutrons) are composed of three quarks, while the mesons (such as pions) are composed of a quark-anti-quark pair. In the theory of the strong interaction known as Quantum Chromo-Dynamics (QCD), gluons mediate the interactions among the quarks and bind them. The existence of the individual quarks was confirmed by an electron proton inelastic scattering experiment.

At low energies, electron-proton scattering is necessarily elastic. But if the incident electron energy is large enough, other particles such as pions, kaons, and other mesons may come out of the reaction. The electron proton inelastic cross section can be written in terms of proton structure functions and a few kinematic variables. In the late 1960's, Bjorken showed that if the quarks were truly elementary particles constituting the proton, then at very high energies, the proton structure functions can be written as functions only of a scaling variable x, which is defined as[17]:

$$x \equiv \frac{-q^\mu q_\mu}{2 q^\mu p_{2\,\mu}} \,, \tag{1.1}$$

where

$q^\mu = p_1^\mu - p_3^\mu$
p_1^μ is the four-momentum of the incoming electron
p_3^μ is the four-momentum of the scattered electron
p_2^μ is the four-momentum of the target proton.

The results of the "deep inelastic electron proton scattering" experiment at SLAC provided experimental evidence of the scaling postulated by Bjorken. This scaling is observed to occur for $q^2 \geq 1$ (GeV/c)^2 and $q^\mu p_{2\,\mu} \geq 3.5$ (GeV/c)^2[17]. Although we believe quarks to be fundamental constituents of baryons and mesons, it is only at such high momentum transfer that the quark-gluon degrees of freedom reveal themselves. For $q^2 \leq 0.45$ (GeV/c)^2, as in the work presented in this thesis, baryons and mesons may be considered as elementary particles.

The pion is a meson with spin 0 and negative parity[18]. It has three charge states, π^+, π^0, π^- corresponding to the three projections of its isospin (T=1). The charged pions have mass 140 MeV, lifetime 2.6×10^{-8} seconds and decay primarily into a muon and a muon-neutrino via the weak interaction. The neutral pion has mass 135 MeV and lifetime 8.4×10^{-17} seconds. It decays electromagnetically into two photons.

Yukawa first predicted the existence of the pion[19]. He suggested that pions were exchanged to mediate the nuclear force by relating the pion mass to the range of the nuclear force. During the exchange of the pion energy conservation is violated[20]. This can happen only for a short period of time allowed by the uncertainty principle such that:

$$\Delta t\, \Delta E \geq \hbar\,. \tag{1.2}$$

The range of the nuclear force is about 1.4 fm and therefore:

$$\Delta r = c\,\Delta t < 1.4\,fm \tag{1.3}$$
$$\Delta t < 1.4\,\frac{fm}{c} \tag{1.4}$$
$$\Delta E > \frac{\hbar}{\Delta t} \tag{1.5}$$
$$\Delta E > 140 MeV\,. \tag{1.6}$$

The mass of the the lightest exchanged particle (m_π) is then 140 MeV/c^2. With a larger value for the nuclear force range, Yukawa predicted the pion mass to be about 100 MeV/c^2[19].

1.2 Pion-Nucleon Interaction

Shown in Figure 1-1 are the πN total cross sections as a function of the pion energy. It is seen that the πN (pion-nucleon) interaction in our energy range is dominated by the formation of a resonance called the "$\Delta(3,3)$ resonance". It has an energy of 1232 MeV, width of 115 MeV, isospin 3/2, spin 3/2, and parity even. The Δ has four charge states corresponding to the isospin projections; Δ^{++}, Δ^{+}, Δ^{0} and Δ^{-}. More than 99 % of the time the Δ decays into a nucleon and a pion; less than 1 % of the time it decays into a nucleon and a photon.

In Figure 1-3 are shown angular distributions of the pion single charge exchange (SCX) cross sections on the proton at several pion kinetic energies. The shape of the angular distributions in Figure 1-3 can be explained by simple scattering theory. In the scattering formalism, the differential scattering cross section is defined as:

$$\frac{d\sigma}{d\Omega} = \sum_{S_N} |f_{\beta\alpha}|^2, \tag{1.7}$$

where

$f_{\alpha\beta}$ is the πN scattering amplitude

α, β are quantum numbers of the initial and final pion

S_N is the nucleon spin.

The quantity $f_{\beta\alpha}$ is given as:

$$f_{\beta\alpha}(E, \hat{k}, \hat{k'}) = f(E,\theta) + g(E,\theta) i\vec{\sigma} \cdot \hat{n}, \tag{1.8}$$

where

$f(E,\theta)$ is the spin-non-flip amplitude

$g(E,\theta)$ is the spin-flip amplitude

$\hat{n} = \frac{(\hat{k} \times \hat{k'})}{|\hat{k} \times \hat{k'}|}$

$\vec{k}$, $\vec{k'}$ are momentum vectors of the initial and final pion

$\vec{\sigma}$ is the Pauli spin matrix for the nucleon

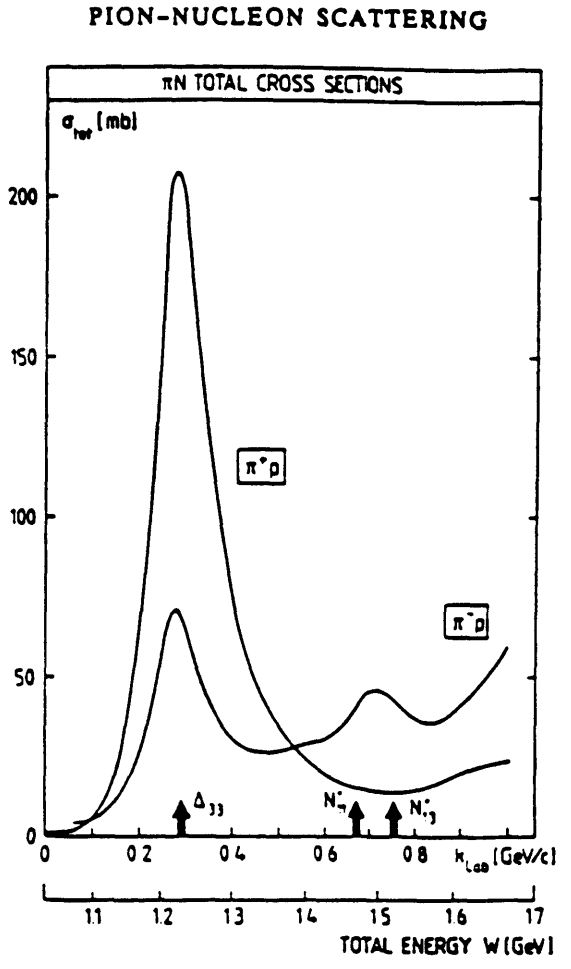

Figure 1-1: Total cross sections for $\pi^+ p$ and $\pi^- p$ scattering as a function of the total c.m. energy W and the pion lab momentum k_{Lab}. (The plot is from Ericson[1].)

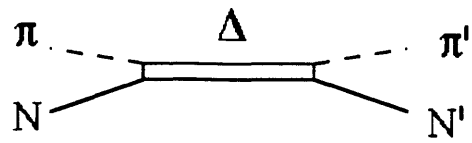

Figure 1-2: The Feynman diagram for a πN scattering through the formation of a Δ.

E is the total energy of the system in the center of mass frame

θ is the angle between $\hat{k}$ and $\hat{k}'$.

The differential cross section is then written as:

$$\frac{d\sigma}{d\Omega}(E,\theta) = |f(E,\theta)|^2 + |g(E,\theta)|^2. \tag{1.9}$$

The amplitudes $f(E,\theta)$ and $g(E,\theta)$ can be expanded in terms of partial waves as follows:

$$f(E,\theta) = \sum_{l=0}^{\infty}\{(l+1)f_{l+}(E) + l f_{l-}(E)\}P_l(\cos\theta), \tag{1.10}$$

$$g(E,\theta) = \sum_{l=0}^{\infty}\{f_{l+}(E) - f_{l-}(E)\}P_l'(\cos\theta)\sin\theta, \tag{1.11}$$

where

$P_l(\cos\theta)$ is a Legendre function, $P_l(x)$, $x = \cos\theta$

$P_l'(x) = \frac{dP_l(x)}{dx}$.

$f_{l\pm}$ means $f_{l\,J=l\pm 1/2}$, since the orbital angular momentum (l) and the total angular momentum (J) are both good quantum numbers of the πN system (in the center of mass frame).

When an intermediate state is a pure Δ state, by the parity and angular momentum conservation argument p-wave (l=1) scattering between the pion and the nucleon is preferred. The scattering amplitudes are then given by:

$$f(E,\theta) = 2f_{3/2}\cos\theta \tag{1.12}$$

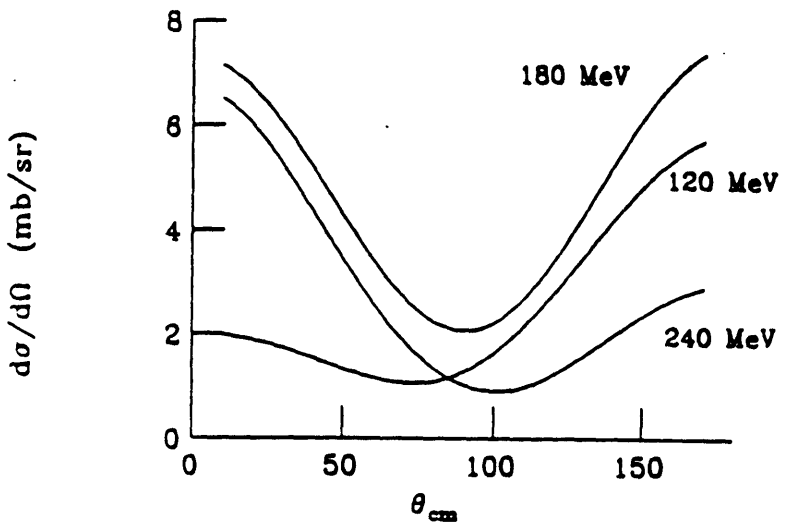

Figure 1-3: Center of Mass differential cross sections for the SCX reaction $\pi^- p \rightarrow \pi^0 n$ at 120, 180 and 240 MeV. The curves are from the phase shift calculations of Arndt *et al.* [2]. (The plot is from Kinney[3].)

and

$$g(E,\theta) = f_{3/2} \cdot 1 \cdot \sin\theta. \tag{1.13}$$

The differential cross section is given as:

$$\frac{d\sigma}{d\Omega} = |f|^2 + |g|^2 = f_{3/2}^2(1 + 3\cos^2\theta). \tag{1.14}$$

In Figure 1-3 the shape of the angular distribution at the Δ resonance energy (180 MeV) indeed follows the angular dependence predicted in Equation (1.14).

The deuteron is the simplest nucleus, being a two-nucleon bound state, with a a binding energy 2.2 MeV. The ground state of the deuteron is primarily a $^3S_1$ state with a small admixture of D state ($4 \sim 7$ %). The neutron and proton in the deuteron are in an isospin singlet state.

The πd reaction has the following channels, in order of decreasing total cross section in the Δ resonance region:

$$\begin{aligned}
\pi^{\pm} &\rightarrow \pi^{\pm}NN \text{ (breakup)} \\
&\rightarrow \pi^{\pm}d \quad \text{(elastic scattering)} \\
&\rightarrow \pi^{0}NN \text{ (charge exchange)} \\
&\rightarrow NN \quad \text{(absorption)} \\
&\rightarrow \pi\pi NN \text{ (pion induced pion production)}
\end{aligned}$$

In the breakup reaction the pion dissociates the deuteron into proton and neutron. Elastic scattering corresponds to the deuteron recoiling coherently against the pion. In a charge exchange reaction on the deuteron only one unit of charge exchange (single charge exchange) is allowed. Pions can also be absorbed in an interaction with the deuteron since energy and momentum conservation allow this reaction if there are two or more nucleons present. Pion-induced-pion-production corresponds to a creation of a second pion and is allowed for incident kinetic energy greater than the threshold energy 165 MeV.

In Figure 1-4 and Figure 1-5 are shown the πd total cross sections as functions of the pion energy. The dashed curves represent the impulse approximation (IA), in which the deuteron consists of two "free" nucleons and the total cross section is the sum of the πp and πn cross section as:

$$\sigma_{\pi d} = \sigma_{\pi p} + \sigma_{\pi n}. \tag{1.15}$$

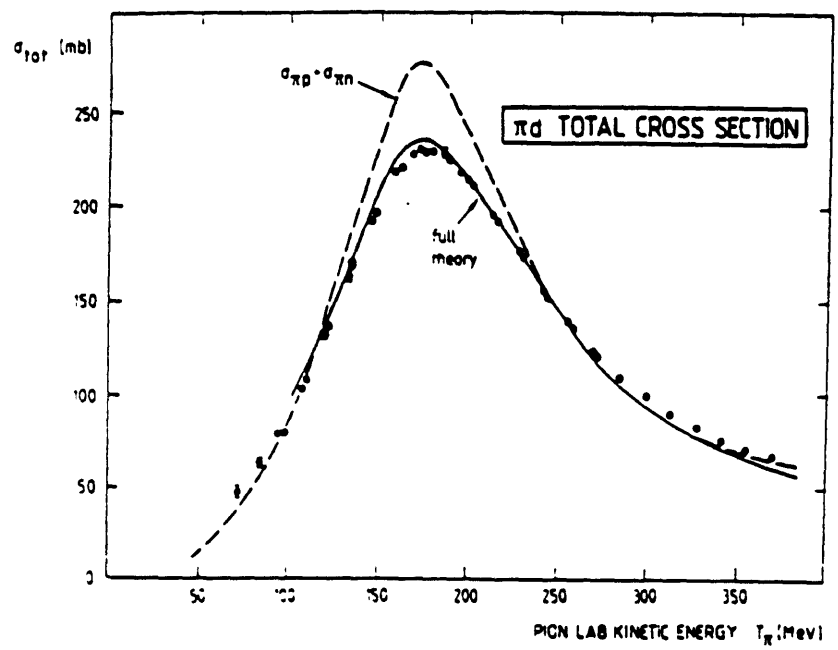

Figure 1-4: The πd total reaction cross section compared to the sum of πn and πp total cross sections in the $\Delta(1232)$ resonance region. The solid line labelled 'full theory' includes nucleon motion and double scattering effects. (The plot is from Ericson[1].)

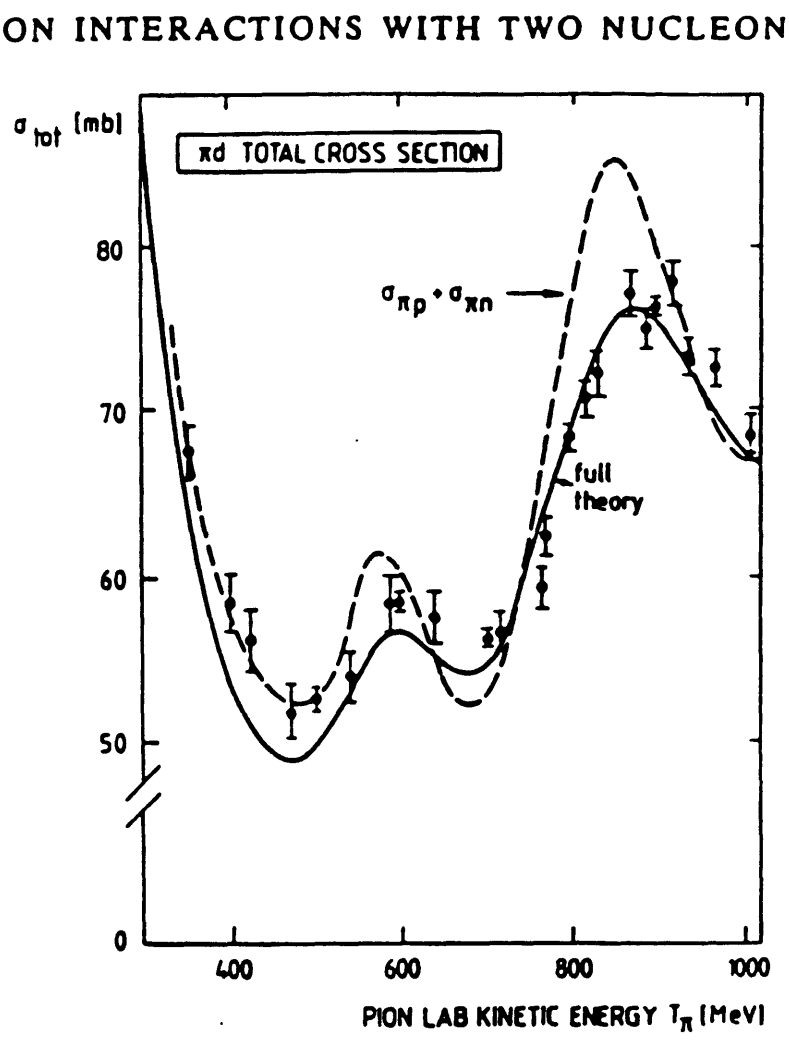

Figure 1-5: The πd total cross section compared to the sum of πn and πp total cross sections in the resonance regions beyond the Δ. The solid line labelled 'full theory' includes nucleon motion and double scattering effects. (The plot is from Ericson[1].)

In view of its simplicity the impulse approximation calculation produces fairly good agreement with the data for pion energies up to 1 GeV as shown. The differences between the data and the IA calculation are seen mainly in the widths and the magnitudes of the resonance peaks. When effects such as nucleon motion and double scattering are included, the solid curve (full calculation) agrees well with the data. Calculations of such effects are described in the remainder of this section.

The proton and the neutron are bound within the deuteron nucleus. The uncertainty principle requires that the nucleons have minimum momenta given as:

$$\begin{aligned} \Delta p \, \Delta x &\geq \hbar \\ \Delta p &\geq \frac{\hbar}{\Delta x} . \end{aligned} \tag{1.16}$$

In the impulse approximation the target nucleons are all fixed, however. When the nucleon motion (Fermi motion) is taken into account, the pion energy entering into the IA calculation should really be the pion energy seen by the nucleons in their rest frames. The energy ω' of the pion in the nucleon's rest frame, to leading order in the nucleon velocity β, is given as:

$$\omega' = \omega - \vec{\beta} \cdot \vec{k}, \tag{1.17}$$

where

ω is the pion energy in the lab frame
$\vec{\beta}$ is the nucleon velocity divided by c
$\vec{k}$ is the pion momentum.

With this substitution in the πn and πp scattering amplitude calculations, the effect of the Fermi motion is to smear the resonance peaks over an energy interval of typically 5% of the incident pion energy[21] as shown in Figure 1-4 and Figure 1-5 .

In Figure 1-4 and Figure 1-5 the πd total cross sections are reduced from the IA predictions in the resonance regions. This is due to the multiple scattering of the pions with the nucleons in the deuteron. In multiple scattering theory the scatterings in the deuteron are expressed in terms of a series of two-body collisions involving the meson with each nucleon separately. From the Lippman-Schwinger Equation, the Watson series can be obtained[15] as:

$$T = V_2 + V_3 + V_2 G_N V_2 + V_3 G_N V_3 + V_2 G_N V_3 + V_3 G_N V_2 + \cdots, \tag{1.18}$$

where

the meson is particle 1 and the nucleons are particles 2 and 3

T is the transition operator

V_i is the interaction potential between the meson and particle i

G_N is the Green's function or propagator.

Equation (1.18) can be written in terms of the t matrices as:

$$T = t_2 + t_3 + t_2 G_N t_3 + t_3 G_N t_2 + t_2 G_N t_3 G_N t_2 + \cdots, \tag{1.19}$$

where the t matrix is defined as:

$$t_i = V_i + V_i G_N t_i. \tag{1.20}$$

In the impulse approximation the t_i's are replaced by the free pion-nucleon t operators (t_i^{free}) and G_N's by the free pion propagator ($G_o^{(+)}$), defined as:

$$G_o^{(+)} \equiv \frac{1}{E + i\eta - H_o}, \tag{1.21}$$

where

E is the pion kinetic energy

H_o is the pion kinetic energy operator

η is taken in the limit $\eta \rightarrow 0^+$ to circumvent the mathematical singularity in the later integration.

The first two terms of Equation (1.19) correspond to single scattering and the next two terms to double scattering. The total cross section is calculated from the square of the T operator evaluated between the initial and final state.

The scattering amplitude for double scattering is given by:

$$< \vec{k'}, d|t_2^{free} G_0^{(+)} t_3^{free}|\vec{k}, d >= \int \psi^*(\vec{p'}) < \vec{k'}, \vec{p'}|t_2^{free} G_0^{(+)} t_3^{free}|\vec{k}, \vec{p} > \psi_d(\vec{p})\, d\vec{p'} d\vec{p}\,, \tag{1.22}$$

where

ψ_d is the deuteron wave function in momentum space

$\vec{k}, \vec{k'}$ are the pion initial and final momenta

$\vec{p}, \vec{p'}$ are the nucleon initial and final momenta.

The deuteron form factor F_d is obtained from ψ_d :

$$F_d(\vec{q}) = \int \psi_d^*(\vec{p} - \frac{1}{2}\vec{q})\psi_d(\vec{p})d\vec{p}, \tag{1.23}$$

where

$$\vec{q} = \vec{k'} - \vec{k}.$$

The amplitude in Equation1.22 is evaluated at the $\vec{q} = 0$ limit since $F_d(\vec{q})$ falls off very rapidly away from $\vec{q} = 0$. The double scattering contribution to the total cross section in the Δ resonance region is to reduce the total cross section by 10% as seen by the solid curve in Figure 1-4.

1.3 Previous Studies of Deuteron SCX

Rogers *et al.* observed the deuteron SCX reaction ($\pi^+ d \rightarrow \pi^0 pp$) at 85 MeV using a diffusion cloud chamber[4]. The data are shown in Figure 1-6. The outgoing proton momenta were measured from their tracks to determine the π^0 energy and scattering angle. The theoretical calculation (solid curve) by Rockmore[5] goes through all the data points within the large error bars. It used the scattering amplitude from the FGW model (Fernbach, Green and Watson[22]) and also included pion absorption and multiple scattering effects. The dashed curve is from the pure impulse approximation, in which the pion interacts only with the neutron in the SCX reaction.

A differential cross section for the deuteron SCX reaction ($\pi^+ d \rightarrow \pi^0 pp$) at 182 MeV was measured by Norem *et al.* using a bubble chamber[6]. The momenta of the two outgoing protons were determined from their stopping range, calculated from the bubble chamber tracks, to yield the π^0 momentum. In Figure 1-7 the measurement is compared against the calculation by Ramakrishnan *et al.*[7], which is an impulse approximation that took account of the Pauli blocking effect and used the Chew-Low amplitude [23] for the πN scattering amplitude. While

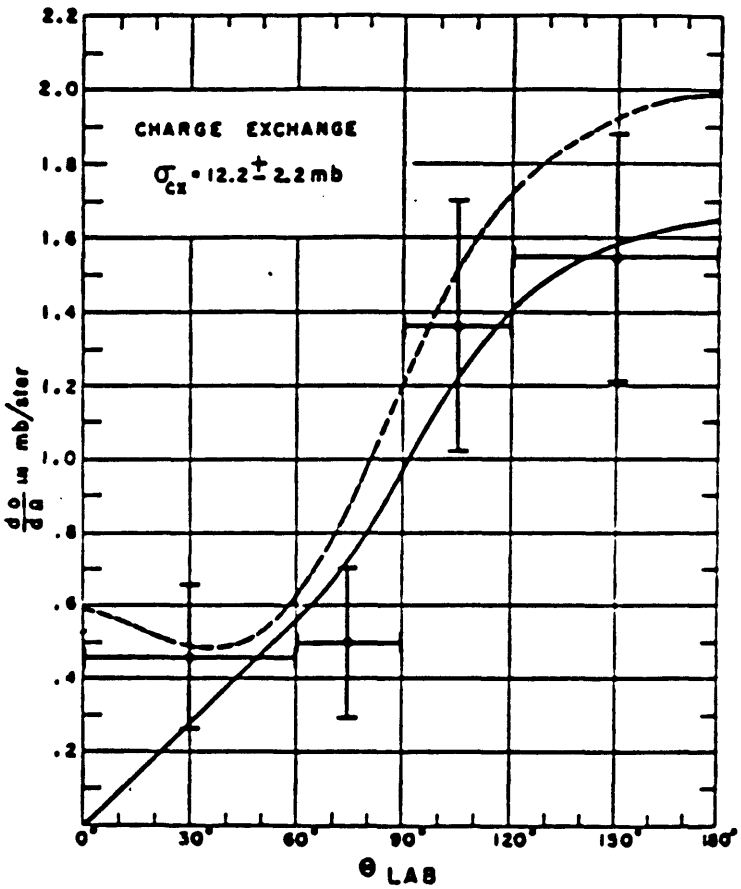

Figure 1-6: The angular distribution for the cross sections for $\pi^- d \rightarrow \pi^0 nn$ at 85 MeV from the measurements of Rogers *et al.*[4]. The solid curve is the calculation by Rockmore[5] and the dashed curve is the phase shift calculation. (The plot is from [4].)

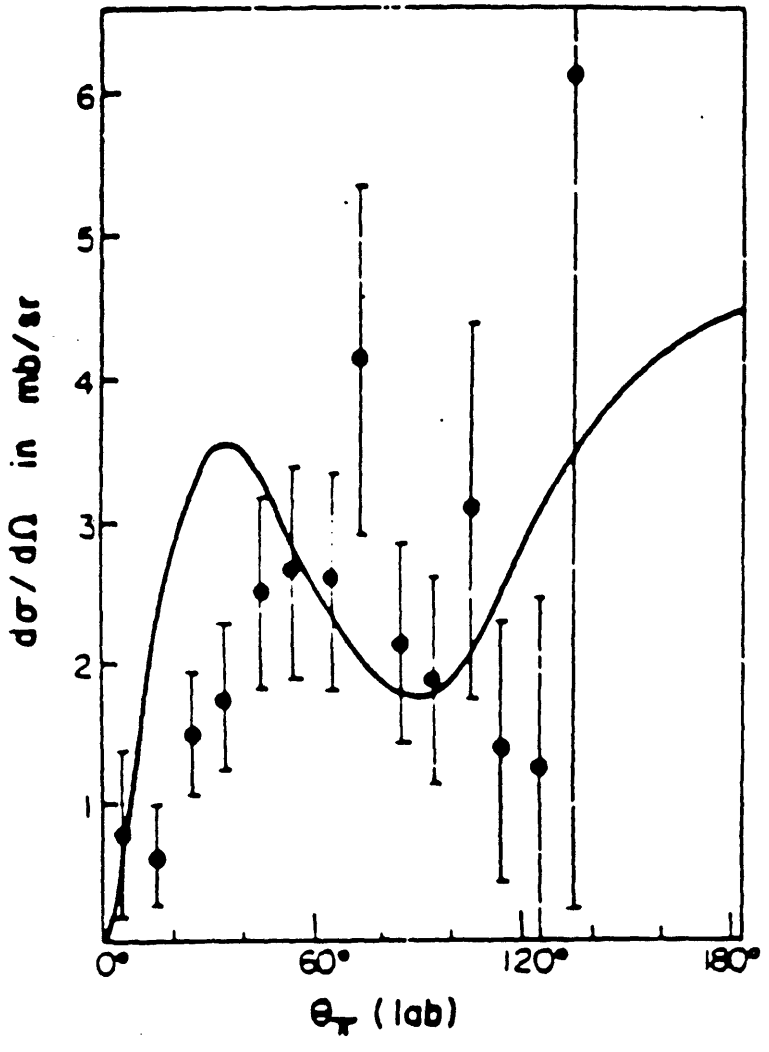

Figure 1-7: The differential cross section for $\pi^+ d \rightarrow \pi^0 pp$ at 182 MeV. The data are from Norem[6] and the curve is the prediction of Ramakrishnan *et al.* [7]. (The plot is from Norem[6].)

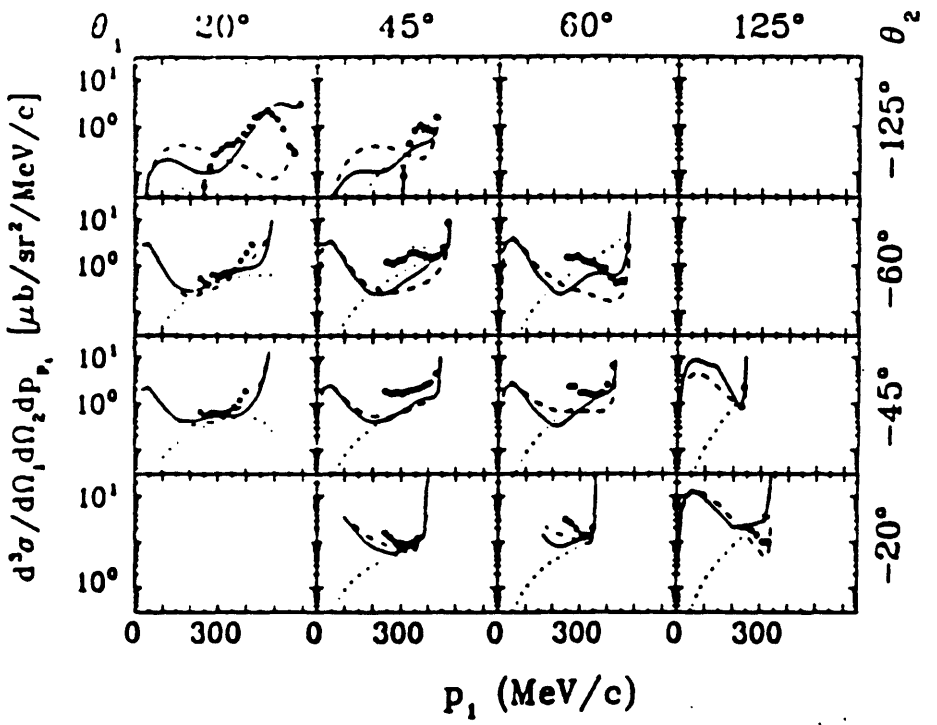

Figure 1-8: Triple differential cross sections for the reaction $d(\pi^+, pp)\pi^0$ at $T_{\pi^+} = 228$ MeV. The solid curves are the relativistic Faddeev calculations by Garcilazo, the dotted curves the phase space, and the dashed curves the impulse approximation.

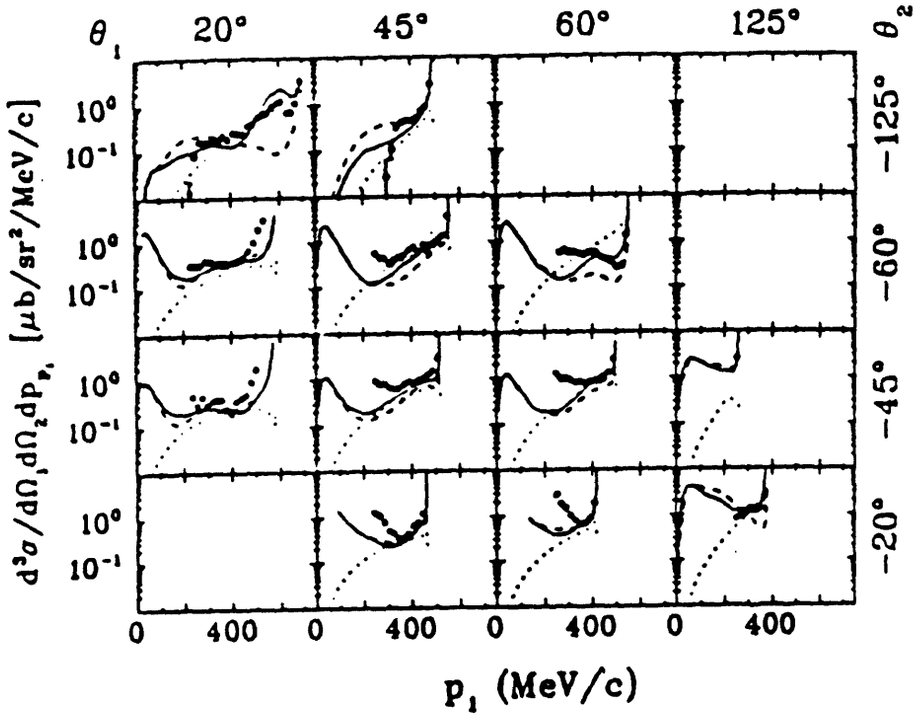

Figure 1-9: Triple differential cross sections for the reaction $d(\pi^+, pp)\pi^0$ at $T_{\pi^+} = 294$ MeV. The solid curves are the relativistic Faddeev calculations by Garcilazo, the dotted curves the phase space, and the dashed curves the impulse approximation.

it predicted the general shape and the forward angle suppression due to Pauli blocking, the overall agreement with the data is not very good.

Tacik *et al.* performed a kinematically complete measurement of the $d(\pi^+, pp)\pi^0$ reaction[24]. They measured a triply differential cross section, $d^3\sigma/d\Omega_{p_1}d\Omega_{p_2}dp_{p_1}$ as a function of the momentum of one proton at T_{π^+}= 228 and 294 MeV. The momenta of the two outgoing protons were determined in coincidence by measurements of their time of flight using plastic scintillators. The data are shown in Figure 1-8 and Figure 1-9. The agreement between the data and the relativistic Faddeev calculation (solid curve) is good only at the regions of high proton recoil momenta. At proton momenta closer to the quasifree kinematics the data points lie much higher than the calculation. Use of an incorrect deuteron wave function and neglect of higher order contributions such as a residual ΔN interaction were suggested as the reasons for such disagreement.

Moinester *et al.* measured the angular distribution of the deuteron SCX differential cross section at 164 MeV[8]. The measurement was done at the LEP (Low Energy Pion) channel at LAMPF using the LAMPF π^0 spectrometer. CD_2 and C targets were used. Subsequently, Garcilazo performed a full relativistic three body Faddeev calculation (solid curve) of the cross section for this reaction. The calculation agreed with the data only at the forward angles as seen in Figure 1-10.

Ouyang *et al.* meausred the deuteron SCX cross sections for $0° < \theta_{\pi^0}^{\rm Lab} < 90°$ at T_{π^-}= 500 MeV using the LAMPF π^0 spectrometer[11]. The absolute value of the detector acceptance was obtained by comparing the yields from the proton SCX to the known cross sections[10], while its energy dependence was commputed by the Monte Carlo program PIANG[13].

The π^0 energy spectra and the angular distribution were reported. The measured π^0 angular distribution is shown in Figure 1-11.

1.4 Motivation for Our Measurements

The πNN system presents a very basic problem in nuclear physics. It is even more basic than the NN system, in the sense that in order for two nucleons to interact they need to exchange virtual pions[16]. Of the πd reaction channels mentioned earlier, charge exchange has been the least studied both experimentally and theoretically.

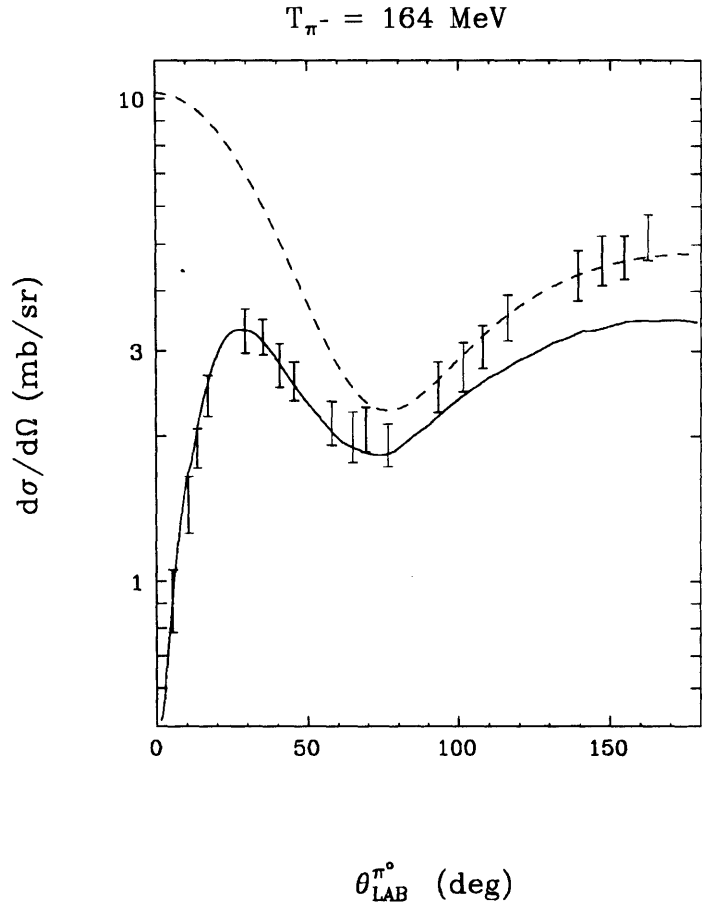

Figure 1-10: The results of the measurement of the $d(\pi^-, \pi^0)nn$ cross section at T_{π^-}= 164 MeV by Moinester *et al.*[8]. The solid curve is the relativistic Faddeev calculation by Garcilazo[9]. The dashed curve is the result of the phase shift calculation[10].

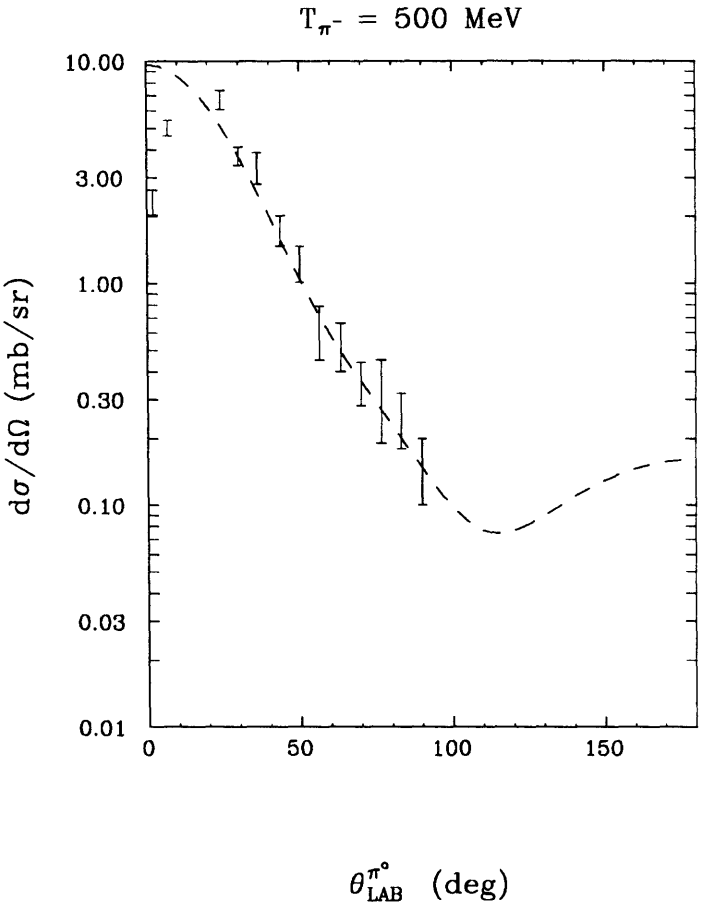

Figure 1-11: The results of the measurement of the $d(\pi^-, \pi^0)nn$ cross section at T_{π^-}= 500 MeV by Ouyang *et al.*[11][12]. The dashed curve is the result of the phase shift calculation[10].

In the impulse approximation, the pion interacts only with the single nucleon required for a charge exchange in the deuteron (such a reaction is called a "quasifree" SCX reaction). It is the effects of the extra nucleon on the reaction that are of main interest to this thesis (for simplicity, we call these "pion-nucleus effects"), since the proton SCX process is well understood.

The energy spectra from the deuteron SCX reaction are expected to be dominated by a peak resulting from the quasifree process. In such a reaction, there are only two particles in the initial (π^- and p) and the final state (π^0 and n), and the π^0 angle and energy are thus kinematically correlated. However, the Fermi momentum of the proton in the deuteron would smear the π^0 angle and the energy correlation. An impulse approximation model (to be discussed in Chapter 5) that included the Fermi motion was constructed to test the hypothesis of dominance of the quasifree process and to observe pion-nucleus effects in the measured energy spectra.

As seen in Figure 1-10, the Faddeev calculation by Garcilazo[9] predicts a 20% reduction in the overall deuteron SCX cross section from the proton SCX values due to multiple scattering at $T_{\pi^-} = 164$ MeV. At the higher energies the multiple scattering effect may diminish since the πN reaction strength is reduced away from the Δ resonance region. The deuteron SCX values at $T_{\pi^-} = 500$ MeV shown in Figure 1-11 are identical to the proton SCX values at large angles, presumably because the multiple scattering effect has become very small at such high energy.

Another pion-nucleus effect seen in Figure 1-10 and Figure 1-11 is the forward angle suppression (Pauli blocking) of the deuteron SCX cross sections compared to the impulse approximation values. This effect occurs because of the Pauli principle applied to the two identical particles in the final state resulting from the SCX reaction on the deuteron. As shown in Figure 1-12, the deuteron is in a $^3S_1$ state and has isospin 0. The nn final state has isospin 1. Since a system of two identical particles must obey the Pauli exclusion principle, its wave function has to be anti-symmetric with respect to a particle exchange. The $^1S_0$ and ^3P states with isospin 1 shown in Figure 1-12 are possible (we exclude $\ell > 1$ states).

The transition from the $^3S_1$ initial state to a $^1S_0$ final state involves a spin flip and its amplitude, $g(E,\theta)$ is proportional to $\sin(\theta)$ as shown in Equation (1.11). In a transition from $^3S_1$ to ^3P states, the spin remains the same and such a transition amplitude is given by the spin-non-flip amplitude ($f(E,\theta)$ in Equation (1.10)). The final state neutrons in the ^3P states have their spins pointing in the same direction and therefore are required by the Pauli exclusion principle to have different quantum numbers in momentum space. In the rest frame of the deuteron both proton and the neutron have an identical Fermi momentum distribution. In the

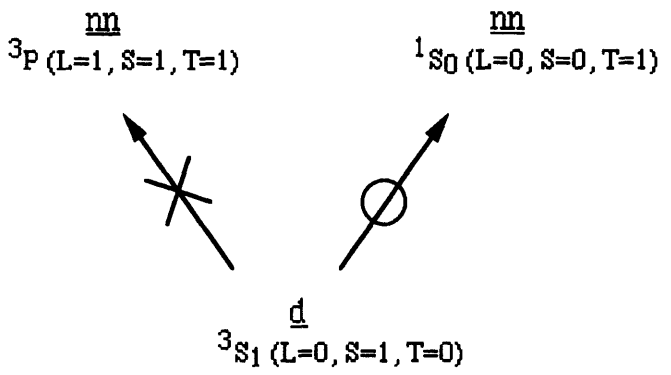

Figure 1-12: A spin flip is required due to the Pauli exclusion principle in the final nn state in the deuteron SCX reaction.

impulse approximation, when the incoming pion exchanges a unit of charge with the proton, turning it into a neutron, it also gives that neutron an additional momentum $\vec{q}$ (momentum transfer). The smaller $\vec{q}$ is the more likely it is that the newly converted neutron will compete for the same momentum state with the original neutron. Therefore at small q, $f(E,\theta)$ is suppressed and this phenomenon is called "Pauli blocking". A model (Fermi sphere model) was built in order to describe this effect and is discussed in Chapter 5.

We measured the cross sections for the deuteron SCX reaction in the Δ resonance region (T_{π^-}= 164 MeV) and at two higher energies (T_{π^-}= 263, 371 MeV) to study the pion-nucleus effects at each energy as well as their behavior as a function of the incoming pion energy. The Δ resonance region was chosen because there the πN interaction is particularly strong and therefore enhancement of the pion-nucleus effects are expected. The particular high energy values (263 and 371 MeV) were chosen because of the availability of proton SCX measurements at those energies[25][26], which we used in the normalization of our data.

Chapter 2

Experimental Apparatus and Data Acquisition

2.1 LAMPF and beam optics

This experiment was carried out at the Clinton P. Anderson Meson Physics Facility (LAMPF), which is located in Los Alamos, New Mexico. (see Figure 2-1) The experimental data were obtained during the month of August, 1992.

LAMPF uses a primary proton beam to produce a secondary pion beam. After the protons are accelerated over a distance of one-half mile to reach an energy of 800 MeV, they impinge on graphite targets (A1 and A2 targets in Figure 2-2) to produce pions.

During our experiment a typical proton bunch was 500 μsec long at a repetition rate of 120 Hz. Each bunch had a microstructure consisting of 0.25 nsec pulses at 5 nsec intervals.

From the A2 target a magnetic transport system steers the pions into the high-energy pion channel, P^3. (See Figure 2-3.) The pion momentum and flux for the channel are largely set by BM01 and MS03. BM01, a dipole magnet, disperses the the pions according to their momenta, while the slit MS03 allows a specified momentum and momentum spread to be transported. A series of quadrupole magnets are used to focus the beam.

While traveling down the channel (19 m), some of the pions decay into muons which in turn decay into electrons. The beam in the channel is therefore composed of electrons (or positrons) and muons as well as pions. In addition, positive pion beams contain protons produced by

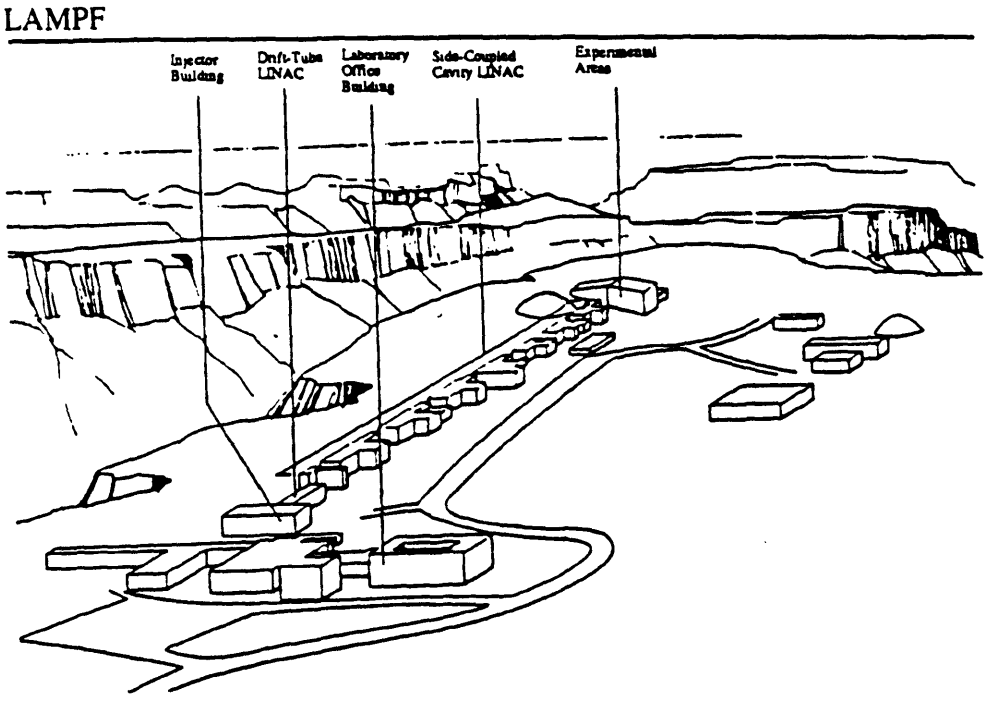

Figure 2-1: Aerial view of LAMPF.

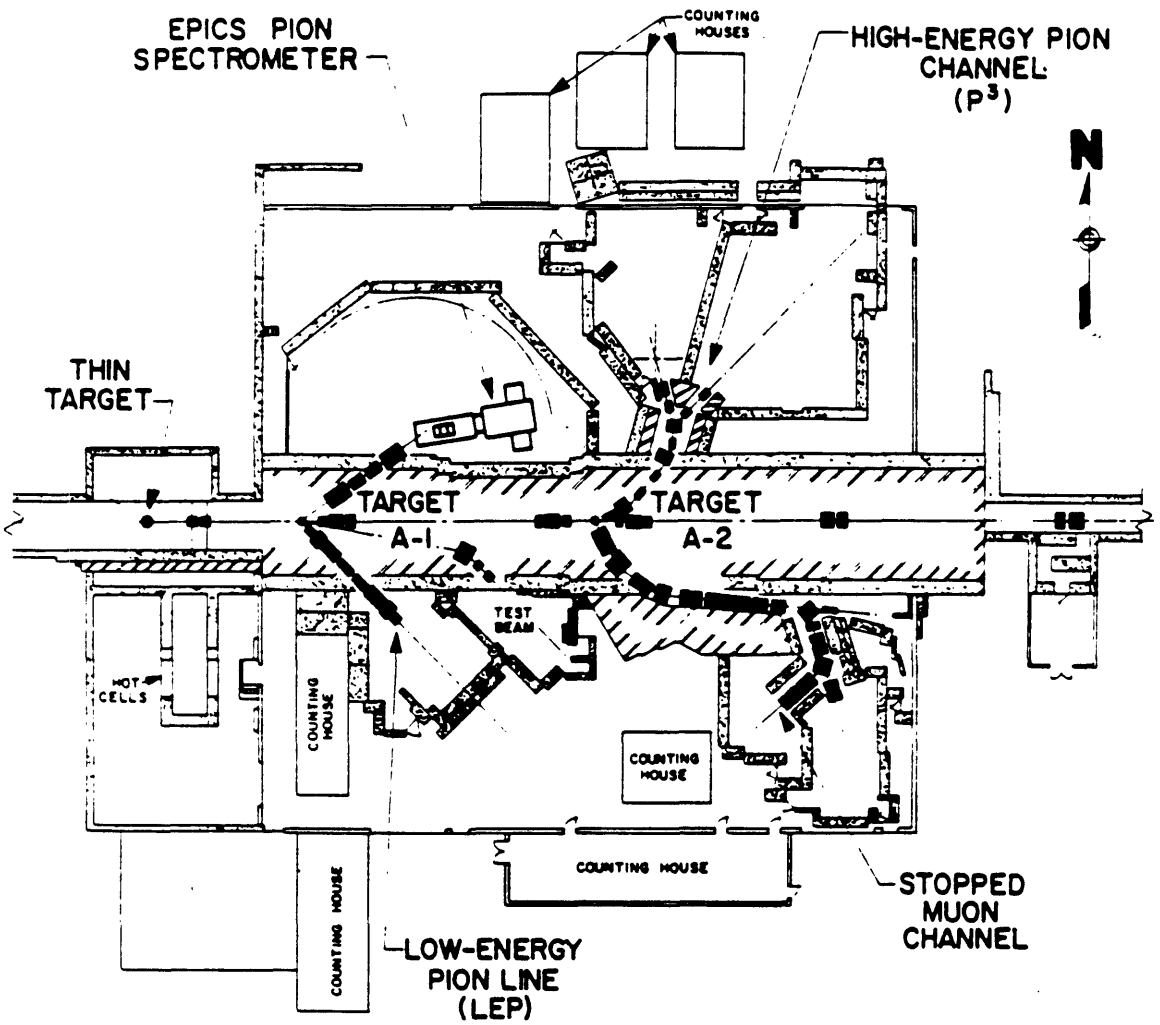

Figure 2-2: LAMPF experimental area A.

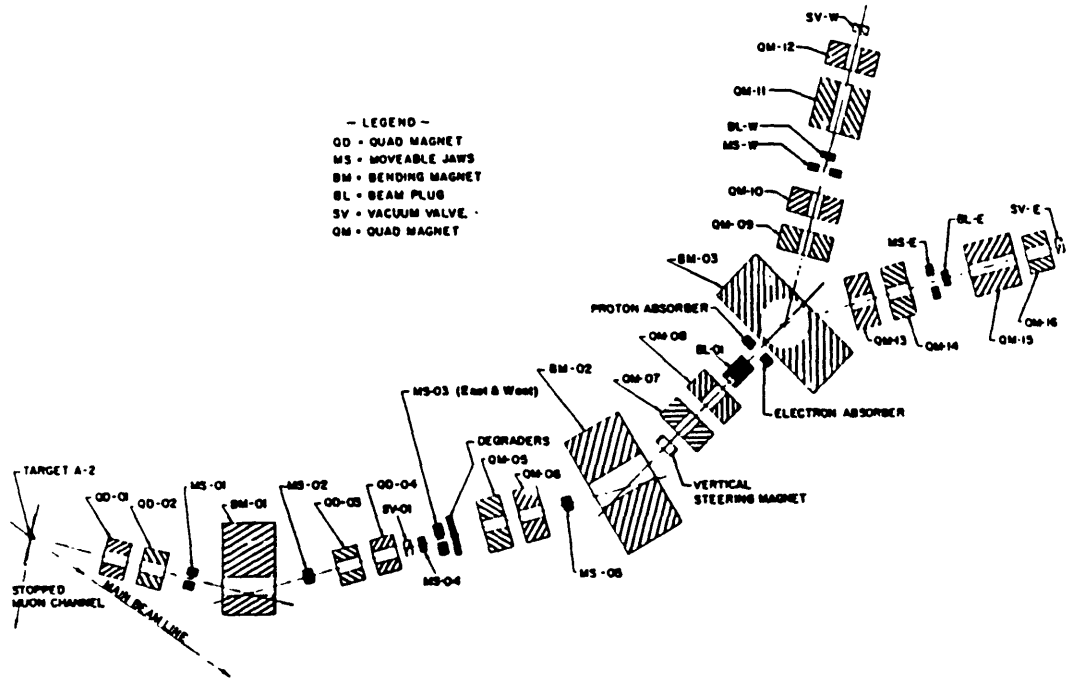

Figure 2-3: The beam transport elements at the P^3 channel.

inelastic scattering in the target. All the particles of different kinds are transported down the channel as long as they have the same magnetic rigidity (the ratio of the momentum to the charge of the particle). However, a combination of energy degrading materials are placed to introduce differential momentum losses to the particles according to their masses. The dipole magnet BM02 then bends the pions keeping them in the beam path while sweeping the undesired particles (electrons, or protons and positrons) away from the beam path into the absorbers. This filtering was not complete and moreover muons were impossible to filter out in this way since their mass is close to that of pions. The fraction of the pion beam contamination by the other particles decreased at higher energy since the pions could travel a longer distance before decaying. The dipole magnet BM03 transported the beam into one of two experimental caves, P^3 West P3 East.

TRANSPORT (a computer program for designing charged particle beam transport systems) calculates the setting of the channel devices for a given pion beam charge, momentum, momentum bite, flux, size and shape at the user target position in the experimental hall. Instead of using the standard deck for P^3 West as an input to the TRANSPORT code with the standard pion beam flux ($\sim 1 \times 10^8$ particles per second on average), a modified deck was used with the desired pion flux ($\sim 5 \times 10^4$ particles per second on average) for this experiment. The modification occurred in the form of a reduced pion beam phase space at the very start of the channel. This was equivalent to what we physically did to the channel, which was to narrow the slits at the upstream end of the channel to cut into the beam. Another program called NEWSHUNT then converted the magnetic field settings to the corresponding current values for the power supplies. These numbers were fed into an interactive program called MON90 that actually set the currents for all the channel magnets.

As a preliminary and illustrative way to see that the beam was tuned, we placed one beam profile monitor upstream and another downstream of the target with all the channel slits wide open. This monitoring device was made up of a pair of small multi-wire proportional chambers. The wire spacing was 1 mm and the two planes of wires were perpendicular to each other in order to trace the shape of the charged particle beam in the horizontal and vertical directions. Connected to each plane of wires was an electronic circuit which took the time average of the signals coming in from each wire and displayed them one next to another on an oscilloscope screen. As one swept BM02 from high to low magnetic field, one could see the peaks corresponding to the different particle types (electrons (or positrons) first, pions plus muons, then protons (for positive beams)) sweeping across on the oscilloscope screen. After cycling BM02 to the value that sent the pions down the channel, final tuning was achieved by adjusting the settings on BM03 and the last four quadrupoles. The beam flux was reduced

($\sim 5 \times 10^4$ particles per second on average) for final tuning and the beam profile monitors were no longer able to monitor the beam at such low flux. Instead, a set of in-beam scintillators was used for beam monitoring, as will be explained later in this chapter.

As we operated the channel at a very low flux, all of the slits upstream of BM03 were set very tightly and small adjustments of the beam intensity during the experiment were made by moving the momentum bite jaws (MS0W and MS0E). A typical momentum bite during our experiment ranged from 0.2 to 0.8 %.

2.2 Experimental Set-Up

2.2.1 General Set-Up

A top view of the experiment set-up is shown in Figure 2-4 and a perspective drawing of the set-up is shown in Figure 2-5. The π^- beam passed through a rectangular opening ($10\ cm \times 10\ cm$) in the shielding wall to the target. The distance between the target and the exit face of the last quadrupole magnet was set at 3.5 m to allow a sufficient distance to form a beam with a narrow and long waist at the target position. A set of three in-beam scintillators was used for both beam monitoring and triggering purposes. Another scintillator (called S3) was placed 5m down-stream of S1, although not shown in Figure 2-4. The combination of S1 and S3 was used to measure the pion content in the beam at the target position (see Appendix A).

2.2.2 History of π^0 detection at LAMPF

The π^0 is a short-lived particle ($\tau = 8 \times 10^{-17}$ sec) with a rest mass of 135 MeV. It decays electromagnetically into two photons 99 % of the time.

The "π^0 spectrometer" was built at LAMPF in 1978[13] and many π^0 detection measurements have been performed using this device since then. In order to detect the π^0 's with better resolution a new-generation π^0 detector was built, namely the NMS (Neutral Meson Spectrometer)[27]. In Figure 2-6 and Figure 2-7 are shown schematic diagrams of the LAMPF π^0 spectrometer and the NMS, respectively.

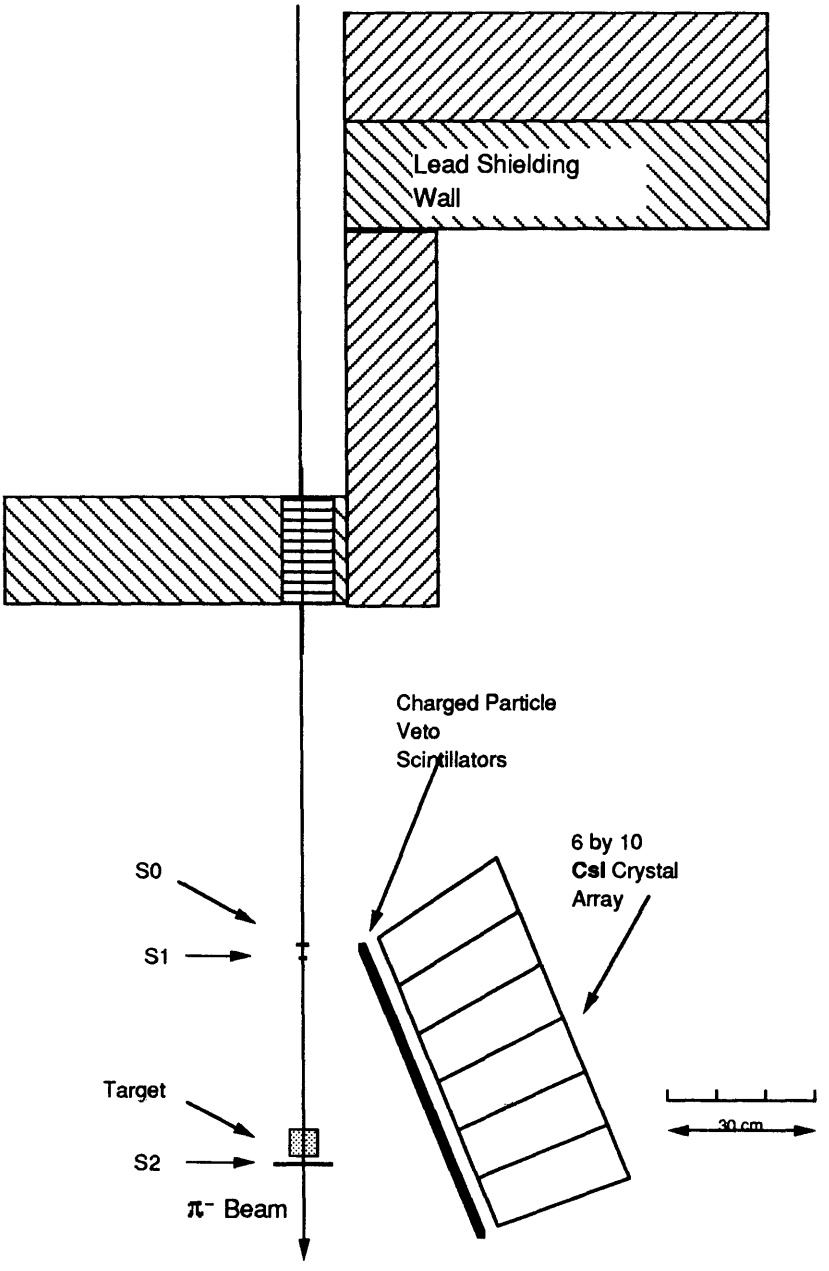

Figure 2-4: A top view of the set-up of the experiment.

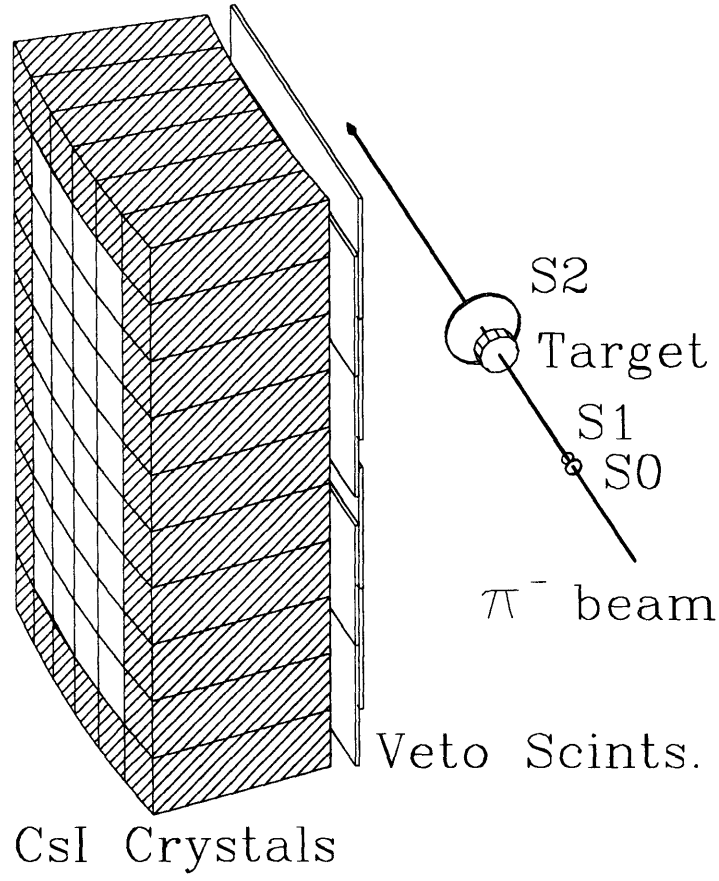

Figure 2-5: A perspective drawing of the experiment set-up.

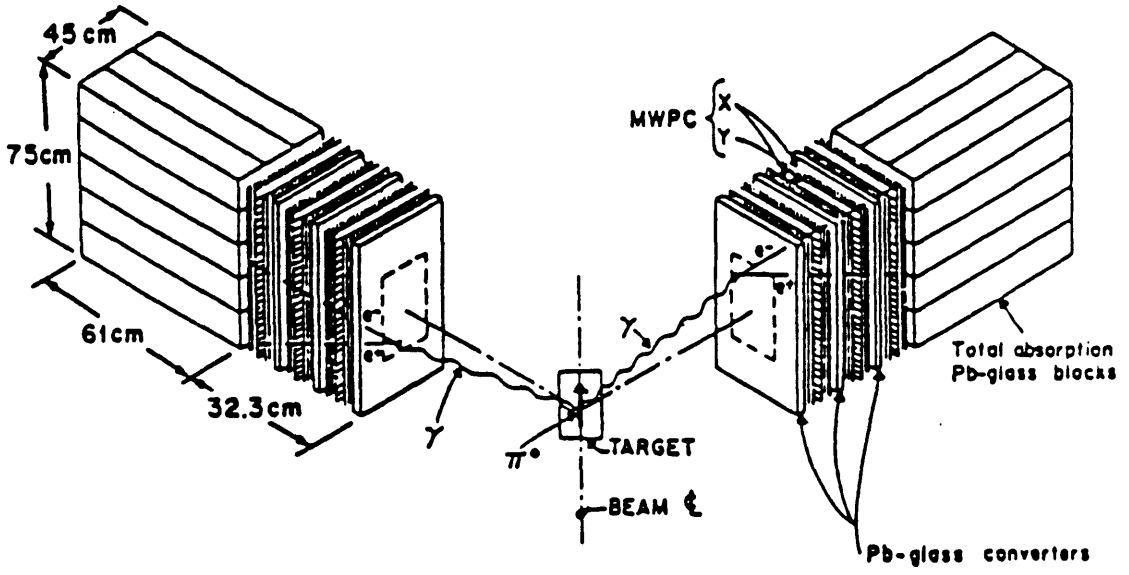

Figure 2-6: Schematic diagram of the LAMPF π^0 spectrometer. (The diagram is from Baer *et al.*. [13]

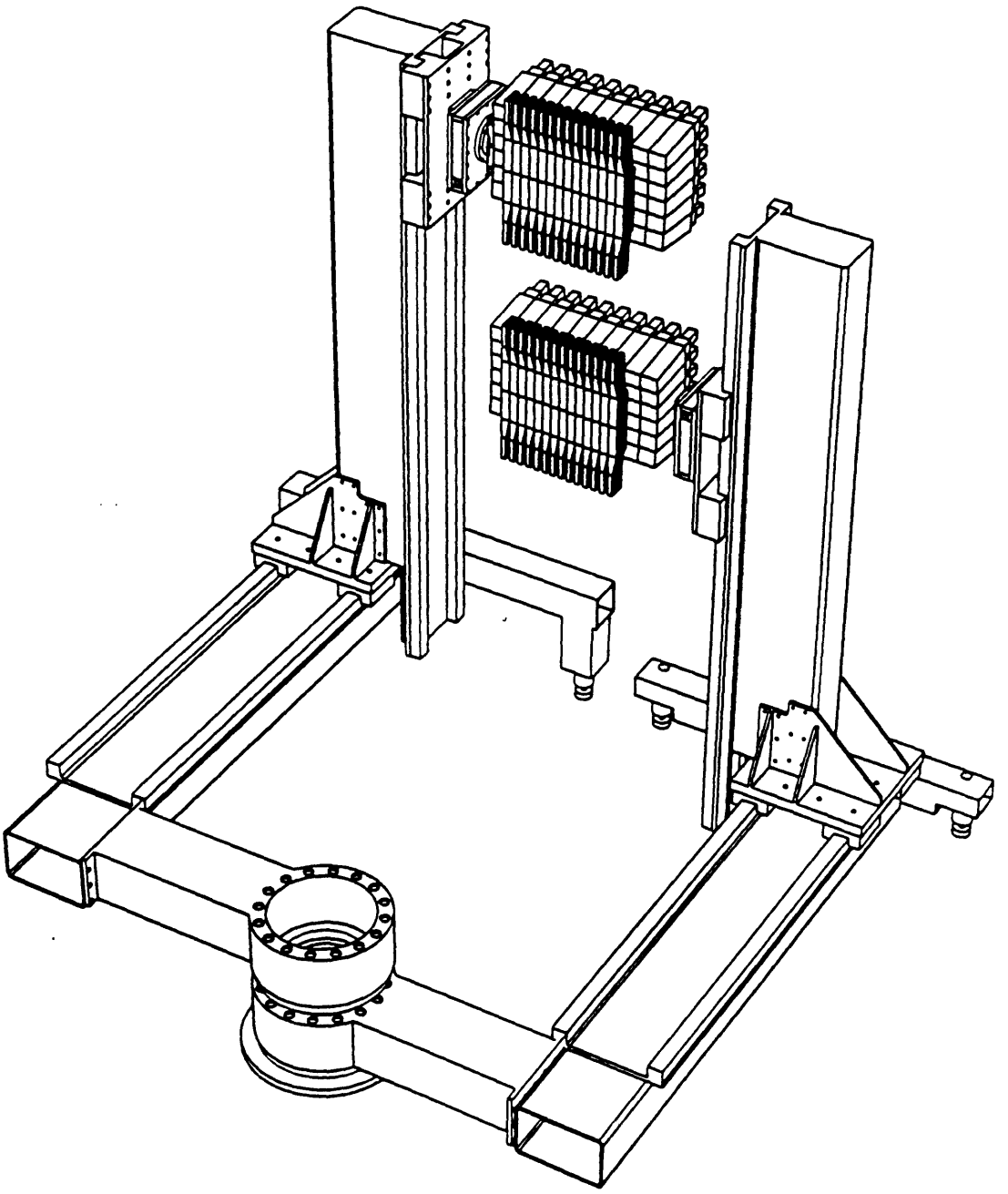

Figure 2-7: Schematic diagram of the NMS. Shown in the diagram are the two detector crates with the BGO converters and the CsI crystals. The wire chambers are not shown.

Both the π^0 spectrometer and the NMS operate on the same principle for detecting π^0 's. The two decay photons are observed in two separate detecting arms in coincidence. In each arm a photon is "detected" when it goes through sets of converters and wire chambers and finally into a total energy calorimeter. The opening angle (the angle between the two photon momenta) and the calorimetry information for each photon then yield the π^0 momentum.

$$W = m_{\pi^0}\, c^2 [\frac{2}{(1 - cos\eta)(1 - x^2)}]^{\frac{1}{2}}, \tag{2.1}$$

and x is given by

$$x = \frac{(\mathrm{E}_1 - \mathrm{E}_2)}{(\mathrm{E}_1 + \mathrm{E}_2)}, \tag{2.2}$$

where

W is the total energy of the π^0

η is the opening angle between the two photon momenta.

E_1 and E_2 are the energies of the two photons.

As can be seen in the above equations, the smaller x is, the smaller is its contribution to W. Thus dx (error in x measurement from calorimetry) contributes a very small amount to dW when x is small. Therefore a very accurate measurement of η with x restricted to a small value (typically less than 0.2), can give a superior energy resolution that would not be possible with calorimetry alone. The NMS was designed to have 300 keV energy resolution, 2 msr solid angle and 10 MHz event rate in each arm. This is ten times better resolution, two times bigger solid angle and ten times the event rate capability of the π^0 spectrometer. These improvements were achieved through new designs of the components such as active-cathode wire chambers and better resolution materials such as bismuth germanate (BGO) and pure cesium iodide (CsI) crystals for the converters and calorimeters respectively.

Table 2.1 shows relevant characteristics of commonly used calorimeter materials. Lead glass was used as the calorimeter material for the original LAMPF π^0 spectrometer[28]. BaF_2 and pure CsI stand out both with good resolution, fast decay times and short radiation lengths (r_l). However CsI becomes much more practical when the cost is considered. It also does not cleave and it is non-hygroscopic (not affected by moisture). These properties simplified the assembly of the 60 individual crystals into each calorimeter crate.

Detector Material	Light Output (Photons/MeV)	Radiation Length (cm)	Decay Time (nsec)	Peak Emission (nm)	Cost $ /(cm^2·r$_l$)
Pb glass	1.5	4.15		300 – 700	
NaI(Tl)	4.0×10^4	2.5	250	410	5.2
BGO	2.8×10^3	1.1	300	480	13.8
CsI(Tl)	4.5×10^4	1.8	600	550	4.5
CsI(pure)	$1.2 - 2.4 \times 10^3$	1.8	20	305	4.5
BaF_2	2.0×10^3	2.1	0.6	220	16.8
CeF_3	1.2×10^3	1.7	27	330	

Table 2.1: Calorimeter Materials

2.2.3 What we used for π^0 detection

In summer of 1992 one CsI crystal array calorimeter for the NMS was completed. In a detection scheme in which the π^0 energy was calculated from pure calorimetry with a single NMS crate, allowing the x to have any value possible ($-\beta$ to β , see Appendix B), it was shown from our Monte Carlo simulation that we could detect π^0 's with a large solid angle of ~100 msr, modest energy resolution of ~10 MeV and angular resolution of ~10 degrees in the energy range below 400 MeV. The energy and angular resolution in this scheme would be adequate for our purpose. In addition, the large solid angle would allow us to use a low π^- flux. This would make possible the counting of the individual π^- 's in the beam, making the π^- flux normalization very accurate. Therefore we carried out our π^0 measurements using a single NMS calorimeter.

2.2.3.1 General properties of the CsI crystal

Each CsI crystal in our detector was 4 inches by 4 inches on the face and 12 inches long (17 radiation lengths). A one degree taper was applied to two opposite sides for "compressive transverse loading"[27]. A cylindrical light guide made of CsI was attached to the end of each crystal. At the end of the light guides were attached Thorn/EMI 9301 QA photomultiplier tubes with 3-in S20 photocathodes to collect the scintillation light from the crystals.

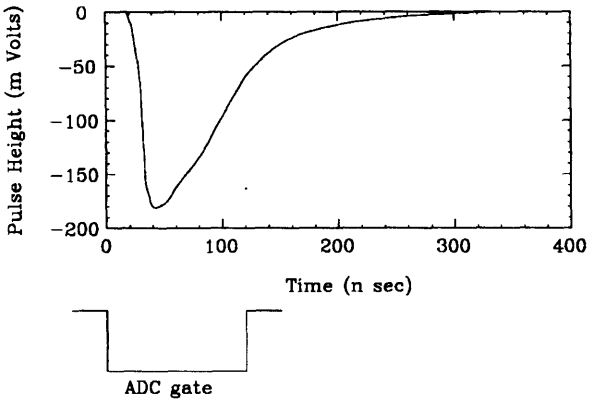

Figure 2-8: The scintillation signal from a CsI crystal

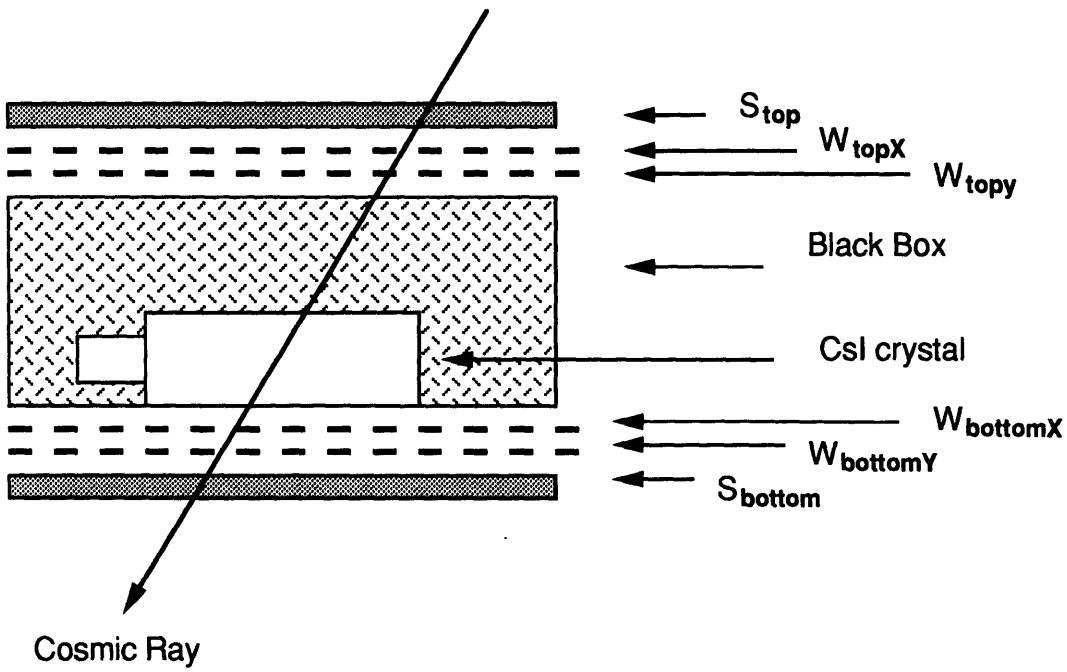

Figure 2-9: The 3-dimensional tomography set-up

The scintillation light from a crystal was composed of two components with different time constants. Empirically, the "fast" component was defined as the fraction of the pulse height integrated over a 100 nsec gate and the "total" component was the fraction integrated over a 1000 nsec gate. The time response of the crystals was tested by averaging over 250 cosmic ray pulse heights in each crystal. In all the crystals, the fast component accounted for more than 75 % of the total light. Shown in Figure 2-8 is a typical scintillation pulse in a crystal obtained during our experiment.

The energy resolution from photo-electron statistics with a 130 MeV photon in a crystal was shown to be 5 %. This was measured using radiative capture ($\pi^- + p \rightarrow \gamma + n$) with a stopped π^- beam in a liquid hydrogen target[29].

The uniformity of the crystals was tested by a 3-dimensional tomography method as shown in Figure 2-9. A crystal was placed in a light-tight black box with high voltage and signal cables for the photomultiplier tube fed in from outside. Both above and below the black box were a scintillator and a pair of wire chambers whose wire planes were perpendicular to each other. When a cosmic ray muon passed through S_{top}, the crystal and S_{bottom}, a trigger was issued by a coincidence formed between S_{top} and S_{bottom}. From the position information above (determined from W_{topX} and W_{topY}) and below (from $W_{bottomX}$ and $W_{bottomY}$) the crystal, the muon track in the crystal was reconstructed. The pulse height from a track was normalized by the length of the track within the crystal. The crystal was then sliced up into thirty 1 cm slices (in the software of course). In each slice the pulse heights whose tracks crossed that slice were averaged. The uniformity for a crystal was calculated as below.

$$\text{Uniformity} = \frac{\text{maximum in set P} - \text{minimum in set P}}{\text{mean of the elements in set P}}, \tag{2.3}$$

where

$$\text{P} = \{\langle \text{ pulseheight } \rangle_{\text{1st slice}}, \ldots, \langle \text{ pulseheight } \rangle_{\text{30th slice}}\}.$$

All of the crystals had a uniformity of better than 5 %.

Each crystal was optically isolated to prevent "cross talk" between crystals. This was achieved by wrapping each crystal with three layers of Teflon sheet (4 mils each) and one layer of aluminized Mylar sheet (0.25 mils). Since the crystals were packed side by side, the effective thickness of the wrapping materials between the crystals was twice the above values.

The front face of the crate was not covered with any support structure material, so that the particles might enter the crystals directly. This was possible since the crystals were being held together inside the crate by transverse compressive forces from all sides. Only a thin Mylar window covered the front face of the crate to protect the crystal faces and to seal the crate. The crate was hermetically sealed to light and was filled with nitrogen gas to keep out moisture.

2.2.3.2 Our π^0 detector

The π^0 decays in its rest frame into two photons whose momenta are equal in magnitude and opposite in direction as seen in Figure 2-10. The distribution of these momenta is isotropic in that frame. θ^* and ϕ^* range uniformly from 0 to π and 0 to 2π, respectively.

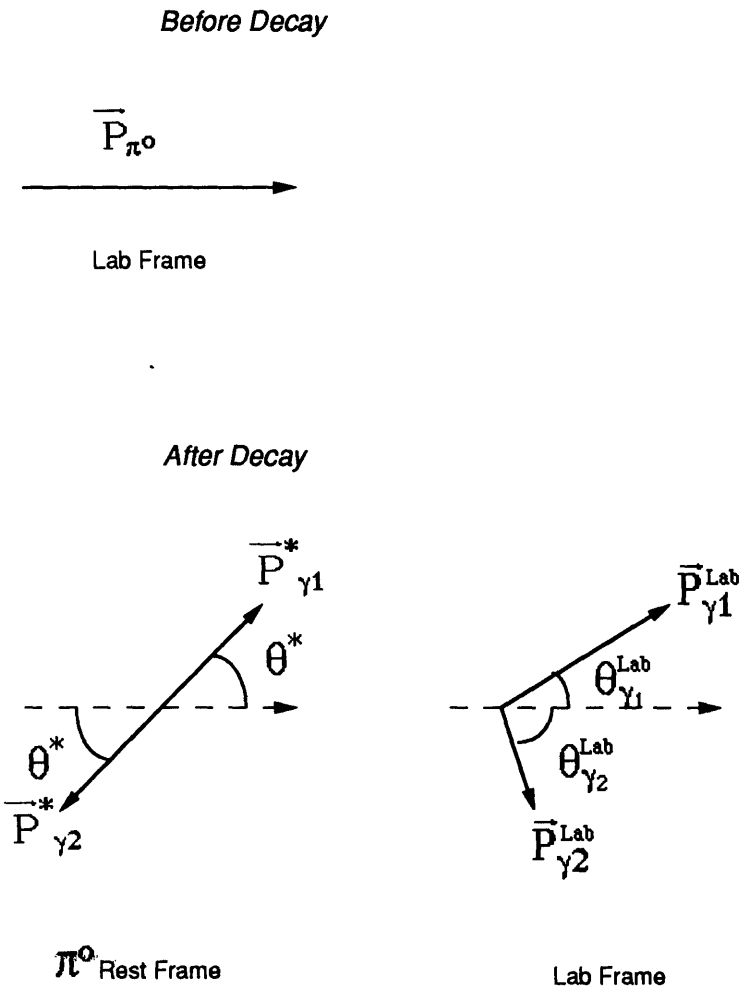

Figure 2-10: The π^0 decay.

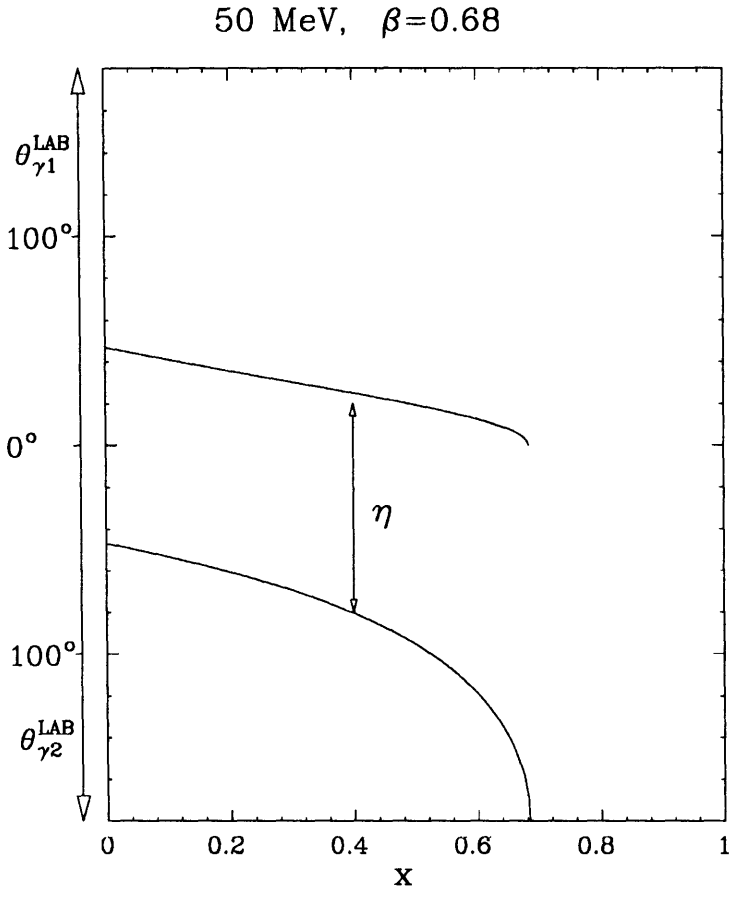

Figure 2-11: The opening angle in π^0 decay.

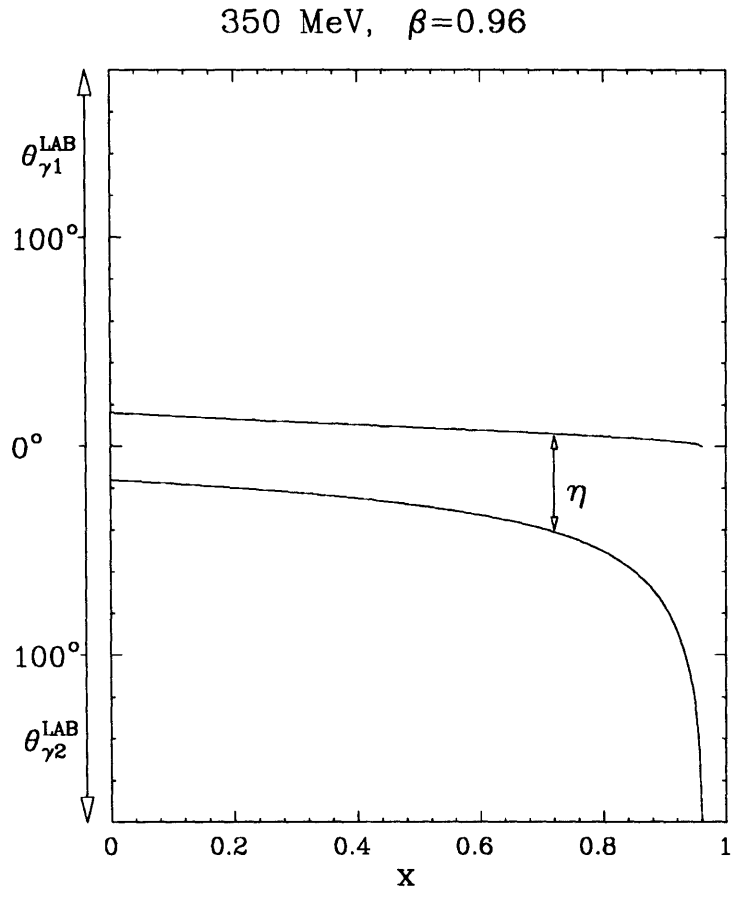

Figure 2-12: The opening angle in π^0 decay.

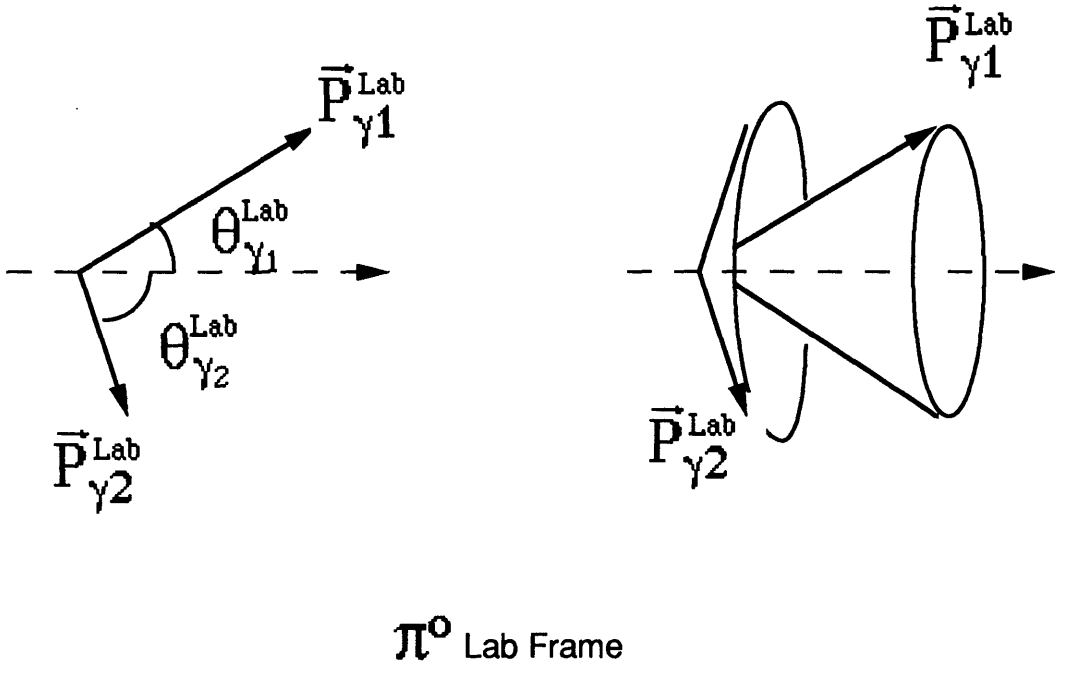

Figure 2-13: The π^0 decay cones.

The photon momenta in the π^0 rest frame are boosted into the lab frame by an amount depending on the π^0 momentum. In Figure 2-11 and Figure 2-12 the lab angles that each photon makes with respect to the π^0 momentum are plotted as a function of the variable x for π^0 energies typical in our experiment (50 and 350 MeV). The quantity x is uniformly distributed from $-\beta$ to β . As long as θ^{Lab} is smaller than 90° the decay photons come out forming a cone with a polar angle θ^{Lab} when ϕ is populated from 0 to 2π. The quantity η is called the "opening angle" and is defined to be $\theta^{Lab}_{\gamma_1} + \theta^{Lab}_{\gamma_2}$. For a typical π^0 energy in our experiment, for most of the x values, both $\theta^{Lab}_{\gamma_1}$ and $\theta^{Lab}_{\gamma_2}$ were smaller than 90° as seen in Figure 2-11 and Figure 2-12. Therefore the photons for most of the decay phase space came out in cones. For a given value of x two different cones are formed corresponding to two decay photons as shown in Figure 2-13. See Appendix B for more discussion on the kinematics of the pion decay.

Our single calorimeter crate, positioned very close to the target to catch both of the photons, was able to intercept a good part of the two photon cones. In contrast, the two-crate NMS would have had much more limited coverage of the phase space, being severely restricted in the azimuthal angle coverage.

Table 3.1 shows the various detector set-ups during our experiment. In the table R (the distance between the target and the detector) is larger for higher energy π^0 detection. And this was afforded without much decrease in the solid angle due to the fact that at the same x, $\theta^{Lab}_{\gamma_1}$ and $\theta^{Lab}_{\gamma_2}$ were smaller for higher energies. Certainly smaller R would have given even bigger solid angles. However, smaller R would have meant poorer photon cluster separation and therefore poorer energy and angular resolution. Hence a compromise had to be struck between a large solid angle and adequate energy and angular resolution, resulting in the values given in Table 3.1.

Another factor in determining R was that in all set-ups a minimum distance of 10 cm was kept between the beam center and the closest part of the detector. The exceptions were the measurements at 10 degrees, in which the detector was positioned directly in the beam.

The detector was mounted on a cart made of steel with four omni-directional wheels. The cart had a line corresponding to the center line of the detector for the angle alignment and a marker corresponding to the front of the detector face for the radius positioning.

2.2.4 Charged Particle Veto Scintillators

The veto scintillators monitored charged particles going into the detector. The information was later used in the software to separate out and reject the charged particle events from the π^0 events.

Eight individual scintillators covered the whole face of the detector. Each scintillator had an active area of 8.5 inches by 25 inches and a thickness of 0.25 inches and was made of a fast-response (decay time 2 nsec) Bicron-408 material. At the end of each light-guide was attached a 2 inch photo-multiplier tube. In addition to the regular high voltage (approximately 1.5 kV), each phototube was connected to a negative high voltage bias (-800 V) at the last dynode where the electron current is the highest to maintain the performance of the tubes at high counting rates.

2.2.5 Targets

In table 2.2 are listed all the targets used in the experiment and their thicknesses and compositions. The CD_2 target was composed of 3 separate discs. Two of the CD_2 discs had a diameter of 1.5 inches. All the other targets were 2.5 inches in diameter. The CD_2 targets contained a small amount of hydrogen as shown in table 2.2. See Appendix C for a description of the CD_2 target assays.

The target ladder was supported from above to leave room on the floor for the detector cart to maneuver. Targets were placed inside the grooves in the target holders as shown in Figure 2-14.

In one of the grooves was placed a "doughnut target", as shown in Figure 2-15. The inner diameter (1.38 inches) of the doughnut target was smaller than our smaller CD_2 discs (1.5 inches in diameter). At each set-up throughout the experiment the doughnut target was used to verify that the lateral extent of the beam at the target position was smaller than 1.5 inches thus ensuring that the beam was properly going through all three CD_2 discs.

Teflon tape contains no hydrogen and therefore was used to further secure the targets in the grooves. The target holder was designed in such a way to minimize the aluminum material that might be in the path of the π^0 decay photons between the target and the detector (see Figure 2-14).

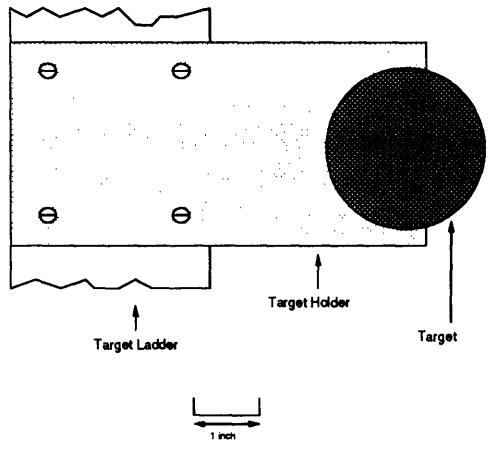

Figure 2-14: The target mount assembly

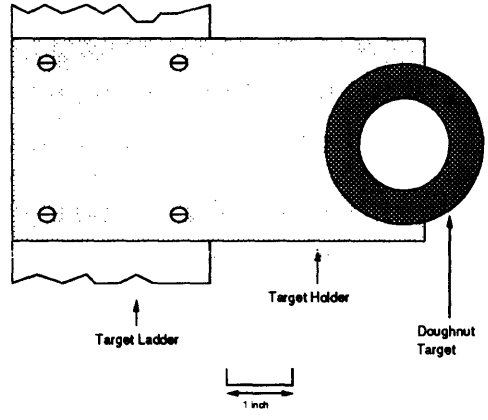

Figure 2-15: The doughnut target

Component	Number of Nuclei $(1/cm^2)$	Error $(1/cm^2)$	%
Single Layer Targets(up to RUN 116)			
d in CD2	7.81×10^{22}	1.09×10^{21}	1.4
p in CD2	1.34×10^{21}	4.0×10^{19}	3.0
p in CH2	9.10×10^{22}	3.7×10^{20}	0.4
C in CD2	3.98×10^{22}	5.6×10^{20}	1.4
C in CH2	4.55×10^{22}	1.8×10^{20}	0.4
C in C	3.99×10^{22}	5.6×10^{20}	0.7
Multiple Layer Targets(from RUN 117)			
d in CD2	2.29×10^{23}	2.5×10^{21}	1.1
p in CD2	5.98×10^{21}	1.256×10^{21}	21
p in CH2	2.52×10^{23}	1.8×10^{21}	0.7
C in CD2	1.17×10^{23}	1.1×10^{21}	0.9
C in CH2	1.26×10^{23}	8×10^{20}	0.7
C in C	1.19×10^{23}	7×10^{20}	0.6

Table 2.2: Target Composition

2.2.6 In-beam Scintillators

Scintillators S0 and S1 were used in tight coincidence (8 nsec) to count incoming charged particles. As shown in Figure 2-4, the two scintillators were placed close to each other (5 cm) and their diameters (2 cm and 1.5 cm for S0 and S1 respectively) were kept to a minimum to prevent random coincidences from a particle other than a beam particle.

S2 had an active area (diameter 12 cm) that was large enough to catch all the beam particles that went through S0, S1 and the target. It would also intercept the muon halo originating from π^- 's that went through S0 and S1. In this way the logical combination of S0 and S1 and $\overline{S2}$ would become true only when a beam particle was removed from the beam after an interaction in the target. As will be mentioned later in the chapter, this information was used in forming the trigger for data taking. The in-beam scintillators S0, S1 and S2 were also used for fine beam tuning. The objective was to maximize the ratio of S0·S1 (number of coincidence events in S0 and S1) to S2 (number of events in S2). The typical ratio during our experiment was above 75 %.

2.2.7 Shielding Walls

The shielding walls (Figure 2-4 and Figure 2-5) consisted of stacked lead bricks covered by steel walls, with steel legs on the bottom to secure them to the floor. They had a minimum lead thickness of 8 inches. This was calculated to be enough material to stop decay muons from the most energetic pion beam used in our experiment. So they protected the π^0 detector and the scintillators from the muon halo originating upstream of the walls. The muon halo was concentrated around the beam and its density dropped radially outward. This was because during the transport in the channel the muons with finite transverse momenta would have been absorbed by the slits, magnet bodies, etc, and not make it into the experimental hall. Therefore we extended the shielding as close to the beam as possible without intercepting the actual pion beam.

2.3 Data Acquisition Electronics

We used the standard electronics originally developed for the NMS. Since they were developed for the NMS, for which they had to collect and pass large amount of information at a high

speed, many of the modules were computer controlled and had very fast processing capabilities. Another distinct aspect of the NMS electronics was that most of the modules were located in the experimental cave. This aspect greatly simplified the number of cables and wires that had to be patched into the counting house from the cave. However since one could not enter the cave while the beam was on, the fine tuning of the electronics, for which real beam was required, took many cave entries.

Figure 2-16 shows a simplified diagram of the overall electronics set-up. The detector put out analog signals from the photo-multiplier tubes. Some copies of the signals were delayed to be integrated later, while others were converted into NIM (Nuclear Instrument Module) standard logic pulses (-750 mV, true) to be used in various logic functions.

2.3.1 Triggering

There were two kinds of triggering during the data acquisition. One kind occurred in relation to the pion beam (beam-related trigger), while the other kind occurred when a cosmic ray entered the detector (cosmic trigger).

The charged particles in the beam first fired the beam counting scintillators, S0 and S1. When there was a charged particle removal from the beam, a triple coincidence $S0 \cdot S1 \cdot \overline{S2}$ was formed. (See Figure 2-17.) If an interaction occurred in the target and a particle headed into the π^0 detector, depending on whether it was charged or neutral it might or might not fire the charged particle veto scintillator first.

The signals from the π^0 detector were sorted into eight groups of 12 depending on the crystal from which they originated for logic purposes, as shown in Figure 2-18. Each group represented the sum of two adjacent rows of crystals in the detector. When the sum of the pulse heights in a group exceeded a computer controlled threshold (set at 40 mV, which corresponded to 60 MeV of summed energy), a "true" logic pulse was issued.

Instead of setting lower threshold values on the pulse heights from individual crystals, this grouping helped to filter random events, since a photon shower tended to light up clusters of neighboring crystals. The top and bottom four groups were summed to form two logic signals called Detector Top Half and Detector Bottom Half.

The PLU (Programmable Logic Unit), as seen in Figure 2-16, handled the central logic formation. The advantage of using this unit was that the logic functions were formed and

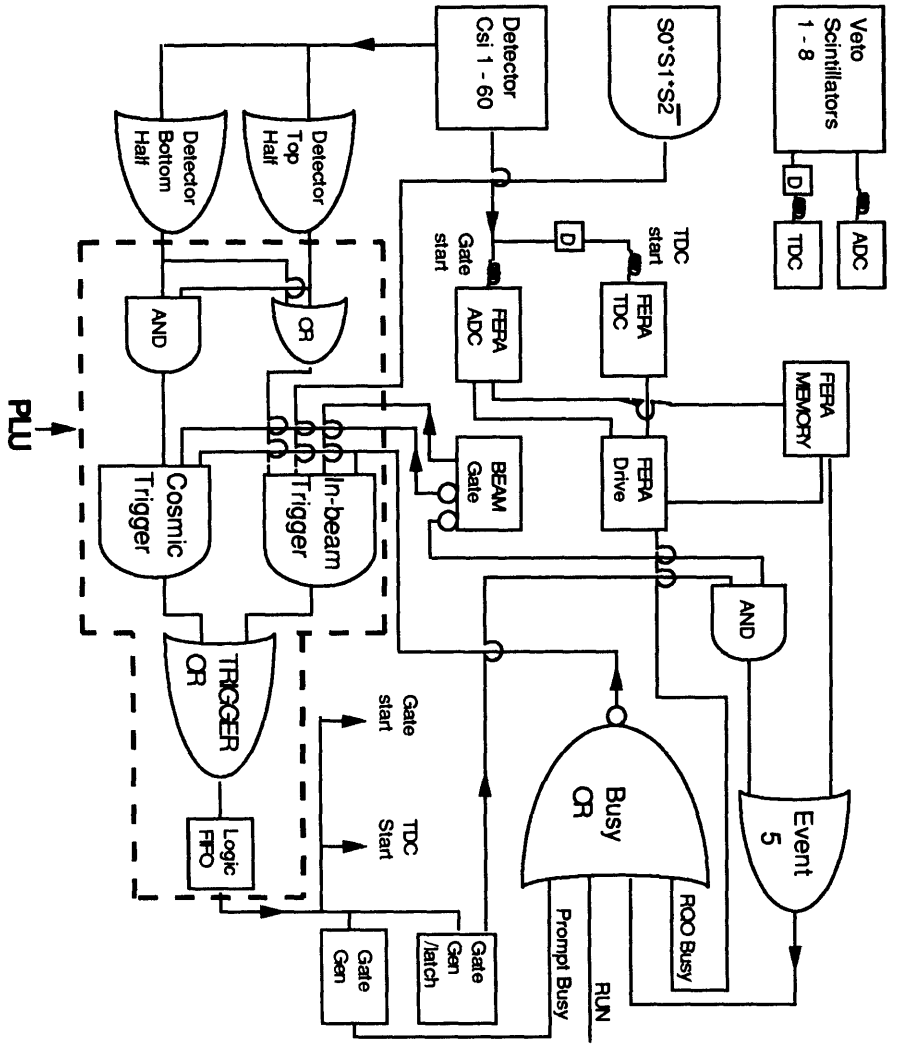

Figure 2-16: The electronics set-up

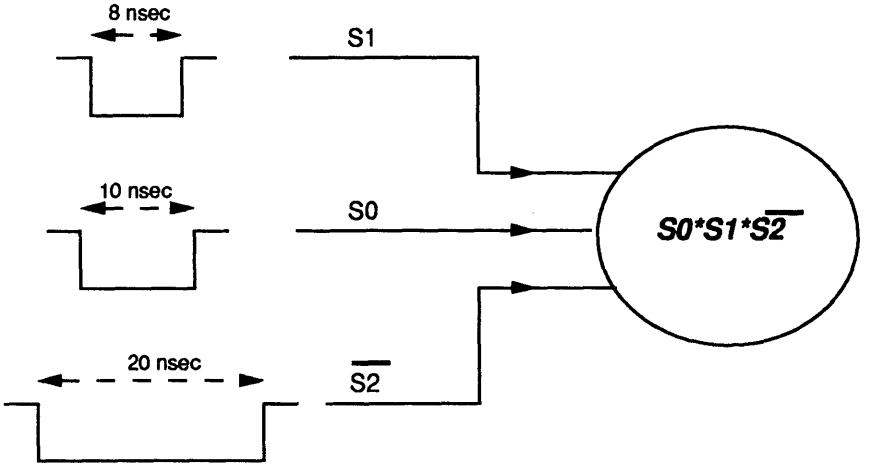

Figure 2-17: Pulse widths in the beam scintillator coincidence

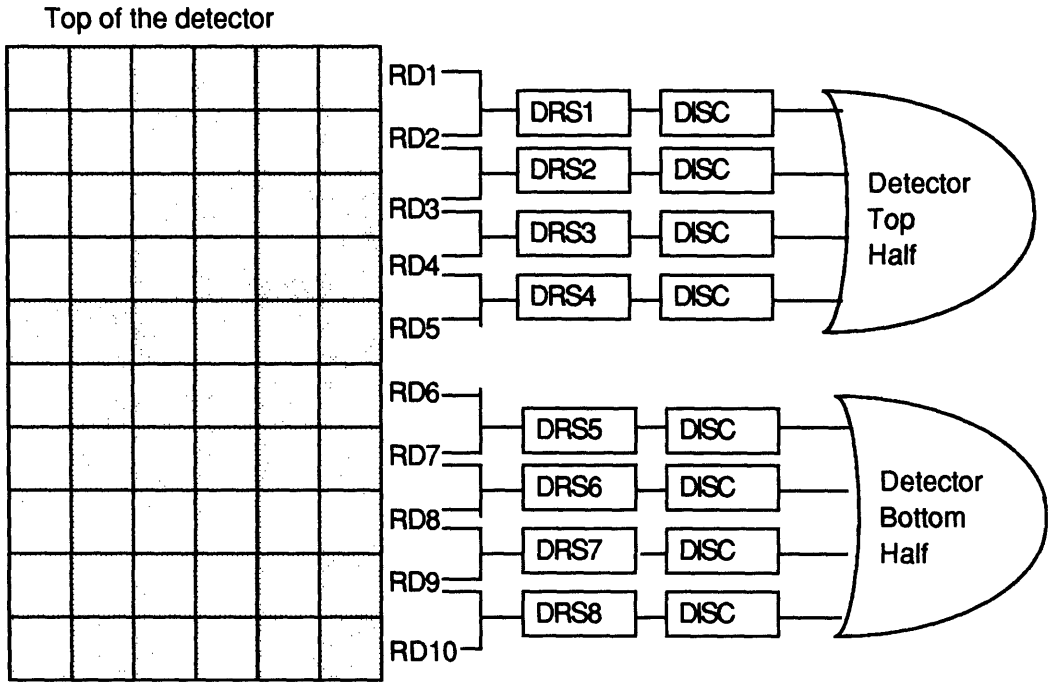

RS: Row Sum, Sum of 6 crystals in a row

DRS: Double Row Sum, Sum of 12 crystals

DISC: Discriminators, thresholds set at 60MeV

Figure 2-18: Calorimeter Row Sums

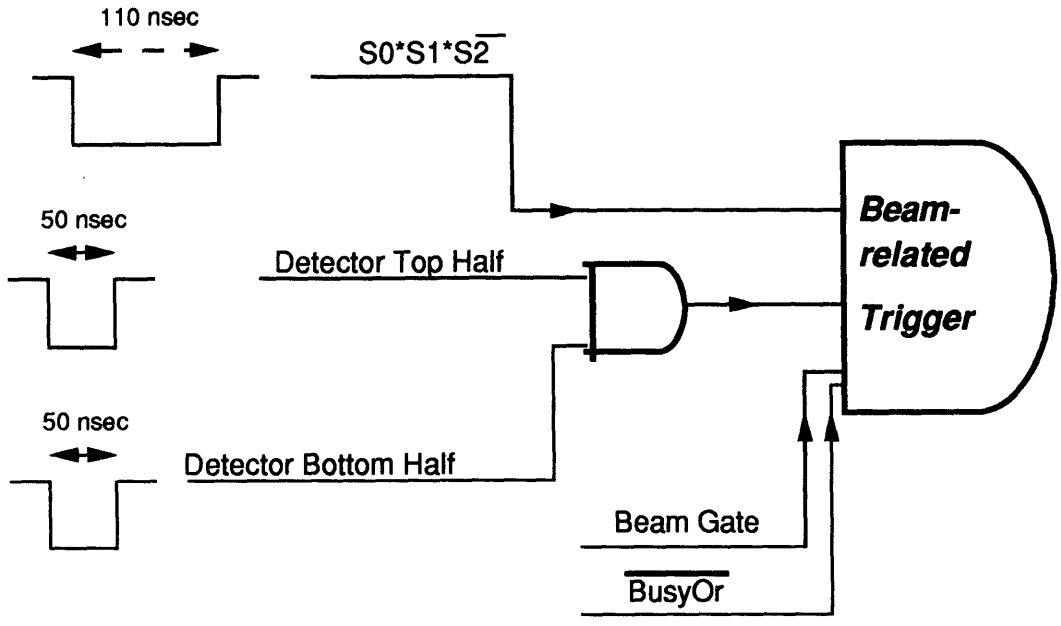

Figure 2-19: The beam-related trigger

executed by a computer command (as opposed to a hard-wiring by hand) allowing for a quick change in the logic functions. Inside the PLU the Detector Top Half and Detector Bottom Half signals were ORed before going into the beam-related trigger. (see Figure 2-19.) The logic signal $S0 \cdot S1 \cdot \overline{S2}$ also went into the beam-related trigger. The beam-related trigger was both busy-gated and beam-gated as will be described later in this chapter. The cosmic trigger was similar to the beam-related trigger except that the detector top half and detector bottom half logic signals were ANDed before entering the cosmic trigger. This was to accept only those cosmic ray events that penetrated both the upper and the lower halves of the detector. This was not the case with the beam-related triggering in order to allow the cases in which the two photon clusters from π^0 decay might appear in the same half of the detector. The cosmic triggers were allowed only in the absence of the beam gate. TriggerOR, the sum of the beam-related and the cosmic triggers, provided a "go ahead" signal for the ADC (Analog to Digital Conversion) integration to start and the TFC (Time to FERA Converter) clock to start ticking.

FERA (Fast Encoding and Readout Analog to digital converter) modules were used for recording the pulse height and the timing information. A FERA module had a conversion time 9 μsec for its 11 bit (2048) channels. Analog signals from the 8 veto counters and 60 CsI crystals were duplicated and delayed by appropriate amounts and sent to the FERA modules to be integrated to give the pulse height information. The duplicated analog signals were converted to logic pulses by discriminators, delayed, then went into the FERA TFC modules to stop the clocks. The FERA TFC's then would generate gates whose width corresponded to the time duration between the clock start and the stop. These gates were integrated by separate FERA modules to give the TDC (Time to Digital Conversion) information.

A FERA channel was reserved for integrating the "Cosmic Gate". The Cosmic Gate was essentially an inverse of the beam gate signal. So the integration of the Cosmic Gate gave a zero value when a beam gate was present and a positive value when it was not. This information was later used in the replay of the data in classifying the events into the beam-related and the cosmic events depending on the cosmic gate integration value.

As a trigger gave a reference point in time for all the subsequent timing operations, it was important that the trigger itself was timed consistently with respect to a π^0 event. To this end the trigger timing was determined by the in-beam scintillator logic signals, $S0 \cdot S1 \cdot \overline{S2}$. The in-beam scintillator pulses were present in all the beam-related events and they had stable timing characteristics. Therefore as seen in Figure 2-19, in forming the beam-related trigger, the logic pulse $S0 \cdot S1 \cdot \overline{S2}$ came in last to determine the coincidence timing. The beam gate was "true" during the beam pulses. The busy input to the trigger in Figure 2-19 came in as a veto when the data acquisition system was too "busy" to take a new data event. It had a very large veto width enveloping the logic pulses from the in-beam scintillators and π^0 detector.

2.3.2 Reading out the signals and passing them to the computer

A combination of CAMAC (Computer Aided Measurement And Control) interfaces, a MBD (Microprogrammable Branch Driver) and a MicroVax Computer was used to transfer and process the data. A system called "Q", developed at LAMPF was used to oversee this operation[30]. The CAMAC interface was a device that housed, powered and communicated with the modules it contained, such as FERA modules, scaler modules, and other programmable modules. Whenever an event was triggered, the Q analyzer would prompt the MBD to read out the appropriate CAMAC modules. The information was then stored into a buffer of memory inside the MBD. When the buffer was full, the MBD would signal the computer to read the contents of the memory. The computer processed some of the events on line and stored all events on a 8mm magnetic tape.

For most of the data acquisition, the electronics system operated in a "multi-event" mode. This was another special feature of the NMS electronics system enabled by the use of the FERA modules. The beam-related events occurred only during a macro-pulse (one of the 120 beam bursts per second) and they were stored in the FERA memory modules. When a macro-pulse was over, as long as there had been one or more beam-related events during that macro-pulse (this was ensured by a latch set by a beam-related event in a discriminator), an event flag (event 5 flag) was generated. This flag in turn caused the Q analyzer to command that the FERA memory be read out and passed onto the computer via the MBD. The cosmic events were recorded and stored in the FERA memory modules only in the absence of the beam gate as previously mentioned, and were read out and passed to the MBD only when the FERA memory buffer filled up. Almost two hundred cosmic events would fill the FERA memory buffers. Obviously the advantage of the scheme was to maximize the data taking rate during a macro-pulse by deferring the data reading and transferring job until the macro-pulse was over.

2.3.3 Busy Gate Formation

A busy gate was used to compute the "live time". Live time is the fraction of the time that the data acquisition system was able to receive and record the incoming events during a given run and was calculated by:

$$Live\ Time = \frac{(Triggers)_{not\ busy}}{(Triggers)_{total}} \tag{2.4}$$

The busy gate was "busy" as long as one of its inputs was "true" (refer to the busy circuitry in Figure 2-16). Databus busy came from the CAMAC driver module and meant that the various

commands were being passed around and implemented within the CAMAC. Event 5 busy came on when the Q analyzer prompted the MBD to read the FERA memory modules and turned off when the Q analyzer acknowledged that the contents of the modules were read out completely. A Run signal was generated by the Q system when the user started a data acquisition run. After each event, the ADC values from the FERA modules would be transferred to the FERA memory modules for a temporary storage. During this transfer process a FERA driver module that was in charge of coordinating the FERA modules, would issue a RQO(ReQuest Output) busy signal and clear it when the transfer was complete. A Prompt busy was a gate of 14 μsec width issued when a TriggerOR was generated to allow the time for the electronics modules to properly convert and store the data in the FERA memory modules.

2.3.4 Scaler Event

Scaler Events were gated by the run gate and were read out and cleared every 13 seconds by the MBD. The number of hits in the individual CsI crystals, veto scintillators, and the beam counting scintillators were recorded in the scaler events. All the logic signals from the PLU were also recorded in the scaler events.

Chapter 3

The Detector Monte Carlo Code

A Monte Carlo code was written to study the performance of the detector and calculate its acceptance (efficiency for detecting π^0 's).

3.1 Geometry

The geometry of an individual crystal, including the 1° taper on two sides, was written into the detector Monte Carlo code. The geometry of the detector (with 60 CsI crystals) in the code was approximated by flat faces in front and back, instead of the concave faces of the real

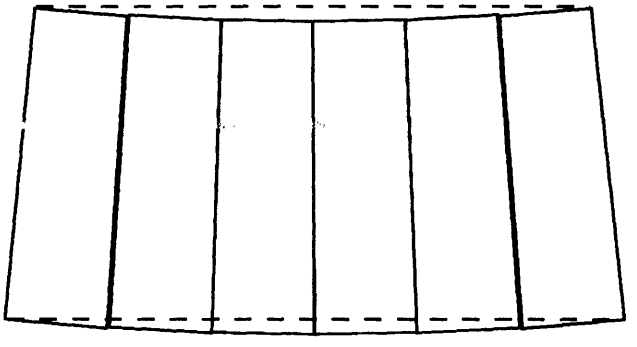

Figure 3-1: Top view of the detector. The dashed line corresponds to the detector geometry as written into the Monte Carlo code.

detector, as shown in Figure 3-1. The eight segmented charged particle veto scintillators were approximated by a single panel. The cylindrical geometry of the targets was written into the code with appropriate dimensions for the single and triple layer targets.

3.2 Event Generation

Due to its short lifetime, a π^0 formed in the target decayed at essentially the same position as where it was formed. The π^0 formation position was distributed uniformly in the direction of the beam, and according to a Gaussian distribution in the radial direction with a width corresponding to the beam width. The beam width (1 cm) was set to be a little less than the diameter (1.5 cm) of the smallest beam counting scintillator (S1).

The π^0 was given a momentum distributed isotropically in space. In practice however, to save computing time, the phase space in which the detector was "blind" to the π^0 's was excluded in the initial π^0 momentum distribution. At the end of a Monte Carlo run, this restriction was appropriately accounted for.

In its rest frame, the π^0 decayed into two photons whose momenta were equal in magnitude and opposite in direction.

3.3 Fiducial Test

After the decay photon momenta were transformed into the lab frame. If both of the photons hit the face of the calorimeter, that event passed the fiducial test and was processed further.

The charged particle veto scintillator would fire whenever charged particles entered the veto scintillator and deposited more than 1.2 MeV (the threshold set in the hardware during data acquisition). This included cases such as a photon conversion in the target (~7% of the time) and in the charged particle veto scintillator itself (~3% of the time). The likelihood of the above cases was calculated by:

$$I = I_o e^{(-d/\lambda)}, \tag{3.1}$$

where

I is the number of the photons after travelling a distance d

I_o is the number of initial photons

d is the distance of travel in the material in units of (g/cm^2)

λ is an attenuation length.

The attenuation length varied with the material, but had a flat dependence on photon energy in the energy range of our experiment. Another case in which the charged particle veto scintillator fired was when the electrons and the positrons from the electromagnetic cascade shower (EM shower) in the calorimeter back-scattered into the scintillator. This process was a dominant source of the charged particle veto events (for example, $\sim$14% of all the π^0 events were vetoed due to the back-scattered charged particles at T_{π^-}= 164 MeV) and was included in the EM shower simulation.

3.4 EM shower

After the fiducial test, when each of the decay photons entered the calorimeter, the resulting EM shower process was simulated by the well known computer code called EGS[31]. In the EM shower, the energetic photon first converts into an electron and a positron pair. The electron and the positron then emit bremsstrahlung photons which in turn convert into more electron and positron pairs, and so on. The process continues until the energy of the electrons and the positrons drops below the critical energy (E_c). While bremsstrahlung radiation is the primary energy loss mechanism for the electrons and positrons at energies above E_c, atomic excitation and ionization start to become more important at energies below E_c. The value of E_c for CsI is about 15 MeV. At the end of the shower process a user-written program collected and recorded the energy deposit in each of the 60 CsI crystals.

3.5 Acceptance

The energy deposit in each of the 60 CsI crystals from both of the decay photons was passed on to the same replay analysis routines that the real data events were subjected to for further π^0 ID tests and momentum reconstruction.

After a large number of trials to obtain good statistics, the acceptance of the detector at a given detector set-up was given by:

$$d\Omega = \frac{\text{number of detected } \pi^{0\prime}\text{s}}{\text{number of "thrown" } \pi^{0\prime}\text{s}} \times 4\pi. \tag{3.2}$$

3.6 Results

In Figure 3-2 is shown a histogram of the difference between the measured and the "thrown" π^0 energy at detector angle 55° and T_{π^-}= 164 MeV. The position of the peak in this curve is not at zero but is shifted to the left. This shift is due to leakage of energy from the sides of the calorimeter. Figure 3-2 shows that the mean energy leak is 9 MeV. The width of the curve (FWHM of 12 MeV) corresponds to the detector energy resolution.

In Figure 3-3 is shown a histogram of the difference between the thrown and the measured π^0 scattering angles. Unlike the energy resolution histogram, this histogram is centered at zero degrees and is symmetric. It shows a detector angular resolution of 8° (FWHM).

In Table 3.1 are listed the detector acceptance and the detector angular and energy resolution calculated from the Monte Carlo code for all of the detector configurations employed during the experiment.

During the experiment "acceptance scans" were performed in which the detector measured the same proton SCX cross section at different R's (distance between the detector and the target). In Figure 3-4 are compared the proton SCX cross section computed from the phase shift calculation $((\frac{d\sigma}{d\Omega})^{SAID}_{p\,SCX})$[10] and from using the acceptance calculated from the detector Monte Carlo code $((\frac{d\sigma}{d\Omega})^{MC}_{p\,SCX})$. The $((\frac{d\sigma}{d\Omega})^{SAID}_{p\,SCX})$ can be expressed as:

$$\left(\frac{d\sigma}{d\Omega}\right)^{SAID}_{p\,SCX} = \frac{\left(\iint Yield_p^{signal} dE_{\pi^0} d\theta_{\pi^0}\right)_{Total}}{N_{\pi^-}^{CH_2\,runs}\; n_p\; d\Omega^{SAID}}\,, \tag{3.3}$$

and $((\frac{d\sigma}{d\Omega})^{MC}_{p\,SCX})$ was calculated as:

$$\left(\frac{d\sigma}{d\Omega}\right)^{MC}_{p\,SCX} = \frac{\left(\iint Yield_p^{signal} dE_{\pi^0} d\theta_{\pi^0}\right)_{Total}}{N_{\pi^-}^{CH_2\,runs}\; n_p\; d\Omega^{MC}}\,. \tag{3.4}$$

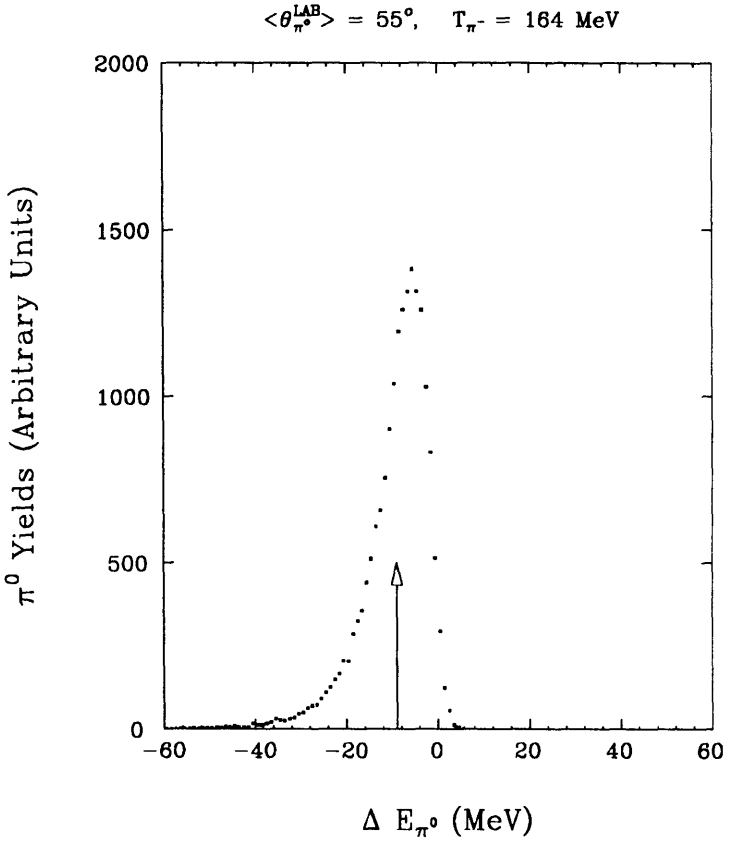

Figure 3-2: Histogram of the detector energy resolution. The x-axis corresponds to the difference in the π^0 energy value (energy measured - energy thrown). The arrow points to the mean energy value of the histogram (9 MeV) corresponding to the mean energy leak value.

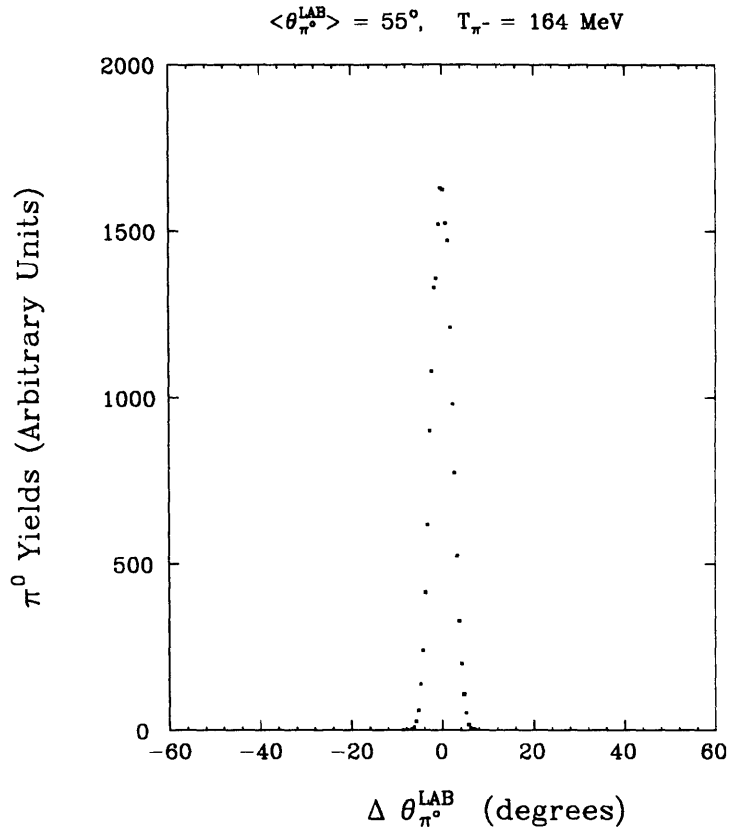

Figure 3-3: Histogram of the detector angular resolution. The x-axis corresponds to the difference in the thrown and the measured π^0 angle.

$< \theta_{\pi^0}^{Lab} >$	R	θ_{π^0} range	$\Delta\theta_{\pi^0}$	T_{π^0} range	ΔE_{π^0}	E_{π^0} leak	$d\Omega$
(deg)	(cm)	(deg)	(deg)	(MeV)	(MeV)	(MeV)	(sr)
10	39.5	0 ~ 40	7.6	150 ~ 167	12	7	55.8
55	30.6	30 ~ 80	8	117 ~ 157	12	9	93.9
85	27.4	50 ~ 110	10	95 ~ 142	12	8	75.6
120	27.4	90 ~ 140	10	81 ~ 109	12	9	76.6
T_{π^-} = 263 MeV							
10	39.5	0 ~ 40	7.5	233 ~ 266	14	9	82.2
45	45.3	20 ~ 60	7	203 ~ 257	13	9	51.9
55	30.6	30 ~ 80	8	173 ~ 247	12	9	116
70	39.5	50 ~ 90	7	160 ~ 219	13	6	63.3
95	34.4	70 ~ 120	8	128 ~ 188	13	8	77.2
125	29.9	100 ~ 150	9	110 ~ 148	13	8	87.3
T_{π^-} = 371 MeV							
10	54.6	0 ~ 30	5	342 ~ 373	15.5	10	48.6
35	55.5	20 ~ 50	5	297 ~ 359	15	10	41.1
60	43.2	40 ~ 80	7	228 ~ 321	13	8	68.5
95	35.5	70 ~ 120	9	163 ~ 256	13	7	83.3
130	34.3	100 ~ 150	8	138 ~ 191	13	7	75.8

Table 3.1: Table of the detector parameters obtained from the Monte Carlo code. The T_{π^0} range was obtained from the θ_{π^0} range according to the two body kinematics of the $\pi^- p \rightarrow \pi^0 n$ reaction.

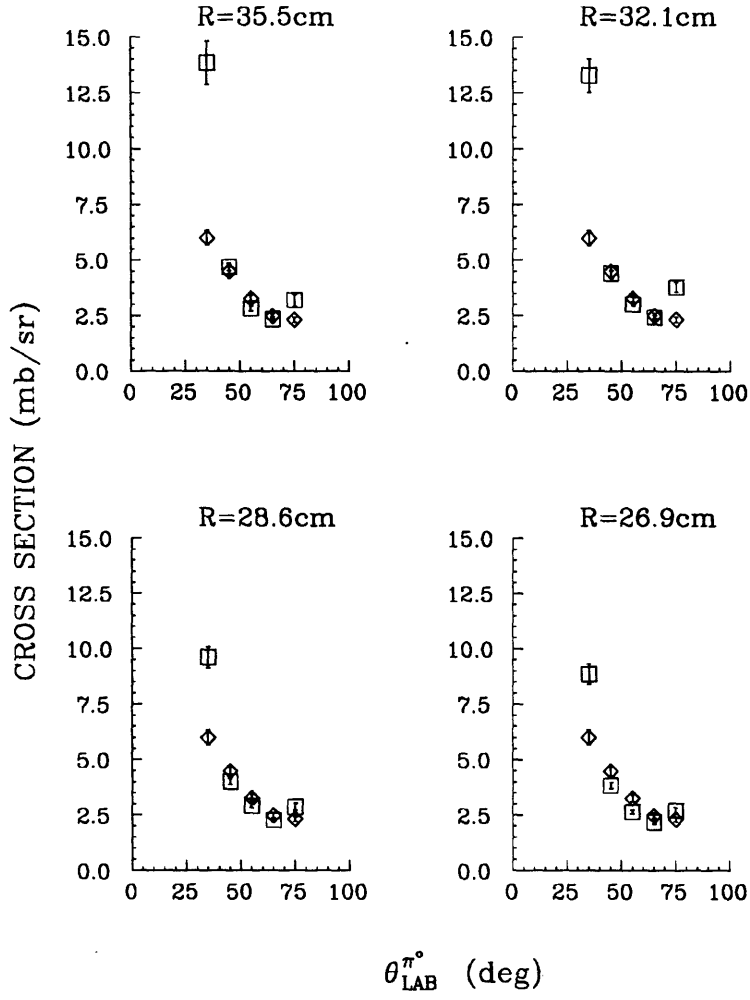

Figure 3-4: The hydrogen SCX cross sections from the acceptance runs. The box symbols correspond to the $(\frac{d\sigma}{d\Omega})^{MC}_{p\,SCX}$'s and the diamond symbols correspond to the $(\frac{d\sigma}{d\Omega})^{SAID}_{p\,SCX}$'s at T_{π^-}= 164 MeV.

The agreement between the $\left(\frac{d\sigma}{d\Omega}\right)^{SAID}_{p\,SCX}$ and $\left(\frac{d\sigma}{d\Omega}\right)^{MC}_{p\,SCX}$ is good within about 10% for the central angle bins. This means that the detector Monte Carlo correctly accounts for the effect of the varying R on the detector acceptance at least at the central angles. The agreement is, however, much worse at the edge angles.

Shown in Figure 3-5 $\sim$ Figure 3-9 are comparisons between the $d\Omega_{SAID}$ and the $d\Omega_{MC}$ at all of the detector set-up configurations used during our experiment. The agreement between the $d\Omega_{SAID}$ and the $d\Omega_{MC}$ is not very good and the average difference is about 30% at the central angles. The difference is ascribed to the geometrical approximations made in the Monte Carlo code and the imperfect nature of the EM shower simulation. At the edge angles, however the agreement is much worse. This is due to the fact that the π^0 's tend to hit the corners of the detector at the edge angles and there the acceptance is presumably even more sensitive to the precise description of the geometry and the EM shower simulation.

Despite the average 30% disagreement in the magnitudes, there is little systematic change in the way $d\Omega_{SAID}$ and $d\Omega_{MC}$ compare with each other over the energy range, from the highest energy ($< \theta^{LAB}_{\pi^0} >= 10°$, $T_{\pi^-}= 371$ MeV) to the lowest energy ($< \theta^{LAB}_{\pi^0} >= 120°$, $T_{\pi^-}=$ 164MeV). Shown in Figure 3-10 are the ratios of the $d\Omega_{MC}$ to the $d\Omega_{SAID}$ as function of the π^0 energy. The $d\Omega$'s calculated at the central angular bin centered at the detector set-up angle are shown in plot (b). In plot (a) and (c) are shown the $d\Omega$'s calculated for the angular bins that are immediate neighbors of the the central angular bin. The dashed lines are the least square fits to the points. The points are scattered around the dashed lines. It is because even within the same angular division (categorized into (a) $\sim$ (c) in Figure 3-10), the decay photons enter the detector at different geometry depending on the R and the detector set-up angles. The slopes of the fitted straight lines can be used to indicate any systematic dependence of the ratios $(\frac{d\Omega_{MC}}{d\Omega_{SAID}})$ on the energy. The slopes of the straight lines in Figure 3-10 are:

$$\begin{aligned}
&\frac{d\left(\frac{d\Omega_{MC}}{d\Omega_{SAID}}\right)}{dE} \\
&= 9.1 \times 10^{-5} \left(\frac{1}{MeV}\right) \; for\ (a), \\
&= -3.0 \times 10^{-5} \left(\frac{1}{MeV}\right) \; for\ (b), \\
&= 2.3 \times 10^{-4} \left(\frac{1}{MeV}\right) \; for\ (c). \qquad (3.5)
\end{aligned}$$

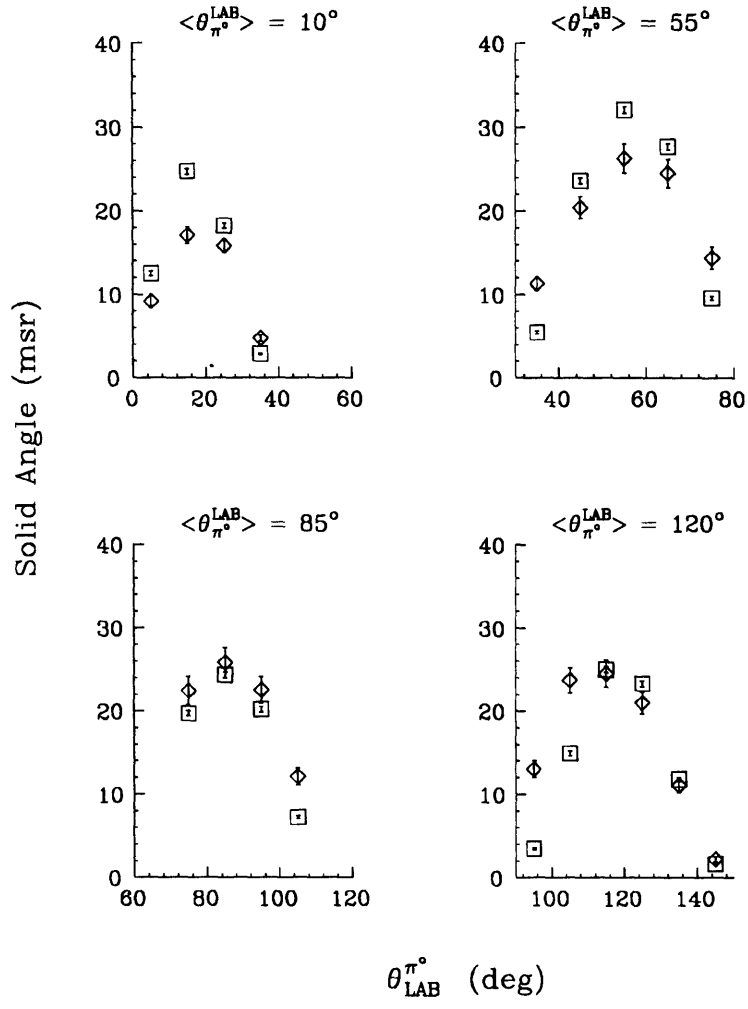

Figure 3-5: The detector acceptance functions at $T_{\pi^-} = 164$ MeV. The box symbols correspond to the $d\Omega_{MC}$'s and the diamond symbols to the $d\Omega_{SAID}$'s.

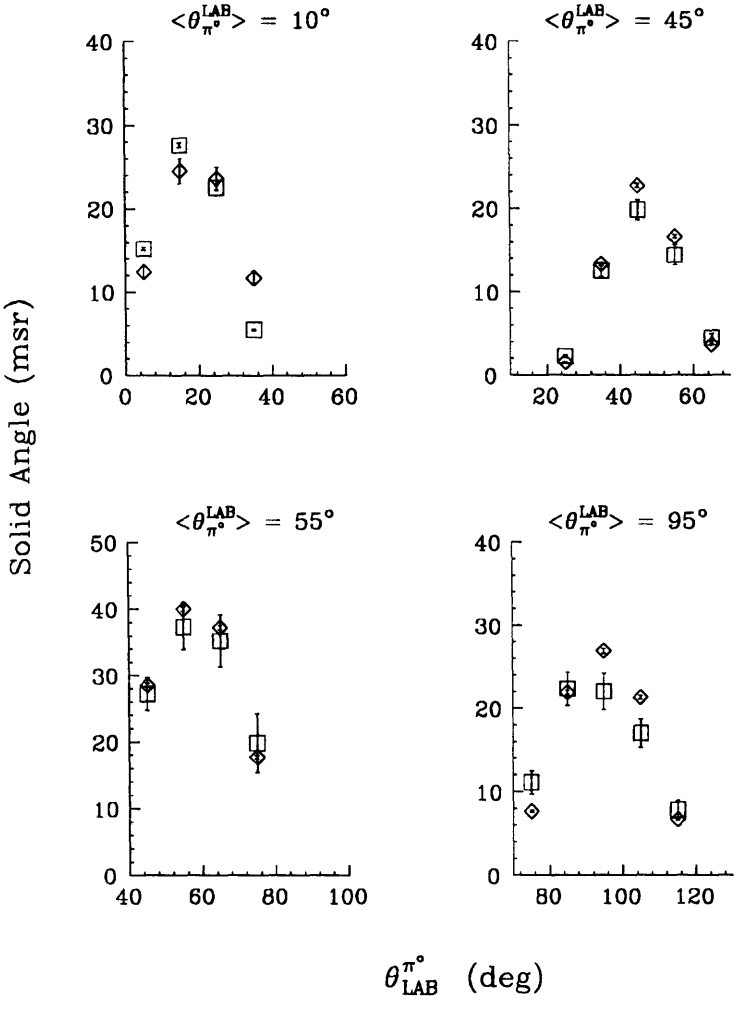

Figure 3-6: The detector acceptance functions at $T_{\pi^-} = 263$ MeV. The box symbols correspond to the $d\Omega_{MC}$'s and the diamond symbols to the $d\Omega_{SAID}$'s.

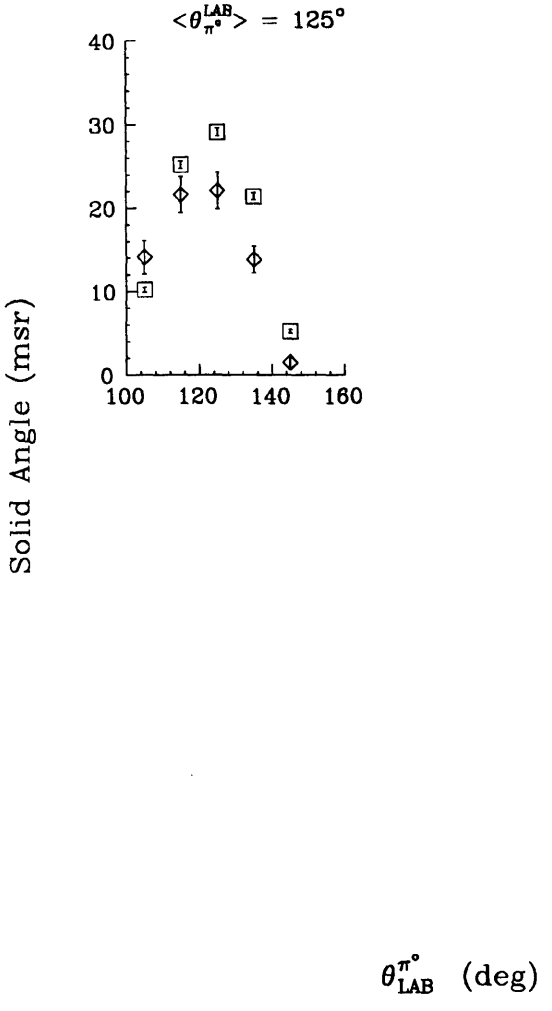

Figure 3-7: The detector acceptance functions at T_{π^-}= 263 MeV. The box symbols correspond to the $d\Omega_{MC}$'s and the diamond symbols to the $d\Omega_{SAID}$'s.

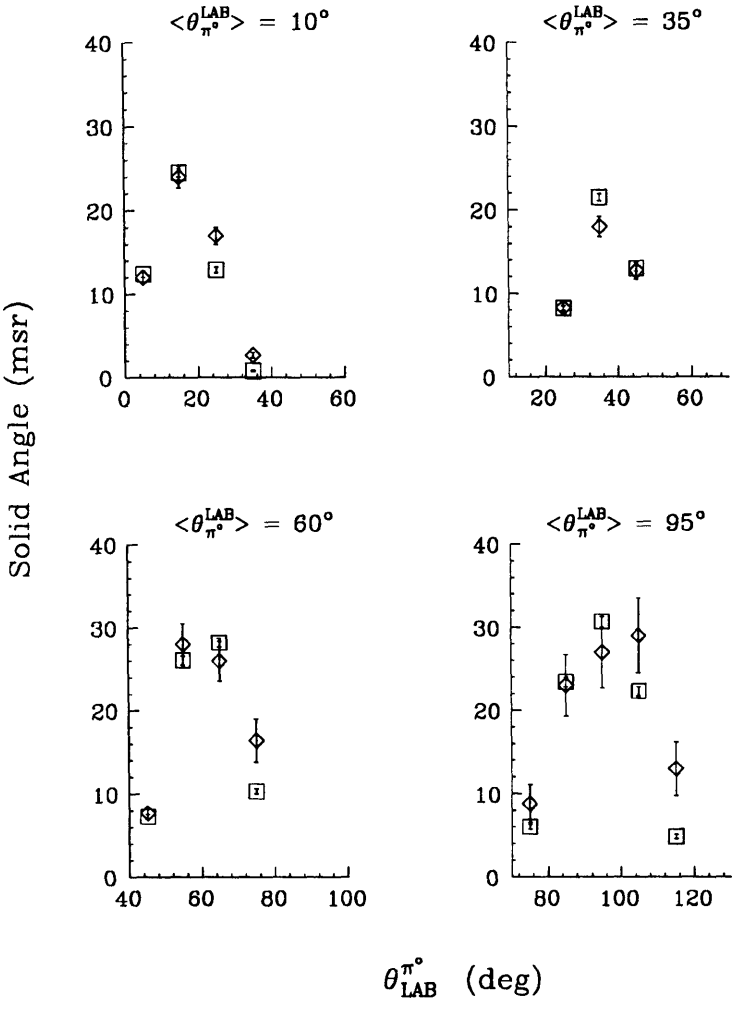

Figure 3-8: The detector acceptance functions at $T_{\pi^-} = 371$ MeV. The box symbols correspond to the $d\Omega_{MC}$'s and the diamond symbols to the $d\Omega_{SAID}$'s.

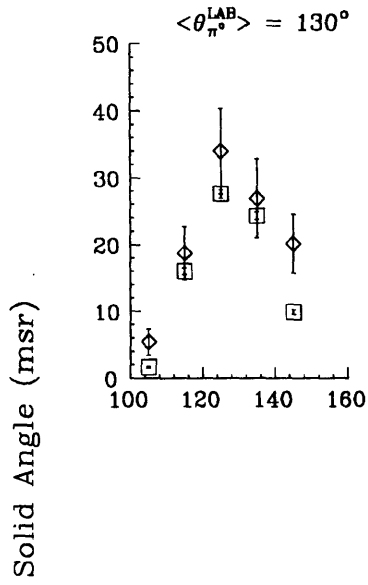

Figure 3-9: The detector acceptance functions at T_{π^-}= 371 MeV. The box symbols correspond to the $d\Omega_{MC}$'s and the diamond symbols to the $d\Omega_{SAID}$'s.

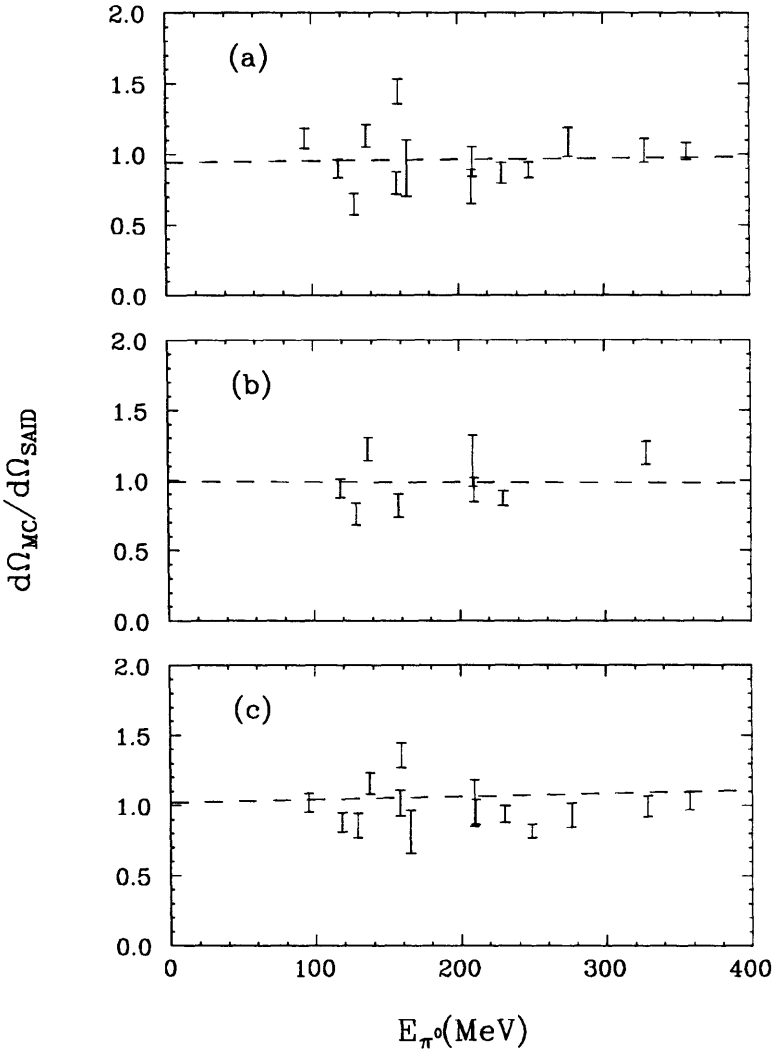

Figure 3-10: Comparison of the $d\Omega_{MC}$ to the $d\Omega_{SAID}$ at varying π^0 energy.

The average slope is given as:

$$\left\langle \frac{d\left(\frac{d\Omega_{MC}}{d\Omega_{SAID}}\right)}{dE} \right\rangle = 9.7 \times 10^{-5} \left(\frac{1}{MeV}\right). \tag{3.6}$$

This slope is small and we conclude that the detector Monte Carlo code can account reasonably well for the energy dependence of the acceptance, if not for the overall magnitude. This conclusion is supported also by the "reasonable" shapes of such histograms as the π^0 energy resolution (Figure 3-2) and the π^0 invariant mass (Figure 4-13) generated by the detector Monte Carlo code. Therefore, for calculation of the doubly differential cross section, $d\Omega_{MC}$ was used to provide the energy dependence of the acceptance with its magnitude scaled until it agreed with $d\Omega_{SAID}$ at each π^0 angular bin.

The slope in Equation (3.6) can be used to indicate the uncertainty introduced by using the $d\Omega_{MC}$ to provide the energy dependence of the acceptance as follows:

$$\frac{\sigma(\textit{energy dependence by } d\Omega_{MC})}{dE} = 9.7 \times 10^{-3} \left(\frac{\%}{MeV}\right). \tag{3.7}$$

The actual values of such systematic uncertainties in the calculation of the doubly differential cross sections will be discussed in Chapter 4.

Chapter 4

Data Analysis

4.1 π^0 Identification

As mentioned in Chapter 2, two kinds of events were accepted by the hardware trigger and recorded during our experiment. They were π^0 events and cosmic ray events. The hardware trigger ($S0 \cdot S1 \cdot \overline{S2} \cdot CsI$) was set loosely. Only minimal requirements needed to be met before an event triggered the detection system and this meant that we were accepting not only the π^0 's and the cosmic rays but other particles that we did not desire (mostly π^- 's and muons), which we call background particles. During the "replay" of the data events more elaborate routines were devised and implemented to distinguish the π^0 's from the background particles. This section describes such routines.

During the data acquisition, a coincidence $S0 \cdot S1 \cdot \overline{S2}$ would be generated when an incoming π^- interacted in the target and disappeared. At the same time if the pulse heights in the crystals combined to be greater than 60 MeV in either the upper or lower half of the detector, then this event was recorded as a π^0 event in the data stream. In addition the π^0 event was gated by the beam gate and $\overline{BUSY}$. The cosmic events were recorded between the beam gates.

If an interaction in the target produced a π^0 that subsequently decayed into two photons, then this event would not fire any of the charged particle veto scintillators. Accordingly, a π^0 identification (ID) test was performed to ensure that none of the 8 charged particle veto scintillators fired. This effectively removed events in which charged particles (from a decay photon conversion or a $\pi^- n$ scattering) were produced in the target and went into the calorimeter.

Since the $\pi^- n$ elastic scattering cross section is much bigger than the SCX cross section (by 4.5 times at $T_{\pi^-} = 164$ MeV), the number of the background events removed in this way was large. Any photon conversion in the charged particle veto scintillator itself also caused that event to be vetoed. A disadvantage of the charged particle veto scintillator, however, was that it vetoed even some of the good π^0's. Such vetos occurred when some of the electrons and positrons from the EM shower in the calorimeter back-scattered into the veto scintillator.

In the software the π^0 detector was divided in halves as shown in Figure 4-1. The area composed of the lightly hatched crystals is called the "fiducial area" of the detector. We were interested only in the events that made coincidences in both halves of the π^0 detector (either top and bottom as in Figure 4-1 (a), or left and right as in in Figure 4-1 (b)). A "lit up" crystal during an event had to have an energy deposit above the software threshold set at 12 MeV. The threshold was set to keep background events with very small pulse heights from causing the software coincidences. A π^0 event had already made an energy deposit above 60 MeV in either half of the detector in order to have formed the trigger coincidence $S0 \cdot S1 \cdot \overline{S2} \cdot CsI$. Therefore a software coincidence of both halves of the detector meant a minimum energy deposit of 60 MeV in one half and 12 MeV in the other.

The EM shower from a decay photon was recorded by a 3×3 array of the crystals centered on a crystal with a maximum pulse height. It was required that the maximum in each half reside within the fiducial area. The middle guard crystals that formed the boundary between the two halves of the detector were excluded from having a maximum pulse height, since a 3×3 shower cluster around such maximum would overlap with fiducial crystals from both halves of the detector. And this would have allowed coincident events whose cluster separation was "ambiguous". Only "unambiguous" cluster separation was allowed and it meant that the closest distance between the two clusters was two crystals apart or more. The outer guard crystals were kept from containing a maximum pulse height since such a maximum would likely to mean a substantial energy leak out of the detector as the shower advanced in the longitudinal direction.

The containment of the EM shower within the 3×3 crystal array in the lateral direction was shown to be adequate from the detector Monte Carlo study. This is shown from Figure 4-2. The histogram "epi0" represents the π^0 energy spectrum in which each photon energy was determined by summing the energy deposited in a 3×3 crystal array, while "epi0t" was a histogram of the π^0 energy spectrum in which each photon energy was determined by summing the energy deposited in all the crystals in the detector half where that photon landed. For this particular case, at 371 MeV, the highest energy in our experiment, the difference between "epi0" and "epi0t" was negligible.

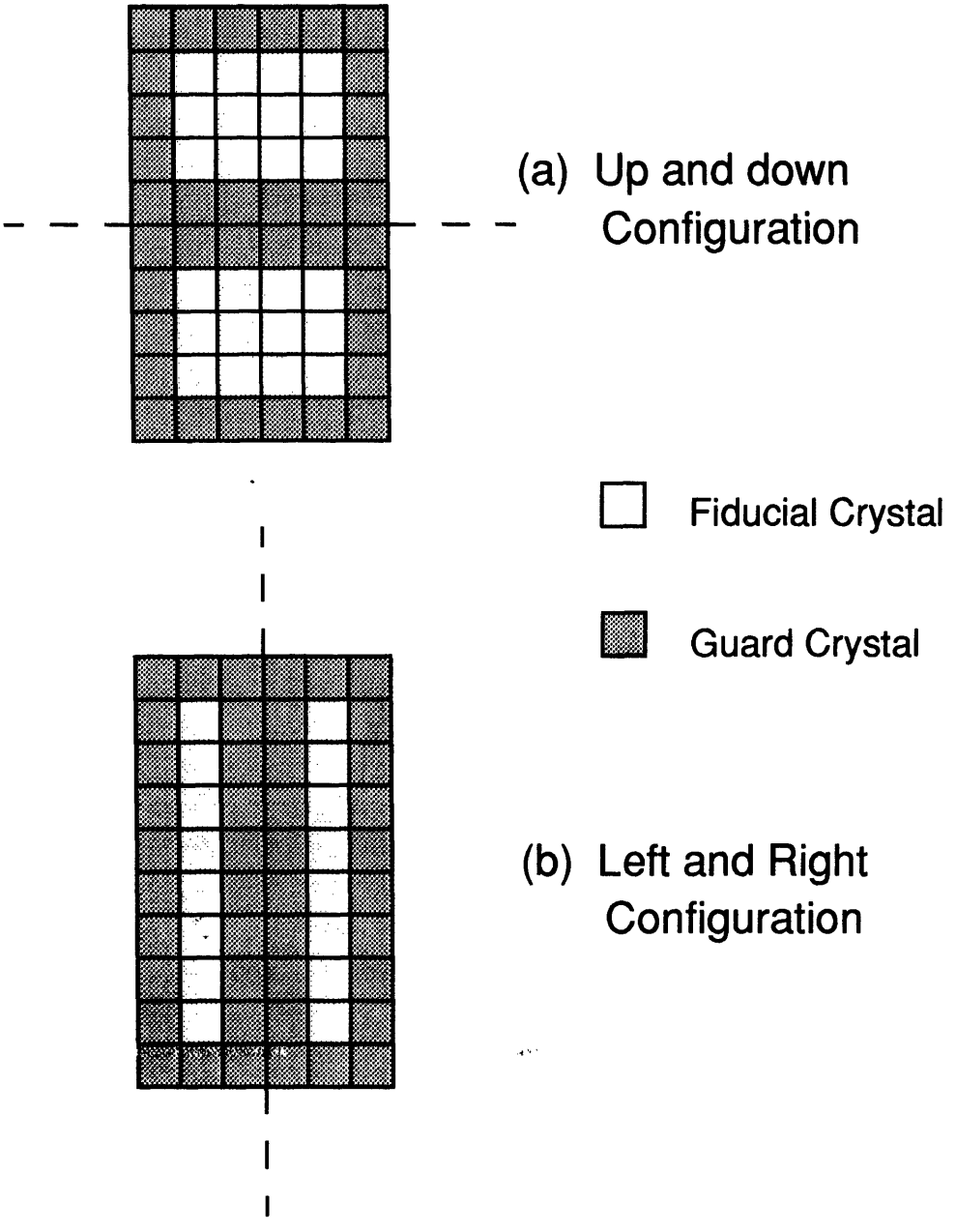

Figure 4-1: The fiducial area of the π^0 detector

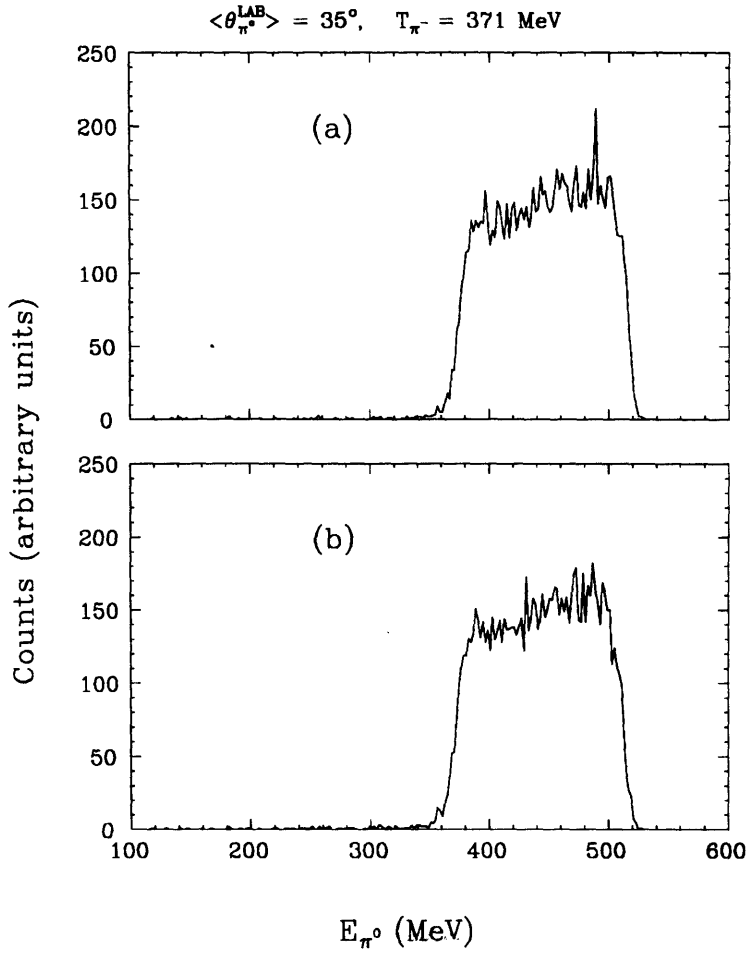

Figure 4-2: (a) is a histogram named "epi0t", (b) is a histogram named "epi0". The histograms were obtained from the Monte Carlo program described in Chapter 3.

This is confirmed by another study that found in any EM shower process regardless of the absorbing material (assuming an infinite length) and energy up to 6 GeV, only 10% of the energy lies outside the Molière radius (R_M) and more than 99 % is contained within the 3 R_M[32][33] [18]. R_M for CsI is 2.6 cm[18]. A 3×3 array of the crystals in our detector contained the lateral shower spread within 5 R_M.

The longitudinal containment of the shower, however, was not as good. Despite the long crystal depth (17 r_l), due to the proximity of the detector to the target, most of the coincident photons from the π^0 decay entered the detector at small angles to the face of the detector. This resulted in effective crystal depths for the photons that were considerably less than the nominal crystal depth of 17 r_l. Because of this, the energy leak out of the detector became a major contribution to the energy resolution of our detector.

Within a 3×3 crystal array, an energy-weighted average was taken in the horizontal and the vertical directions to determine the effective lateral conversion position of the decay photons. The effective conversion depth of the photon within the crystal was set at 4.5 r_l. This was determined from the detector Monte Carlo study to be the optimum conversion depth that resulted in the best π^0 angular resolution.

The π^0 ID tests discussed so far worked well for most of the runs except the very forward angle ones. As shown in Figure 4-3, for the 10° set-ups, part of the detector was directly in the beam. Typically the beam removal events were only a small fraction of the total beam flux (a few percent at T_{π^-} = 164 MeV) and the rest of the beam particles entered the detector. When a beam particle came directly into the detector it would trigger S2 and therefore this event would be vetoed and not fire the hardware trigger. However the scintillation pulse heights in the CsI crystals had very long tails (typically 400 nsec as shown in Figure 2-8). If a beam removal event ($S0 \cdot S1 \cdot \overline{S2}$) happened while the pulse height tail from a previous beam particle still remained and was large enough to fire any of the row sum discriminators, then a hardware trigger ($S0 \cdot S1 \cdot \overline{S2} \cdot CsI$) would be formed and this event would be recorded. Some such events managed to survive the π^0 ID tests described so far and appeared in the low energy region in the π^0 energy spectra as shown in Figure 4-4 (a). The exponential shape of the low energy tail was due to the fact that at the instant when a beam particle removal event happened there was a greater chance that the "tail" portion of the CsI pulse height from the previous beam particle would be sampled by the ADC gate than the "head" portion. This was because the CsI pulse height had a narrow head and a long tail, as shown in Figure 2-8.

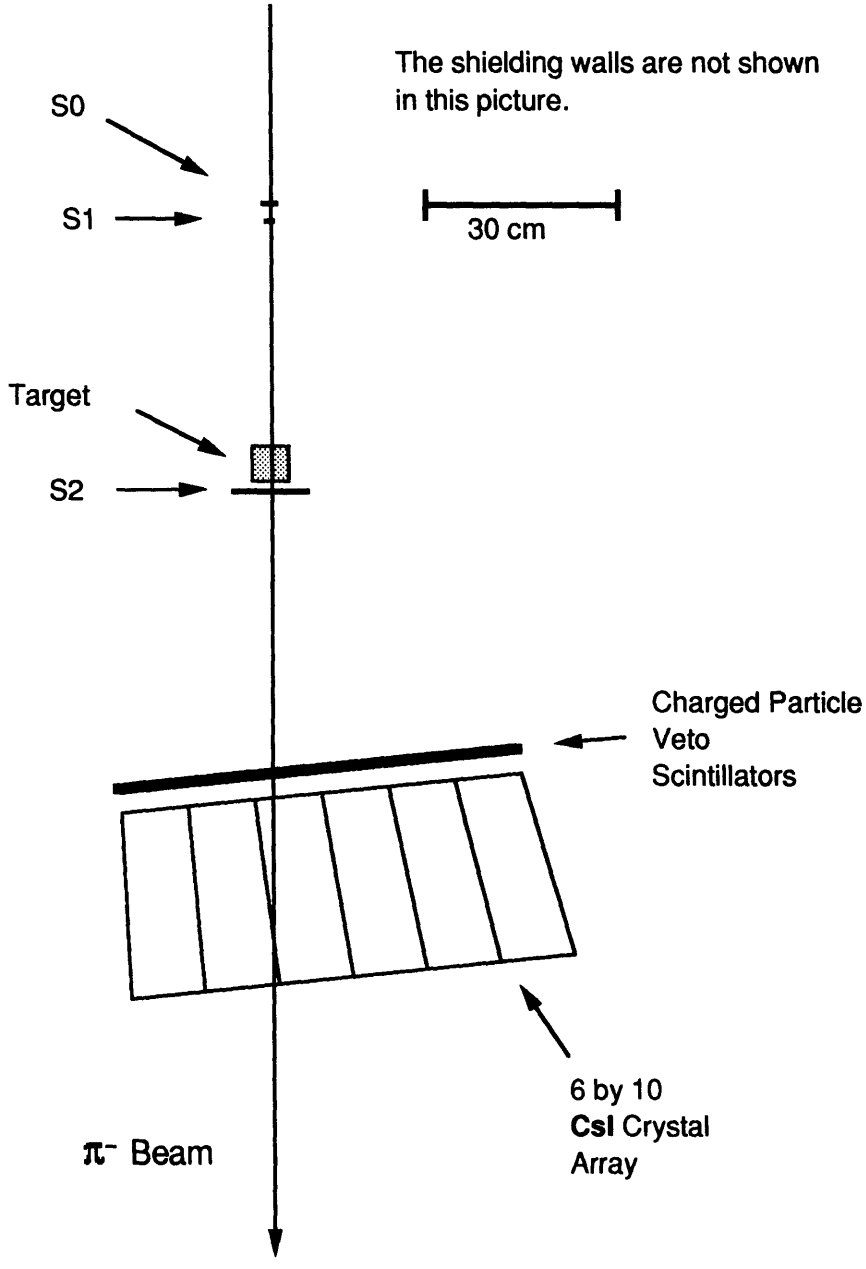

Figure 4-3: 10° detector set up

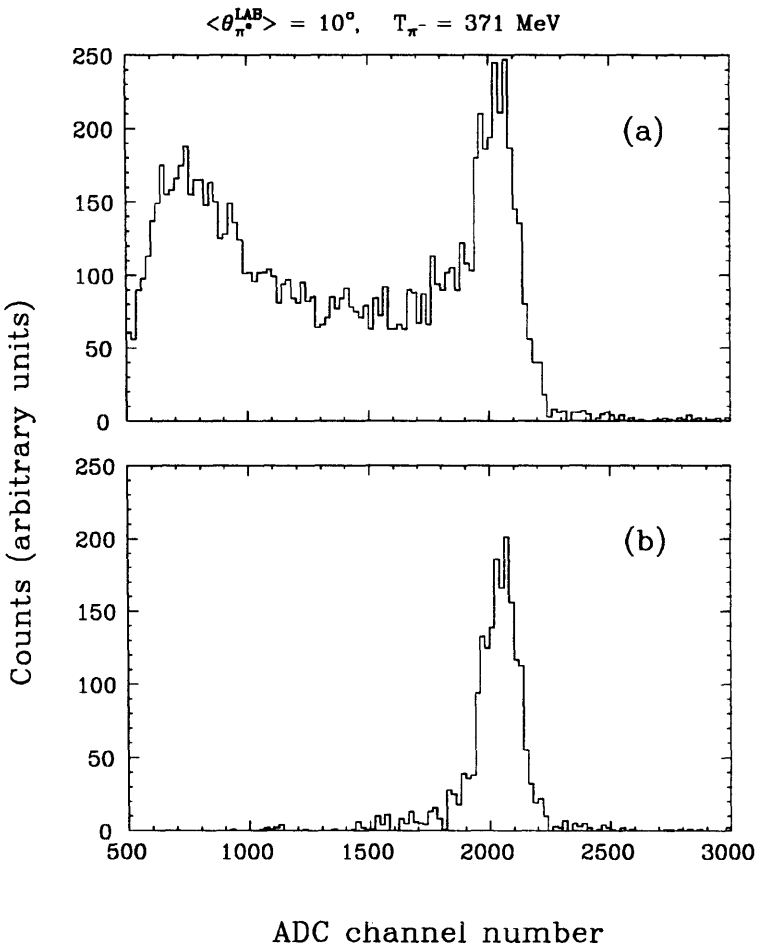

Figure 4-4: Deuteron SCX energy spectra

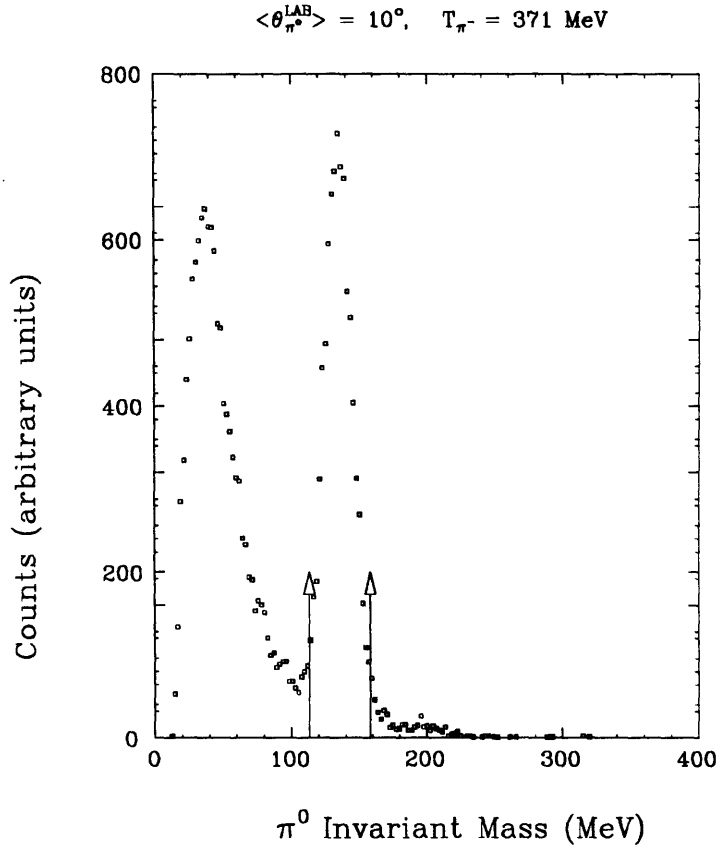

Figure 4-5: π^0 invariant mass spectrum. The two arrows make up the gate set for one of the π^0 ID tests.

An invariant mass gate was devised to eliminate this type of background events. The π^0 invariant mass is defined by:

$$\begin{aligned} {m_{\pi^0}}^2 &= P_{\pi^0\,\mu} P_{\pi^0}{}^{\mu} \\ &= {E_{\pi^0}}^2 - {p_{\pi^0}}^2 \\ &= (135\ MeV)^2 \end{aligned} \tag{4.1}$$

When it was required that all the π^0 events had to have an invariant mass within the gate specified in Figure 4-5 by the two arrows, the low energy tail present in in Figure 4-4 (a) disappeared from the spectrum as shown in figure (b).

As a cross-check to see if the good π^0 ID test scheme so far was sufficient or if there might be more background particles that needed to be filtered out, we studied the CsI crystal TDC and ADC spectra. In Figure 4-6 is shown a correlated plot of TDC values on the x-axis and ADC pulse heights on the y-axis for a crystal. The top picture is a raw histogram in which the TDC and ADC values from all the π^0 events in a given run were accumulated for the crystal without any π^0 ID tests. The bottom picture is a plot in which only the events that successfully passed all the π^0 ID tests were included. The top histogram has many scattered points around a prominent "L-shaped" band, while the bottom one has a clean L-shaped band. Ideally, instead of a L-shaped band, one would have expected a straight vertical band in a TDC-ADC correlation plot. The particles that fired the hardware trigger and proceeded into the detector would have left pulse heights of various magnitudes in the ADC spectrum and a constant value in the TDC spectrum. The TDC value would have been constant since the electrons as well as the photons, the carriers of the shower, were travelling practically at the speed of light inside the CsI during the shower process. The L-shaped band is an artifact due to the type of discriminators used to convert the CsI analog signals into the logic signals which stopped the TDC clocks. These were leading-edge discriminators and thus the time they took to produce the logic signals after the arrival of the input signals depended on the magnitudes of the input pulses. Notwithstanding its shape, the fact that the π^0 ID tests filtered out random background events to give a clean correlation band confirmed that our π^0 ID tests were indeed adequate.

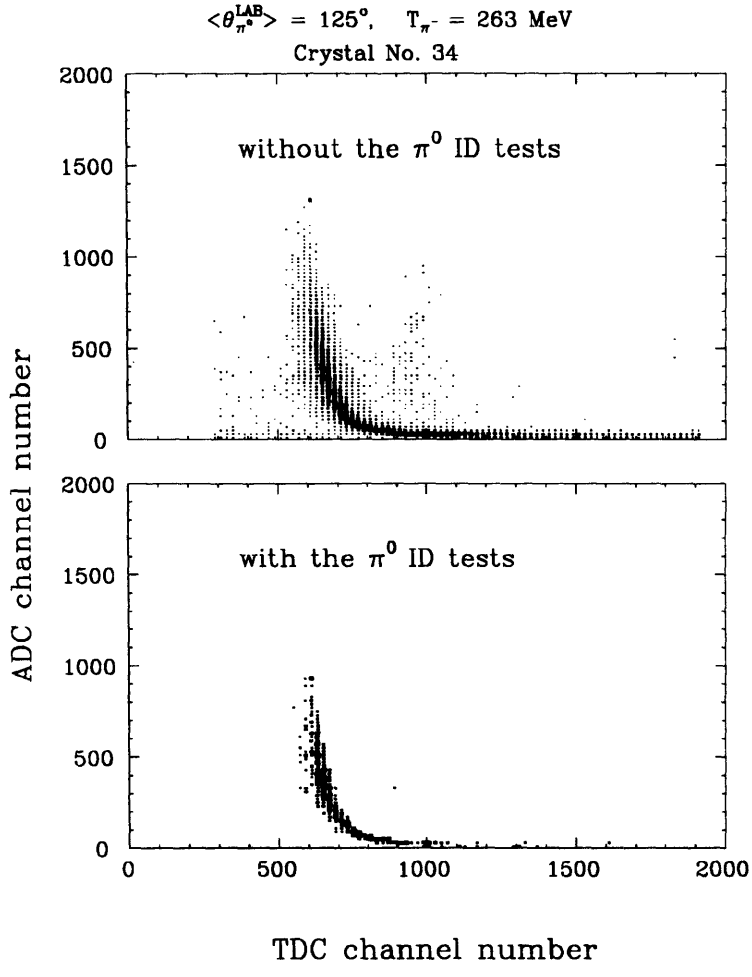

Figure 4-6: The TDC-ADC correlation plot

4.2 Energy Calibration

Throughout the experiment the temperature in the experimental cave did not stay constant. Also, during the forward angle measurements where the detector was placed at 10°, a number of the crystals intercepted the incoming π^- flux. The temperature change affected the gain of all the CsI crystals, where the gain of a crystal is defined by the combination of the CsI crystal and the attached phototube and base to be the number of the photo-electrons per unit energy deposit. On the other hand, the radiation damage effect from the beam particles was isolated only to the in-beam crystals during the 10° measurements. These effects were monitored and corrected for using the cosmic ray energy measurements made during every run.

The raw ADC channel numbers in the FERA modules that corresponded to the energy deposit inside the CsI crystals were offset by amounts called "pedestals". A pedestal was a zero signal reference point inserted by the FERA module. It also acted as a monitor of the electronics gain drift due to a temperature change, where the electronics gain was defined by the ADC channel number per unit number of electrons out of a photo-multiplier tube base.

As will be shown, we combined π^0 yields obtained from a number of runs (typically 6 to 10 runs) to calculate the cross section at a given π^0 angle and π^- energy. Also in a run there were 60 ADC channels corresponding to the number of the CsI crystals. Therefore it was necessary to make corrections so that the original energy deposit in each crystal would translate to the ADC channel number in a uniform fashion.

4.2.1 Pedestal Subtraction

When an event triggered, it was very unlikely that all the detectors (60 CsI crystals) fired. The large number of detectors that did not fire would not send any signal to the FERA modules. The FERA modules automatically injected a small charge at the leading edge of the ADC gate during their integration processes. Therefore, in the absence of any signal from the detector, the FERA modules would still integrate a small charge and put out positive ADC values, which are called "pedestals". In any ADC spectrum corresponding to the detector signals, the pedestals would show up at the low ADC channel end and would serve as the zero signal reference points. In addition, the pedestal positions would move in proportion to any change in the electronics gain due to a temperature change.

For most of the runs in our experiment, however, this change in the gain was assumed to be ignorable and the ADC pedestals were "suppressed" inside the FERA ADC modules before the data words were read out. For pedestal-suppressed runs, predetermined values that were equal to the pedestal values at a sample run (with real pedestals) were subtracted from the ADC channel numbers before they were read out of the FERA ADC's. This was done to reduce the number of data words assigned to an event. The same set of pedestals was subtracted throughout the experiment. In order to check our assumption of the stability of the electronics gain, we took a number of pedestal sample runs throughout the experiment with the "pedestal suppression" turned off, reading out the real pedestal values generated inside the FERA ADC's at the time. The pedestal values from these sample runs were indeed shown to have been very stable throughout the experiment. This showed that the electronics gain was stable, justifying the pedestal-suppression mode of operation.

At the beginning of the experiment until the "pedestal suppression mode" was operational, the runs were taken with the real pedestals, and they were subtracted later in the replay analysis.

4.2.2 Energy Calibration using the Cosmic Ray Events

The Cosmic rays striking the earth's atmosphere are mostly protons. Pions are made in pN interactions in the atmosphere and muons are created when the pions decay. The primary cosmic ray protons are slowed down in the atmosphere by Coulomb interactions with the atmospheric particles and most of the time do not make it to sea level. Most of the pions decay in flight due to their short life time. At sea level, therefore, approximately 75 % of all the cosmic ray particles are muons. Although these muons have a wide energy spectrum, at sea level they have a mean energy of approximately 2 GeV[18]. We recorded the energy deposit into each CsI crystal from such muons during every run. This information was used to monitor and correct for the crystal gain shift.

In the replay, the raw cosmic ray events were passed through sets of software tests that permitted only those events whose trajectories into a given crystal were close to vertical. For a fiducial crystal this was achieved by requiring that the crystal above and below it also fired at the same time. Top and bottom crystals on the other hand did not have neighbors both above and below, so it was required that the vertical neighbor fired and the crystals in the immediate neighboring columns did not fire in order to select the vertical cosmic ray events. At 2 GeV average energy, the muons are minimum ionizing and moreover those that passed the vertical

trajectory tests had travelled similar distances inside the crystals. Therefore, the average of many cosmic ray events within a single crystal (typically 5000 events per crystal that passed the vertical trajectory test during a two hour run) gave a narrow peak with its shape and centroid values ($\sim$ channel 290) similar for all the crystals. A typical cosmic ray spectrum is shown in Figure 4-7.

4.2.2.1 Temperature Effect

Throughout the experiment the cosmic ray centroids varied over the range of channel 270 to 310. This variation was mostly due to the fluctuation in the ambient temperature of the experimental hall.

4.2.2.2 Radiation Damage Effect

During the forward-angle measurements in which the detector was set at 10°, four crystals in the vicinity of the beam path were directly hit by the π^- beam particles. The radiation from the beam particles affected those in-beam crystals in such a way that their gain decreased as a function of the time that they were subjected to the direct beam.

In Figure 4-8 is shown the cosmic ray centroids of an in-beam crystal (crystal 45) as a function of time (run number). The first arrow in the figure indicates the time when the crystal was put in the beam path and the second one when the beam was turned off completely. Several data points after the second arrow are the pure cosmic runs taken over several days after the beam was turned off. The cosmic centroid was flat as a function of the run number until the crystal was hit directly by the beam. The small fluctuations in the centroid value here were due to the change in the ambient temperature. When the beam began to come directly into the crystal, however, the cosmic centroid started going down steadily. This decline in the centroid value occurred only with the in-beam crystals and was attributed to radiation damage from the beam particles. If it were a photo-tube base heating effect due to a higher current drawn from the base by an increased counting rate, the gain should have stabilized after a while. However, the centroid value kept decreasing for the duration of the in-beam runs (51 hours) as shown in Figure 4-8. The centroid value remained low for several days even after the beam was off (second arrow), showing that the gain decline was due to radiation damage to the crystal. The damage was not permanent, however. Three months after our experiment was concluded some

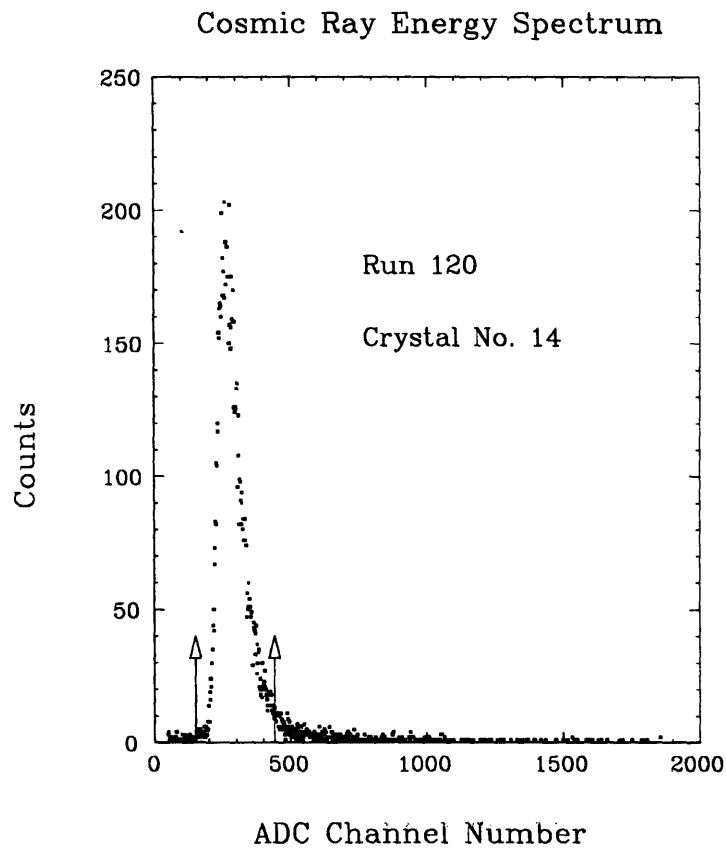

Figure 4-7: A typical cosmic ray energy spectrum. The arrows correspond to the integration limits used to compute the centroid.

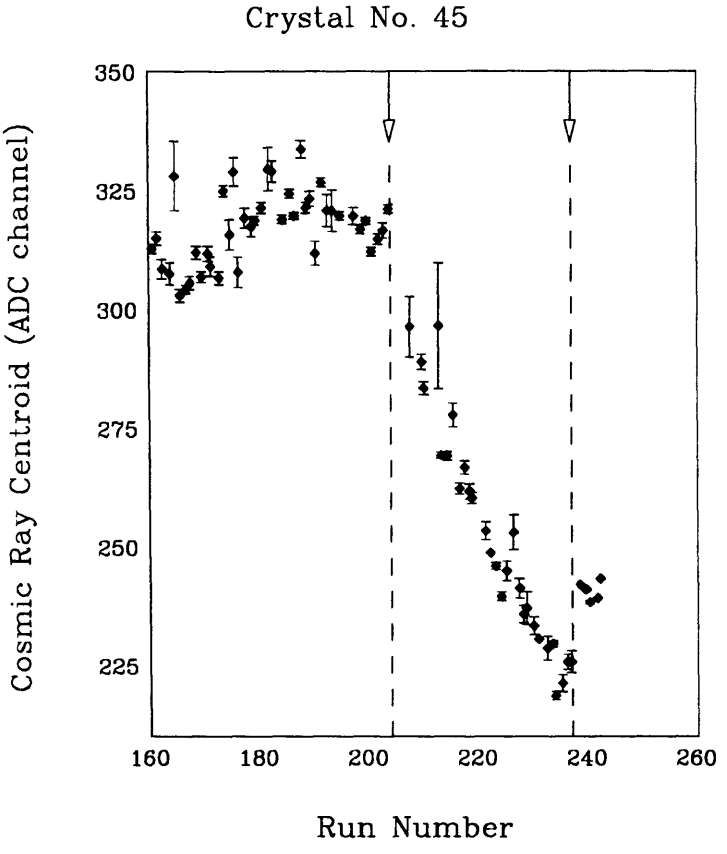

Figure 4-8: The radiation effect on the CsI scintillation response. Note suppressed zero.

of the in-beam crystals were tested and were shown to have fully recovered from the damage in terms of their scintillation response[34].

The crystal 45 shown in the figure was at the beam center and therefore had taken the highest radiation dosage. And it had as much as 30% reduction in its gain response during the in-beam runs as shown in Figure 4-8. This was a surprisingly large decrease in the crystal gain from such a small dose of radiation, considering the known radiation hardness of the CsI crystals[35]. In Appendix D a detailed calculation of the radiation dosage is given and compared with the previously reported radiation hardness of CsI crystals.

4.2.2.3 Cosmic Ray Gain Calibration

We corrected our π^0 energy spectra for the above two effects, namely the temperature and the radiation damage effect, by using the cosmic ray centroid measurements. For each run after the pedestal correction, the ADC channel numbers were multiplied by software gain correction factors so that the cosmic centroids averaged over that run would appear at ADC channel 290. Channel 290 was chosen, because it was the mean cosmic centroid throughout the experiment for most of the crystals.

$$\text{Software gain correction factor} = \frac{290}{\text{Cosmic centroid average}} . \tag{4.2}$$

Assuming a linear relationship between the energy and the ADC channel, then the π^0 energy would be related to ADC channel number by the same proportionality factor in all the runs.

4.2.3 Energy Calibration Plot

An energy calibration plot (Figure 4-9) was prepared to establish a relationship between the ADC channel number and the true energy for our π^0 spectra.

Plotted along the y-axis in Figure 4-9 are the π^0 energies corresponding to the peak positions of the hydrogen SCX cross section at every detector set-up computed from two-body kinematics, while along the x-axis are plotted the corresponding ADC channel numbers. As previously discussed, each decay photon suffered some energy leak out of the detector due to an incomplete containment of the longitudinal component of the EM shower. Therefore the original ADC channel numbers corresponding to the peak positions had to be shifted by an average amount

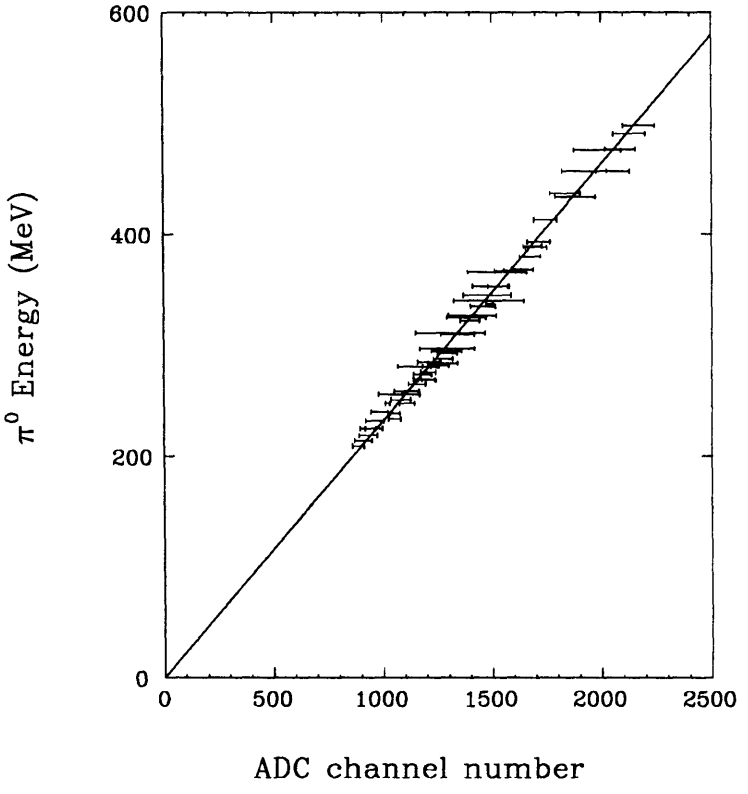

Figure 4-9: The energy calibration plot. It is drawn through the data points and has a slope corresponding to a conversion factor of 4.31 channel/MeV.

of energy leak at the given detector set up. The average energy leak values used here were calculated by the detector Monte Carlo code (see Table 3.1). A straight line going through the origin meant that the energy calibration operations were done correctly and also that the linearity assumption made in the previous section in the correspondence between the energy and the ADC channel was a valid one.

4.3 Energy and Angular Resolution

In Figure 4-10 is shown a 2 dimensional correlation plot of π^0 angle and total energy for proton SCX at T_{π^-}= 164 MeV and detector angle 55°. The proton SCX reaction has two bodies in the final state, and therefore, the outgoing π^0 energy and angle are kinematically correlated. The collection of these correlated π^0 's form a band called the "2-body kinematics band" as shown in Figure 4-10. The negative slope of this band corresponds to the fact that at smaller angles the π^0 energy is higher.

This band also gives information about the detector resolution. Ideally with an infinitely high resolution detector we would see a line in place of a band. Finite widths in energy and angle directions of this band arise from the finite energy and angular resolutions of the detector. In Figure 4-10 when a horizontal slice of the band is taken, with its vertical thickness corresponding to a π^0 scattering angle bin from 51° to 59°, and is projected onto the energy axis, we obtain a π^0 energy spectrum shown in Figure 4-11. If a vertical slice of the band is taken, with its horizontal thickness corresponding to a π^0 energy bin from 135 MeV to 137 MeV, and is projected onto the angular axis, we obtain a π^0 angular spectrum as shown in Figure 4-12.

The peak in Figure 4-11 has a FWHM of 21 MeV. This width is a convolution of the detector energy resolution and the kinematic broadening.

$$\Delta E_{Total} = \sqrt{(\Delta E_{detector})^2 + (\Delta E_{kinematic\,broadening})^2}. \tag{4.3}$$

The $\Delta E_{kinematic\,broadening}$ is the energy range covered by the 2-body kinematic relationship within the given scattering angle bin (from 51° to 59°) set in Figure 4-11. However, the scattering angle itself has a finite resolution, which we assume to be 10° here. Therefore the

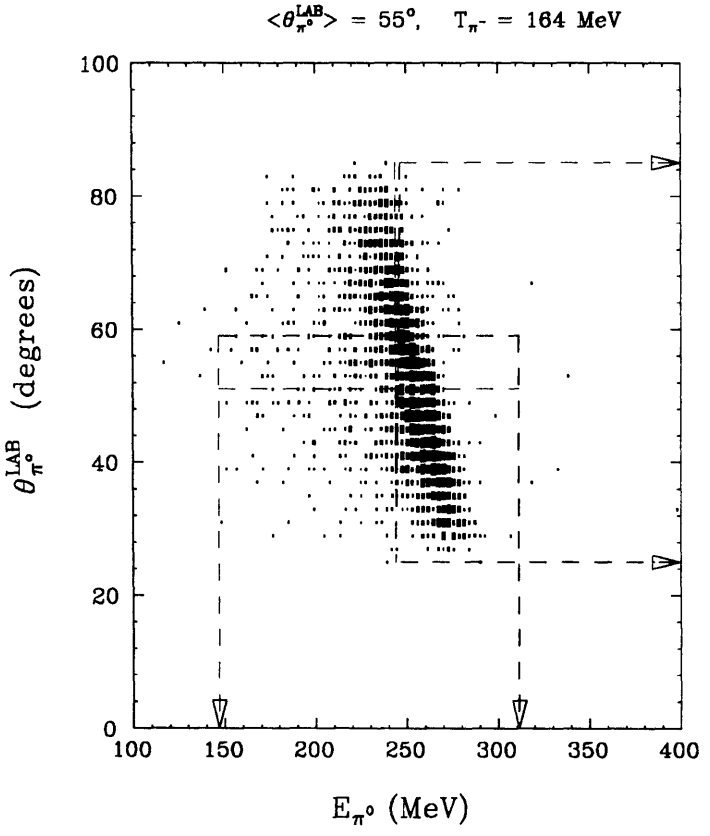

Figure 4-10: The 2 body kinematics correlation plot

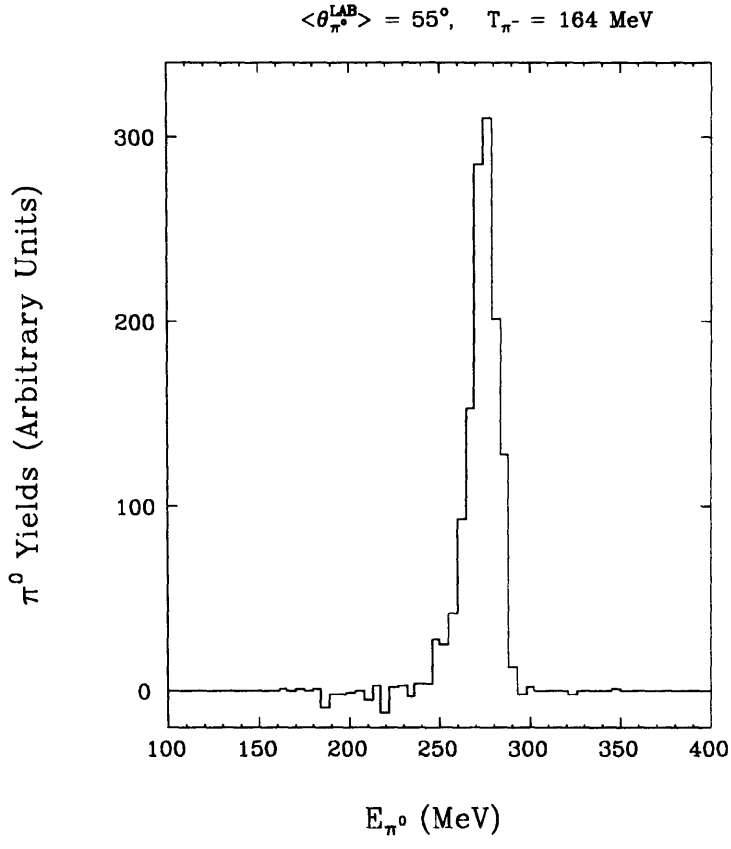

Figure 4-11: The π^0 energy spectrum

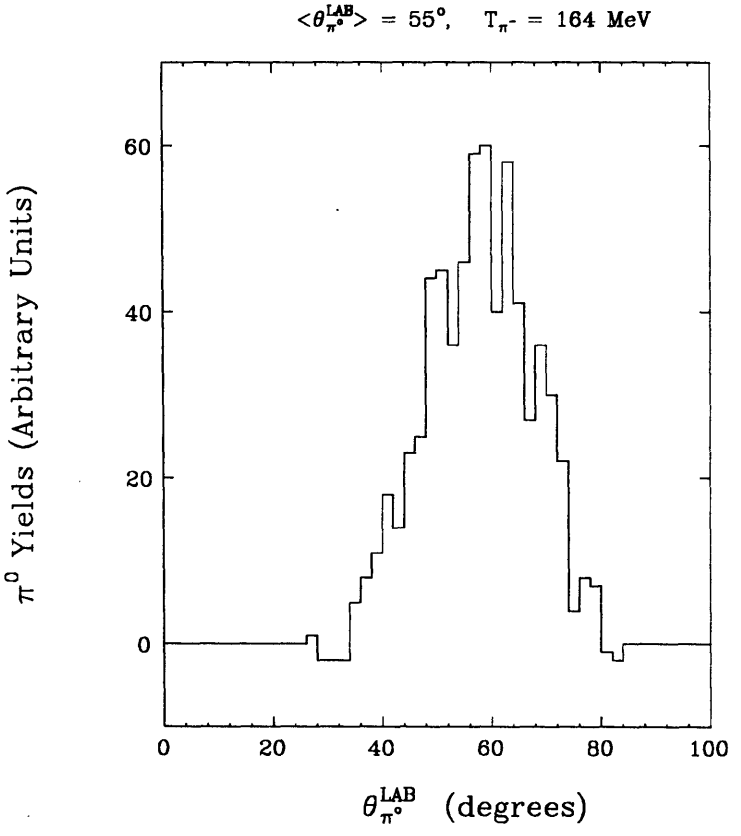

Figure 4-12: The π^0 angular distribution

actual scattering angles covered would be from 46° to 64° . So we have:

$$\begin{aligned}\Delta E_{kinematic\,broadening} &= \frac{\Delta E}{\Delta\theta_{\pi^o}} \times \Delta\theta_{\pi^o} \\ &\left|\frac{T_{\pi^o}(\theta = 46^o) - T_{\pi^o}(\theta = 64^o)}{64^o - 46^o}\right| \times (18^o) \\ &\left|\frac{146MeV - 129MeV}{18^o}\right| \times (18^o) = 17MeV. \end{aligned} \tag{4.4}$$

Therefore,

$$\Delta E_{detector} = \sqrt{21^2 - 17^2} = 12MeV. \tag{4.5}$$

This result agrees well with the detector Monte Carlo result at the same set-up. The Monte Carlo study showed the following three factors to be causes of the detector energy resolution: the energy leak out of the detector (9 MeV), photo-electron statistics (6 MeV), imperfect separation of the pulse height distribution associated with each photon (4 MeV). The individual contributions from the above were added in quadrature to give the 12 MeV resolution.

The detector angular resolution can be determined similarly. The peak in Figure 4-12 has a FWHM of 23° .

$$\Delta\theta_{Total} = \sqrt{(\Delta\theta_{detector})^2 + (\Delta\theta_{kinematic\,broadening})^2}. \tag{4.6}$$

The energy bin set for Figure 4-12 was from 135 MeV to 137 MeV. However with 12 MeV $\Delta E_{detector}$, the actual energy range covered was from 129 MeV to 143 MeV. So we have:

$$\Delta\theta_{kinematic\,broadening} = \frac{\Delta\theta_{\pi^o}}{\Delta E} \times \Delta E \tag{4.7}$$

$$\begin{aligned} &= \left|\frac{\theta(T_{\pi^o} = 129MeV) - \theta(T_{\pi^o} = 143MeV)}{12MeV + 2MeV}\right| \times (\Delta E) \\ &= \left|\frac{67^\circ - 47^\circ}{14MeV}\right| \times (14MeV) \\ &= 20^o. \end{aligned} \tag{4.8}$$

Therefore,

$$\Delta\theta_{detector} = \sqrt{23^{o2} - 20^{o2}} = 11^\circ. \tag{4.9}$$

At this particular set up R (the distance between the target and the face of the detector) was 30.6 cm. If the photon position resolving power were only as much as the modularity of the detector, namely the width of the CsI crystals (10 cm), then this would have given

$$\Delta\theta_{detector} = \frac{10cm}{30.6cm} = 27^{\circ}. \tag{4.10}$$

Therefore the energy weighted averaged position determination method mentioned in the previous section improved the angular resolution by a factor of 2 for this particular set up. The detector Monte Carlo code gave an angular resolution of 8° at this setup (Table 3.1), which agrees reasonably well with the 11° resolution calculated above.

In Figure 4-13 are compared the π^0 invariant mass histograms obtained from the replay and from the detector Monte Carlo code at detector angle 55° and T_{π^-}= 164 MeV. The replay histogram shows the center of the invariant mass around 135 MeV with about 10 MeV error, which validates the energy calibration procedure discussed in the previous section. Detector energy and angular resolution contribute to the finite width in the invariant mass spectra. The larger width in the replay invariant mass spectrum than in the detector Monte Carlo spectrum can be attributed the poorer angular resolution.

4.4 Singly Differential Cross Section

4.4.1 Net Yield Calculation

Once the good π^0 's were identified in a given run, we grouped them according to their scattering angle bins. As seen in Table 3.1, the average π^0 scattering angle resolution was about 10°. So we chose 10° bins. In Figure 4-14 are shown π^0 yields as a function of energy grouped in a $\theta_{\pi^o}^{Lab}$ bin between 50° and 60° from a run with T_{π^-} at 164 MeV and the detector set at 55°.

After subtracting the carbon contributions (dotted lines) with appropriate corrections from the CD_2 yield and CH_2 yield (dashed), the net π^0 energy spectra (solid) from deuterons and protons respectively are obtained. The width of the deuteron SCX peak (top) is larger than that of the proton SCX peak (bottom) due to the Fermi motion of the nucleons in the deuteron.

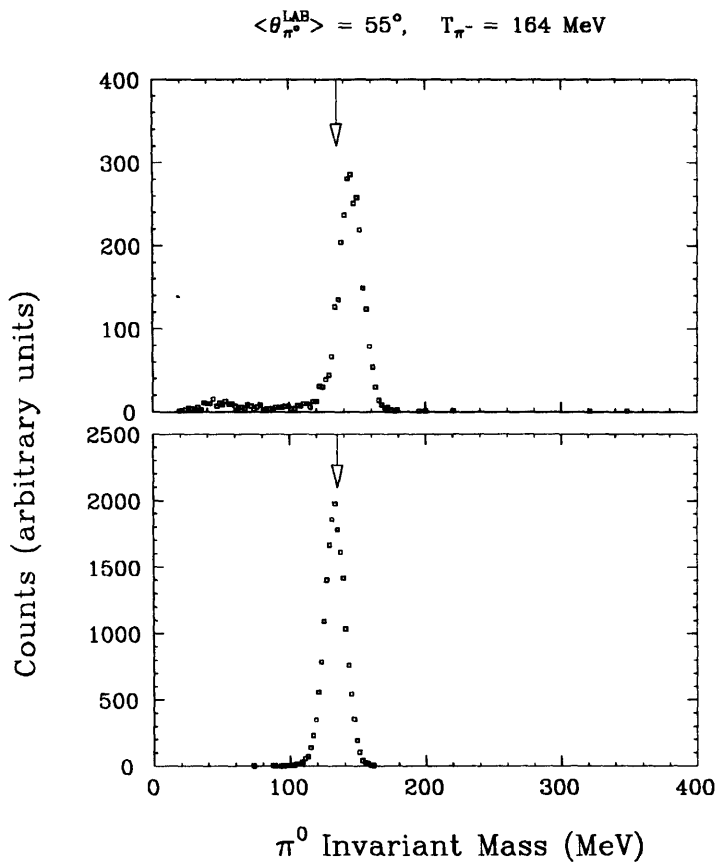

Figure 4-13: The invariant mass histogram. The top histogram is from data replay and the bottom histogram is from the detector Monte Carlo code. The arrows point to the π^0 invariant mass value of 135 MeV.

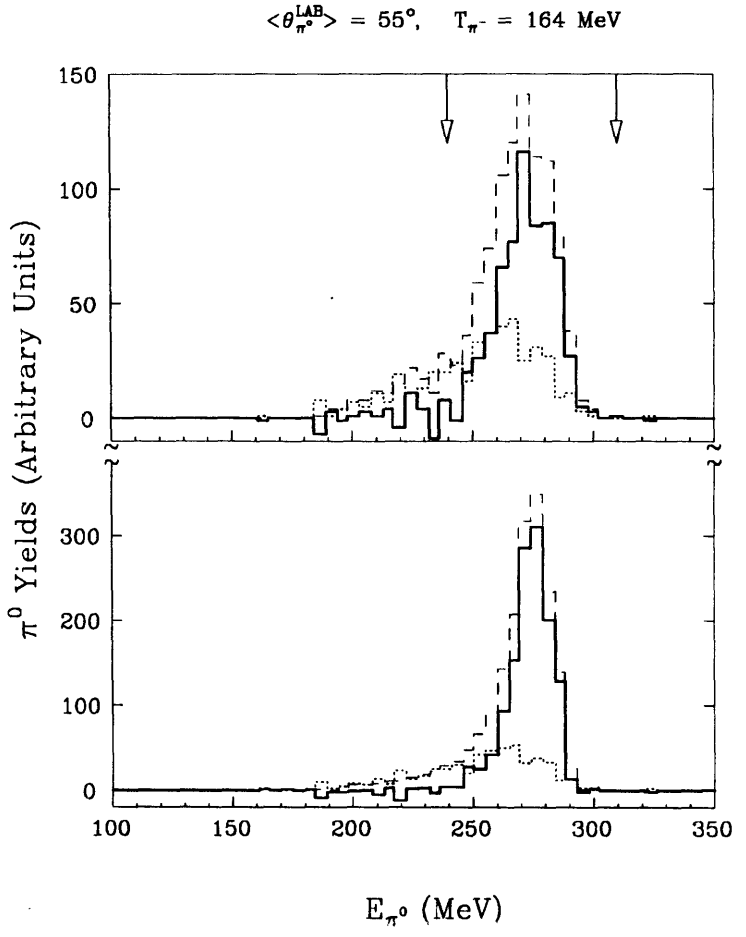

Figure 4-14: Net π^0 yields from deuterons and protons. The arrows correspond to the gate 2 set to integrate the π^0 's to obtain the net deuteron SCX yield.

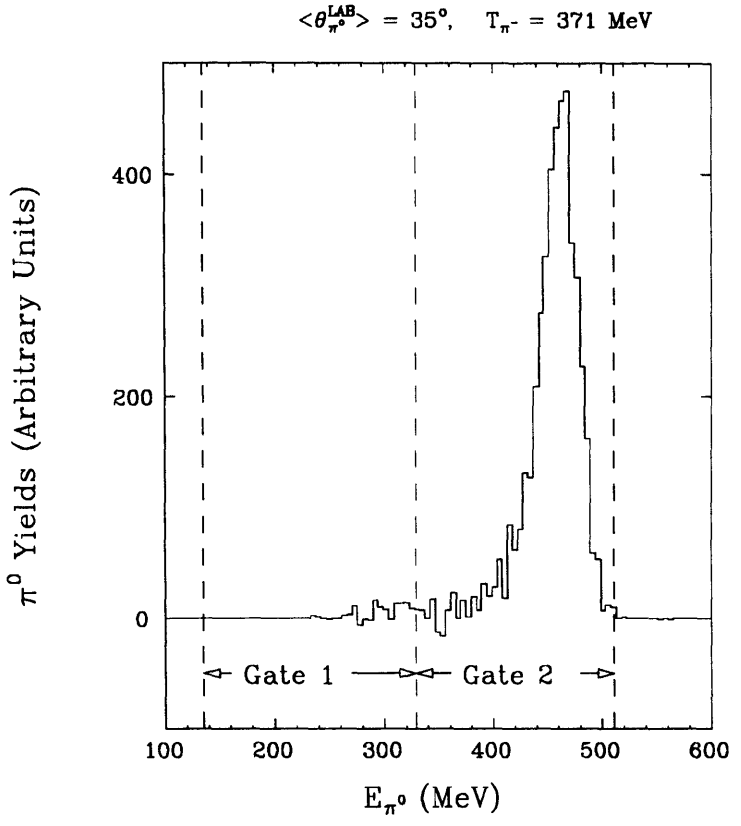

Figure 4-15: Net π^0 yield from deuterons

To show how the net π^0 yields were obtained, in Figure 4-15 is shown a net π^0 energy spectrum from a deuterium run with T_{π^-} at 371 MeV and the detector angle at 35° . The π^0 's in the above energy spectra were summed within the gate 2 to give the total yield. Gate 2 included the deuteron SCX spectrum. The lower limit in gate 2 was set just above the upper threshold for the Pion-induced-pion-production (PIPP). Gate 1 was set according to the the π^0 energy range from the PIPP kinematics. This is discussed further in Appendix E. The gates for T_{π^-}= 263 MeV were set similarly. T_{π^-}= 164 MeV was below the PIPP threshold (165 MeV) and therefore only gate 2 was set around the deuteron peak as shown by the arrows in Figure 4-14.

For a CH_2 run the net SCX yield from the protons was determined as below:

$$\begin{aligned}\iint Yield_p^{signal} dE_{\pi^0} d\theta_{\pi^o} = \\ \iint Yield^{CH_2\,run} dE_{\pi^0} d\theta_{\pi^o} \left[\frac{1}{Live\ Frac^{CH_2\,run}}\right] \\ - \iint Yield^{C run} dE_{\pi^0} d\theta_{\pi^o} \left[\frac{N_{\pi^-}^{CH_2\,run}}{N_{\pi^-}^{C\,run}} \frac{n_C\ in\ CH_2 target}{n_C\ in\ C\ target} \frac{1}{Live\ Frac^{C run}}\right],\end{aligned} \quad (4.11)$$

where

N_{π^-} is the number of π^- 's that entered the target in a run.

n_C is the number of carbon nuclei per cm^2 in the C target.

the Live Fraction was calculated by

$$\text{Live Fraction} = \frac{\text{Number of beam related triggers gated by } \overline{\text{BUSY}}}{\text{Total number of beam related triggers}} \quad (4.12)$$

For CD_2 runs, in addition to the carbon background, a hydrogen background needed to be subtracted to give the net SCX yield from the deuteron. This was because the CD_2 targets contained a small amount of hydrogen.

$$\iint Yield_d^{signal} dE_{\pi^0} d\theta_{\pi^o} =$$

$$\iint Yield^{CD2\,run} dE_{\pi^0} d\theta_{\pi^o} \left[\frac{1}{Live\ Frac^{CD_2\,run}}\right]$$
$$- \iint Yield^{C\,run} dE_{\pi^0} d\theta_{\pi^o} \left[\frac{N_{\pi^-}^{CD_2\,run}}{N_{\pi^-}^{C\,run}} \frac{n_C\ in\ CD_2 target}{n_C\ in\ C\ target} \frac{1}{Live\ Frac^{C\,run}}\right]$$
$$- \iint Yield_p^{BKG} dE_{\pi^0} d\theta_{\pi^o}. \tag{4.13}$$

The π^0 yield from the hydrogen contained in the CD_2 target was accounted for as follows:

$$\iint Yield_p^{BKG} dE_{\pi^0} d\theta_{\pi^o} =$$
$$- \iint Yield_p^{signal} dE_{\pi^0} d\theta_{\pi^o} \left[\frac{N_{\pi}^{-CD_2\,run}}{N_{\pi^-}^{CH_2\,run}} \frac{n_p\ in\ CD_2\ target}{n_p\ in\ CH_2\ target}\right] \tag{4.14}$$

n_p is the number of hydrogen nuclei per cm^2 in a given target.

For one detector set-up angle several runs were taken with a given target and the yields from all the runs with the same target were added to give the total yield from that target (Appendix F).

Included in the $\iint Yield^{C\,run} dE_{\pi^0} d\theta_{\pi^o}$ were π^0 's produced from the target frame. The target frame contribution was independently measured by placing an empty target holder in the target position at each detector set-up. The target frame yields were measured to be negligible. This was due to the fact that the beam spot size was much smaller than the target frame at the target position.

The small beam spot size was confirmed by comparing the difference in the π^0 yields between a run with an empty target frame and a run with a doughnut target (see Figure 2-14). No difference in the π^0 yields between the two targets was seen and this meant that the beam was successfully going through the inner diameter (1.38 inches) of the doughnut target. The comparison was done at all set-ups throughout the experiment.

4.4.2 Cross Section

The deuteron SCX differential cross section was obtained by comparing the π^0 yield from the deuteron to that from the proton at the same angular bin.

By definition,

$$\left(\frac{d\sigma}{d\Omega}\right)_p = \frac{\left(\iint Yield_p^{signal} dE_{\pi^0} d\theta_{\pi^o}\right)_{Total}}{N_{\pi^-}^{CH_2\,runs}\; n_p\; d\Omega_p} \tag{4.15}$$

and

$$\left(\frac{d\sigma}{d\Omega}\right)_d = \frac{\left(\iint Yield_d^{signal} dE_{\pi^0} d\theta_{\pi^o}\right)_{Total}}{N_{\pi^-}^{CD_2\,runs}\; n_d\; d\Omega_d} \,. \tag{4.16}$$

We first calculated the ratios of the deuteron to the proton cross section which were given by

$$\frac{\left(\frac{d\sigma}{d\Omega}\right)_d}{\left(\frac{d\sigma}{d\Omega}\right)_p} = \frac{\left[\iint Yield_d^{signal} dE_{\pi^0} d\theta_{\pi^o}\right]_{Total}}{\left[\iint Yield_p^{signal} dE_{\pi^0} d\theta_{\pi^o}\right]_{Total}} \frac{N_{\pi^-}^{CH_2\,runs}}{N_{\pi^-}^{CD_2\,runs}} \frac{n_p}{n_d} \frac{d\Omega_p}{d\Omega_d}. \tag{4.17}$$

Each detector set-up configuration had overlapping coverage of the π^0 angles. At a given angle, contributions to the differential cross section from the different set-up configurations were appropriately added. This is shown in Appendix G.

The final deuteron SCX cross section is given by

$$\left(\frac{d\sigma}{d\Omega}\right)_d = \left\langle \frac{\left(\frac{d\sigma}{d\Omega}\right)_d}{\left(\frac{d\sigma}{d\Omega}\right)_p} \right\rangle \left(\frac{d\sigma}{d\Omega}\right)_{\text{SAID}} . \tag{4.18}$$

where

$\left\langle \frac{\left(\frac{d\sigma}{d\Omega}\right)_d}{\left(\frac{d\sigma}{d\Omega}\right)_p} \right\rangle$ is the ratio of the deuteron and the proton cross sections averaged over the results from the different detector set-ups, as given in Appendix G.

The various quantities that normalize the cross section in the above equation are explained in the next section.

4.4.3 Normalization

4.4.3.1 Phase Shift Calculation

In Equation (4.18), $\left(\frac{d\sigma}{d\Omega}\right)_{\rm SAID}$ is the proton SCX cross sections calculated using the program SAID (Scattering Analysis Interactive Dial-in), which calculates the π-N cross sections by partial-wave analysis[10].

4.4.3.2 Detector Acceptance

The reason for using the proton SCX yield and the phase shift calculation in equation (4.18) to compute the deuteron SCX cross section was so that in equation (4.17) the detector acceptances would cancel out. This was desirable because the acceptance calculation from the detector Monte Carlo code had an average uncertainty of 30%, while the uncertainty due to using the proton SCX yield along with the phase shift calculation was much smaller.

The quantities $d\Omega_p$ and $d\Omega_d$ in the above equations were the detector acceptances at a given set-up averaged over the π^0 energy range. The acceptance was dependent on π^0 energy and, from the computational point of view, the ratio of the $d\Omega_p$ to $d\Omega_d$ can be written as:

$$\frac{d\Omega_d}{d\Omega_p} = \frac{\left[\iint \frac{Yield_d^{signal}}{d\Omega(E_{\pi^0})} dE_{\pi^0} d\theta_{\pi^o}\right]_{Total}}{\left[\iint \frac{Yield_p^{signal}}{d\Omega(E_{\pi^0})} dE_{\pi^0} d\theta_{\pi^o}\right]_{Total}} \frac{\left(\iint Yield_p^{signal} dE_{\pi^0} d\theta_{\pi^o}\right)_{Total}}{\left(\iint Yield_d^{signal} dE_{\pi^0} d\theta_{\pi^o}\right)_{Total}}. \tag{4.19}$$

The above ratio was evaluated using the acceptance functions generated from the detector Monte Carlo code at several detector set-up configurations at each π^- energy. It was shown to be unity with less than one percent deviation due to the fact that the deuteron and the proton SCX energy spectra had the same peak position and similar shapes.

4.4.3.3 Beam Flux

For the ratio of the incoming π^-'s in equation (4.17), ratio of the incoming charged particles counted by the beam counting scintillators ($S0 \cdot S1$) was used in practice. The fraction of π^-'s in the beam was assumed to be a constant only varying with the beam energy.

Therefore the pion fraction of the beam never entered the actual cross section calculation, although we successfully measured it at each energy (Appendix A).

4.5 Doubly Differential Cross Section

The doubly differential cross section was calculated as shown below:

$$\left(\frac{d\sigma}{d\Omega}\right)_d = \left(\int\int \frac{Yield_d^{signal}}{d\Omega} dE_{\pi^0} d\theta_{\pi^o}\right)_{Total} \frac{1}{N_{\pi^-}^{CD_2\,runs}\, n_d\, dE_{\pi^0}} . \tag{4.20}$$

Here the π^0 angular integration interval was 10° as before, while the energy interval was 10 MeV.

The $d\Omega$ value used in Equation (4.20) was calculated from the detector Monte Carlo code. As discussed in Chapter 3, the acceptance calculated from the detector Monte Carlo code ($d\Omega_{MC}$) was multiplied by a scaling factor($f_{MC}^{correction}$) to give:

$$\begin{aligned}\left(\int\int \frac{Yield_d^{signal}}{d\Omega} dE_{\pi^0} d\theta_{\pi^o}\right)_{Total} & \frac{1}{N_{\pi^-}^{CD_2\,runs}\, n_d\, dE_{\pi^0}} \\ = \left(\int\int \frac{Yield_d^{signal}}{d\Omega_{MC} f_{MC}^{correction}} dE_{\pi^0} d\theta_{\pi^o}\right)_{Total} & \frac{1}{N_{\pi^-}^{CD_2\,runs}\, n_d\, dE_{\pi^0}} ,\end{aligned} \tag{4.21}$$

where $f_{MC}^{correction}$ was determined in each angular bin such that:

$$\begin{aligned}\left(\frac{d\sigma}{d\Omega}\right)_{dSCX} & \\ = \int \left\{\left(\int\int \frac{Yield_d^{signal}}{d\Omega_{MC} f_{MC}^{correction}} dE_{\pi^0} d\theta_{\pi^o}\right)_{Total} \frac{1}{N_{\pi^-}^{CD_2\,runs}\, n_d\, dE_{\pi^0}}\right\} & dE_{\pi^0} .\end{aligned} \tag{4.22}$$

This meant that:

$$d\Omega = d\Omega_{MC} f_{MC}^{correction} . \tag{4.23}$$

In this way, the acceptance calculated from the detector Monte Carlo code accounted for the energy dependence of the acceptance, while the overall scaling was determined by the parameter $f_{MC}^{correction}$. The magnitude of the $f_{MC}^{correction}$ was about 30% on average. In Figure 4-16 is shown

a typical acceptance function generated from the detector Monte Carlo code. As shown in the figure the energy dependence of the acceptance was parameterized with straight lines for simplicity in calculation.

4.6 Error Analysis

4.6.1 Statistical Uncertainty

The statistical uncertainty was due to the uncertainty in the number of the π^0 's detected. From Poisson Statistics, it was proportional to the square root of the number of the π^0 's identified in each run.

4.6.2 Systematic Uncertainty

4.6.2.1 Uncertainty in the Phase Shift Calculation

The largest systematic uncertainty came from the normalization using the SAID phase shift calculation. The experimental data[25][26] that were used as input to the SAID calculation had an average systematic uncertainty of 5 % in our energy region.

4.6.2.2 Uncertainty in the Target Density

The target densities had an uncertainty of approximately one percent as shown in Table 2.2. The number of hydrogen nuclei in the CD_2 target was, however, an exception and had a large uncertainty of 21 %. However its contribution to the uncertainty in the deuteron net yield ($\int\int Yield_d^{signal} dE_{\pi^0} d\theta_{\pi^0}$) was small since the hydrogen content in the CD_2 target was small (~3% (atomic)).

4.6.2.3 Beam Counting Uncertainty

The beam counting scintillators and the associated electronics had limited counting rate capabilities and that limitation contributed an uncertainty in our beam flux counting.

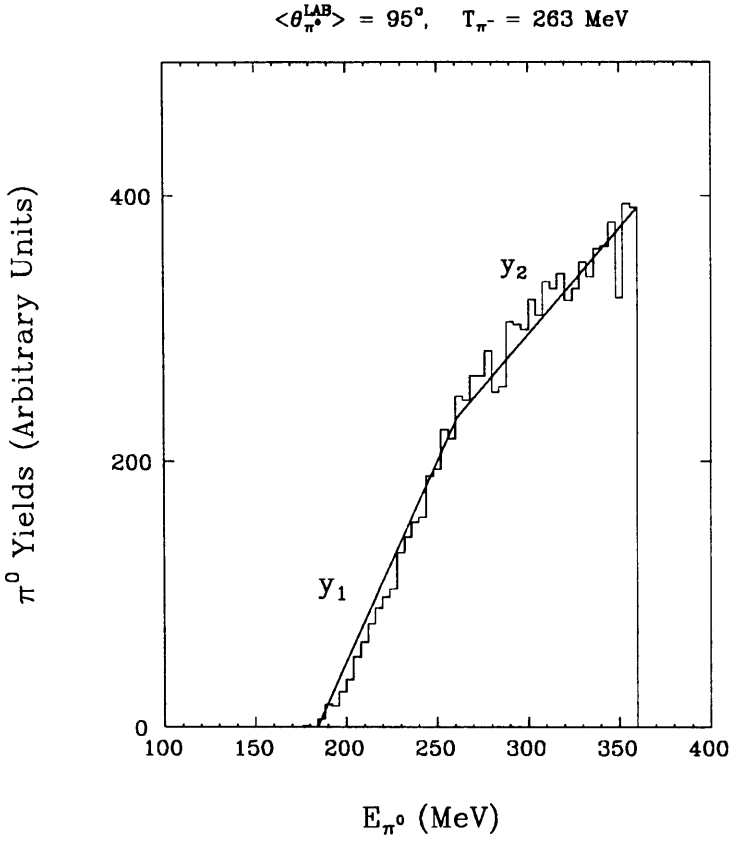

Figure 4-16: The detector acceptance function for $\theta_{\pi^0} = 90°$ to 100 ° . The straight lines y_1 and y_2 are functions parameterizing the energy dependence of the acceptance.

The beam counting system was composed of the scintillators S0 and S1 with fast rise time (2 nsec), 300 MHz discriminators to make logic signals from the S0 and S1 signals, and a 300 MHz coincidence unit to form coincidences $S0 \cdot S1$. The maximum counting rate capability of this system was therefore limited at 300 MHz. The typical beam flux rate during our experiment was 35 kHz on average and the maximum rate was 50 kHz on average. Due to the pulsed nature of the beam (6 % duty factor) at LAMPF, the instantaneous rate of the beam at 50 kHz average flux was:

$$50kHz \times \frac{1}{6\%} = 800kHz \text{ (instantaneous rate).} \tag{4.24}$$

As previously mentioned the beam came in a microstructure consisting of 0.25 nsec pulses at 5 nsec intervals. If more than one particle came in one of the 0.25 nsec pulses, the beam counting electronics was not fast enough to count them as multiple particles but would count them as one particle. We estimate the probability that this type of "double counting" error occurred during our experiment.

We take the worst case (the highest beam rate, 800 kHz) for our calculation. An average number of particles found in a 5 nsec interval is given by:

$$8 \times 10^5 \left(\frac{particles}{sec}\right) \times 5\ (nsec) = 4 \times 10^{-3}\ particles. \tag{4.25}$$

According to Poisson statistics the probability to have no particle in the 5 nsec interval is:

$$\frac{(4 \times 10^{-3})^0}{0!} \times exp(-4 \times 10^{-3}) = 0.996. \tag{4.26}$$

The probability of having one particle is:

$$\frac{(4 \times 10^{-3})^1}{1!} \times exp(-4 \times 10^{-3}) = 4.0 \times 10^{-3}. \tag{4.27}$$

The probability of having two particles is:

$$\frac{(4 \times 10^{-3})^2}{2!} \times exp(-4 \times 10^{-3}) = 8.0 \times 10^{-6}. \tag{4.28}$$

Therefore the probability of a double counting is:

$$\frac{8 \times 10^{-6}}{4 \times 10^{-3}} = 0.2\%. \tag{4.29}$$

4.6.2.4 Uncertainty Related to the Change in the Detector Set-Up

The ratios of the deuteron and the proton SCX cross sections (Equation (4.18)) from the different detector set-ups were compared (as shown in Figure 4-17 $\sim$ Figure 4-19) for a given π^0 angle bin and π^- energy to investigate any systematic error that might have arisen in changing the detector configuration during the experiment. The possible source of this uncertainty would have been experimental quantities that depended on the detector configuration, such as the positioning uncertainty of the detector with respect to the target, the decay photons escaping the target at different angles and the muon halos entering the detector from different directions, etc. In Appendix H, it is shown that the systematic uncertainty introduced due to the change in the detector set-up configurations was negligible.

4.6.2.5 Uncertainty Related to $d\Omega_{MC}$

In Chapter 3, the uncertainty introduced by using $d\Omega_{MC}$ to provide the energy dependence of the acceptance was shown to be:

$$\frac{\sigma(energy\ dependence\ by\ d\Omega_{MC})}{dE} = 9.7 \times 10^{-3} \left(\frac{\%}{MeV}\right) . \tag{4.30}$$

At T_{π^-}= 164 and 263 MeV, the π^0 energy spectra covered the energy range of about 200 MeV on average. The uncertainty from using $d\Omega_{MC}$ in this energy range is thus:

$$\begin{aligned} &\sigma(energy\ dependence\ by\ d\Omega_{MC}) \\ &= (9.7 \times 10^{-3} \frac{\%}{MeV})(200\,MeV) \\ &= 2\% . \end{aligned} \tag{4.31}$$

At T_{π^-}= 371 MeV, the energy range covered was about 300 MeV and the uncertainty is found similarly to be 3%.

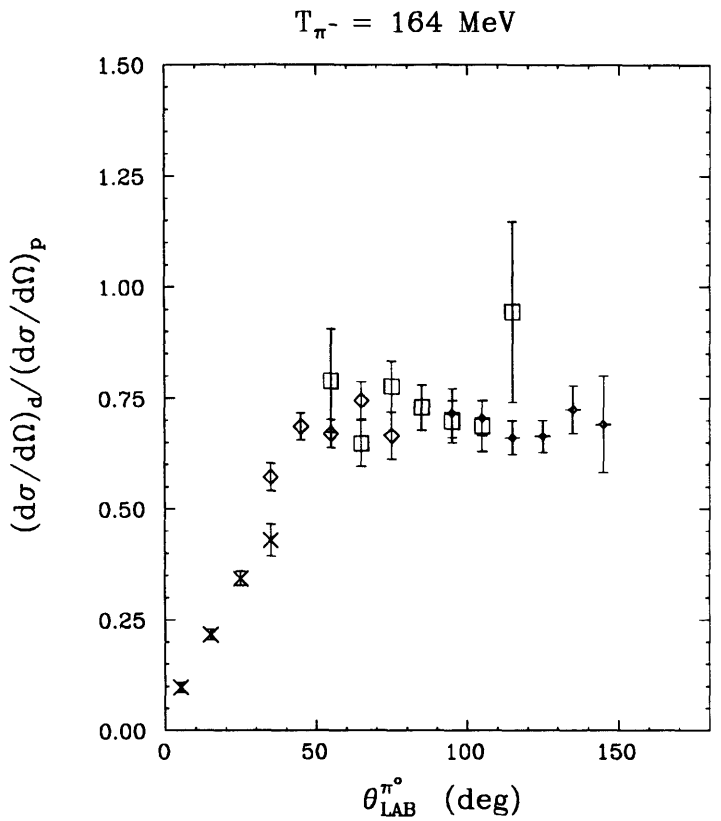

Figure 4-17: Ratio of the cross sections at 164 MeV

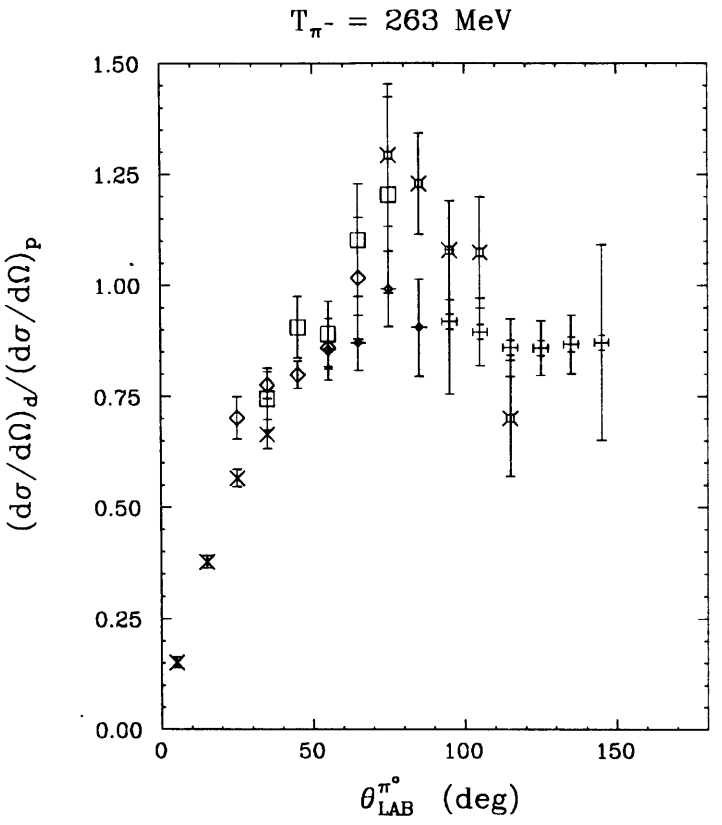

Figure 4-18: Ratio of the cross sections at 263 MeV

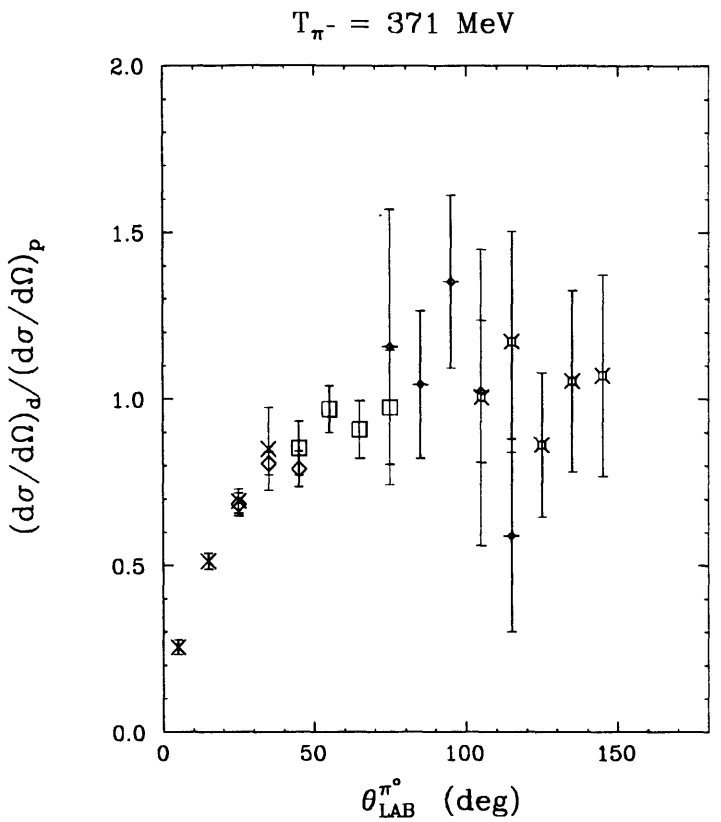

Figure 4-19: Ratio of the cross sections at 371 MeV

Chapter 5

Results and Phenomenological Interpretation

In this chapter are presented the experimental results for the deuteron SCX cross sections, along with phenomenological models and their descriptions of the cross sections.

A Fermi sphere model constructed to explain the angular distribution of the cross sections did not work well. At the conclusion of this thesis work, however a modified Fermi sphere model was constructed by Peterson *et al.*[12] and it provided a good description of the data. Both models are discussed in Section 5.1. An impulse approximation model (in Section 5.2) was used to describe the doubly differential cross sections and to identify pion-nucleus effects.

The cross section values are presented in Appendix I.

5.1 Angular Distribution

5.1.1 Results

Shown in Figure 5-1 are the measured angular distributions for SCX on the deuteron at energies 164, 263 and 371 MeV. The larger error bars associated with each point represent the total uncertainty whereas the smaller error bars represent the statistical uncertainty only. The origins of the uncertainties were explained in Chapter 3. The dashed curves are the impulse approximation calculations using the phase shift analysis (*i.e.* the $\pi^- + p \rightarrow \pi^0 + n$ cross section)[10].

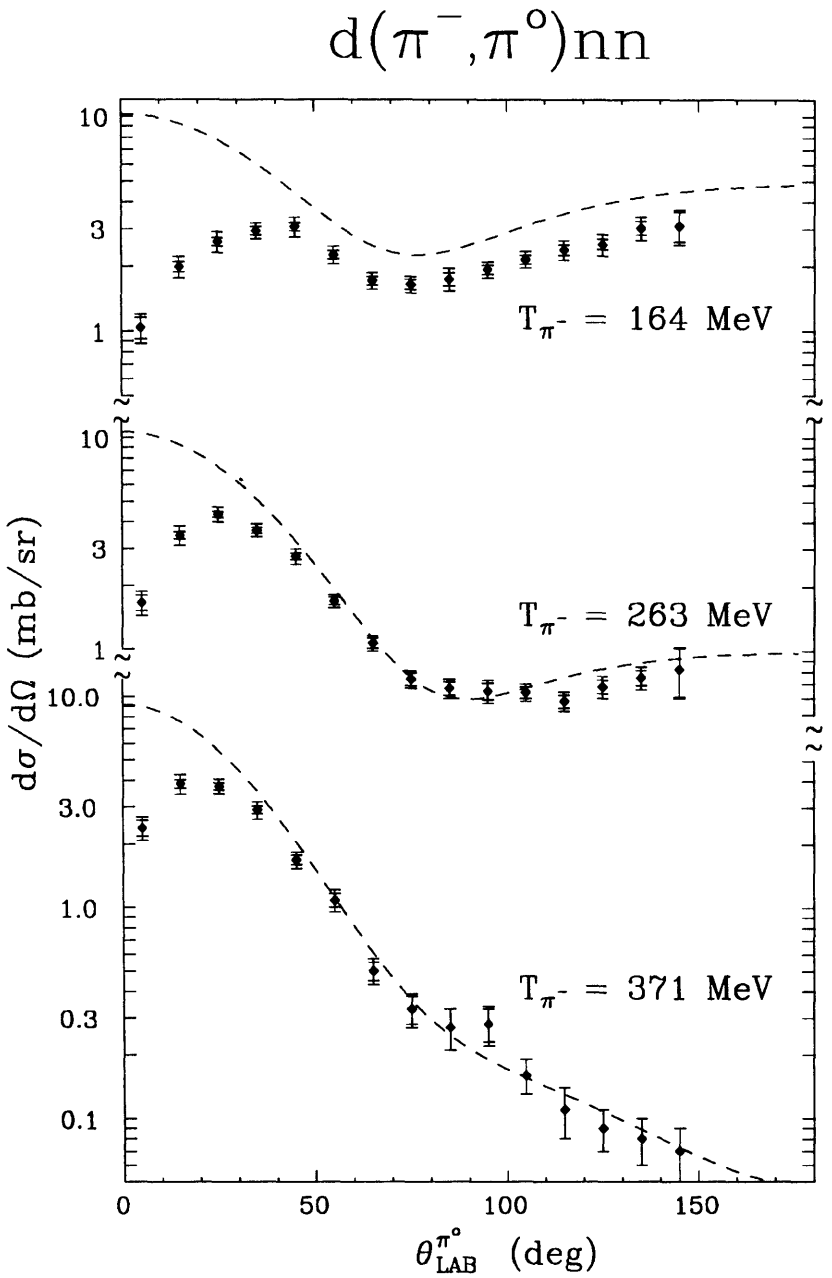

Figure 5-1: Deuteron SCX measurements

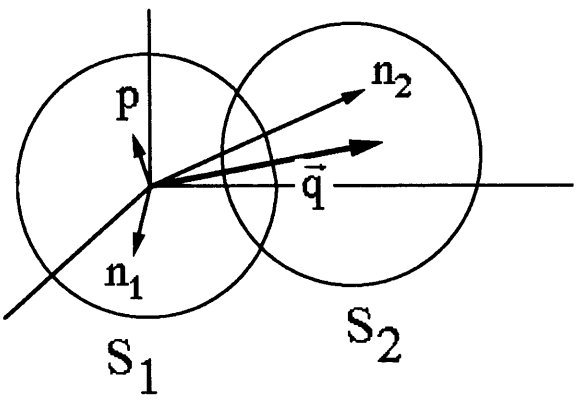

Figure 5-2: Two Fermi Spheres in momentum space

5.1.2 Fermi Sphere Model

The angular distributions shown in Figure 5-1 exhibit a forward angle suppression at all three energies due to Pauli blocking. As expected, the strength of the suppression diminishes as T_{π^-} gets bigger. The ratio of the impulse approximation values to our data at 10° goes from 6 to 3 to 2 as the energy changes from 164 to 263 to 371 MeV. At 164 MeV the angular distribution shows an overall reduction in the deuteron SCX cross sections compared to the impulse approximation values by about 20%, presumably due to multiple scattering effects. We constructed a Fermi sphere model to describe the angular distributions of the deuteron SCX cross sections. The Fermi sphere idea had previously been used by Czyz[36] and by Peterson *et al.*[37] to describe Pauli blocking effects in heavier nuclei.

In the impulse approximation the deuteron SCX cross section is given in terms of the non-spin-flip amplitude ($f(E,\theta)$) and the spin-flip amplitude ($g(E,\theta)$) as:

$$\left(\frac{d\sigma}{d\Omega}\right)^{IA}_{d\,SCX} = |f(E,\theta)|^2 + |g(E,\theta)|^2. \tag{5.1}$$

As discussed earlier in Chapter 1, $^1S_0$ and ^3P states are possible for the final state neutrons in the deuteron SCX reaction (excluding $l > 1$). The transition from the $^3S_1$ initial state to a $^1S_0$ final state involves a spin-flip ($S = 1 \rightarrow S = 0$) and its amplitude ($g(E,\theta)$) is proportional to sin θ. The transition from a $^3S_1$ state to ^3P final states keeps the spin the same and its amplitude is given by $f(E,\theta)$. The final state neutrons in ^3P states have their spins pointing in the same direction ($S = 0$) and therefore are required by the Pauli exclusion principle to occupy

different quantum states in momentum space. Such a restriction placed on the spin-non-flip transition can be quantitatively described by the Fermi sphere model.

In Figure 5-2 are shown two overlapping spheres in nucleon momentum space with radii k_F, which we call Fermi spheres. Sphere S_1 is at the origin while sphere S_2 is displaced by $\vec{q}$. The original neutron, n_1, and the proton, p, in the deuteron have their momenta distributed isotropically inside the sphere S_1. After a SCX reaction the momentum distribution of the charge-exchanged neutron n_2 (from the initial proton) is displaced by $\vec{q}$ to reside inside the sphere S_2. By the Pauli exclusion principle, n_2 is not allowed to be in the region of momentum space that is already occupied by the original neutron, n_1. Therefore, the "Pauli blocked" region corresponds to the intersection volume of the two spheres. The amount of the restriction placed on the phase space for n_2 can be expressed by the Pauli suppression factor, Q:

$$Q = \begin{cases} 1 & q > 2k_F \\ 1 - \frac{\text{intersection volume}}{\text{vol. of the sphere}} & 0 \leq q \leq 2k_F \end{cases} \tag{5.2}$$

At a small q, $f(E,\theta)$ is suppressed and is proportional to Q, while $g(E,\theta)$ is small due to its $\sin\theta$ dependence. At large q, $g(E,\theta)$ is no longer negligible but there, the Pauli blocking effect is small and Q is close to 1. So the Pauli suppression factor was applied directly to $\left(\frac{d\sigma}{d\Omega}\right)^{IA}_{d\,SCX}$ which is the sum of $|f(E,\theta)|^2$ and $|g(E,\theta)|^2$.

At 164 MeV, the deuteron SCX cross sections were smaller than the impulse approximation values by about 20% at large angles (see Figure 5-3). The Garcilazo calculation[9] (solid curve) correctly reproduced this reduction and attributed it to multiple scattering effects. So we built in an overall normalization factor f_M into our fitting function Y_{model} at each energy to account for the multiple scattering effects. The Pauli blocking effect is incorporated in terms of the Pauli reduction factor, Q to give Y_{model} as

$$Y_{model}(q, k_F, f_M) = Q(q, k_F) \times f_M. \tag{5.3}$$

Y_{model} was then fitted to the ratios of $\left(\frac{d\sigma}{d\Omega}\right)_{d\,scx}$ to $\left(\frac{d\sigma}{d\Omega}\right)^{IA}_{d\,scx}$ varying f_M for each energy, keeping k_F the same for all three energies. The quantity f_M was an energy dependent parameter, since the multiple scattering is an energy dependent effect. The quantity k_F was not dependent on the energy since it only has to do with the nucleon momentum distribution in the deuteron.

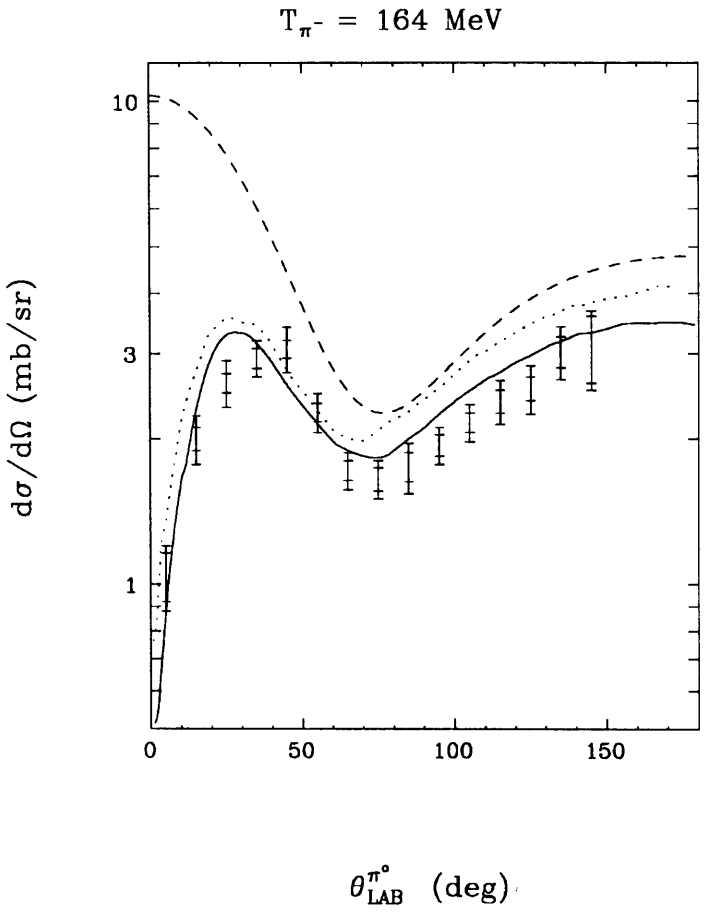

Figure 5-3: Our d SCX data at 164 MeV. The larger error bars correspond to the total errors, while the smaller error bars correspond to the statistical error only. The dashed curve is from the T^{IA}_{SCX}, dotted curve from the $T^{IA+Pauli}_{SCX}$ and the solid curve from the T^{Full}_{SCX} from Garcilazo[9].

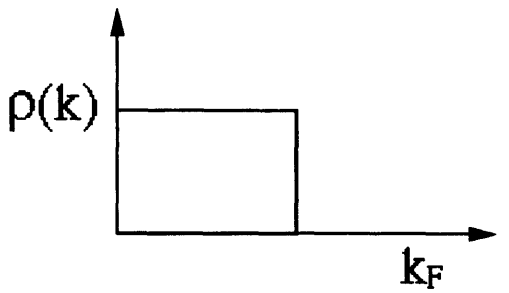

Figure 5-4: Fermi gas momentum distribution.

T_{π^-}	k_F	f_M	χ^2_r
164 MeV	150 (MeV/c)	0.75	1.7
263 MeV	150 (MeV/c)	0.85	3.3
371 MeV	150 (MeV/c)	0.90	2.0

Table 5.1: Fermi sphere model fit with the Fermi gas momentum distribution.

5.1.2.1 Using the Fermi Gas Momentum Distribution

We first used a "Fermi gas model" for the nucleon momentum distribution inside the deuteron as shown in Figure 5-4. The momentum density is uniform until the Fermi momentum, k_F, is reached and beyond k_F the density goes to zero.

The results from using this distribution are shown in Figure 5-5 $\sim$ Figure 5-7. In Table 5.1 are shown the reduced χ^2 and the parameters (k_F and f_M) for the best fit at each energy.

As seen in the figures the Y_{Model}'s fit the data reasonably well. Shown in Figure 5-8 are all three Y_{Model}'s at their respective energies in the same plot. All three curves approach the plateau at the same q value as a result of the requirement that the parameter k_F be the same for all the energy settings. The plateau is reached when the two Fermi spheres begin to separate from each other and hence when q is equal to twice the sphere radius. f_M goes up as a function of energy. This is reasonable since the multiple scattering effects are expected to diminish at higher energies as the πN interaction moves away from the Δ resonance region. At 164 MeV, the best fit occurs when f_M is 0.75. This implies an overall reduction in the deuteron cross

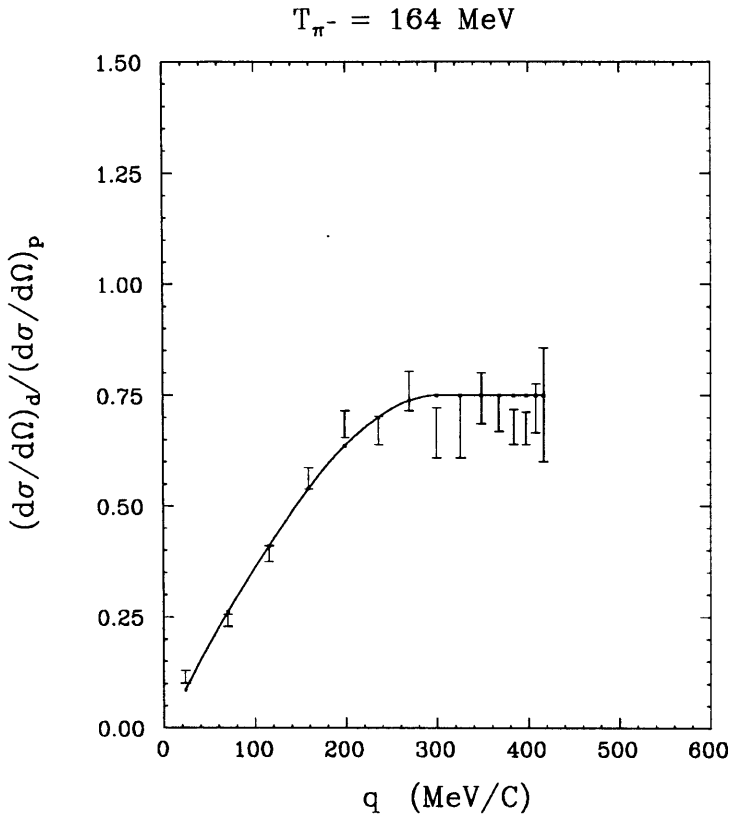

Figure 5-5: The Fermi sphere model fit using a Fermi gas momentum density distribution at T_{π^-}=164 MeV.

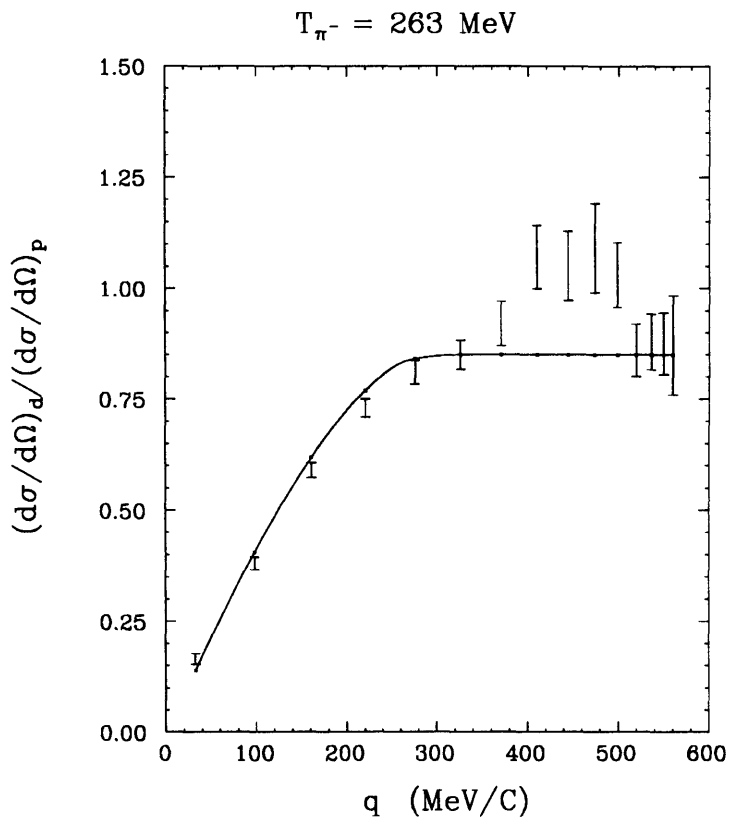

Figure 5-6: The Fermi sphere model fit using a Fermi gas momentum density distribution at T_{π^-}=263 MeV.

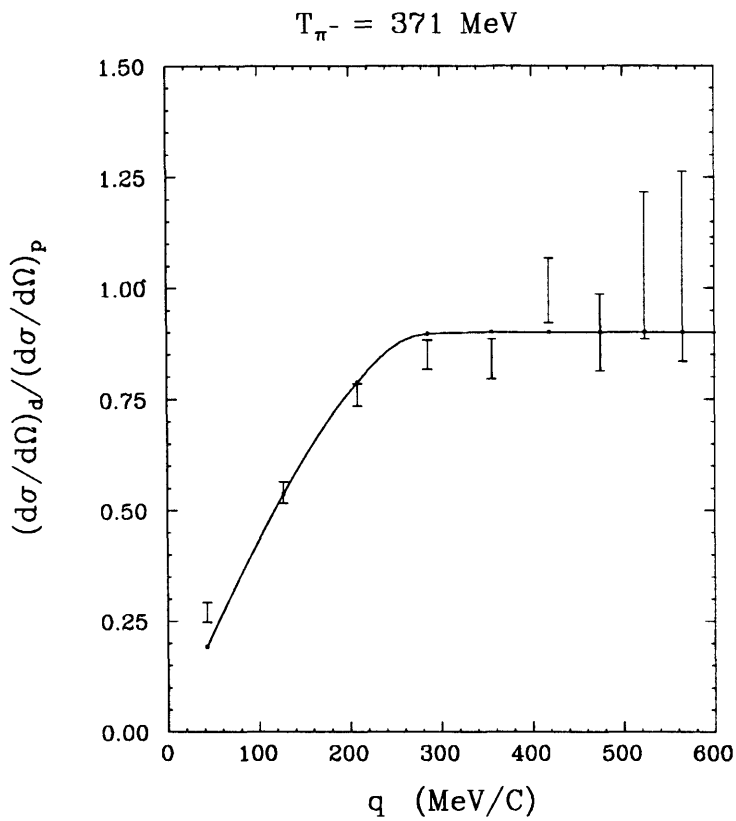

Figure 5-7: The Fermi sphere model fit using a Fermi gas momentum density distribution at T_{π^-}=371 MeV.

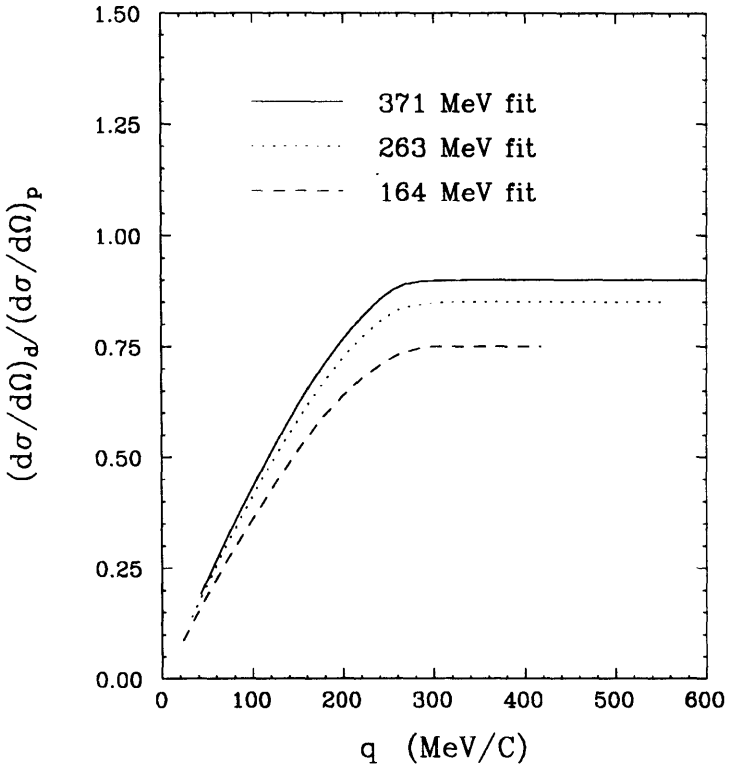

Figure 5-8: The Fermi sphere model fit using a Fermi gas momentum density distribution at 164, 263 and 371 MeV.

T_{π^-}	f_M	χ^2_r
164 MeV	0.56	21
263 MeV	0.67	31
371 MeV	0.75	7

Table 5.2: Fermi sphere model fit with the realistic momentum distribution.

sections from the impulse approximation values of 25% and is close to the 20% reduction due to multiple scattering effects predicted by Garcilazo[9]. The reduction was 15% for the 263 MeV fit and 10% for the 371 MeV fit. (see Table 5.1.)

Despite such good fits to the data, however, the parameter k_F makes little physical sense. The value of k_F 150 MeV/c, obtained (Table 5.1) for the best fit is much larger than the value expected from the realistic nucleon momentum distribution in the deuteron. In Figure 5-9 is shown the realistic momentum distribution obtained from an $(e, e'p)$ experiment[14] along with two Fermi gas distributions with different k_F's normalized to the same area as the realistic distribution. From the figure it is seen that a Fermi gas distribution with $k_F = 55$ MeV/c, a much smaller value than 150 MeV/c, would be required to describe the actual momentum distribution.

5.1.2.2 Using a Realistic Momentum Distribution

We modified the Fermi sphere model using a realistic momentum distribution (Figure 5-10) in the hope of obtaining more consistent results than using the Fermi gas distribution.

The results of the fits using the realistic distribution are shown in Figure 5-11 $\sim$ Figure 5-13. In Figure 5-14 are shown all three Y_{Model}'s in the same plot. The fitting parameters are shown in Table 5.2. Here, k_F is not shown in the table, since it was not a parameter but a fixed quantity already determined from the realistic momentum distribution corresponding to the q value beyond which the momentum density becomes practically negligible. Due to the long tail in the momentum density (Figure 5-10) in the range of the q in our experimental data, the two Fermi spheres never fully separated.

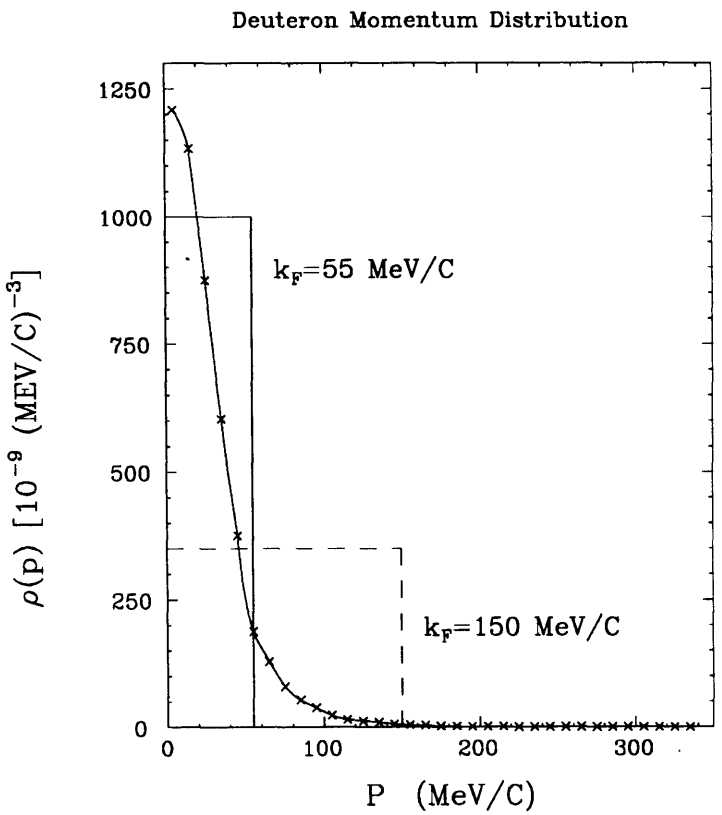

Figure 5-9: The realistic momentum distribution[14] and the Fermi gas boxes with the same area

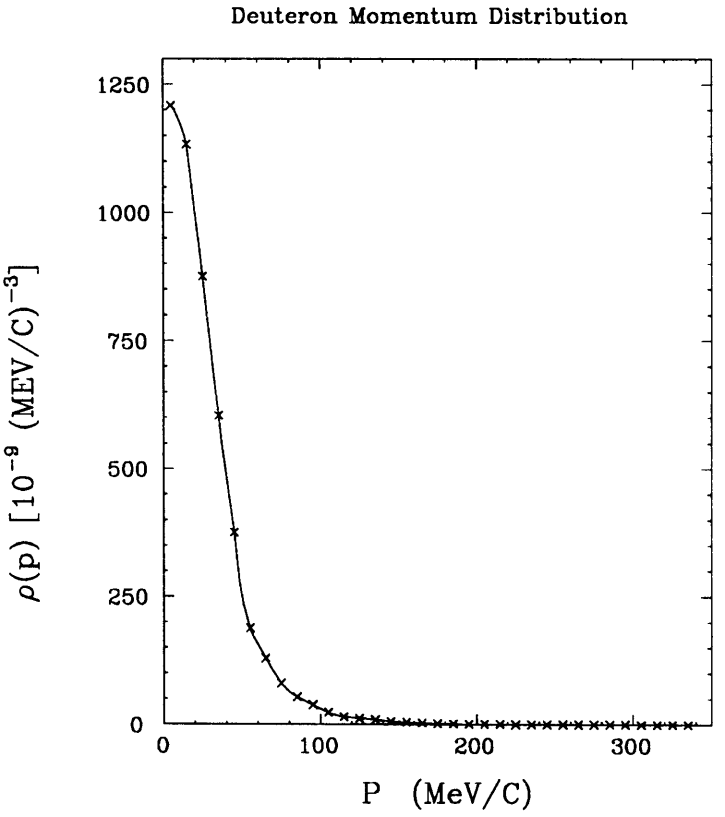

Figure 5-10: Realistic deuteron momentum distribution from Bernheim *et al.* [14] The line drawn through the data points is to guide the eye.

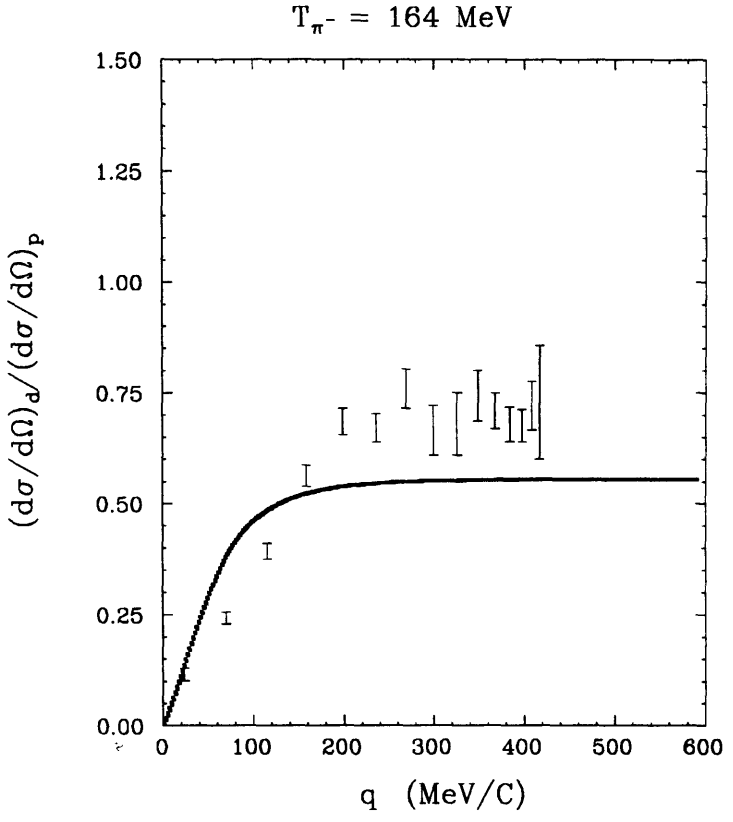

Figure 5-11: The Fermi sphere model fit with the realistic momentum distribution at 164 MeV.

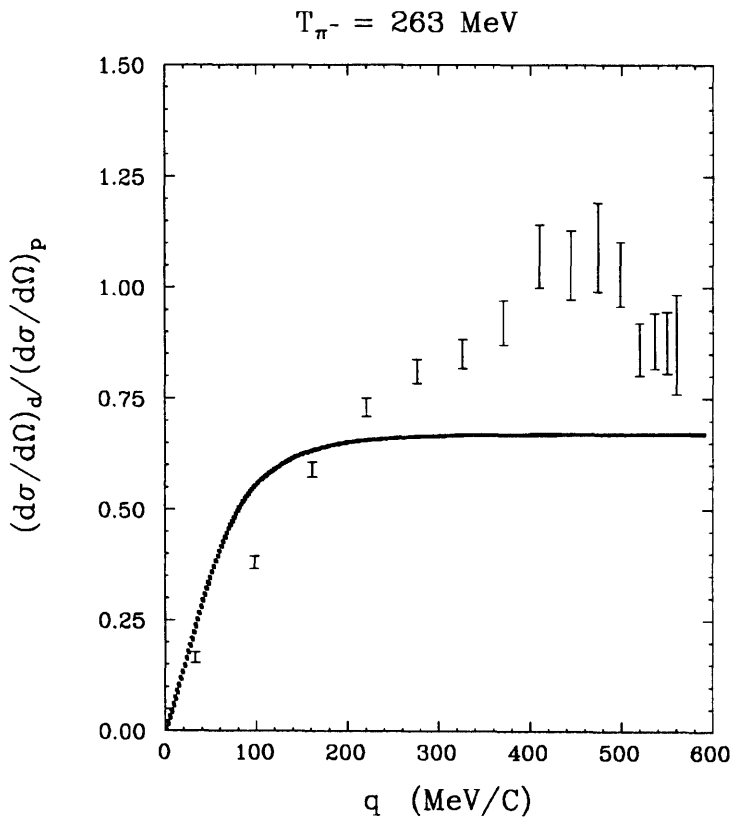

Figure 5-12: The Fermi sphere model fit with the realistic momentum distribution at 263 MeV.

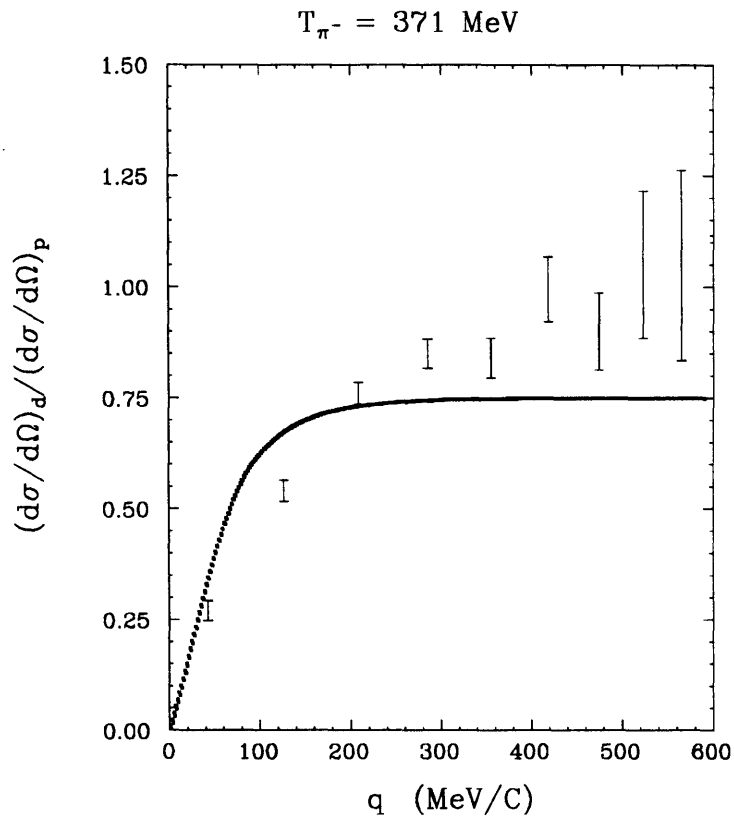

Figure 5-13: The Fermi sphere model fit with the realistic momentum distribution at 371 MeV.

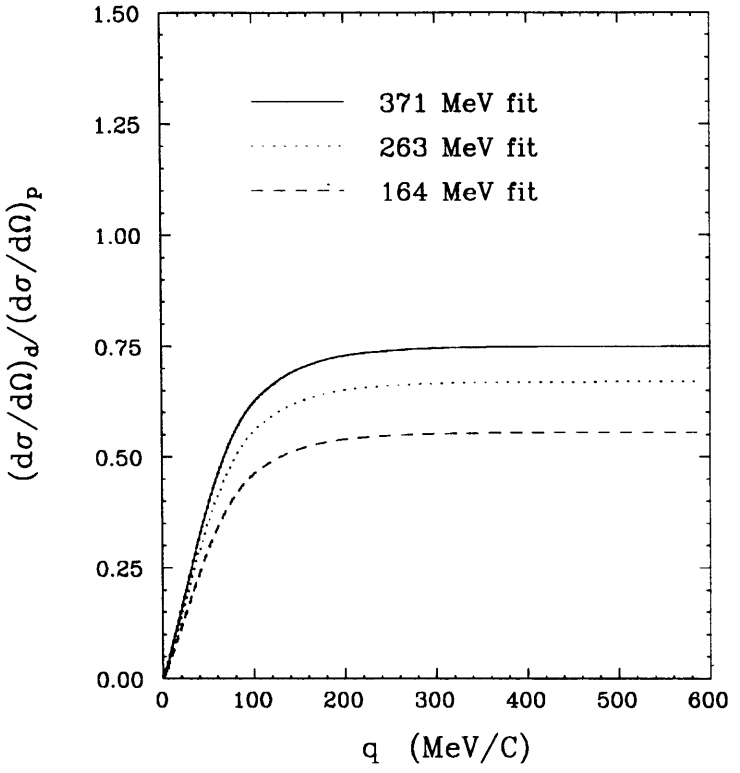

Figure 5-14: The Fermi sphere model fit with the realistic momentum distribution at 164, 263 and 371 MeV

The fits to the data are not very good, as can be seen in Figure 5-11 ~ Figure 5-13. Although the reduction strength in the ratio of the deuteron SCX cross sections to the impulse approximation values lessens as the energy goes up, at 164 MeV the overall normalization factor, f_M was 0.56. This corresponds to a 44% reduction of the deuteron cross sections from the impulse approximation values, a much bigger value than the 20% reduction seen in the data.

5.1.2.3 Conclusion

Using a Fermi gas momentum distribution, the fit to the data was good. However it took a physically unreasonable parameter (k_F = 150 MeV/c) to achieve the good fit. When we used a realistic density distribution instead, the fit was poor.

Peterson *et al.* built a Fermi sphere model in which $\left(\frac{d\sigma}{d\Omega}\right)^{IA}_{d\ SCX}$ was first separated into the spin-flip and spin-non-flip amplitude and the Pauli reduction factor Q was applied only to the spin-non-flip amplitude[12]. The nucleon momentum distribution was obtained from a Fourier transformation of an exponential deuteron wave function, proportional to $e^{-\gamma r}$, with γ determined from the deuteron binding energy. The Pauli blocking factor Q then was calculated to be:

$$Q = 1 - \frac{1}{(1+x^2)^2}, \tag{5.4}$$

where

$$x = \frac{q}{4\gamma}. \tag{5.5}$$

In Figure 5-15 ~ Figure 5-17 the results of the Fermi sphere model by Peterson *et al.* are compared to our data. The dashed curves show the differential cross sections from the impulse approximation. The spin-flip cross sections are shown as dotted curves. Dot-dashed curves are the spin-non-flip cross sections multiplied by Q. The solid curves are the sum of the dotted and the dot-dashed curves. The agreement between the data and the calculation is good at all energies.

In light of the success of the Fermi sphere model by Peterson *et al.*, the reason for the poor results from our Fermi sphere model must lie in the fact that in our model the Pauli blocking factors were applied to the $\left(\frac{d\sigma}{d\Omega}\right)^{IA}_{d\ SCX}$'s. The real difference arises at an intermediate region of the momentum transfer ($100 \leq q \leq 300$ MeV/c) where the spin flip amplitude becomes significant and the Pauli blocking effect still persists ($Q \neq 1$).

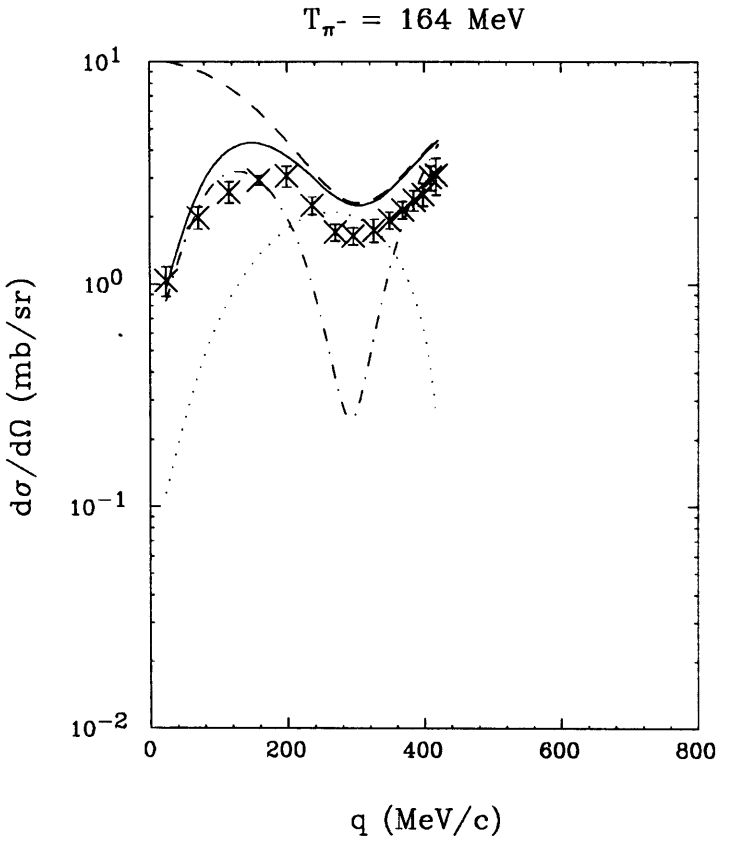

Figure 5-15: Angular distribution of the deuteron SCX reaction at T_{π^-}=164 MeV. Dashed curves are from the impulse approximation. Dotted curves are spin-flip cross sections, while the spin-non-flip cross sections are suppressed by Q and shown as dot-dashed curves. The solid curves are the sum of the dotted and the dot-dashed curves. At 164 MeV, when the overall scale factor of 0.9 (equivalent to our f_M) is taken into account, the agreement between the solid curve and the data is good. The calculations are from Peterson *et al.*[12].

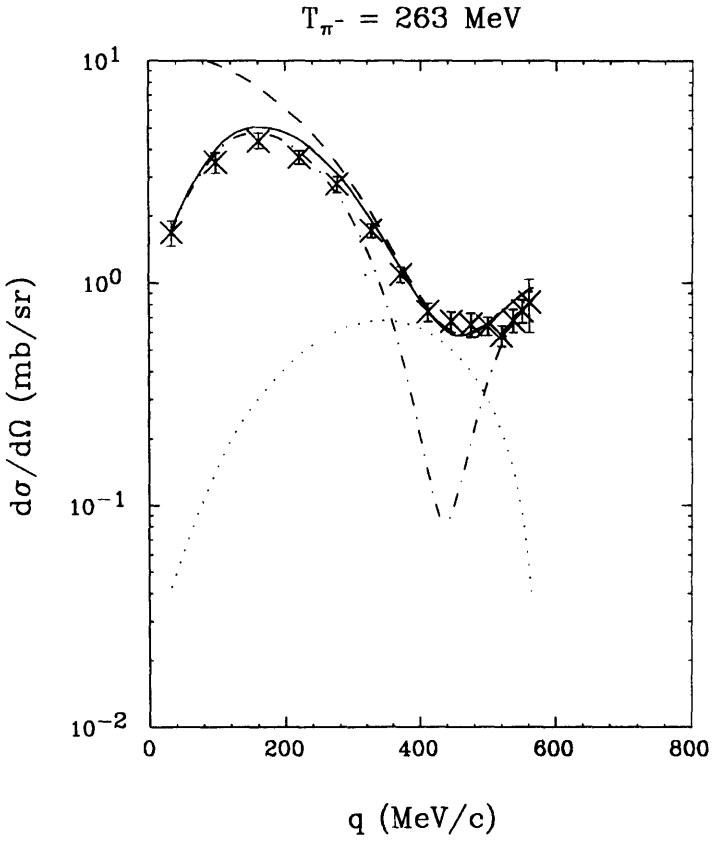

Figure 5-16: Angular distribution of the deuteron SCX reaction at T_{π^-}= 263MeV. Dashed curves are from the impulse approximation. Dotted curves are spin-flip cross sections, while the spin-non-flip cross sections are suppressed by Q and shown in dot-dashed curves. The solid curves are the sum of the dotted and the dot-dashed curves. The calculations are from Peterson *et al.*[12].

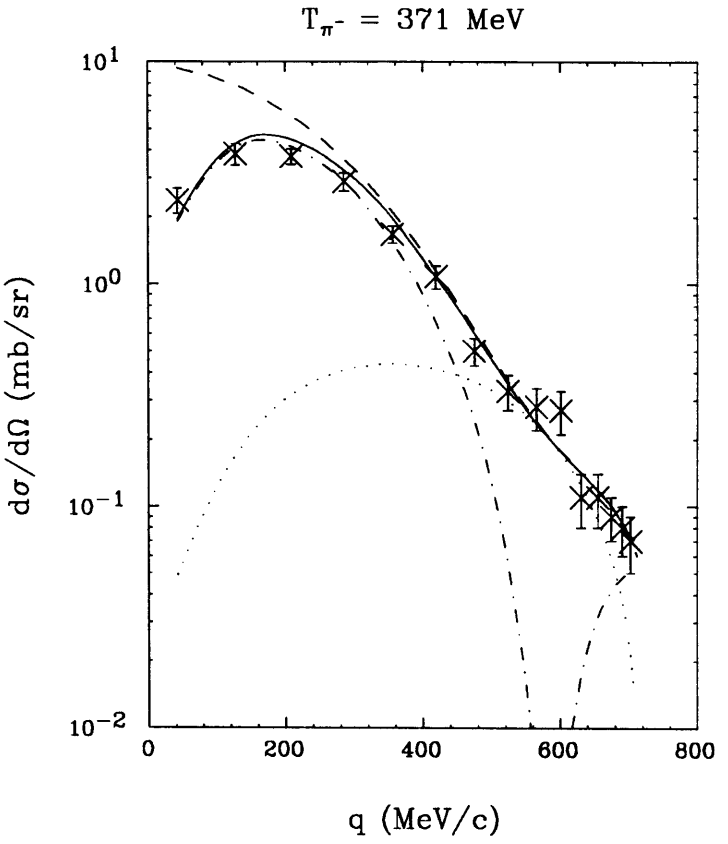

Figure 5-17: Angular distribution of the deuteron SCX reaction at T_{π^-}=MeV. Dashed curves are from the impulse approximation. Dotted curves are spin-flip cross sections, while the spin-non-flip cross sections are suppressed by Q and shown in dot-dashed curves. The solid curves are the sum of the dotted and the dot-dashed curves. The calculations are from Peterson *et al.*[12].

T_{π^-} (MeV)	$\sigma_{d\,SCX}$ (mb)
164	29.8 ± .8
263	16.3 ± .4
371	9.1 ± .3

Table 5.3: The deuteron SCX total cross sections

5.2 Total Cross Sections

The total cross sections were obtained by integrating the singly differential cross section values as:

$$\begin{aligned} \sigma_{d\,SCX} &= \int \left(\frac{d\sigma}{d\Omega}\right)_{d\,SCX} d\Omega \\ &= \int \left(\frac{d\sigma}{d\Omega}\right)_{d\,SCX} sin\theta\, d\theta\, d\phi \\ &= 2\pi \sum_{i=1}^{18} \left(\frac{d\sigma}{d\Omega}(\theta_i)\right)_{d\,SCX} (sin\theta_i)\,(10^\circ)\,. \end{aligned} \tag{5.6}$$

The total errors at each angle were added in quadrature to give the error for the total cross section.

Our singly differential cross section measurement ranged up 150° and beyond that we used the cross section values obtained from the Garcilazo calculation for T_{π^-}=164 MeV (shown in Figure 6-4) and from the phase shift calculation for higher energies (shown in Figure 5-1). The errors in the cross section values beyond 150° were set by averaging the percent errors between 0° and 150° at each energy. The result is shown in table 5.3.

5.3 Doubly Differential Cross Sections

5.3.1 Results

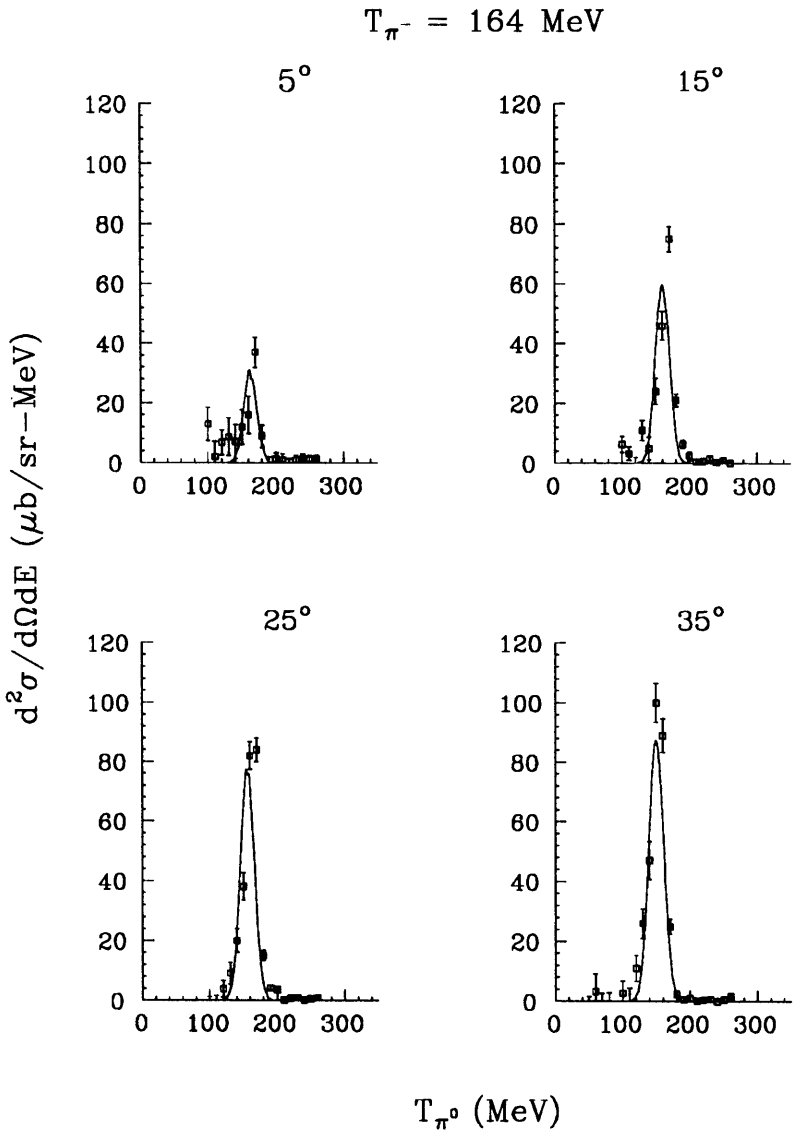

Figure 5-18: Deuteron SCX measurements at 164 MeV. The solid curve is from the IAP calculation

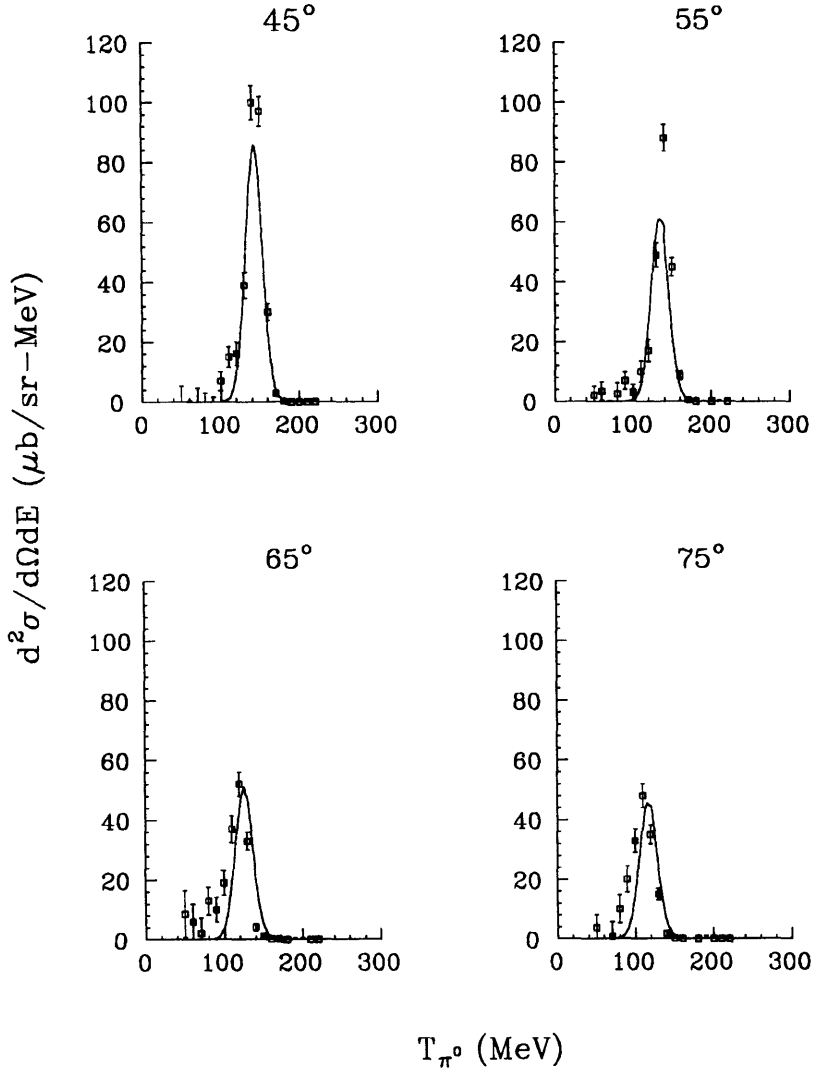

Figure 5-19: Deuteron SCX measurements at $T_{\pi^-} = 164$ MeV. The solid curve is from the IAP calculation.

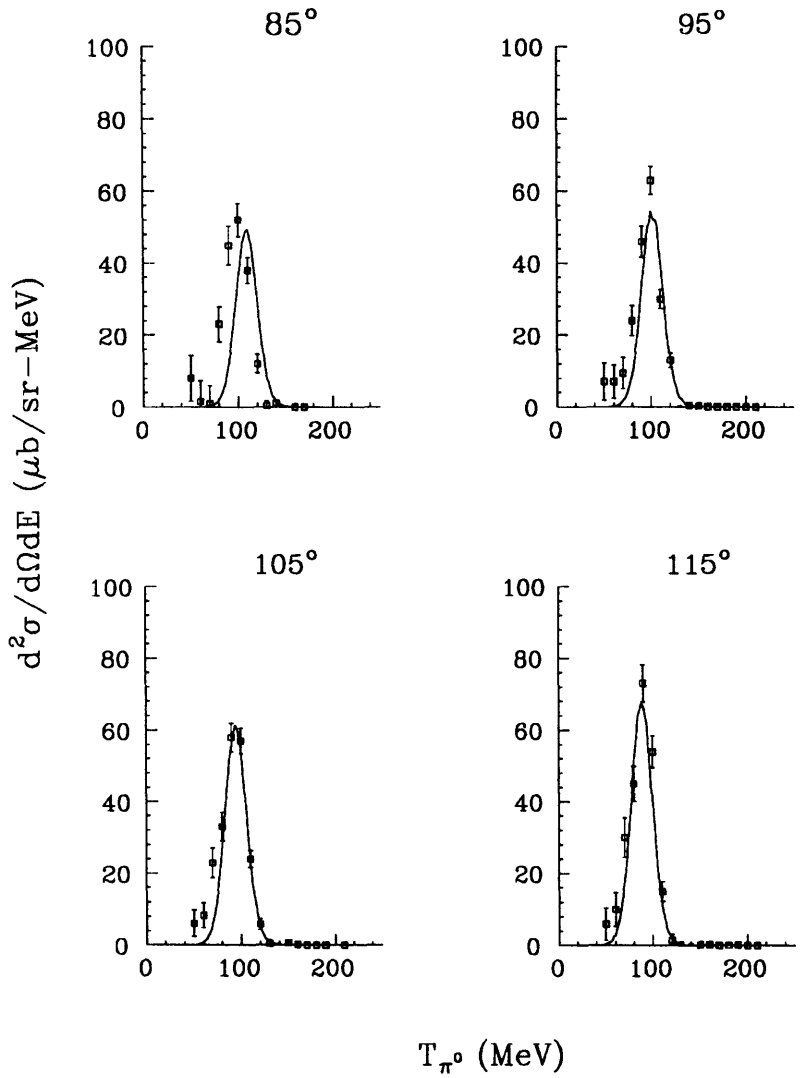

Figure 5-20: Deuteron SCX measurements at $T_{\pi^-} = 164$ MeV. The solid curve is from the IAP calculation.

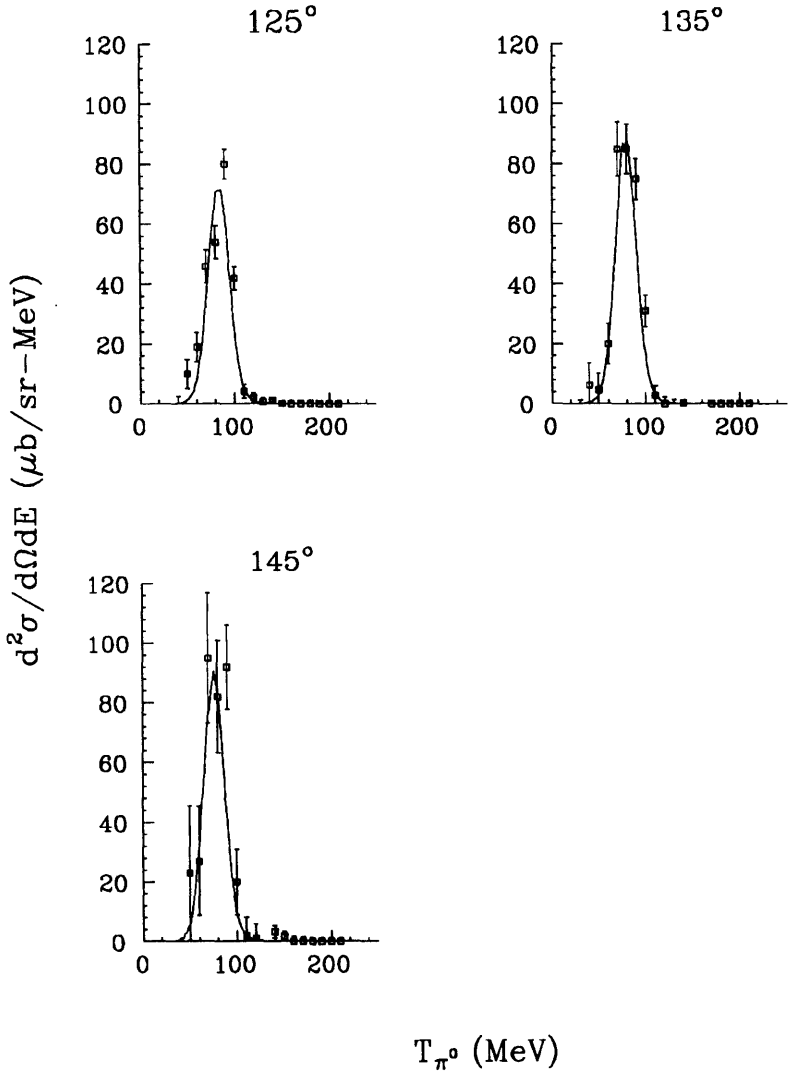

Figure 5-21: Deuteron SCX measurements at $T_{\pi^-} = 164$ MeV. The solid curve is from the IAP calculation.

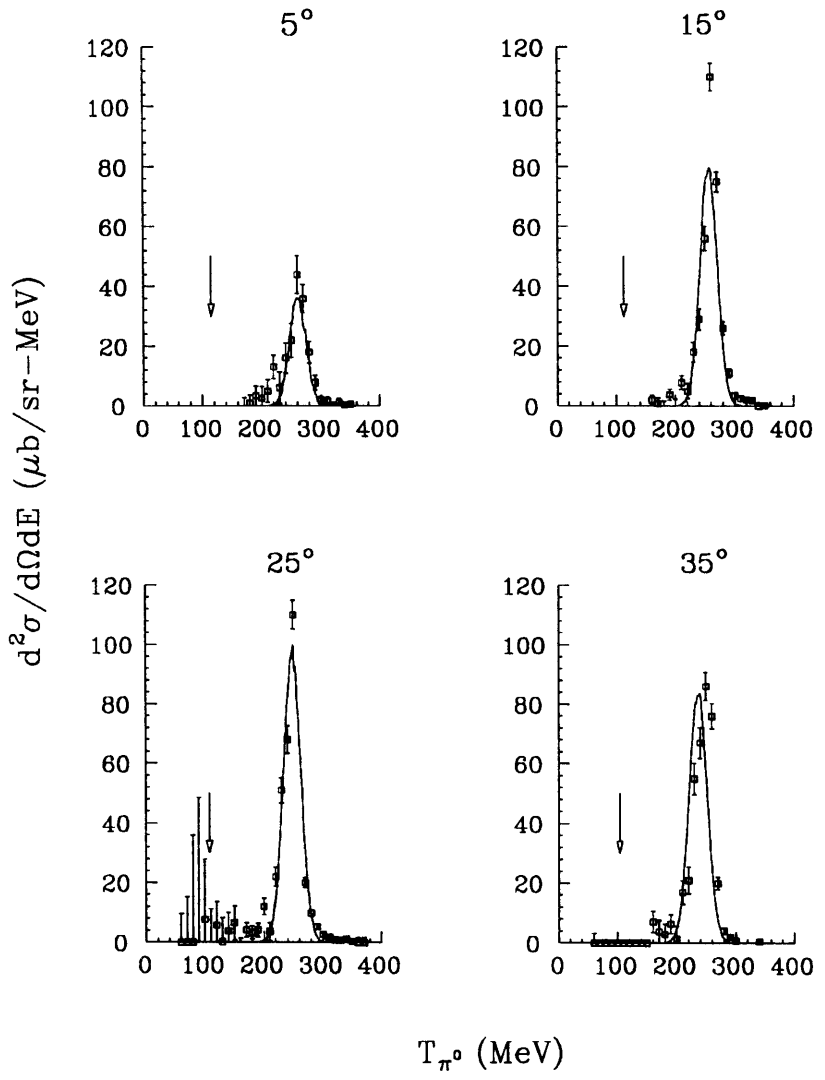

Figure 5-22: Deuteron SCX measurements at T_{π^-}= 263 MeV. The solid curve is from the IAP calculation. The arrow corresponds to the maximum kinematic energy of π^0 from PIPP (Pion-Induced-Pion-Production).

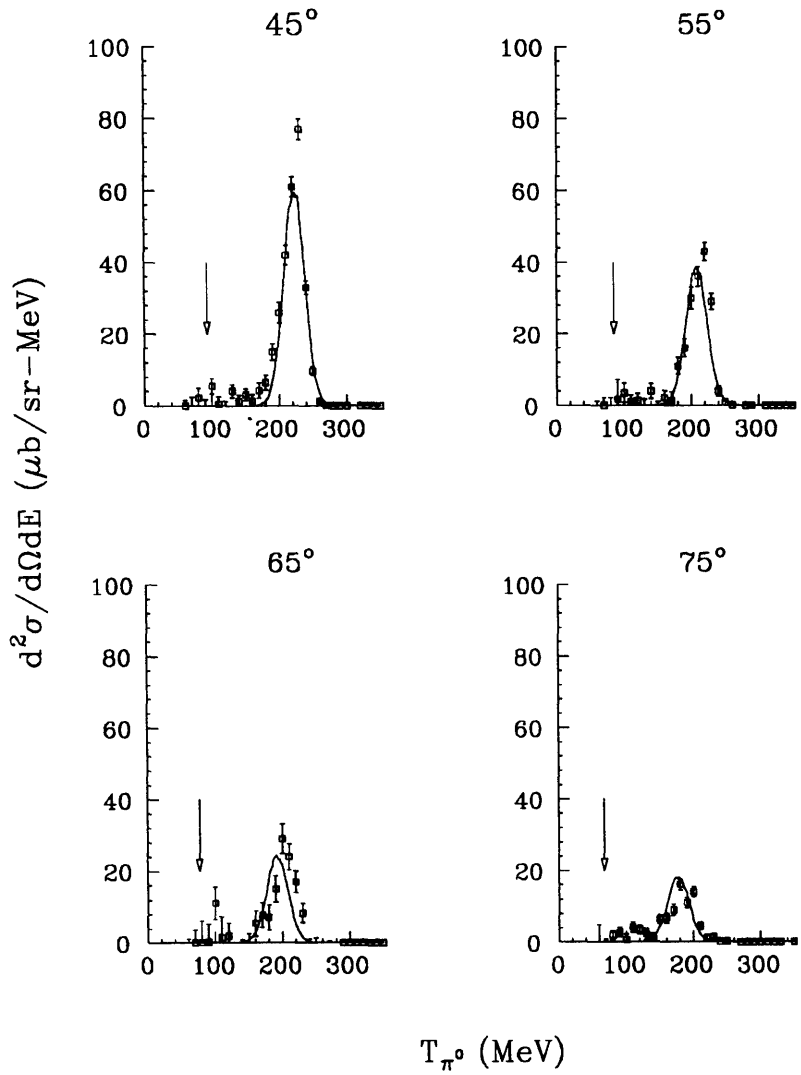

Figure 5-23: Deuteron SCX measurements at T_{π^-}= 263 MeV. The solid curve is from the IAP calculation. The arrow corresponds to the maximum kinematic energy of π^0 from PIPP (Pion-Induced-Pion-Production).

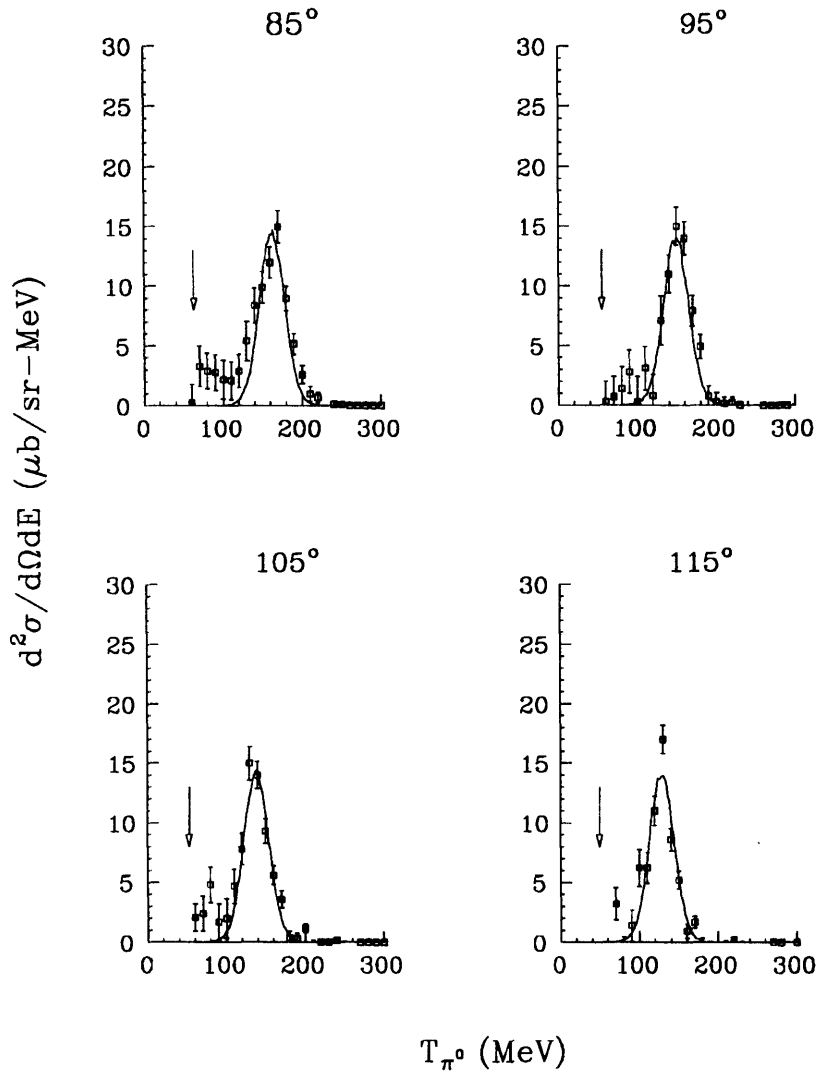

Figure 5-24: Deuteron SCX measurements at T_{π^-}= 263 MeV. The solid curve is from the IAP calculation. The arrow corresponds to the maximum kinematic energy of π^0 from PIPP (Pion-Induced-Pion-Production).

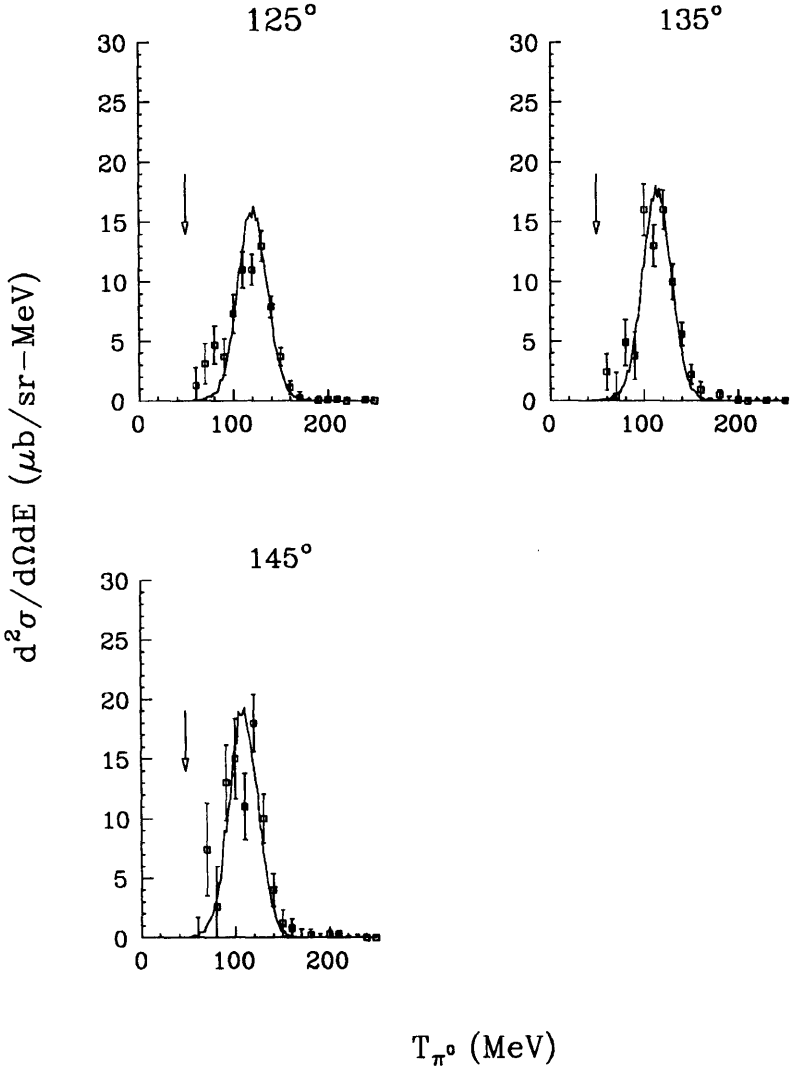

Figure 5-25: Deuteron SCX measurements at $T_{\pi^-} = 263$ MeV. The solid curve is from the IAP calculation. The arrow corresponds to the maximum kinematic energy of π^0 from PIPP (Pion-Induced-Pion-Production).

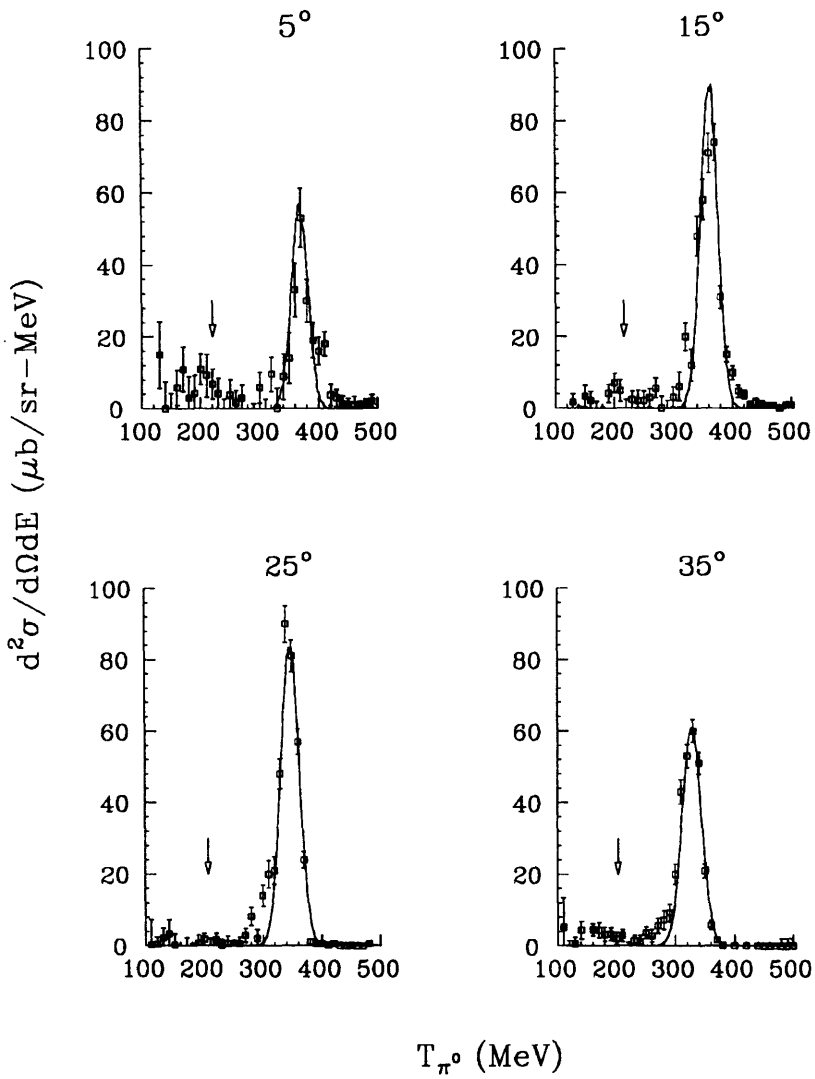

Figure 5-26: Deuteron SCX measurements at T_{π^-}= 371 MeV. The solid curve is from the IAP calculation. The arrow corresponds to the maximum kinematic energy of π^0 from PIPP (Pion-Induced-Pion-Production).

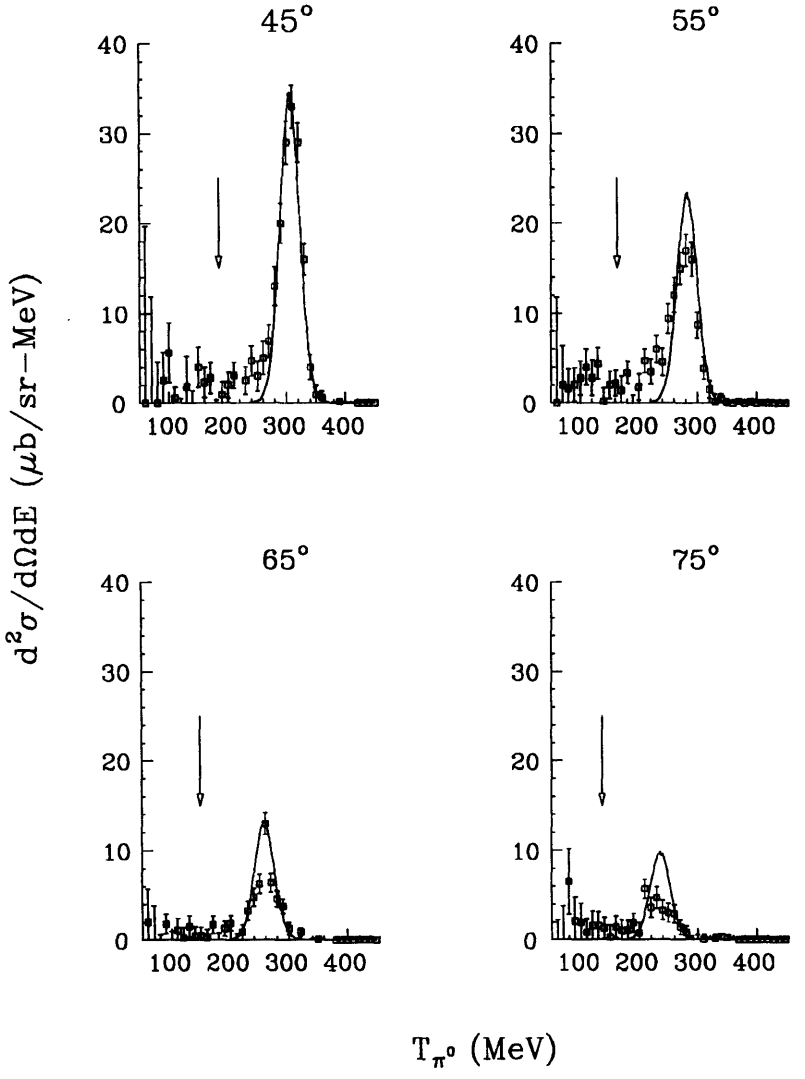

Figure 5-27: Deuteron SCX measurements at T_{π^-}= 371 MeV. The solid curve is from the IAP calculation. The arrow corresponds to the maximum kinematic energy of π^0 from PIPP (Pion-Induced-Pion-Production).

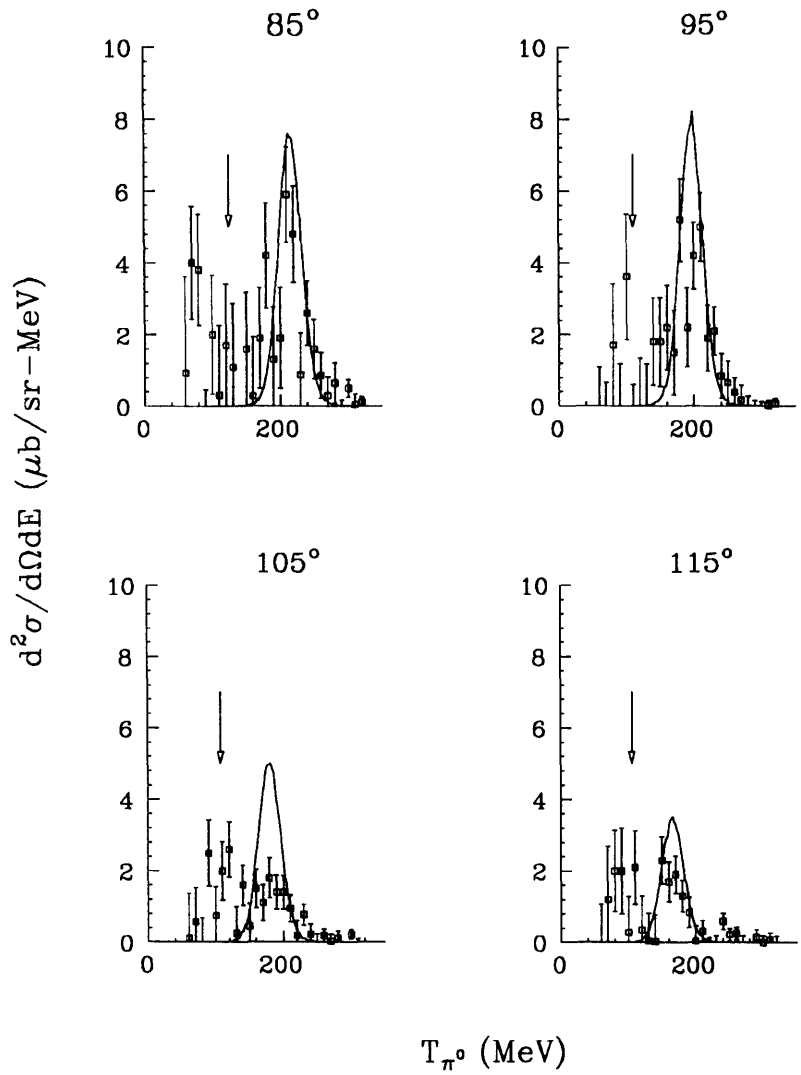

Figure 5-28: Deuteron SCX measurements at T_{π^-}= 371 MeV. The solid curve is from the IAP calculation. The arrow corresponds to the maximum kinematic energy of π^0 from PIPP (Pion-Induced-Pion-Production).

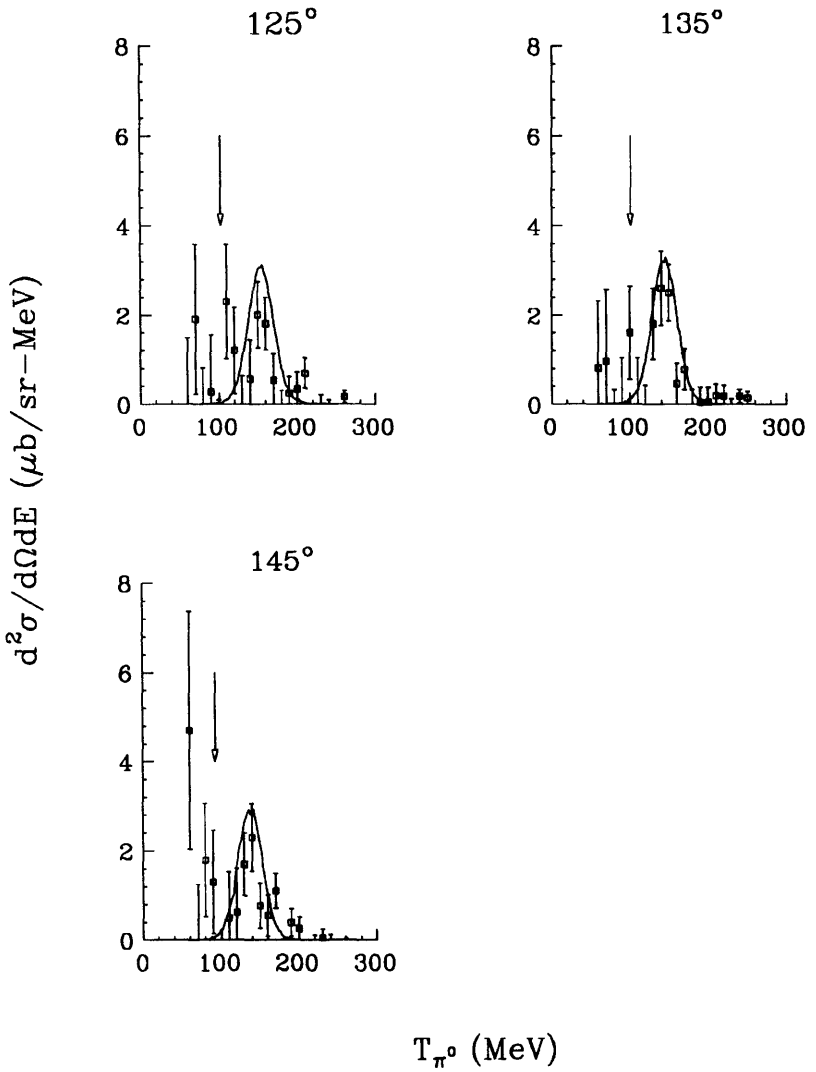

Figure 5-29: Deuteron SCX measurements at $T_{\pi^-} = 371$ MeV. The solid curve is from the IAP calculation. The arrow corresponds to the maximum kinematic energy of π^0 from PIPP (Pion-Induced-Pion-Production).

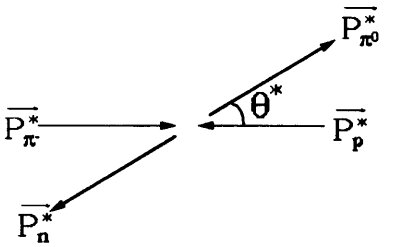

Figure 5-30: The deuteron single charge exchange in the center of mass frame under the quasifree scattering approximation.

The doubly differential cross sections for the deuteron SCX reaction are shown in Figure 5-18 $\sim$ Figure 5-29. The uncertainties shown are statistical only. The systematic uncertainty was discussed in Chapter 3.

5.3.2 Impulse Approximation Model

A model was built to describe the shape of the energy spectra in the doubly differential cross sections. It was based on the impulse approximation and included a phenomenological reduction factor obtained from comparing the deuteron to the proton angular distributions. For this reason it was named IAP (Impulse Approximation with a Phenomenological reduction factor). The goal of building this model was two-fold: first to see how well this simple model would explain the shapes of the energy spectra, and second to be able to attribute any disagreement between the calculation and the data to more complicated effects not included in the IAP model.

In the IAP model, the π^- interacts only with the proton in the deuteron SCX reaction (quasifree scattering approximation). In the lab frame the deuteron is at rest and the proton moves with a Fermi momentum which can be determined from the $(e, e'p)$ reaction[14]. In the center of mass frame, the π^- and the proton collide head-on with the same magnitude of momentum (see Figure 5-30). After a charge exchange, π^0 and the neutron go out at an angle θ^*. The likelihood of an event with a particular angle θ^* is determined according to the free proton SCX cross section, $\frac{d\sigma}{d\Omega^*}(\theta^*_{\pi^0})$ obtained from the phase shift calculation[10]. When the $\vec{p^*_{\pi^0}}$ is transformed to the lab frame, the π^0 scattering angle (θ_{π^0}) and energy (E_{π^0}) is determined for that event. The detector angular resolution is folded into the θ_{π^0} and the detector energy resolution into the E_{π^0}, according to Gaussian distribution. After all the events are collected in proportion to the individual weights, they form an energy spectrum within a given π^0 scattering

angle and energy bin. The energy spectrum was then multiplied by an overall scaling factor R_R (reduction ratio), where

$$R_R = \frac{(\frac{d\sigma}{d\Omega})_{\mathrm{d\,SCX}}}{(\frac{d\sigma}{d\Omega})_{\mathrm{p\,SCX}}}. \tag{5.7}$$

R_R represents the combination of effects such as Pauli blocking and multiple-scattering.

5.3.2.1 Comparison to the Data

The agreement in the overall magnitudes between the data and the IAP calculation is not surprising (Figure 5-18 $\sim$ Figure 5-29), since the area under the energy spectra (from the data) should be the same as that under the IAP curve by the construction of the IAP model.

The IAP model correctly predicts the peak positions of the energy spectra. The deuteron has a binding energy of 2.2 MeV, but its contribution to the peak position is washed out by the $\sim$ 12 MeV detector energy resolution. In the model the peak positions were calculated from two body kinematics under the quasifree SCX approximation. The model also predicts the widths of the energy spectra well. The momentum distribution of the proton, along with the detector angle and energy resolution were included in the IAP model to produce these widths.

In most of the energy spectra there are small deviations from the IAP curve in the low energy tails of the spectra. These low energy tails not present in the IAP calculation can be attributed to multiple scattering effects. Among the multiple scattering processes discussed in Chapter 1, the following processes are likely to be responsible for such low energy tails:

$$\pi^- + p \rightarrow \pi^0 + n \Rightarrow \pi^0 + n \rightarrow \pi^0 + n, \tag{5.8}$$

$$\pi^- + n \rightarrow \pi^- + n \Rightarrow \pi^- + p \rightarrow \pi^0 + n, \tag{5.9}$$

where the π^0 still appears and would be detected with a lower energy after the second scattering. The other multiple scattering processes such as:

$$\pi^- + p \rightarrow \pi^0 + n \Rightarrow \pi^0 + n \rightarrow \pi^- + p, \tag{5.10}$$

and

$$\pi^- + p \rightarrow \pi^0 + n \Rightarrow \pi^0 + n \rightarrow n, \tag{5.11}$$

do not produce a π^0 in the final state and must be responsible for part of the reduction factor R_R.

Chapter 6

Comparison with a Theoretical Calculation

The angular distribution of the deuteron SCX cross sections at $T_{\pi^-} = 164$ MeV has been calculated by Garcilazo[9] using a relativistic three body Faddeev theory[9]. No other calculation is currently available for comparison with our measurement. In this section we briefly describe Garcilazo's calculation and compare it to our data.

6.1 The Faddeev Calculation

In Chapter 1 we discussed the impulse approximation and the correction terms within the framework of the impulse approximation used to describe the πd scattering total cross sections. In these calculations the πN scattering amplitudes were always on-shell, the NN interactions were neglected, and the nucleons remained fixed.

The relativistic three body Faddeev calculation, however, has off-shell πN scattering amplitudes and treats the multiple scattering in the presence of the dynamics of the scattering system (*e.g.* the NN interaction). Also, instead of V_i's (two-body interaction potential), it deals with t_i's (two-body scattering amplitude matrix), which may be more directly accessible experimentally[15]. In this section, we briefly derive the relativistic three body Faddeev equation following Eisenberg and Koltun[15].

The Lippmann-Schwinger equation is a good place to start in formulating the 3 body scattering theory as follows:

$$\begin{aligned} < \vec{k_1'}\vec{k_2'}\vec{k_3'}|T(E)|\vec{k_1}\vec{k_2}\vec{k_3} > \;\; = \;\; & < \vec{k_1'}\vec{k_2'}\vec{k_3'}|V|\vec{k_1}\vec{k_2}\vec{k_3} > \\ & + \int < \vec{k_1}\vec{k_2}\vec{k_3}|V|\vec{k_1''}\vec{k_2''}\vec{k_3''} > \\ & \times \frac{1}{E - (k_1''^2/2m_1) - (k_2''^2/2m_1) - (k_3''^2/2m_1) + i\eta} \\ & \times < \vec{k_1''}\vec{k_2''}\vec{k_3''}|T(E)|\vec{k_1}\vec{k_2}\vec{k_3} > \frac{d\vec{k_1''}}{(2\pi)^3}\frac{d\vec{k_2''}}{(2\pi)^3}\frac{d\vec{k_3''}}{(2\pi)^3} \end{aligned} \tag{6.1}$$

where

T is a three-body amplitude

E is the total energy of the three body system

the $\vec{k_i}$s are the ith particle momentum

the interaction potential V is made up of three pair-wise interactions

$V = V_1 + V_2 + V_3$, $V_i \equiv V(\vec{r_j}, \vec{r_k})$, i, j, k cyclic.

This integral equation has two problems for practical applications, however. First, the kernel of the Equation (6.1) is not square integrable, which means that an analytic solution of the equation is not guaranteed[38]. Another problem with Equation (6.1)is that for some strong short range forces the matrix element of V_i may not converge.

Faddeev's solution to these problems was to rearrange the infinite series in Equation (6.1) to replace the possibly problematic interaction potential V_i's with well-behaved scattering amplitudes t_i's[39][40][41][38]. We can see how this works by first dividing Equation (6.1) into 3 parts depending on the particle pair in which the last interaction occurred to obtain:

$$T = T_1 + T_2 + T_3. \tag{6.2}$$

Here T_1, for example, includes all the single and multiple scatterings in which the last scattering occurred between the particle 2 and 3. Figure 6-1 shows the sum of all the scattering diagrams to make up T_1. Included in T_1 is t_1, the full two particle amplitude for the particle 2 and 3, G_0, the free three-body propagator and the other subpartitions T_2 and T_3 of the full amplitude.

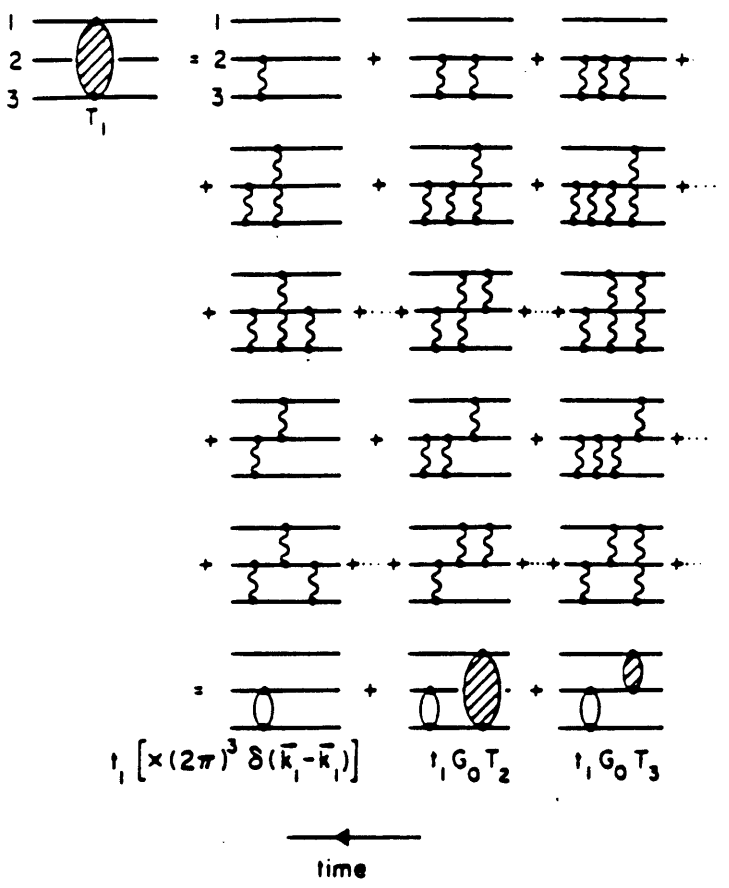

Figure 6-1: Sample diagrams for three interacting particles. The full amplitude T is expressed as a sum over three subamplitudes, defined according to which pair interacted last. In this figure are included all the scatterings in which the particle 2 and 3 scattered last contributing to the subamplitude T_1. The diagrams are to be read from right to left. (The plot is from Koltun[15].)

Faddeev showed that the kernel of the resulting coupled integral equation was square-integrable, thus guaranteeing an unique solution.

Now, we consider the scattering of a meson (particle 1) from a deuteron (made up of particles 2 and 3). The integral equation is written as:

$$T = (V_2 + V_3) + (V_2 + V_3)G^{(1)}T\ , \tag{6.3}$$

where

$$G^{(1)} \equiv \frac{1}{E - K - V_1 + i\eta}\ . \tag{6.4}$$

The Hamiltonian for the three body system is

$$H = K + V = (k_1 + k_2 + k_3) + (V_1 + V_2 + V_3), \tag{6.5}$$

where

k_i is the kinetic energy operator for particle i

V_i is the interaction potential for particle j and k.

This Hamiltonian can be broken up as

$$H = H_1 + H_1' = (K + V_1) + (V_2 + V_3). \tag{6.6}$$

In this way the interaction between the two nucleons in the unperturbed part H_1 is included in $G^{(1)}$ (in Equation (6.4)). After algebraic operations, we obtain a Lippmann-Schwinger equation written in the Faddeev scheme as:

$$t_1 = V_1 + V_1 G_0 t_1. \tag{6.7}$$

The G_0 is a free three body propagator and is given by:

$$G_0 \equiv \frac{1}{E - K + i\eta}. \tag{6.8}$$

The t_1 is a two body t-matrix for scattering of particle 2 and 3 replacing V_1 as:

$$t_1 = \frac{V_1}{1 - V_1 G_0}. \tag{6.9}$$

The full Faddeev amplitude in Equation (6.3) can now be broken up as:

$$T = T_2 + T_3, \tag{6.10}$$

with

$$T_i = V_i + V_i G^{(1)} T \text{ with } i = 2, 3\,. \tag{6.11}$$

After some more algebraic steps, we obtain the Watson series written in the Faddeev format as:

$$\begin{aligned} T_i &= V_i + V_i G_0 T + V_i G_0 t_1 G_0 T \\ &= V_i + V_i G_0 (T_i + T_j) + V_i G_0 t_1 G_0 T, \end{aligned} \tag{6.12}$$

where

$i = 2,3;\ j = 2,3;\ j \neq i.$

While in Equation (1.18) (Watson series written in the impulse approximation format) the NN interaction is embedded in the propagator G_N, in Equation (6.12) it is explicitly written in terms of the t_1 matrix (the scattering amplitude between the two nucleons).

With the definition:

$$T_1 \equiv t_1 G_0 T \equiv t_1 G_0 (T_2 + T_3), \tag{6.13}$$

we obtain the Faddeev Equation for a pion scattering from a two-nucleon bound system to be:

$$T_i = (1 - \delta_{i1}) t_i + \sum_{j \neq i} t_i G_k T_j, \tag{6.14}$$

where

G_k is the propagator for the exchanged particle k ($i \neq j \neq k$).

6.2 Garcilazo's Calculation

In the previous section we derived the three body relativistic Faddeev equation in a general form for a meson (particle 1) scattering from a two nucleon bound system (particle 2 and 3) to obtain:

$$T_i = (1 - \delta_{i1})t_i + \sum_{j \neq i} t_i G_k T_j, \tag{6.15}$$

where

T_i is a full two body amplitude between particle j and k

t_i is a t-matrix for the scattering of particle j and k ($i \neq j \neq k$)

G_k is the propagator for exchanged particle k ($i \neq j \neq k$).

Garcilazo makes two simplifying approximations to this equation to calculate the quantity T[16][9][42]. T is the Faddeev amplitude for the deuteron breakup reaction ($\pi d \rightarrow \pi NN$) and is given as:

$$T = T_2 + T_3. \tag{6.16}$$

The deuteron SCX reaction is treated as a special case of the breakup reaction. In first approximation, it is assumed that in a breakup reaction the spectator particle is always on the mass shell ("the spectator on-shell approach"), while the particles directly participating in the reaction are always off the mass shell. The second approximation is called "the isobar ansatz". In the isobar ansatz, the πNN system is made up of d and Δ isobar channels. The d isobar is a NN system with a pion as a spectator particle, while the Δ isobar is a πN system with a nucleon as a spectator. With these approximations, the two body scattering amplitude t_i is given as follows:

$$t_i(S_i) = \sum_{m_i=-j_i}^{j_i} \Gamma_{I \rightarrow j+k} | \phi^{j_i}_{m_i} > \tau_i(s_i) < \overline{\phi}^{j_i}_{m_i} | \Gamma^{+}_{I \rightarrow j+k}, \tag{6.17}$$

where

$i\,j\,k$ are cyclic particle indices

s_i is the invariant mass squared of an isobar i

j_i is the spin of an isobar i

m_i is the helicity of an isobar i

$\phi^{j_i}_{m_i}$ is an isobar spinor of mass $\sqrt{s_i}$

τ_i is the propagator for an isobar i

$\Gamma_{I\to j+k}$ is a vertex function that couples the isobar I to particles j and k.

When we combine the above three equations under the spectator on shell and isobar ansatz approximations, we obtain an effective two body equation as:

$$F_{i1} = (1-\delta_{i1})V_{i1} + \sum_{j\neq i} V_{ij}\tau_j F_{j1}, \tag{6.18}$$

where we have defined a new amplitude F_{i1} and a transition potential V_{ij} as:

$$T_i|\phi_d> = \Gamma_{I\to j+k}|\phi^{j_i}> \tau_i(S_i)F_{i1}, \tag{6.19}$$

$$V_{ij} = \Gamma^+_{I\to j+k} G_k \Gamma_{J\to k+i}. \tag{6.20}$$

Two kinds of transition potentials used in the deuteron breakup reaction are shown in Figure 6-2 and are written as:

$$V_{\Delta d} = \Gamma^+_{\Delta\to 1+2} G_2 \Gamma_{d\to 2+3}, \tag{6.21}$$

$$V_{\Delta\Delta} = \Gamma^+_{\Delta\to 1+2} G_1 \Gamma_{\Delta\to 1+2}. \tag{6.22}$$

As shown in the figure, under the $V_{\Delta d}$ a nucleon is exchanged between a πN and NN isobars while a pion is exchanged between two πN isobars under the $V_{\Delta\Delta}$. Shown in Figure 6-3 are the Feynman diagrams in which the transition potentials are responsible for a first (top figure) and a second (bottom figure) scattering in a deuteron SCX reaction.

As input to the πN channels, $S_{11}(L_{2I,2J})$, S_{31}, , P_{11}, P_{13}, P_{31} and P_{33} states are used and two-nucleon states ${}^3S_1({}^{2S+1}L_J)$, ${}^3P_1$ and ${}^1S_0$ are used as input to the NN channels.

The πN isobar amplitude is given by:

$$t_{\pi N} = \Gamma_{\Delta\to\pi+N}|\phi^\Delta> \tau_\Delta < \overline{\phi}^\Delta|\Gamma^+_{\Delta\to\pi+N}\,. \tag{6.23}$$

The isobar propagator τ_Δ and the vertex function $\Gamma_{\Delta\to\pi+N}$ are constructed from the experimental pion nucleon phase shifts and the solutions of the fixed t dispersion relations[43]. The NN isobar amplitude is given as:

$$t_{NN} = \Gamma_{d\to N+N}|\phi^d> \tau_d < \overline{\phi}^d|\Gamma^+_{d\to N+N}\,. \tag{6.24}$$

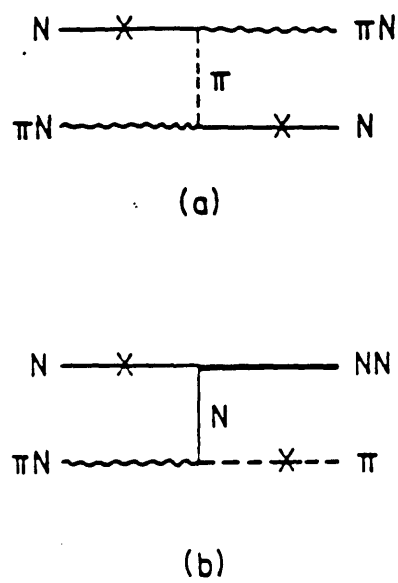

Figure 6-2: The transition potentials of the πNN system, where the crosses in the particles mean that they are on mass shell. (a) Transition between two πN isobars via pion exchange. (b) Transition from a NN isobar to a πN isobar by means of nucleon exchange. (The plot is from Garcilazo[16].)

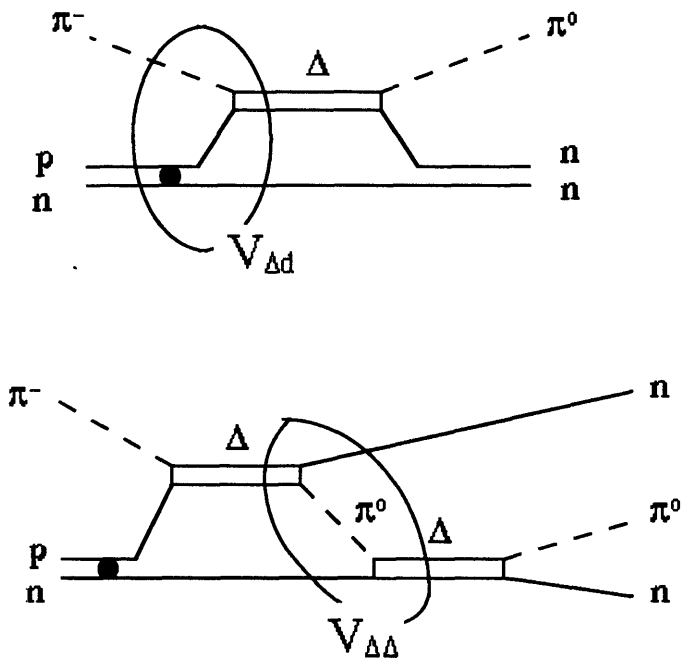

Figure 6-3: Some of the Feynman diagrams for the deuteron SCX reaction. The transition potentials are shown in a single scattering (top figure) and a double scattering (bottom figure).

Here τ_d and $\Gamma_{d\to\pi+N}$ are obtained by applying the unitary pole approximation to the Paris potential[44]. For the deuteron SCX reaction, it is here that charge exchange amplitudes are projected through the isospin part of the vertex functions as a special case of the deuteron break-up reaction.

The full SCX amplitude is now given by:

$$T_{SCX}^{Full} = \sum_{i=2}^{3}(\Gamma_{\Delta i} + \Gamma_{d1}\tau_{d1}V_{d1\,\Delta i})\tau_{\Delta i}F_{\Delta i\,d}, \tag{6.25}$$

where

i designates the spectator particle at a given channel.

When only the first term in the above equation is taken without the summation, an impulse approximation is obtained to give:

$$T_{SCX}^{IA} = \Gamma_{\Delta}\tau_{\Delta}V_{\Delta d}. \tag{6.26}$$

When the summation is performed on the first term of the Equation (6.25), the Pauli blocking effect is incorporated to give:

$$\begin{aligned} T_{SCX}^{IA+Pauli} &= \sum_{i=2}^{3}\Gamma_{\Delta i}\tau_{\Delta i}V_{\Delta i\,d} \\ &= \Gamma_{\Delta 2}\tau_{\Delta 2}V_{\Delta 2\,d} + \Gamma_{\Delta 3}\tau_{\Delta 3}V_{\Delta 3\,d}. \end{aligned} \tag{6.27}$$

In this equation the second term is a particle-exchanged diagram of the first term. The Pauli exclusion principle demands that if particles 2 and 3 have the same set of quantum numbers, then:

$$V_{\Delta 2\,d} = -V_{\Delta 3\,d}, \tag{6.28}$$

which in turn means that:

$$T_{SCX}^{IA+Pauli} = 0. \tag{6.29}$$

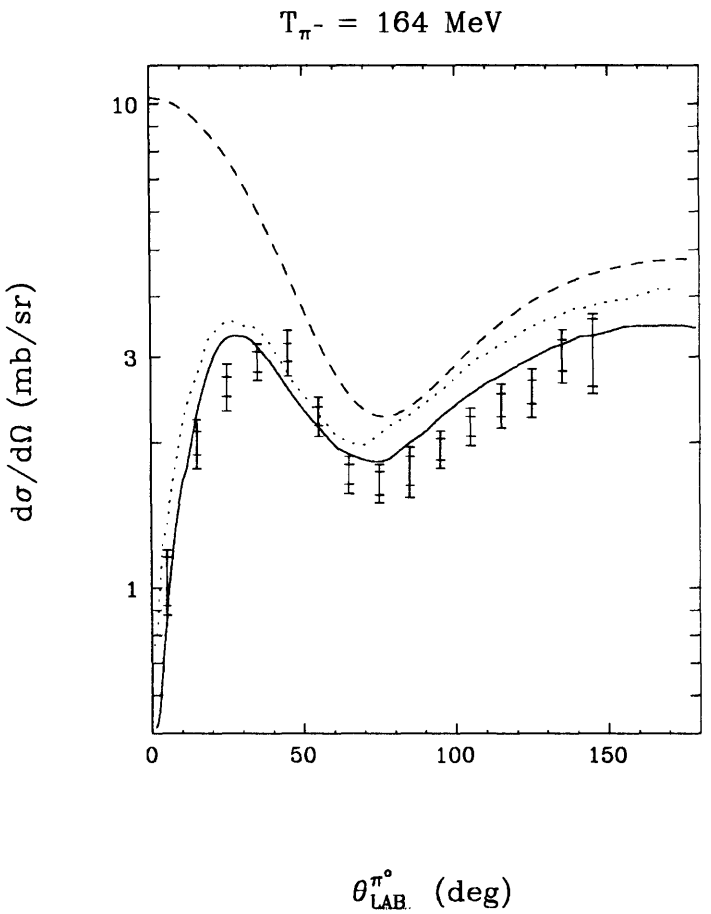

Figure 6-4: Our deuteron SCX data at T_{π^-}= 164 MeV. The larger error bars correspond to the total uncertainty, while the smaller error bars correspond to the statistical uncertainty only. The dashed curve is from the T^{IA}_{SCX}, dotted curve from the $T^{IA+Pauli}_{SCX}$ and the solid curve from the T^{Full}_{SCX} in Garcilazo calculation[9].

6.3 Comparison to the Data

Shown in Figure 6-4 is the comparison of Garcilazo's calculation to our data at T_{π^-}= 164 MeV. In the figure the dashed curve represents T_{SCX}^{IA}, dotted curve $T_{SCX}^{IA+Pauli}$ and the solid curve T_{SCX}^{Full}.

When the impulse approximation is combined with the Pauli blocking effect, the $T_{SCX}^{IA+Pauli}$ roughly predicts the overall shape. However, only the full calculation (T_{SCX}^{Full}), which also includes the multiple scattering effect, predicts the data very well. The multiple scattering accounts for the overall reduction of the data by 20% from the impulse approximation result[9]. It would be interesting to see if the same calculation can describe the higher energy data correctly as well and if so, what the major contributing effects to the cross sections might be.

Chapter 7

Conclusion

The πNN system is of fundamental importance in the study of the nucleon-nucleon system since for nucleons to interact with each other, they must exchange pions. There are several reaction channels in the πNN system such as breakup ($\pi^{\pm}d \rightarrow \pi^{\pm}NN$), elastic scattering ($\pi^{\pm}d \rightarrow \pi^{\pm}d$), charge exchange ($\pi^{\pm}d \rightarrow \pi^{0}NN$), absorption ($\pi^{\pm}d \rightarrow NN$), pion induced pion production ($\pi^{\pm}d \rightarrow \pi\pi NN$). Of these reaction channels, charge exchange has been least studied in the laboratory. With the exception of some early, poor-statistics cloud- and bubble-chamber measurements, a previous measurement at $T_{\pi^-} = 164$ MeV constituted the only data[8] below 500 MeV[11]. There, the agreement between a Faddeev calculation[9] and the data was not very good at large angles.

In the pion single charge exchange reaction on the deuteron there is one extra nucleon beyond the one required for the charge exchange. By comparing the deuteron SCX cross sections against the impulse approximation prediction in which that extra nucleon is ignored, one can learn about pion-nucleus effects in the simplest nuclear system.

The experiment described in this thesis was performed using the high-energy pion channel ("P^3") at the Clinton P. Anderson Meson Physics Facility (LAMPF) in 1992. Differential cross sections for the $d(\pi^-,\pi^0)nn$ reaction were measured for π^0 laboratory angles $0° \sim 145°$ at incident pion energies of 164, 263 and 371 MeV. Both decay photons from the outgoing π^0 were detected in a single 6 $\times$ 10 array of pure CsI crystals (a component of the complete NMS detector). The detector acceptance was accounted for by comparing the π^0 yield from the $p(\pi^-,\pi^0)n$ reaction to the known cross section from a phase shift calculation[10] and also by using a Monte Carlo code which mapped out the energy dependence of the detector acceptance.

The incident pion flux could be kept low ($\sim$ one million/sec instantaneous) because of the large acceptance of the detector ($\sim$ 100 msr), which in turn allowed the accurate counting of the incident flux. The energy deposited in the 60 CsI crystal calorimeter was calibrated by relating the ADC channel numbers to the π^0 peak centroid positions in the proton SCX reaction in which the π^0 energy is determined from two body kinematics. The cosmic ray peak centroid values were monitored at every run to account for any shift in the detector response due to changes in the ambient temperature.

The shapes of the deuteron SCX energy spectra were compared against the results from an impulse approximation model (IAP model), in which the incoming pion interacted with the proton moving with a Fermi momentum in the deuteron. The peak positions and the widths of the deuteron SCX energy spectra are well described by the IAP model. The energy spectra deviate from the prediction of the model at low energies. The low energy tails that appear in the data are the π^0 's with energies lower than the quasifree values as a result of multiple scattering.

The angular distributions of the deuteron SCX cross sections exhibit two features distinct from that predicted by the impulse approximation[10]. First is a suppression of the deuteron cross sections from the impulse approximation values at the forward angles, which is due to the Pauli principle applied to the two final state neutrons. The suppression effect lessens at higher energies as more momentum transfer becomes available to overcome the Pauli blocking at a given angle. Second is an overall reduction of the deuteron SCX cross sections compared to the impulse approximation values due to multiple scattering processes in which π^0 's from the SCX reaction disappear through absorption or another SCX. At 164 MeV as much as a 20% reduction is seen. Such multiple scattering effects weaken at higher energies away from the Δ resonance region.

A relativistic Faddeev calculation was performed by Garcilazo at 164 MeV[9]. In his calculation, using the spectator on-shell and isobar ansatz approximations, the three-body Faddeev equation was reduced to an effective two-body equation. Properties of the πN and NN interaction were used as inputs to the calculation. The result agrees well with the data at 164 MeV.

To describe the forward angle suppression of the deuteron SCX angular distribution, a Fermi Sphere model was built. In the model the amount of suppression due to Pauli blocking at a given q (momentum transfer) was related to the fraction of the momentum phase space that the final neutrons would have to compete for at that q. Both a Fermi gas momentum

distribution and a realistic momentum distribution obtained from $(e, e'p)$ experiments[14] were used. The model failed to give a good description of the deuteron SCX angular distribution.

However, when the differential cross section given by the impulse approximation was first divided into spin-flip and spin-non-flip amplitudes and the suppression was applied only to the spin-non-flip amplitude, such a Fermi sphere model described the data well[12].

Recently the deuteron SCX cross sections at $T_{\pi^-} = 65$ and 98.5 MeV were measured using the NMS at LAMPF by Peterson *et al.*[45]. When the result of that experiment becomes available, it along with our data and the 500 MeV data by Ouyang[11] will make up a comprehensive set of deuteron SCX cross section measurements between 65 and 500 MeV. The phenomenological models such as IAP and Fermi sphere model (with the suppression applied only to the spin-non-flip amplitude) can be used to extract the pion-nucleus effects and observe their behavior as a function of energy over a broad energy range. It would be interesting to see if the Faddeev calculation by Garcilazo can reproduce the data at all energies.

Appendix A

Pion Fraction in the Beam

At the target position the beam consisted of particles such as π^-, μ^- and e^-, with the same momentum but different speeds due to their mass difference. The fraction of the pions in the beam was calculated by measuring the difference in the time-of-flight of these particles between the scintillator S1 and S3. S3 had a large active area (34 cm in diameter) to intercept all the beam particles that traveled 5 m down-steam from S1.

Shown in Figure A-1 is a schematic diagram for the pion fraction measurement set-up. When a beam particle went through S1, a logic pulse from the associated discriminator was sent to a "Pre Scaler" which 0.1% of the time produced an input to the "Synchronizer". A RF pulse (201 MHz Radio Frequency pulse from the accelerator) nearest in time to the S1 logic signal caused a Synchronizer output. The Synchronizer output started the TDC clocks. A delayed S1 logic pulse stopped the TDC for S1, while a delayed S3 logic pulse would stop the TDC for S3. In this way the RF signal acted as a zero reference point from which the the firing times of S1 and S3 were measured respectively. S3 had two photo-multiplier tubes and the signals from each tube were fed into the "Mean Timer". This combination was used in order to reduce the position dependence of the TDC timing in S3.

We first consider the T_{π^-}= 164 MeV case. Shown in Figure A-2 is a two dimensional histogram of the S1 and S3 TDC values, where the x-axis corresponds to the S1 TDC value and the y-axis to the S3 TDC value. Three separate clusters of points are seen. The particle 1's (particles in box 1) are pions, particles 2's are electrons and particle 3's are muons. This can be verified by looking at the relative positions of the clusters as follows:

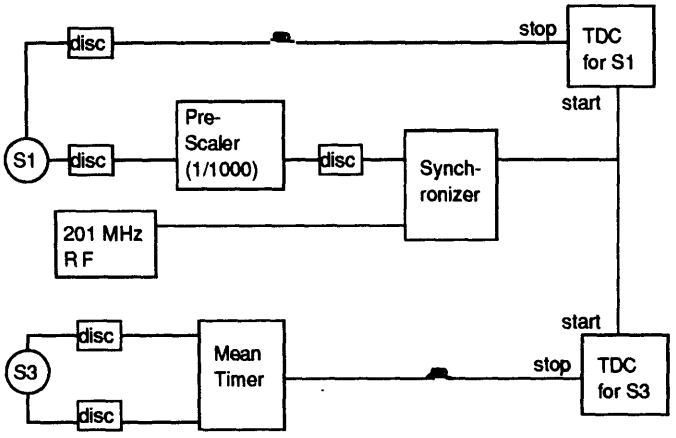

Figure A-1: Schematic diagram of the pion fraction measurement set-up.

T_{π^-}	P_{π^-}	$t_{\pi^-} - t_{\mu^-}\,(nsec)$		$t_{\pi^-} - t_{e^-}\,(nsec)$		$t_{\mu^-} - t_{e^-}\,(nsec)$	
(MeV)	(MeV/c)	calculated	measured	calculated	measured	calculated	measured
164	269	0.9	1.0	2.1	2.3	1.3	1.3
263	377	0.5	-	1.1	1.1	0.6	-
371	491	0.3	-	0.8	-	0.4	-

Table A.1: The time-of-flight difference

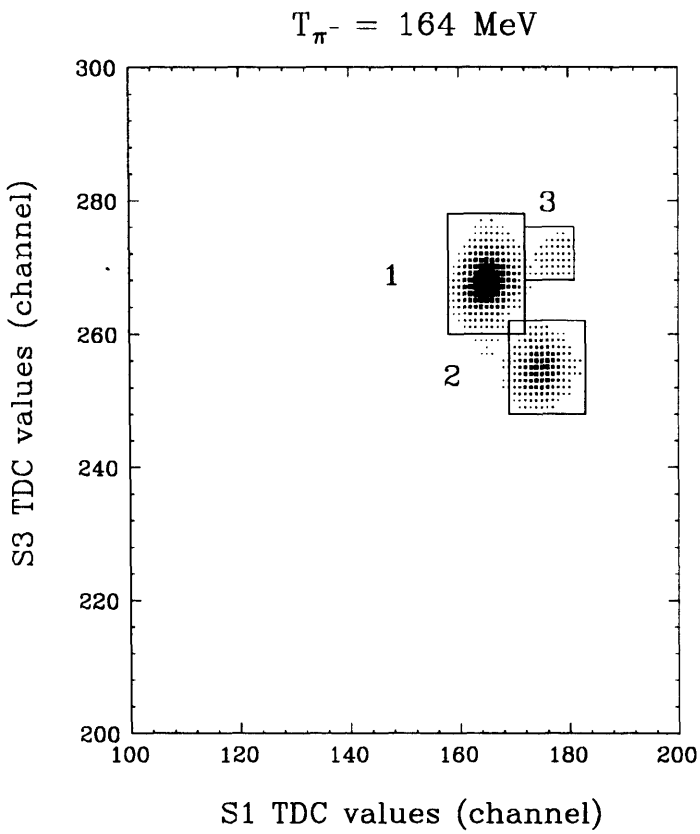

Figure A-2: Two dimensional histogram of the S1 and S3 TDC values at T_{π^-} = 164 MeV. Box 1 corresponds to the pions, box 2 to the electrons and box 3 to the muons.

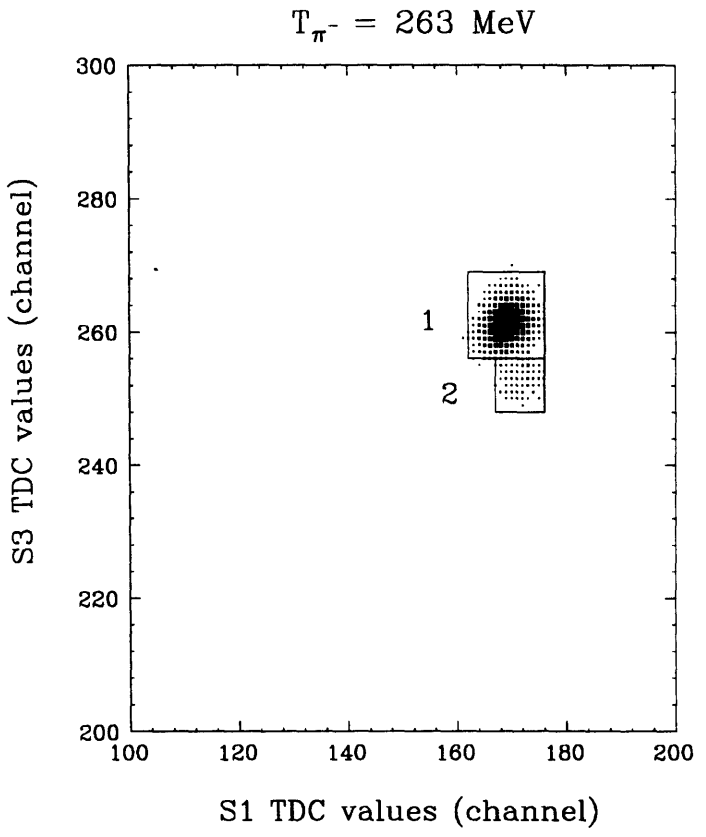

Figure A-3: Two dimensional histogram of the S1 and S3 TDC values at T_{π^-}= 263MeV. Box 1 corresponds to the pions, box 2 to the electrons.

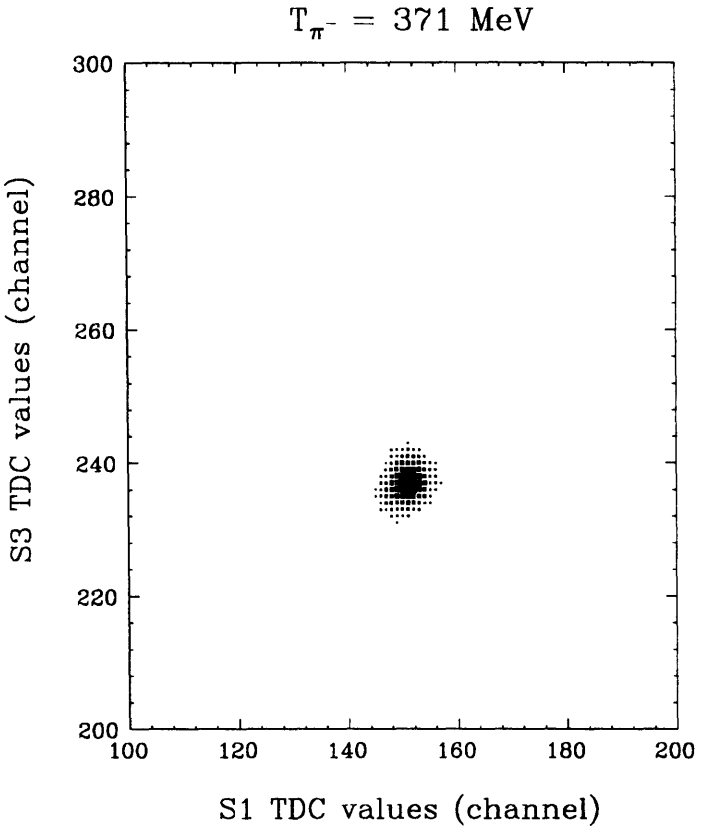

Figure A-4: Two dimensional histogram of the S1 and S3 TDC values at $T_{\pi^-} = 371$ MeV.

$< x^1 >= 165$ $< y^1 >= 268$ for particle 1,

$< x^2 >= 175$ $< y^2 >= 255$ for particle 2,

$< x^3 >= 178$ $< y^3 >= 271$ for particle 3.

We first consider particles 1 and 2. On average particle 2 comes into S1 later than particle 1 by 10 TDC channels, but comes into S3 earlier than particle 1 by 13 channels as:

$$\begin{aligned} < x^2 > - < x^1 > &= 10\ channels \\ < y^2 > - < y^1 > &= -13\ channels \end{aligned}$$

Therefore, the time of flight between S1 and S3 for particle 2 was shorter than that for particle 1 by 23 channels, or 2.3 nsec. The time-of-flight difference for the other particle pair can be calculated similarly as shown in Table A.1. At $T_{\pi^-} = 164$ MeV the measured time of flight differences agree well with the values calculated from the momenta as shown in Tabletable:trf12.

The pion fraction (f_{π^-}) can be calculated from the sum of the particles in the individual clusters as:

$$f_{\pi^-} = \frac{sum\ of\ particle1's}{sum\ of\ particle1,\ 2,\ and\ 3's.} = 73\% . \tag{A.1}$$

This is not the end of the story, however. 28% of the pions decay on average in flight from S1 to S3 as calculated by:

$$I = I_0 e^{-\frac{xm}{p\tau}}, \tag{A.2}$$

where

I is the number of π^-'s at the S3 position,

I_0 is the number of π^-'s at the S1 position,

x is the distance between S1 and S3 (5 m),

m is the pion mass,

p is the pion momentum,

τ is the pion life time.

Some of the decay muons are intercepted by S3. A Monte Carlo code was written to calculate the likelihood of such interception. In the code, a π^- decayed into a μ^- and a ν_μ isotropically in the rest frame of the π^-. It was calculated that for 9% of the the pions in flight, their decay μ^-'s were intercepted by S3 at T_{π^-}= 164 MeV. Such events would show up as pion events smearing the π^- cluster in Figure A-2, since decay muons would travel faster or slower than the original pions depending on their decay directions with respect to the pion momentum. The remainder of the decay muons would not show up in the figure. The pion fraction calculated in Equation (A.1) had to be corrected for this effect to give:

$$f_{\pi^-}^{164\,MeV} = 76\,\% \,.$$

When averaged over several runs the pion fraction was measured to be:

$$< f_{\pi^-}^{164\,MeV} >= 76 \pm 2\,\%.$$

The uncertainty here was evaluated from the deviation of the measurements from different runs and can be attributed to imperfect cluster separations.

In Figure A-3 is shown a two dimensional histogram of S1 and S3 TDC values at T_{π^-}= 263 MeV. Here only two clusters of points are seen, corresponding to the pions and electrons. The time-of-flight difference only between the pions and electrons (1.1 nsec) was long enough to form separate clusters and the muons were not distinguishable but included in the pion and the electron clusters. However the muon fraction can be estimated as:

$$\begin{aligned} f_{\mu^-}^{263\,MeV} &= f_{\mu^-}^{164\,MeV} \times \frac{1-\left(\frac{I}{I_0}\right)_{263\,MeV}}{1-\left(\frac{I}{I_0}\right)_{164\,MeV}} \\ &= (1.7\%)\left(\frac{0.665}{0.785}\right) \qquad \text{(A.3)} \\ &= 1.4\%\,, \qquad \text{(A.4)} \end{aligned}$$

where

$f_{\mu^-}^{164\,MeV}$ is the muon fraction calculated from Figure A-2,

I is the number of pions at the position of S1 ($x = 23\,m$),

I_0 is the number of pions at the A2 target ($x = 0\,m$).

This is a small fraction and was thus ignored.

The measured time-of-flight difference between the pion and the electron clusters agrees with the prediction as shown in Table A.1. After the pion decay in flight from S1 to S3 is appropriately accounted for, the pion fraction is given as:

$$f_{\pi^-}^{263\ MeV} = 93 \pm 3\ \% \ .$$

The 3% uncertainty came from adding the uncertainty from ignoring the muons (1.4%) and the uncertainty from the cluster separation (2%) in quadrature.

At $T_{\pi^-} = 371$ MeV only one cluster is seen. The time-of-flight difference between the pions and the electrons would have been 0.8 nsec and would be barely enough to form two clusters if there were any electrons. Therefore we conclude that the pion fraction here is 100%.

The pion fraction measurements reported here are consistent with the values quoted in the LAMPF User Handbook[46].

Appendix B

The π^0 Decay

The decay of the π^0 is isotropic in its rest frame. By the relativistic transformation,

$$E_1 = \gamma(E_1^* + \vec{\beta} \cdot \vec{P_1^*}), \tag{B.1}$$

$$E_2 = \gamma(E_2^* + \vec{\beta} \cdot \vec{P_2^*}), \tag{B.2}$$

$$c \equiv 1. \tag{B.3}$$

where

$\vec{\beta}$ is in the direction of the π^0 lab momentum.

E_1, E_2 are the energies of the decay photons in the lab frame.

E_1^*, E_2^* and $\vec{P_1^*}$, $\vec{P_2^*}$ are the energies and momenta of the decay photons in the π^0 rest frame.

Since the photon is massless,

$$E_1^* = E_2^* = |\vec{P_1^*}| = |\vec{P_2^*}|. \tag{B.4}$$

Now we have,

$$E_1 = \gamma(E_1^* + \beta \vec{P_1^*} cos\theta^*), \tag{B.5}$$

$$E_2 = \gamma(E_1^* - \beta \vec{P_1^*} cos\theta^*). \tag{B.6}$$

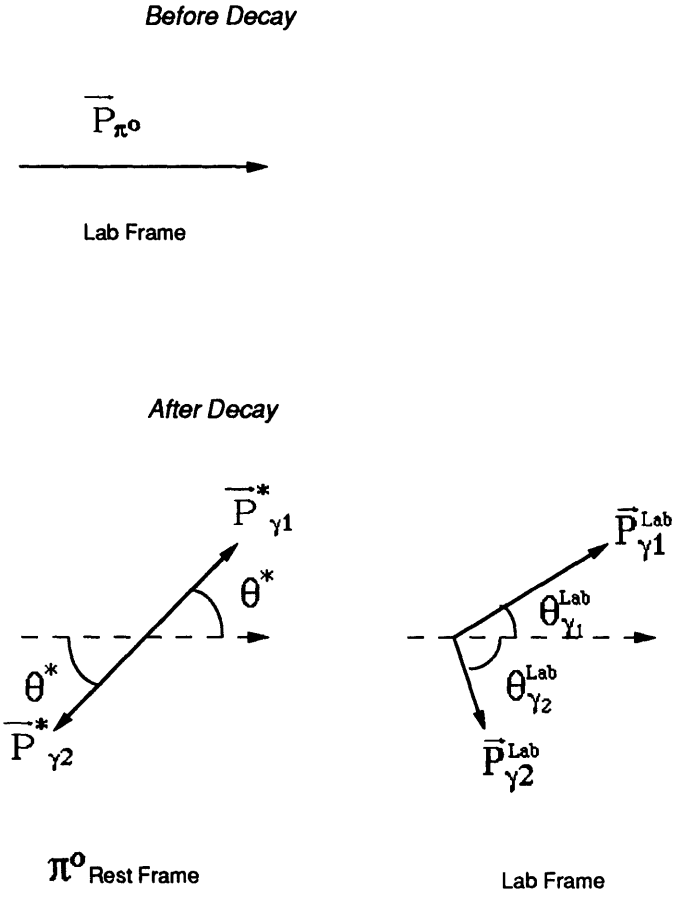

Figure B-1: The π^0 decay

X was defined previously as:

$$x \equiv \frac{E_1 - E_2}{E_1 + E_2}. \tag{B.7}$$

Now,

$$x = \frac{E_1 - E_2}{E_1 + E_2} = \beta cos\theta^*. \tag{B.8}$$

where

θ^* is the polar angle in the π^0 rest frame as seen in Figure B-1.

An isotropic distribution in the π^0 rest frame means that $cos\theta^*$ is uniformly distributed between -1 and 1. And this means that x is distributed uniformly between $-\beta$ and β.

Appendix C

Target Assay

The small amount of hydrogen contained in the CD_2 targets was assayed and the results are shown in Table C.1.

The Burman target was assayed using an X-ray scan[47][48].

The Matthews and Morris targets were assayed by using a pion elastic scattering reaction. The two CD_2 targets were placed in the 400 MeV π^+ beam at LAMPF. CH_2 and C targets with known density were also used for comparison with the CD_2 target and for background subtraction, respectively. The LAMPF Large Acceptance Spectrometer (LAS) was stationed at 40 degrees to detect the π^+'s elastically scattered from the nucleons in the target With the CD_2 target, after subtracting the π^+yield from the carbon, the following elastic scattering reactions were possible at the spectrometer setting. First, from the nucleons bound in the

Owner	Total Areal Density	p in CD_2	Diameter
J. Matthews	$1.047 g/cm^2(\pm 0.7\%)$	$.0034 g/cm^2(\pm 46\%)$	1.5 inches
C. Morris	$1.006 g/cm^2(\pm 0.3\%)$	$.0043 g/cm^2(\pm 30\%)$	1.5 inches
R. Burman	$1.054 g/cm^2(\pm 1.4\%)$	$.0022 g/cm^2(\pm 3\%)$	2.5 inches

Table C.1: The CD_2 target hydrogen contents

deuteron nuclei,

$$\begin{aligned} \pi^+ + p &\rightarrow \pi^+ + p \\ \pi^+ + n &\rightarrow \pi^+ + n. \end{aligned} \tag{C.1}$$

Second, from the protons constituting the hydrogen nuclei,

$$\pi^+ + p \rightarrow \pi^+ + p. \tag{C.2}$$

With the CH_2 target the net π^+yield after the carbon yield subtraction was only due to the Reaction C.2.

The net π^+energy spectrum obtained with the CD_2 target was compared with that obtained with the CH_2 target. The net π^+energy spectrum with the CD_2 target had a sharp peak due to Reaction C.2 riding on top of a peak with the same centroid but broadened by the nucleon motion in the deuteron (Reaction C.1). The sharp peak was fitted based on the the peak shape obtained from the π^+p elastic scattering with the CH_2 target.

From integrating the area under the sharp and the broad peaks separately in the net π^+energy spectrum with the CD_2 target, the π^+ yields from the the hydrogen and the deuteron in the CD_2 target respectively were measured. When compared against the known cross section values for the Reaction C.1 and C.2 obtained from the phase shift calculation[10], the values in the table above were obtained.

Appendix D

Radiation Effects on the CsI Crystals

Here we calculate the radiation dosage that the in-beam crystals received during the forward angle measurements in which the detector was in the beam.

There were four crystals in the neighborhood of the beam path, but we assume that only two took all the hits for the worst case. There were three beam energy settings during our in-beam runs, from 164 to 263 and 371 MeV. At 371 MeV, the π^- 's are minimum ionizing and the energy deposit would be (2 MeV)/(g/cm^2). With the CsI density of 4.5 g/cm^3, the total energy deposit in a crystal would be

$$2\frac{MeV}{g/cm^2} \times 4.5\frac{MeV}{g/cm^3} \times 12\, inches = 270 MeV. \tag{D.1}$$

The π^- 's would be exiting the crystal with 100 MeV of energy at which point they would still be minimum ionizing. At 164 and 263 MeV, all the energy would be deposited in the crystal and the π^- 's would stop.

The in-beam runs lasted for 51 hours and the average beam flux was 20 kHz. So the total energy deposited into two crystals by the beam particles per unit crystal volume is

$$\begin{aligned} &\frac{20\, kHz \times 51\, hrs \times 270\, MeV}{2 \times (4 \times 4 \times 12\, inches^3 \times 4.5 g/cm^3)} = \\ &= 5.6 \times 10^{-6}\, Joule/g\, \frac{100\, Rad}{Joule/kg} \\ &= .56\, Rad. \end{aligned} \tag{D.2}$$

This is indeed a very modest dose compared to kRads that the crystals in [35] were tested with and still not damaged.

Appendix E

Pion Induced Pion Production

At the higher energies of our experiment (263 and 371 MeV) in addition to the SCX peaks, much smaller peaks were seen at the lower energy sides in the π^0 energy spectra. An example is shown in Figure E-1. From kinematic considerations, we speculated that they might result from PIPP (Pion Induced Pion Production) and calculated the yield due to such peaks.

Since we were detecting only π^0 's in our experiment, the following two PIPP reactions were possible. Here we assume the dominance of quasifree production for the PIPP reaction in the deuteron[49].

$$\begin{aligned} \pi^- + p &\rightarrow \pi^0 + \pi^0 + n \\ \pi^- + p &\rightarrow \pi^0 + \pi^- + p \end{aligned}$$

We considered the diagram shown in Figure E-2 for the reactions. The three final state particles were considered to be products of an isotropic decay in the rest frame of the intermediate particle with the total mass equivalent to the total energy of the system. Figure E-3 shows a histogram of the π^0 's from such a process as a function of the π^0 energy within the π^0 scattering angle range that was covered in a typical detector set-up. The two arrows correspond to the minimum and the maximum π^0 energy kinematically allowed in the PIPP reaction. They are the same arrows that were shown in Figure E-1 that corresponded to the integration limit for "the small peak" cross section calculation.

The result of the small peak cross section calculation is shown in Figure E-4 and Figure E-5. The detector acceptance in each calculation was generated from the detector Monte Carlo

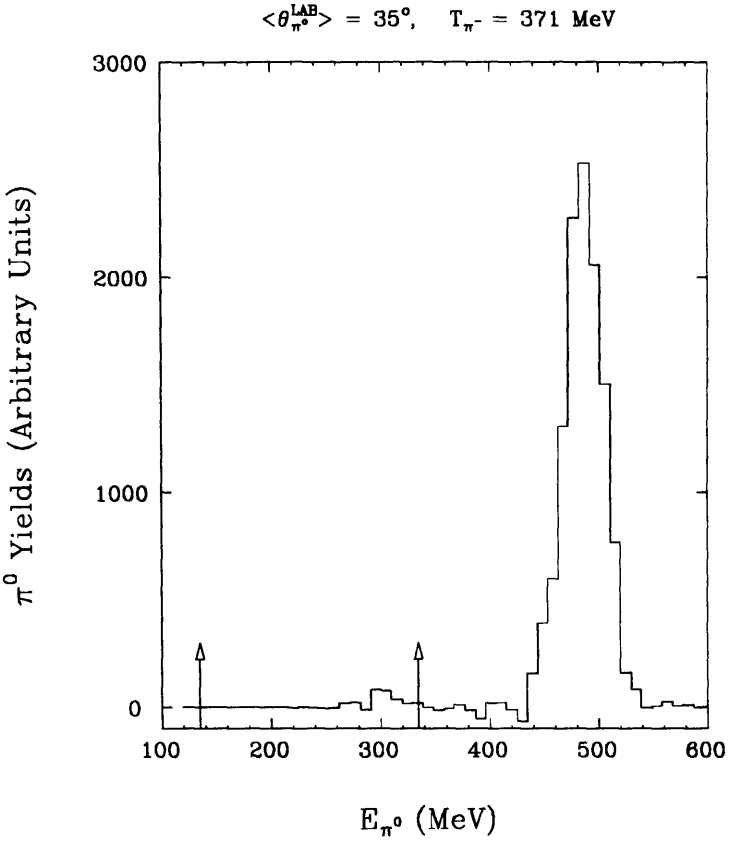

Figure E-1: Net π^0 energy spectrum from proton SCX.

Figure E-2: A Feynman diagram for the PIPP reaction.

code. The dashed line in the figure corresponds to the known PIPP total cross section assuming a constant angular distribution of the cross section. These lines were used because only the total cross section measurements were available[50]. The agreement between the cross section from the "small peaks" and the known cross section is acceptable within the large error bars. Therefore we conclude that the "small peaks" are due to PIPP.

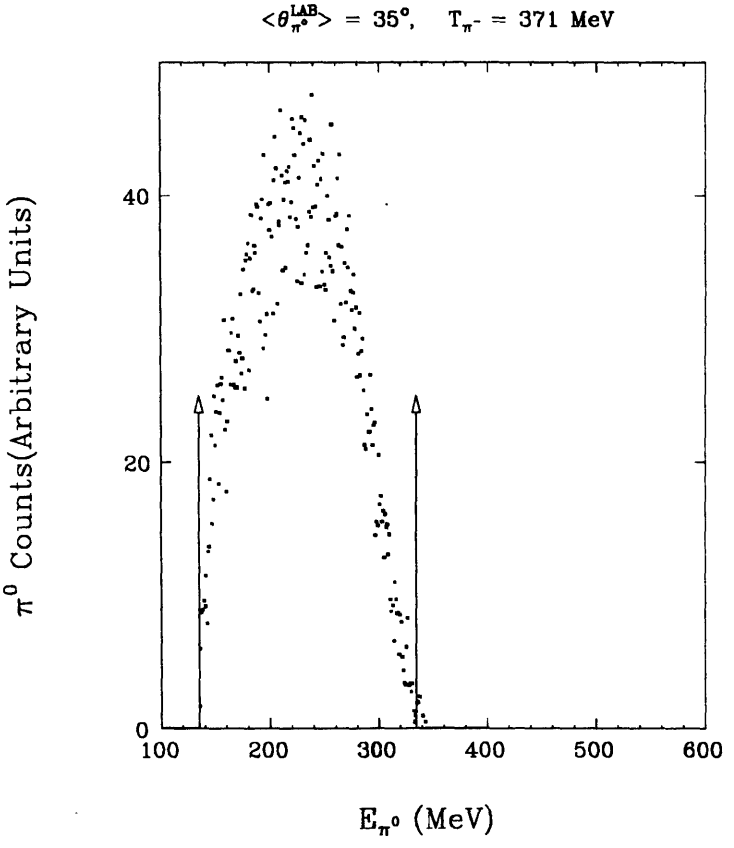

Figure E-3: Distribution of the decay π^0 's in the energy space.

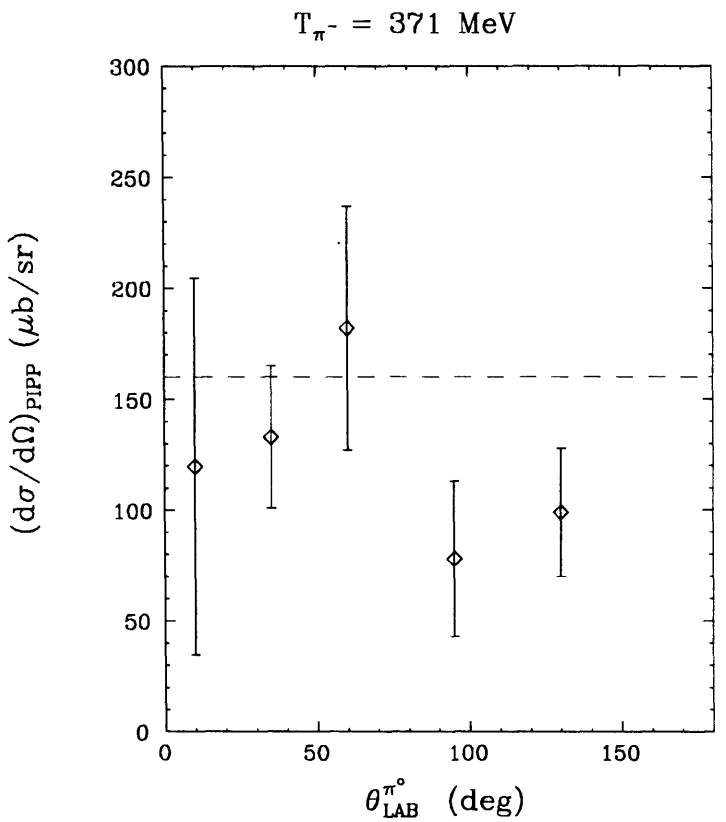

Figure E-4: A comparison of the extracted PIPP cross section to the known cross section at T_{π^-}=371MeV.

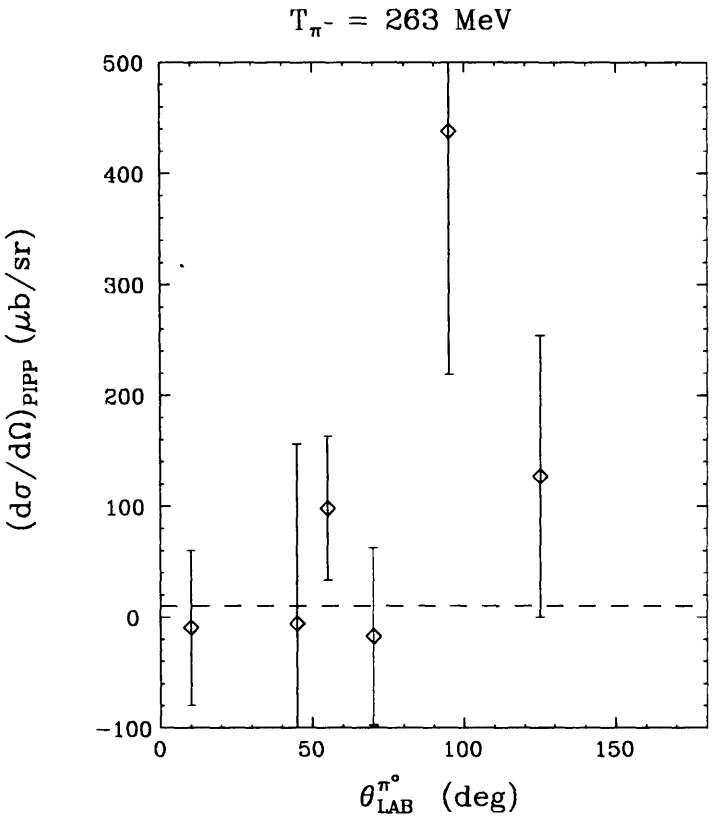

Figure E-5: A comparison of the extracted PIPP cross section to the known cross section at T_{π^-}=263MeV.

Appendix F

Calculation of the Total π^0 Yield

At a given energy and angle set-up, sets of runs were repeated, where each set contained runs with the CD_2, CH_2 and C targets. This was done to distribute any systematic effect such as room temperature change, beam position etc., more evenly among the runs with different targets.

For CH_2 runs the total net SCX yield from the protons was determined as follows:

$$\left(\iint Yield_p^{signal} dE_{\pi^0} d\theta_{\pi^0}\right)_{Total} =$$
$$\sum_{\mathrm{i}=1}^{CH_2\ runs} \left(\iint Yield^{CH_2,\mathrm{ith}\ run} \frac{1}{Live\ Frac^{CH_2,\mathrm{ith}\ run}} dE_{\pi^0} d\theta_{\pi^o}\right)$$
$$-\left\{\sum_{\mathrm{k}=1}^{C\ runs} \left(\iint Yield^{C,\mathrm{kth}\ run} \frac{1}{Live\ Frac^{C,\mathrm{kth}\ run}} dE_{\pi^0} d\theta_{\pi^o}\right)\right\} \left[\frac{N_{\pi^-}^{CH_2\ runs}}{N_{\pi^-}^{C\ runs}} \frac{n_C\ in\ CH_2 target}{n_C\ in\ C\ target}\right]. \tag{F.1}$$

where

$N_{\pi^-}^{CH_2\ runs}$ is the total number of π^- 's that entered the target in all the runs with the CH_2 target.

n_C is the number of carbon nuclei per cm^2 in a target.

For CD_2 runs the total net SCX yield from the deuterons was determined by

$$\left(\iint Yield_d^{signal} dE_{\pi^0} d\theta_{\pi^0}\right)_{Total} =$$
$$\sum_{i=1}^{CD_2\ runs} \left(\iint Yield^{CD_2,\,ith\,run} \frac{1}{Live\ Frac^{CD_2,ith\,run}} dE_{\pi^0} d\theta_{\pi^o}\right)$$
$$- \left\{\sum_{k=1}^{C\ runs} \left(\iint Yield^{C,\,kth\,run} \frac{1}{Live\ Frac^{C,\,kth\,run}} dE_{\pi^0} d\theta_{\pi^o}\right)\right\} \left[\frac{N_{\pi^-}^{CD_2\ runs}}{N_{\pi^-}^{C\ runs}} \frac{n_C\ in\ CD_2 target}{n_C\ in\ C\ target}\right]$$
$$- \left(\iint Yield_p^{signal} dE_{\pi^0} d\theta_{\pi^0}\right)_{Total} \left[\frac{N_{\pi^-}^{CD_2\ runs}}{N_{\pi^-}^{CH_2\ runs}} \frac{n_C\ in\ CD_2 target}{n_C\ in\ CH_2\ target}\right]. \qquad \text{(F.2)}$$

Appendix G

Calculation of the Ratio of the Cross Sections

$$R = \frac{\left(\frac{d\sigma}{d\Omega}\right)_d}{\left(\frac{d\sigma}{d\Omega}\right)_p} = \frac{\left[\iint Yield_d^{signal} dE d\theta_{\pi^o}\right]_{Total}}{\left[\iint Yield_p^{signal} dE d\theta_{\pi^o}\right]_{Total}} \frac{N_{\pi^-}^{CH_2\, runs}}{N_{\pi^-}^{CD_2\, runs}} \frac{n_p}{n_d} \frac{d\Omega_p}{d\Omega_d}. \tag{G.1}$$

In the above equation, R was calculated from the combination of all the runs with CD_2, CH_2, and C targets in a given detector set up angle and π^- energy. In the calculation the ratio of the detector solid angles for the proton runs and the deuteron runs was assumed to be unity for the reasons explained in Chapter 4.

For most of the time in our experiment, for a given π^0 angular bin there were two or three corresponding detector configurations whose angular range included that angular bin. The above ratios (R's) from each detector set up configuration were then added according to the formula below.

$$\begin{aligned} \langle R \rangle &= \left\langle \frac{\left(\frac{d\sigma}{d\Omega}\right)_d}{\left(\frac{d\sigma}{d\Omega}\right)_p} \right\rangle \\ &= \frac{\sum_{i=1}^{number\ of\ set\ ups} \left(\frac{R_{ith\ set\ up}}{\sigma_i{}^2}\right)}{\sum_{i=1}^{number\ of\ set\ ups} \left(\frac{1}{\sigma_i{}^2}\right)}, \end{aligned} \tag{G.2}$$

where

σ_i was the uncertainty in R_i.

The uncertainty in R was

$$\sigma^2\langle R\rangle = \frac{1}{\sum_{i=1}^{number\ of\ set\ ups}\left(\frac{1}{\sigma_i{}^2}\right)}. \tag{G.3}$$

Appendix H

Uncertainty due to the Detector Set-Up

Here we investigate any systematic uncertainty stemming from the changes of the detector set-up configurations. Since a given π^0 angular bin was covered by more than one detector set-up configuration, the extent of the overlap or the deviation among the data points from the different set-ups for the same π^0 angle would serve as an indication of any systematic error introduced.

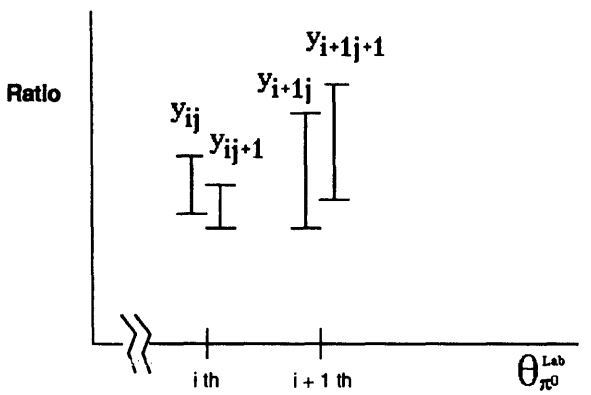

Figure H-1: The ratio of the deuteron to proton SCX

Shown in Figure H-1 is a simplified version of the plots previously shown in Figure 4-17 ~ Figure 4-19.

In Figure H-1 the index i runs over π^0 angular bins ($5^o \sim 145^0$ in steps of 10^0) at a given π^- energy while the index j runs over number of different detector set-up configurations at a given angular bin.

If the deviations among the data points (ratios of the deuteron and the proton SCX) at a given i exceed the statistical uncertainty, then the excess deviation can be attributed to a systematic error arising from the changes in the detector set-up configurations. We do this comparison using all the data points in a given π^- energy.

In an angular bin the average statistical variance of the data is given by

$$(\sigma_i)^2 = \frac{1}{\sum_{j=1}^{detector\ set\ ups} \frac{1}{(\sigma_{ij})^2}}, \tag{H.1}$$

where

σ_{ij} is the statistical uncertainty of r_{ij}.

The statistical variance averaged over all the angular bins in a given π^- energy is given by

$$\sigma^2 = \frac{\sum_{i=1}^{\pi^0\ angles} \sigma_i^2}{\sum_{i=1}^{\pi^0\ angles} 1}. \tag{H.2}$$

The deviation among the data points from different detector set-ups in a given angular bin is

$$(\sigma_i^{dev})^2 = \frac{\sum_{j=1}^{detector\ set\ ups} \frac{|\bar{r_i} - r_{ij}|}{\bar{r_i}(\sigma_{ij})^2}}{\sum_{j=1}^{detector\ set\ ups} \frac{1}{(\sigma_{ij})^2}}, \tag{H.3}$$

where

$$\bar{r_i} = \frac{\sum_{j=1}^{detector\ set\ ups} \frac{r_{ij}}{(\sigma_{ij})^2}}{\sum_{j=1}^{detector\ set\ ups} \frac{1}{(\sigma_{ij})^2}}. \tag{H.4}$$

The deviation averaged over the angular bins at a given energy is calculated as follows:

$$(\sigma^{dev})^2 = \frac{\sum_{i=1}^{\pi^0\ angles} (\sigma_i^{dev})^2}{\sum_{i=1}^{\pi^0\ angles} 1}. \tag{H.5}$$

T_{π^-}	σ	σ^{dev}
164 MeV	(5.0 ± 1.0) %	(7.3 ± 1.4) %
263 MeV	(5.7 ± 1.2) %	(8.8 ± 1.7) %
371 MeV	(14.6 ± 2.8) %	(14.3 ± 2.8) %

Table H.1: Uncertainty due to the set up change

In table H.1 is shown the calculated values for σ and σ^{dev} for the three energies in our experiment. The data points were assumed to follow a Gaussian distribution and the uncertainties in σ and σ^{dev} were estimated as follows:

$$\text{uncertainty in } \sigma = \frac{\sigma}{\sqrt{2(n-1)}}, \tag{H.6}$$

$$\text{uncertainty in } \sigma^{dev} = \frac{\sigma^{dev}}{\sqrt{2(n-1)}}, \tag{H.7}$$

where n is the number of contributing data points at a given energy.

The σ's and σ^{dev}'s agree with each other within their uncertainties at all three energies. Therefore the effect of changing the detector configurations on the determination of the cross section was negligible.

Appendix I

Table for the Cross Sections

Listed here are the singly and the doubly differential cross section values. All quantities are expressed in the "lab" frame.

$d(\pi^-,\pi^0)nn$					
T_{π^-} = 164 MeV		T_{π^-} = 263 MeV		T_{π^-} = 371 MeV	
θ_{π^0} (°)	$d\sigma/d\Omega$ mb/sr	θ_{π^0} (°)	$d\sigma/d\Omega$ mb/sr	θ_{π^0} (°)	$d\sigma/d\Omega$ mb/sr
5	1.04 ± 0.16	5	1.69 ± 0.22	5	2.38 ± 0.31
15	2.00 ± 0.23	15	3.50 ± 0.37	15	3.86 ± 0.42
25	2.61 ± 0.29	25	4.38 ± 0.35	25	3.75 ± 0.30
35	2.94 ± 0.25	35	3.69 ± 0.25	35	2.89 ± 0.27
45	3.07 ± 0.33	45	2.79 ± 0.23	45	1.68 ± 0.15
55	2.27 ± 0.21	55	1.72 ± 0.12	55	1.08 ± 0.13
65	1.72 ± 0.15	65	1.09 ± 0.09	65	0.50 ± 0.07
75	1.65 ± 0.15	75	0.74 ± 0.07	75	0.33 ± 0.06
85	1.75 ± 0.21	85	0.67 ± 0.07	85	0.27 ± 0.06
95	1.94 ± 0.17	95	0.65 ± 0.08	95	0.28 ± 0.06
105	2.16 ± 0.19	105	0.64 ± 0.06	105	0.16 ± 0.03
115	2.39 ± 0.25	115	0.58 ± 0.06	115	0.11 ± 0.03
125	2.54 ± 0.29	125	0.68 ± 0.08	125	0.09 ± 0.02
135	3.03 ± 0.38	135	0.75 ± 0.09	135	0.08 ± 0.02
145	3.10 ± 0.58	145	0.82 ± 0.22	145	0.07 ± 0.02

Table I.1: Table of the singly differential cross sections for deuteron SCX reaction. The errors reflect the total uncertainties.

$d(\pi^-,\pi^0)nn$					
T_{π^-} = 164 MeV		T_{π^-} = 263 MeV		T_{π^-} = 371 MeV	
θ_{π^0} (°)	$d\sigma/d\Omega$ mb/sr	θ_{π^0} (°)	$d\sigma/d\Omega$ mb/sr	θ_{π^0} (°)	$d\sigma/d\Omega$ mb/sr
5	1.04 ± 0.12	5	1.69 ± 0.14	5	2.38 ± 0.21
15	2.00 ± 0.11	15	3.50 ± 0.13	15	3.86 ± 0.18
25	2.61 ± 0.12	25	4.38 ± 0.13	25	3.75 ± 0.14
35	2.94 ± 0.14	35	3.69 ± 0.11	35	2.89 ± 0.12
45	3.07 ± 0.13	45	2.79 ± 0.09	45	1.68 ± 0.09
55	2.27 ± 0.10	55	1.72 ± 0.07	55	1.08 ± 0.08
65	1.72 ± 0.08	65	1.09 ± 0.06	65	0.50 ± 0.05
75	1.65 ± 0.09	75	0.74 ± 0.05	75	0.33 ± 0.05
85	1.75 ± 0.12	85	0.67 ± 0.05	85	0.27 ± 0.06
95	1.94 ± 0.10	95	0.65 ± 0.06	95	0.28 ± 0.05
105	2.16 ± 0.10	105	0.64 ± 0.04	105	0.16 ± 0.03
115	2.39 ± 0.13	115	0.58 ± 0.04	115	0.11 ± 0.03
125	2.54 ± 0.14	125	0.68 ± 0.05	125	0.09 ± 0.02
135	3.03 ± 0.22	135	0.75 ± 0.06	135	0.08 ± 0.02
145	3.10 ± 0.49	145	0.82 ± 0.21	145	0.07 ± 0.02

Table I.2: Table of the singly differential cross sections for deuteron SCX reaction. The errors reflect the statistical uncertainties only.

$d(\pi^-, \pi^0)nn$, $T_{\pi^-} = 164$ MeV							
$\theta = 5°$		$\theta = 15°$		$\theta = 25°$		$\theta = 35°$	
T_{π^0} MeV	$d^2\sigma/d\Omega dT_{\pi^0}$ $\mu b/sr - MeV$	T_{π^0} MeV	$d^2\sigma/d\Omega dT_{\pi^0}$ $\mu b/sr - MeV$	T_{π^0} MeV	$d^2\sigma/d\Omega dT_{\pi^0}$ $\mu b/sr - MeV$	T_{π^0} MeV	$d^2\sigma/d\Omega dT_{\pi^0}$ $\mu b/sr - MeV$
100	13.0 ± 5.6	100	6.3 ± 2.6	100	-1.6 ± 2.8	50	-7.8 ± 9.4
110	2.1 ± 5.2	110	3.2 ± 2.2	110	-0.8 ± 2.5	60	3.2 ± 5.8
120	6.9 ± 4.2	120	-0.9 ± 2.9	120	3.9 ± 2.8	70	-8.8 ± 11.4
130	8.8 ± 6.3	130	11.0 ± 3.4	130	9.1 ± 3.6	80	-3.1 ± 6.1
140	7.2 ± 5.6	140	4.9 ± 3.8	140	20.0 ± 4.0	90	-7.8 ± 5.1
150	12.0 ± 5.8	150	24.0 ± 4.4	150	38.0 ± 4.6	100	2.8 ± 4.1
160	16.0 ± 6.2	160	46.0 ± 4.8	160	82.0 ± 4.6	110	-0.2 ± 4.6
170	37.0 ± 5.1	170	75.0 ± 4.2	170	84.0 ± 4.0	120	11.0 ± 4.4
180	9.0 ± 3.8	180	21.0 ± 2.1	180	15.0 ± 1.7	130	26.0 ± 4.9
190	-0.1 ± 2.2	190	6.4 ± 1.4	190	4.3 ± 0.9	140	47.0 ± 6.3
200	1.3 ± 2.0	200	2.4 ± 1.4	200	3.6 ± 0.8	150	100.0 ± 6.5
210	1.1 ± 1.9	210	0.6 ± 0.8	210	0.3 ± 0.6	160	89.0 ± 5.6
220	-0.2 ± 1.6	220	0.6 ± 1.0	220	0.9 ± 0.5	170	25.0 ± 2.6
230	1.1 ± 1.4	230	1.6 ± 0.8	230	0.9 ± 0.5	180	2.4 ± 1.1
240	1.4 ± 1.5	240	0.3 ± 0.7	240	0.2 ± 0.5	190	0.6 ± 1.0
250	1.4 ± 1.2	250	1.0 ± 0.7	250	0.6 ± 0.4	200	1.1 ± 0.8
260	1.2 ± 1.2	260	0.0 ± 0.8	260	1.0 ± 0.3	210	0.3 ± 0.7
						220	0.5 ± 0.7
						230	0.6 ± 0.9
						240	0.0 ± 0.8
						250	0.6 ± 0.7
						260	1.7 ± 0.8

Table I.3: Table of the doubly differential cross sections for deuteron SCX reaction at $T_{\pi^-} =$ 164 MeV. The errors reflect the statistical uncertainties only.

$d(\pi^-,\pi^0)nn$, T_{π^-} = 164 MeV							
$\theta = 45°$		$\theta = 55°$		$\theta = 65°$		$\theta = 75°$	
T_{π^0} MeV	$d^2\sigma/d\Omega dT_{\pi^0}$ $\mu b/sr - MeV$	T_{π^0} MeV	$d^2\sigma/d\Omega dT_{\pi^0}$ $\mu b/sr - MeV$	T_{π^0} MeV	$d^2\sigma/d\Omega dT_{\pi^0}$ $\mu b/sr - MeV$	T_{π^0} MeV	$d^2\sigma/d\Omega dT_{\pi^0}$ $\mu b/sr - MeV$
50	-4.3 ± 9.6	50	2.0 ± 3.1	50	8.6 ± 7.9	50	3.6 ± 4.5
60	-12.0 ± 12.3	60	3.4 ± 3.1	60	5.9 ± 6.1	60	-4.9 ± 4.8
70	-1.5 ± 6.2	70	-5.6 ± 5.8	70	2.0 ± 5.2	70	0.8 ± 4.9
80	-1.0 ± 4.0	80	2.5 ± 3.8	80	13.0 ± 4.6	80	10.0 ± 4.7
90	-1.5 ± 3.2	90	6.9 ± 3.0	90	10.0 ± 4.2	90	20.0 ± 4.3
100	7.0 ± 3.2	100	3.0 ± 2.6	100	19.0 ± 4.2	100	33.0 ± 4.0
110	15.0 ± 3.5	110	10.0 ± 3.4	110	37.0 ± 4.4	110	48.0 ± 4.0
120	16.0 ± 4.0	120	17.0 ± 3.7	120	52.0 ± 4.1	120	35.0 ± 3.2
130	39.0 ± 4.3	130	49.0 ± 4.0	130	33.0 ± 3.0	130	15.0 ± 2.0
140	100.0 ± 5.6	140	88.0 ± 4.4	140	4.1 ± 1.2	140	1.7 ± 1.0
150	97.0 ± 5.0	150	45.0 ± 3.1	150	1.2 ± 0.6	150	0.1 ± 0.3
160	30.0 ± 2.8	160	8.6 ± 1.5	160	0.1 ± 0.5	160	0.1 ± 0.3
170	2.8 ± 0.9	170	0.5 ± 0.4	170	0.2 ± 0.4	170	0.0 ± 0.3
180	0.2 ± 0.5	180	0.1 ± 0.4	180	0.0 ± 0.7	180	0.0 ± 0.9
190	0.0 ± 0.5	190	-0.2 ± 0.4	190	0.0 ± 0.7	190	0.0 ± 0.9

Table I.4: Table of the doubly differential cross sections for deuteron SCX reaction at T_{π^-} = 164 MeV. The errors reflect the statistical uncertainties only.

$d(\pi^-,\pi^0)nn$, T_{π^-} = 164 MeV							
$\theta = 85°$		$\theta = 95°$		$\theta = 105°$		$\theta = 115°$	
T_{π^0} MeV	$d^2\sigma/d\Omega dT_{\pi^0}$ $\mu b/sr - MeV$	T_{π^0} MeV	$d^2\sigma/d\Omega dT_{\pi^0}$ $\mu b/sr - MeV$	T_{π^0} MeV	$d^2\sigma/d\Omega dT_{\pi^0}$ $\mu b/sr - MeV$	T_{π^0} MeV	$d^2\sigma/d\Omega dT_{\pi^0}$ $\mu b/sr - MeV$
50	8.0 ± 6.3	50	7.0 ± 5.1	50	6.1 ± 3.7	50	5.9 ± 4.4
60	1.5 ± 5.8	60	7.0 ± 4.6	60	8.3 ± 3.5	60	10.0 ± 4.6
70	1.0 ± 5.0	70	9.4 ± 4.4	70	23.0 ± 4.2	70	30.0 ± 5.6
80	23.0 ± 4.9	80	24.0 ± 4.2	80	33.0 ± 4.0	80	45.0 ± 4.9
90	45.0 ± 5.4	90	46.0 ± 4.2	90	58.0 ± 4.0	90	73.0 ± 5.1
100	52.0 ± 4.6	100	63.0 ± 3.9	100	57.0 ± 3.6	100	54.0 ± 4.5
110	38.0 ± 3.6	110	30.0 ± 2.7	110	24.0 ± 2.3	110	15.0 ± 2.7
120	12.0 ± 2.6	120	13.0 ± 2.0	120	5.8 ± 1.5	120	1.4 ± 1.8
130	0.5 ± 1.3	130	-0.8 ± 1.2	130	0.4 ± 0.9	130	-0.4 ± 1.3
140	1.1 ± 0.7	140	0.6 ± 0.5	140	-0.3 ± 0.5	140	-0.4 ± 0.8
150	0.0 ± 0.3	150	0.3 ± 0.3	150	0.5 ± 0.3	150	0.2 ± 0.4
160	0.0 ± 0.2	160	0.0 ± 0.2	160	0.1 ± 0.2	160	0.3 ± 0.2
170	0.0 ± 0.2	170	0.0 ± 0.2	170	0.0 ± 0.2	170	0.0 ± 0.2

Table I.5: Table of the doubly differential cross sections for deuteron SCX reaction at T_{π^-} = 164 MeV. The errors reflect the statistical uncertainties only.

$d(\pi^-,\pi^0)nn$, T_{π^-} = 164 MeV					
$\theta = 125°$		$\theta = 135°$		$\theta = 145°$	
T_{π^0} MeV	$d^2\sigma/d\Omega dT_{\pi^0}$ $\mu b/sr - MeV$	T_{π^0} MeV	$d^2\sigma/d\Omega dT_{\pi^0}$ $\mu b/sr - MeV$	T_{π^0} MeV	$d^2\sigma/d\Omega dT_{\pi^0}$ $\mu b/sr - MeV$
40	-2.2 ± 4.6	30	-7.0 ± 8.2	40	-61.0 ± 51.9
50	10.0 ± 4.9	40	6.2 ± 7.4	50	23.0 ± 22.6
60	19.0 ± 4.9	50	4.6 ± 5.5	60	27.0 ± 18.4
70	46.0 ± 5.6	60	20.0 ± 6.8	70	95.0 ± 21.8
80	54.0 ± 5.5	70	85.0 ± 9.0	80	82.0 ± 18.8
90	80.0 ± 4.9	80	85.0 ± 8.3	90	92.0 ± 14.1
100	42.0 ± 3.9	90	75.0 ± 6.8	100	20.0 ± 11.1
110	4.2 ± 2.3	100	31.0 ± 5.3	110	1.7 ± 6.3
120	2.0 ± 1.6	110	2.7 ± 3.2	120	0.9 ± 4.8
130	0.6 ± 1.2	120	0.1 ± 2.3	130	-2.8 ± 2.8
140	1.2 ± 0.7	130	-0.5 ± 1.8	140	3.2 ± 2.1
150	0.2 ± 0.3	140	0.3 ± 0.9	150	1.7 ± 1.6
160	0.0 ± 0.2	150	-0.7 ± 0.6	160	0.0 ± 1.5
170	0.0 ± 0.2	160	-0.2 ± 0.4	170	0.0 ± 1.4
180	0.0 ± 0.2	170	0.0 ± 0.4	180	0.0 ± 1.3

Table I.6: Table of the doubly differential cross sections for deuteron SCX reaction at T_{π^-} = 164 MeV. The errors reflect the statistical uncertainties only.

$d(\pi^-, \pi^0)nn$, $T_{\pi^-} = 263$ MeV							
$\theta = 5°$		$\theta = 15°$		$\theta = 25°$		$\theta = 35°$	
T_{π^0} MeV	$d^2\sigma/d\Omega dT_{\pi^0}$ $\mu b/sr - MeV$	T_{π^0} MeV	$d^2\sigma/d\Omega dT_{\pi^0}$ $\mu b/sr - MeV$	T_{π^0} MeV	$d^2\sigma/d\Omega dT_{\pi^0}$ $\mu b/sr - MeV$	T_{π^0} MeV	$d^2\sigma/d\Omega dT_{\pi^0}$ $\mu b/sr - MeV$
160	-3.1 ± 2.6	160	1.9 ± 1.7	60	0.0 ± 9.5	150	3.0 ± 5.8
170	-0.1 ± 2.9	170	0.8 ± 2.0	70	0.0 ± 15.1	160	7.1 ± 3.5
180	0.9 ± 2.8	180	-0.2 ± 1.9	80	0.0 ± 35.9	170	3.8 ± 3.8
190	3.3 ± 3.3	190	3.8 ± 1.9	90	-45.0 ± 93.5	180	2.9 ± 3.6
200	2.4 ± 4.1	200	-0.2 ± 2.5	100	7.6 ± 20.3	190	6.4 ± 3.1
210	4.9 ± 3.8	210	7.8 ± 2.3	110	-0.1 ± 11.4	200	1.4 ± 4.3
220	13.0 ± 4.0	220	4.9 ± 2.5	120	5.7 ± 7.9	210	17.0 ± 4.0
230	6.1 ± 5.3	230	18.0 ± 3.3	130	0.1 ± 8.3	220	21.0 ± 4.5
240	16.0 ± 5.1	240	29.0 ± 3.5	140	3.8 ± 6.3	230	55.0 ± 5.2
250	22.0 ± 5.7	250	56.0 ± 4.1	150	6.5 ± 5.7	240	67.0 ± 5.1
260	44.0 ± 6.4	260	110.0 ± 4.6	160	-0.5 ± 2.0	250	86.0 ± 4.7
270	36.0 ± 4.7	270	75.0 ± 3.3	170	4.2 ± 2.4	260	76.0 ± 4.2
280	18.0 ± 3.6	280	26.0 ± 2.1	180	3.3 ± 2.2	270	20.0 ± 2.1
290	7.8 ± 2.5	290	11.0 ± 1.4	190	4.1 ± 2.3	280	4.1 ± 1.0
300	1.8 ± 1.5	300	3.5 ± 1.0	200	12.0 ± 2.8	290	2.0 ± 0.5
310	1.7 ± 1.3	310	2.4 ± 0.9	210	3.6 ± 2.9	300	0.7 ± 0.4
320	-0.3 ± 1.3	320	2.0 ± 0.8	220	22.0 ± 3.2	310	-0.1 ± 0.2
330	1.2 ± 1.3	330	1.8 ± 0.8	230	51.0 ± 4.2	320	-0.2 ± 0.3
340	0.3 ± 0.9	340	0.0 ± 0.7	240	68.0 ± 4.6	330	-0.2 ± 0.3
350	0.4 ± 1.1	350	0.2 ± 0.7	250	110.0 ± 4.8	340	0.5 ± 0.3
				260	130.0 ± 4.5	350	-0.1 ± 0.2
				270	20.0 ± 1.7		
				280	9.8 ± 1.2		
				290	5.3 ± 0.9		
				300	2.6 ± 0.7		
				310	1.7 ± 0.5		
				320	0.9 ± 0.5		
				330	0.6 ± 0.5		
				340	1.2 ± 0.3		
				350	0.4 ± 0.3		
				360	0.0 ± 1.7		
				370	0.0 ± 1.7		

Table I.7: Table of the doubly differential cross sections for deuteron SCX reaction at $T_{\pi^-} =$ 263 MeV. The errors reflect the statistical uncertainties only.

$d(\pi^-,\pi^0)nn$, T_{π^-} = 263 MeV							
$\theta = 45°$		$\theta = 55°$		$\theta = 65°$		$\theta = 75°$	
T_{π^0} MeV	$d^2\sigma/d\Omega dT_{\pi^0}$ $\mu b/sr - MeV$	T_{π^0} MeV	$d^2\sigma/d\Omega dT_{\pi^0}$ $\mu b/sr - MeV$	T_{π^0} MeV	$d^2\sigma/d\Omega dT_{\pi^0}$ $\mu b/sr - MeV$	T_{π^0} MeV	$d^2\sigma/d\Omega dT_{\pi^0}$ $\mu b/sr - MeV$
60	0.1 ± 1.5	60	-0.2 ± 1.3	60	-0.1 ± 1.1	60	0.0 ± 4.8
70	-0.2 ± 2.6	70	0.0 ± 2.2	70	0.0 ± 3.6	70	-1.0 ± 1.8
80	2.3 ± 2.6	80	-5.4 ± 7.6	80	0.1 ± 6.1	80	2.0 ± 1.1
90	-1.1 ± 2.9	90	1.8 ± 5.3	90	0.2 ± 5.1	90	2.7 ± 1.3
100	5.4 ± 2.2	100	3.5 ± 2.7	100	11.0 ± 4.6	100	0.7 ± 1.5
110	0.5 ± 2.1	110	1.0 ± 1.9	110	1.5 ± 5.8	110	4.2 ± 1.3
120	-0.3 ± 1.6	120	1.2 ± 2.1	120	2.0 ± 3.5	120	3.4 ± 1.2
130	4.1 ± 1.9	130	-0.8 ± 2.6	130	-3.4 ± 3.5	130	2.2 ± 1.5
140	1.3 ± 1.7	140	4.0 ± 2.1	140	-2.4 ± 3.2	140	1.1 ± 1.4
150	3.2 ± 1.7	150	-1.0 ± 2.1	150	-0.4 ± 3.0	150	6.4 ± 1.4
160	1.4 ± 1.7	160	2.1 ± 2.0	160	5.5 ± 3.5	160	6.7 ± 1.4
170	4.3 ± 2.2	170	1.4 ± 2.5	170	7.8 ± 3.4	170	9.0 ± 1.6
180	6.5 ± 2.1	180	11.0 ± 2.3	180	7.1 ± 3.5	180	16.0 ± 1.5
190	15.0 ± 2.3	190	16.0 ± 2.5	190	15.0 ± 3.7	190	11.0 ± 1.4
200	26.0 ± 2.8	200	30.0 ± 3.0	200	29.0 ± 4.1	200	14.0 ± 1.4
210	42.0 ± 2.7	210	36.0 ± 2.7	210	24.0 ± 3.7	210	4.5 ± 1.0
220	61.0 ± 2.8	220	43.0 ± 2.5	220	17.0 ± 3.0	220	1.2 ± 0.8
230	77.0 ± 2.9	230	29.0 ± 2.2	230	8.3 ± 2.7	230	1.5 ± 0.7
240	33.0 ± 1.9	240	4.0 ± 1.4	240	-0.8 ± 1.8	240	0.1 ± 0.5
250	9.7 ± 1.2	250	0.8 ± 1.0	250	-0.1 ± 1.3	250	0.2 ± 0.3
260	1.4 ± 0.5	260	0.0 ± 0.5	260	-0.6 ± 0.8	260	-0.1 ± 0.2
270	0.1 ± 0.2	270	-0.1 ± 0.2	270	0.0 ± 0.5	270	0.0 ± 0.2
280	0.1 ± 0.1	280	0.0 ± 0.2	280	-0.2 ± 0.5	280	0.0 ± 0.2
290	0.1 ± 0.1	290	0.1 ± 0.2	290	0.0 ± 0.4	290	0.0 ± 0.2
300	0.0 ± 0.1	300	0.0 ± 0.1	300	0.0 ± 0.4	300	0.0 ± 0.2

Table I.8: Table of the doubly differential cross sections for deuteron SCX reaction at T_{π^-} = 263 MeV. The errors reflect the statistical uncertainties only.

$d(\pi^-,\pi^0)nn$, T_{π^-} = 263 MeV							
$\theta = 85°$		$\theta = 95°$		$\theta = 105°$		$\theta = 115°$	
T_{π^0} MeV	$d^2\sigma/d\Omega dT_{\pi^0}$ $\mu b/sr - MeV$	T_{π^0} MeV	$d^2\sigma/d\Omega dT_{\pi^0}$ $\mu b/sr - MeV$	T_{π^0} MeV	$d^2\sigma/d\Omega dT_{\pi^0}$ $\mu b/sr - MeV$	T_{π^0} MeV	$d^2\sigma/d\Omega dT_{\pi^0}$ $\mu b/sr - MeV$
60	0.3 ± 1.5	60	0.3 ± 1.7	60	2.1 ± 1.1	60	-1.4 ± 1.1
70	3.3 ± 1.7	70	0.7 ± 1.7	70	2.4 ± 1.5	70	3.2 ± 1.4
80	2.9 ± 1.5	80	1.4 ± 1.8	80	4.8 ± 1.5	80	-0.9 ± 1.3
90	2.8 ± 1.5	90	2.8 ± 1.8	90	1.7 ± 1.5	90	1.4 ± 1.3
100	2.2 ± 1.6	100	0.3 ± 2.2	100	2.0 ± 1.6	100	6.2 ± 1.5
110	2.1 ± 1.6	110	3.1 ± 1.8	110	4.7 ± 1.4	110	6.2 ± 1.3
120	2.9 ± 1.4	120	0.8 ± 1.8	120	7.8 ± 1.3	120	11.0 ± 1.2
130	5.4 ± 1.6	130	7.1 ± 2.0	130	15.0 ± 1.4	130	17.0 ± 1.2
140	8.4 ± 1.5	140	11.0 ± 1.6	140	14.0 ± 1.2	140	8.6 ± 0.9
150	9.9 ± 1.3	150	15.0 ± 1.6	150	9.3 ± 1.0	150	5.2 ± 0.7
160	12.0 ± 1.3	160	14.0 ± 1.4	160	5.6 ± 0.8	160	1.0 ± 0.6
170	15.0 ± 1.4	170	7.9 ± 1.3	170	3.6 ± 0.7	170	1.7 ± 0.5
180	9.0 ± 1.0	180	4.9 ± 1.0	180	0.4 ± 0.6	180	0.0 ± 0.3
190	5.2 ± 0.9	190	0.8 ± 0.9	190	0.3 ± 0.4	190	-0.2 ± 0.3
200	2.6 ± 0.8	200	0.3 ± 0.8	200	1.2 ± 0.4	200	-0.3 ± 0.3
210	1.0 ± 0.6	210	0.1 ± 0.5	210	-0.1 ± 0.3	210	-0.1 ± 0.2
220	0.7 ± 0.4	220	0.2 ± 0.4	220	0.0 ± 0.2	220	0.2 ± 0.1
230	-0.4 ± 0.4	230	0.0 ± 0.3	230	0.0 ± 0.2	230	0.0 ± 0.1
240	0.1 ± 0.2	240	-0.3 ± 0.2	240	0.1 ± 0.1	240	0.0 ± 0.1
250	0.1 ± 0.2	250	-0.1 ± 0.1	250	0.0 ± 0.1	250	0.0 ± 0.1
260	0.0 ± 0.1	260	0.0 ± 0.1	260	0.0 ± 0.1	260	0.0 ± 0.1

Table I.9: Table of the doubly differential cross sections for deuteron SCX reaction at T_{π^-} = 263 MeV. The errors reflect the statistical uncertainties only.

$d(\pi^-, \pi^0)nn$, $T_{\pi^-} = 263$ MeV					
$\theta = 125°$		$\theta = 135°$		$\theta = 145°$	
T_{π^0} MeV	$d^2\sigma/d\Omega dT_{\pi^0}$ $\mu b/sr - MeV$	T_{π^0} MeV	$d^2\sigma/d\Omega dT_{\pi^0}$ $\mu b/sr - MeV$	T_{π^0} MeV	$d^2\sigma/d\Omega dT_{\pi^0}$ $\mu b/sr - MeV$
60	1.3 ± 1.5	60	2.4 ± 1.5	60	-1.5 ± 3.2
70	3.1 ± 1.7	70	0.3 ± 2.0	70	7.4 ± 3.9
80	4.7 ± 1.6	80	4.9 ± 1.9	80	2.6 ± 3.4
90	3.7 ± 1.5	90	3.8 ± 2.0	90	13.0 ± 3.2
100	7.3 ± 1.6	100	16.0 ± 2.2	100	15.0 ± 3.4
110	11.0 ± 1.5	110	13.0 ± 1.7	110	11.0 ± 2.8
120	11.0 ± 1.3	120	16.0 ± 1.6	120	18.0 ± 2.4
130	13.0 ± 1.3	130	10.0 ± 1.5	130	10.0 ± 2.1
140	7.9 ± 0.9	140	5.6 ± 1.0	140	4.0 ± 1.4
150	3.7 ± 0.8	150	2.2 ± 0.8	150	1.2 ± 1.1
160	1.1 ± 0.6	160	0.9 ± 0.7	160	0.8 ± 0.8
170	0.3 ± 0.5	170	-0.4 ± 0.6	170	0.0 ± 0.7
180	-0.2 ± 0.4	180	0.5 ± 0.4	180	0.2 ± 0.4
190	0.1 ± 0.3	190	0.0 ± 0.4	190	-0.1 ± 0.4
200	0.1 ± 0.2	200	0.0 ± 0.3	200	0.3 ± 0.3
210	0.2 ± 0.2	210	0.0 ± 0.2	210	0.3 ± 0.3
220	0.0 ± 0.1	220	0.0 ± 0.2	220	-0.1 ± 0.3
230	-0.1 ± 0.1	230	0.0 ± 0.1	230	0.0 ± 0.2
240	0.1 ± 0.1	240	0.0 ± 0.1	240	0.0 ± 0.2
250	0.0 ± 0.1	250	0.0 ± 0.1	250	0.0 ± 0.2
260	0.0 ± 0.1	260	0.0 ± 0.1	260	0.0 ± 0.2
270	0.0 ± 0.1	270	0.0 ± 0.1	270	0.0 ± 0.2
280	0.0 ± 0.1	280	0.0 ± 0.1	280	0.0 ± 0.2

Table I.10: Table of the doubly differential cross sections for deuteron SCX reaction at $T_{\pi^-} = 263$ MeV. The errors reflect the statistical uncertainties only.

$d(\pi^-, \pi^0)nn$, $T_{\pi^-} = 371$ MeV							
$\theta = 5°$		$\theta = 15°$		$\theta = 25°$		$\theta = 35°$	
T_{π^0} MeV	$d^2\sigma/d\Omega dT_{\pi^0}$ $\mu b/sr - MeV$	T_{π^0} MeV	$d^2\sigma/d\Omega dT_{\pi^0}$ $\mu b/sr - MeV$	T_{π^0} MeV	$d^2\sigma/d\Omega dT_{\pi^0}$ $\mu b/sr - MeV$	T_{π^0} MeV	$d^2\sigma/d\Omega dT_{\pi^0}$ $\mu b/sr - MeV$
130	15.0 ± 9.3	130	1.8 ± 2.2	110	0.3 ± 6.9	110	5.2 ± 8.2
140	0.1 ± 7.4	140	-2.2 ± 2.8	120	0.4 ± 2.1	120	-2.3 ± 3.8
150	-2.7 ± 6.9	150	3.4 ± 3.1	130	2.2 ± 2.8	130	0.5 ± 2.0
160	5.8 ± 4.9	160	2.1 ± 2.6	140	3.3 ± 4.0	140	4.4 ± 2.4
170	11.0 ± 6.2	170	-0.5 ± 2.5	150	0.3 ± 2.9	150	-3.6 ± 2.4
180	3.0 ± 6.0	180	-2.7 ± 3.0	160	-3.0 ± 2.5	160	4.5 ± 1.7
190	4.3 ± 5.1	190	4.1 ± 2.5	170	-0.5 ± 2.7	170	4.4 ± 2.2
200	11.0 ± 4.3	200	7.1 ± 2.7	180	-1.4 ± 2.0	180	3.2 ± 2.0
210	9.2 ± 6.0	210	4.9 ± 3.0	190	0.8 ± 2.3	190	3.3 ± 1.8
220	6.8 ± 4.1	220	0.0 ± 2.5	200	1.8 ± 1.6	200	2.1 ± 1.7
230	4.1 ± 4.3	230	2.4 ± 2.4	210	-0.1 ± 2.0	210	2.9 ± 1.7
240	-1.9 ± 4.6	240	2.1 ± 3.0	220	1.6 ± 1.8	220	-0.6 ± 1.5
250	3.8 ± 4.3	250	2.1 ± 2.8	230	0.2 ± 1.7	230	1.4 ± 1.5
260	1.6 ± 3.4	260	2.9 ± 2.5	240	0.6 ± 2.1	240	1.1 ± 1.8
270	2.9 ± 3.7	270	5.6 ± 2.7	250	-0.3 ± 1.8	250	3.7 ± 1.7
280	-4.7 ± 4.5	280	0.1 ± 3.2	260	0.7 ± 1.8	260	2.8 ± 1.8
290	-2.7 ± 4.1	290	-0.6 ± 2.7	270	2.9 ± 2.0	270	5.6 ± 2.1
300	5.8 ± 4.3	300	3.1 ± 2.8	280	8.2 ± 2.5	280	7.2 ± 2.6
310	-2.3 ± 4.9	310	6.1 ± 4.1	290	2.1 ± 2.5	290	9.2 ± 2.5
320	9.6 ± 4.8	320	20.0 ± 3.9	300	14.0 ± 3.0	300	20.0 ± 2.8
330	0.1 ± 5.6	330	12.0 ± 4.5	310	20.0 ± 3.9	310	43.0 ± 3.4
340	8.8 ± 6.4	340	48.0 ± 5.5	320	21.0 ± 3.9	320	53.0 ± 3.2
350	14.0 ± 7.0	350	58.0 ± 5.6	330	48.0 ± 4.3	330	60.0 ± 3.2
360	33.0 ± 7.5	360	71.0 ± 5.5	340	90.0 ± 5.2	340	51.0 ± 3.1
370	53.0 ± 8.2	370	74.0 ± 5.1	350	81.0 ± 4.5	350	21.0 ± 2.0
380	30.0 ± 6.0	380	31.0 ± 3.1	360	57.0 ± 3.6	360	5.8 ± 1.3
390	19.0 ± 4.9	390	15.0 ± 2.1	370	24.0 ± 2.3	370	1.7 ± 0.7
400	16.0 ± 3.9	400	9.9 ± 1.9	380	1.2 ± 0.7	380	0.2 ± 0.1
410	18.0 ± 3.4	410	4.8 ± 1.7	390	0.6 ± 0.3	390	-0.1 ± 0.1
420	3.8 ± 3.0	420	3.8 ± 1.1	400	0.5 ± 0.4	400	0.0 ± 0.1
430	2.9 ± 2.4	430	1.0 ± 1.0	410	0.3 ± 0.2	410	-0.1 ± 0.1
440	1.4 ± 2.2	440	1.6 ± 1.2	420	0.5 ± 0.3	420	0.0 ± 0.1
450	1.1 ± 1.9	450	1.0 ± 1.0	430	0.1 ± 0.2	430	-0.1 ± 0.1
460	1.1 ± 2.3	460	0.9 ± 0.8	440	0.0 ± 0.2	440	0.0 ± 0.1
470	1.0 ± 1.2	470	0.8 ± 0.9	450	0.1 ± 0.2	450	0.0 ± 0.1
480	1.1 ± 1.6	480	0.1 ± 0.6	460	0.1 ± 0.2	460	0.0 ± 0.1
490	2.1 ± 1.9	490	1.0 ± 0.7	470	0.0 ± 0.2	470	0.1 ± 0.1
500	-0.5 ± 1.5	500	0.8 ± 0.5	480	0.6 ± 0.6	480	0.0 ± 2.1
510	1.0 ± 1.1	510	0.2 ± 0.4	490	-0.4 ± 0.6	490	0.0 ± 2.0
520	0.3 ± 1.4	520	0.3 ± 0.7	500	-0.7 ± 0.6	500	0.0 ± 2.0
530	0.5 ± 1.2	530	0.8 ± 0.6	510	0.4 ± 0.5	510	0.0 ± 1.9
540	1.0 ± 1.0	540	0.1 ± 0.4	520	-0.1 ± 0.5	520	0.0 ± 1.9
550	0.9 ± 0.9	550	0.3 ± 0.4	530	0.4 ± 0.5	530	0.0 ± 1.8
				540	0.2 ± 0.5	540	0.0 ± 1.8
				550	0.0 ± 0.5	550	0.0 ± 1.7

Table I.11: Table of the doubly differential cross sections for deuteron SCX reaction at $T_{\pi^-} =$ 371 MeV. The errors reflect the statistical uncertainties only.

$d(\pi^-,\pi^0)nn$, T_{π^-} = 371 MeV							
$\theta = 45°$		$\theta = 55°$		$\theta = 65°$		$\theta = 75°$	
T_{π^0} MeV	$d^2\sigma/d\Omega dT_{\pi^0}$ $\mu b/sr - MeV$	T_{π^0} MeV	$d^2\sigma/d\Omega dT_{\pi^0}$ $\mu b/sr - MeV$	T_{π^0} MeV	$d^2\sigma/d\Omega dT_{\pi^0}$ $\mu b/sr - MeV$	T_{π^0} MeV	$d^2\sigma/d\Omega dT_{\pi^0}$ $\mu b/sr - MeV$
60	0.0 ± 19.7	60	0.0 ± 11.8	60	2.0 ± 3.7	60	-0.1 ± 2.3
70	-0.2 ± 12.0	70	2.0 ± 4.4	70	-0.2 ± 4.1	70	-1.5 ± 5.3
80	0.0 ± 4.6	80	1.6 ± 2.2	80	-0.7 ± 1.3	80	6.5 ± 3.6
90	2.5 ± 3.2	90	2.0 ± 1.9	90	1.8 ± 1.1	90	2.1 ± 2.7
100	5.6 ± 3.3	100	2.8 ± 1.9	100	-0.4 ± 1.3	100	1.9 ± 2.2
110	0.6 ± 1.2	110	4.0 ± 2.0	110	1.1 ± 1.3	110	0.8 ± 1.5
120	-1.4 ± 1.9	120	2.8 ± 2.0	120	0.3 ± 1.1	120	1.6 ± 1.6
130	1.8 ± 3.4	130	4.4 ± 1.7	130	1.5 ± 1.2	130	1.6 ± 1.5
140	-1.2 ± 2.5	140	0.2 ± 1.6	140	0.5 ± 1.0	140	1.3 ± 1.2
150	4.0 ± 2.2	150	2.0 ± 1.6	150	0.5 ± 1.0	150	0.3 ± 1.4
160	2.3 ± 1.7	160	2.2 ± 1.5	160	0.3 ± 0.9	160	1.4 ± 1.2
170	2.8 ± 1.7	170	1.4 ± 1.6	170	1.7 ± 1.0	170	1.0 ± 1.2
180	-1.1 ± 1.4	180	3.4 ± 1.2	180	0.0 ± 0.8	180	1.1 ± 1.1
190	0.9 ± 1.4	190	-0.3 ± 1.3	190	1.3 ± 0.8	190	1.9 ± 1.1
200	2.0 ± 1.4	200	1.8 ± 1.5	200	1.9 ± 0.9	200	0.8 ± 1.2
210	3.1 ± 1.4	210	4.7 ± 1.3	210	-0.1 ± 0.8	210	5.7 ± 1.1
220	-1.9 ± 1.3	220	3.5 ± 1.4	220	0.9 ± 0.9	220	3.6 ± 1.1
230	2.5 ± 1.5	230	6.0 ± 1.5	230	3.3 ± 1.0	230	4.7 ± 1.2
240	4.7 ± 1.7	240	4.6 ± 1.5	240	4.8 ± 1.0	240	3.3 ± 1.1
250	3.0 ± 1.7	250	9.4 ± 1.6	250	6.3 ± 1.1	250	3.0 ± 1.1
260	5.0 ± 1.8	260	12.0 ± 1.9	260	13.0 ± 1.2	260	2.9 ± 1.0
270	6.9 ± 1.8	270	15.0 ± 1.8	270	6.4 ± 1.0	270	1.4 ± 0.8
280	13.0 ± 2.2	280	17.0 ± 1.8	280	4.6 ± 0.9	280	0.8 ± 0.7
290	20.0 ± 2.2	290	16.0 ± 1.9	290	3.8 ± 0.8	290	-0.2 ± 0.7
300	29.0 ± 2.4	300	8.7 ± 1.4	300	1.3 ± 0.7	300	-0.1 ± 0.6
310	33.0 ± 2.4	310	3.9 ± 1.2	310	-0.4 ± 0.5	310	0.0 ± 0.5
320	29.0 ± 2.2	320	1.5 ± 1.0	320	0.9 ± 0.4	320	-0.3 ± 0.5
330	16.0 ± 1.8	330	0.1 ± 0.9	330	-0.5 ± 0.4	330	0.1 ± 0.5
340	4.0 ± 1.4	340	0.4 ± 0.6	340	-0.1 ± 0.3	340	0.3 ± 0.3
350	0.9 ± 1.0	350	0.1 ± 0.5	350	0.1 ± 0.2	350	0.2 ± 0.3
360	0.6 ± 0.7	360	0.0 ± 0.3	360	-0.1 ± 0.1	360	0.0 ± 0.2
370	-0.3 ± 0.3	370	0.2 ± 0.2	370	-0.1 ± 0.1	370	0.0 ± 0.2
380	-0.1 ± 0.2	380	0.0 ± 0.1	380	0.0 ± 0.1	380	0.0 ± 0.2
390	0.2 ± 0.2	390	0.1 ± 0.1	390	0.0 ± 0.1	390	0.0 ± 0.2
400	0.0 ± 0.1	400	0.0 ± 0.1	400	0.0 ± 0.1	400	0.0 ± 0.2
410	0.0 ± 0.1	410	0.1 ± 0.1	410	0.0 ± 0.1	410	0.0 ± 0.2

Table I.12: Table of the doubly differential cross sections for deuteron SCX reaction at T_{π^-} = 371 MeV. The errors reflect the statistical uncertainties only.

$d(\pi^-, \pi^0)nn$, $T_{\pi^-} = 371$ MeV							
$\theta = 85°$		$\theta = 95°$		$\theta = 105°$		$\theta = 115°$	
T_{π^0} MeV	$d^2\sigma/d\Omega dT_{\pi^0}$ $\mu b/sr - MeV$	T_{π^0} MeV	$d^2\sigma/d\Omega dT_{\pi^0}$ $\mu b/sr - MeV$	T_{π^0} MeV	$d^2\sigma/d\Omega dT_{\pi^0}$ $\mu b/sr - MeV$	T_{π^0} MeV	$d^2\sigma/d\Omega dT_{\pi^0}$ $\mu b/sr - MeV$
60	0.9 ± 2.7	60	-0.2 ± 1.3	60	0.1 ± 1.3	60	-2.2 ± 3.3
70	4.0 ± 1.6	70	-1.1 ± 1.8	70	0.6 ± 1.0	70	1.2 ± 1.5
80	3.8 ± 1.5	80	1.7 ± 1.7	80	-0.4 ± 1.1	80	2.0 ± 1.1
90	-2.1 ± 2.5	90	-0.9 ± 2.1	90	2.5 ± 0.9	90	2.0 ± 1.2
100	2.0 ± 1.7	100	3.6 ± 1.8	100	0.8 ± 0.8	100	0.3 ± 1.0
110	0.3 ± 2.0	110	-1.0 ± 1.6	110	2.0 ± 0.8	110	2.1 ± 1.0
120	1.7 ± 1.7	120	-0.3 ± 1.6	120	2.6 ± 0.8	120	0.3 ± 1.0
130	1.1 ± 1.8	130	-0.2 ± 1.4	130	0.3 ± 0.7	130	0.0 ± 0.8
140	-1.8 ± 1.8	140	1.8 ± 1.2	140	1.6 ± 0.6	140	0.0 ± 0.7
150	1.6 ± 1.6	150	1.8 ± 1.2	150	0.4 ± 0.6	150	2.3 ± 0.7
160	0.3 ± 1.7	160	2.2 ± 1.2	160	1.5 ± 0.5	160	1.7 ± 0.6
170	1.9 ± 1.4	170	1.5 ± 1.2	170	1.1 ± 0.5	170	1.9 ± 0.5
180	4.2 ± 1.5	180	5.2 ± 1.1	180	1.8 ± 0.6	180	1.3 ± 0.4
190	1.3 ± 1.5	190	2.2 ± 1.1	190	1.4 ± 0.5	190	0.8 ± 0.4
200	1.9 ± 1.4	200	4.2 ± 0.9	200	1.4 ± 0.5	200	0.0 ± 0.4
210	5.9 ± 1.3	210	5.0 ± 1.0	210	0.9 ± 0.4	210	0.3 ± 0.3
220	4.8 ± 1.4	220	1.9 ± 0.9	220	0.2 ± 0.4	220	-0.1 ± 0.3
230	0.9 ± 1.2	230	2.1 ± 0.7	230	0.8 ± 0.3	230	-0.1 ± 0.2
240	2.6 ± 0.9	240	0.8 ± 0.6	240	0.2 ± 0.3	240	0.6 ± 0.2
250	1.6 ± 0.8	250	0.7 ± 0.6	250	0.0 ± 0.2	250	0.2 ± 0.2
260	0.9 ± 0.6	260	0.4 ± 0.4	260	0.2 ± 0.2	260	0.3 ± 0.2
270	0.3 ± 0.5	270	0.2 ± 0.4	270	0.0 ± 0.2	270	0.0 ± 0.2
280	0.6 ± 0.6	280	-0.2 ± 0.4	280	0.1 ± 0.2	280	-0.2 ± 0.2
290	-0.3 ± 0.4	290	-0.1 ± 0.3	290	-0.2 ± 0.2	290	0.2 ± 0.2
300	0.5 ± 0.2	300	-0.2 ± 0.3	300	0.2 ± 0.1	300	0.0 ± 0.2
310	0.1 ± 0.3	310	0.0 ± 0.1	310	0.0 ± 0.1	310	0.1 ± 0.2
320	0.1 ± 0.2	320	0.1 ± 0.1	320	-0.2 ± 0.1	320	0.0 ± 0.2

Table I.13: Table of the doubly differential cross sections for deuteron SCX reaction at $T_{\pi^-} =$ 371 MeV. The errors reflect the statistical uncertainties only.

$d(\pi^-,\pi^0)nn$, T_{π^-} = 371 MeV					
$\theta = 125°$		$\theta = 135°$		$\theta = 145°$	
T_{π^0} MeV	$d^2\sigma/d\Omega dT_{\pi^0}$ $\mu b/sr - MeV$	T_{π^0} MeV	$d^2\sigma/d\Omega dT_{\pi^0}$ $\mu b/sr - MeV$	T_{π^0} MeV	$d^2\sigma/d\Omega dT_{\pi^0}$ $\mu b/sr - MeV$
60	0.0 ± 1.5	60	0.8 ± 1.5	60	4.7 ± 2.7
70	1.9 ± 1.7	70	1.0 ± 1.6	70	-0.4 ± 1.7
80	-0.5 ± 1.4	80	-1.0 ± 1.3	80	1.8 ± 1.3
90	0.3 ± 1.3	90	-0.1 ± 1.2	90	1.3 ± 1.2
100	-0.9 ± 1.0	100	1.6 ± 1.0	100	-1.2 ± 1.1
110	2.3 ± 1.3	110	-0.1 ± 1.1	110	0.5 ± 1.0
120	1.2 ± 1.0	120	-0.4 ± 0.8	120	0.6 ± 1.0
130	-0.2 ± 0.8	130	1.8 ± 0.8	130	1.7 ± 0.7
140	0.6 ± 0.9	140	2.6 ± 0.8	140	2.3 ± 0.8
150	2.0 ± 0.7	150	2.5 ± 0.6	150	0.8 ± 0.5
160	1.8 ± 0.6	160	0.5 ± 0.5	160	0.6 ± 0.5
170	0.5 ± 0.6	170	0.8 ± 0.5	170	1.1 ± 0.4
180	-0.2 ± 0.5	180	0.0 ± 0.3	180	-0.4 ± 0.3
190	0.2 ± 0.4	190	0.0 ± 0.3	190	0.4 ± 0.3
200	0.3 ± 0.4	200	0.1 ± 0.3	200	0.3 ± 0.3
210	0.7 ± 0.3	210	0.2 ± 0.3	210	-0.3 ± 0.2
220	-0.4 ± 0.2	220	0.2 ± 0.2	220	-0.1 ± 0.2
230	0.0 ± 0.3	230	-0.1 ± 0.2	230	0.1 ± 0.2
240	-0.1 ± 0.2	240	0.2 ± 0.2	240	0.0 ± 0.1
250	-0.3 ± 0.2	250	0.1 ± 0.1	250	-0.2 ± 0.1
260	0.2 ± 0.1	260	-0.1 ± 0.1	260	-0.1 ± 0.1

Table I.14: Table of the doubly differential cross sections for deuteron SCX reaction at T_{π^-} = 371 MeV. The errors reflect the statistical uncertainties only.

Bibliography

[1] T. Ericson and W. Weise. *Pions and Nuclei.* Oxford Science Publications, Oxford, 1988.

[2] R. Arndt et al. *Nuov. Cim*, **43A**, 219 (1978).

[3] E. Kinney. *Inclusive Pion Double Charge Exchange in ^4He at Intermediate Energies*, Ph. D. Thesis, Massachusetts Institute of Technology (1988).

[4] K. Rogers et al. *Physical Review*, **105**, 247 (1957).

[5] R. Rockmore. *Physical Review*, **105**, 256 (1957).

[6] J. Norem. *Nuclear Physics*, **B33**, 512 (1971).

[7] A. Ramakrishnan et al. *Nuclear Physics*, **29**, 680 (1962).

[8] M. Moinester et al. "XI International Conference on Particles and Nuclei (Kyoto 1987)," . Abstract c-72.

[9] H. Garcilazo. *Physical Review Letters*, **65**, 293 (1990).

[10] R. Arndt et al. *Physical Review D*, **43**, 2131 (1991). *Scattering Analysis Interactive Dial-in* (SAID), solution SM92, private communication.

[11] J. Ouyang. *Quasi-Free Pion Single Charge Exchange*, Ph. D. Thesis, University of Colorado (1992).

[12] R. Peterson et al. private communication (1995).

[13] H. Baer et al. *Nuclear Instruments and Methods*, **180**, 445 (1981).

[14] M. Bernheim et al. *Nuclear Physics*, **A365**, 349 (1981).

[15] J. Eisenberg and D. Koltun. *Theory of Meson Interactions with Nuclei.* John Wiley and Sons, New York, 1980.

[16] H. Garcilazo. *Physical Review C*, **35**, 1804 (1987).

[17] D. Griffiths. *Introduction to Elementary Particles.* John Wiley and Sons, New York, 1987.

[18] "Review of Particle Properties," *Physical Review D*, **45** (1992).

[19] H. Yukawa *Proc. Physc. Math. Soc. Japan*, **17**, 48 (1946).

[20] H. F. A. deShalit. *Theoretical Nuclear Physics, Vol. I.* John Wiley and Sons, New York, 1974.

[21] G. Faldt et al. *Nuclear Physics*, **B8**, 1 (1968).

[22] S. Fernbach. *Physical Review*, **84**, 1084 (1951).

[23] G. Chew. *Phyical Review*, **101**, 1570 (1956).

[24] R. Tacik et al. *Physical Review C*, **42** (1990).

[25] J. Comiso et al. *Physical Review D*, **12**, 738 (1975).

[26] P. Berado et al. *Physical Review D*, **6**, 756 (1972).

[27] NMS-Collaboration. *Proposal for a High Resolution Spectrometer for Neutral Mesons*, Los Alamos National Laboratory (1989).

[28] S. Gilad. *Design, Construction and Performance of a High-Resolution π^0 Spectrometer for Nuclear Physics Experiment*, Ph. D. Thesis, Tel- Aviv University (1988).

[29] J. Amann. private communication (1993).

[30] "Introduction to Q," and references therein, LAMPF internal report MP-1-3401-3.

[31] W. Nelson et al. *The EGS4 Code System*, SLAC-Report-265, UC-32 (1985).

[32] G.Bathow et al. *Nuclear Physics*, **B20** (1970).

[33] W. R. Nelson et al. *Physical Review*, **149** (1966).

[34] NMS-Collaboration. The NMS collaboration notes, DAC Vax Cluster, LAMPF, New Mexico. no. 3-159 (1993).

[35] S. Childress. Proc. Third International Conference on Calorimetry in High Energy Physics, edited by P. Hale and J. Siegrist, World Scientific, pg. 253 (1993).

[36] W. Czyz. *Annals of Physics*, **21**, 47 (1963).

[37] R. Peterson et al. *Physics Letters B*, **297**, 238 (1992).

[38] S. Weinberg. *Physical Review*, **B232**, 133 (1964).

[39] L. Faddeev. *Soviet Physics Dokl.*, **7**, 600 (1963).

[40] L. Faddeev. *Mathematical Aspects of the Three-Body Problem in the Quantum Scattering Theory.* (Israel Program of Scientific Translation), Jerusalem, 1965.

[41] C. Lovelace *Physical Review*, **135B**, 1225 (1964).

[42] H. Garcilazo. *Physical Review C*, **47**, 957 (1993).

[43] H. Nielsen et al. *Nuclear Physics*, **B49**, 573 (1972).

[44] J. Haidenbauer et al. *Physical Review C*, **30**, 1822 (1984).

[45] R. Peterson, spokesperson, LAMPF Research Proposal (1994).

[46] "LAMPF Users Handbook", LAMPF internal report MP-DO-3-UHB (1984).

[47] B. Preedom et al. *Physical Review C*, **17** (1978).

[48] R. Burman. private communication (1992).

[49] E. Piasetzky et al. *Physical Review Letters*, **53**, 540 (1984).

[50] J. Beringer. πN *Newsletter*, **No. 6** (1992).